

AFOSR TR 97-0413

REPORT DOCUMENTATION PAGE

Form Approved
OMB No. 0704-0188

Public reporting burden for this collection of information is estimated to average 1 hour per response, including the time for reviewing instructions, searching existing data sources, gathering and maintaining the data needed, and completing and reviewing the collection of information. Send comments regarding this burden estimate or any other aspect of this collection of information, including suggestions for reducing this burden, to Washington Headquarters Services, Directorate for Information Operations and Reports, 1215 Jefferson Davis Highway, Suite 1204, Arlington, VA 22202-4302, and to the Office of Management and Budget, Paperwork Reduction Project (0704-0188), Washington, DC 20503.

1. AGENCY USE ONLY (Leave blank)		2. REPORT DATE	3. REPORT TYPE AND DATES COVERED FINAL REPORT 01 Apr 93 - 31 Mar 97	
4. TITLE AND SUBTITLE (MURI) Environmental Degradation/Fatigue in Aircraft Structural Materials: Relationship Between Environmental Duty/Component Life			5. FUNDING NUMBERS 61103D 3484/ES	
6. AUTHOR(S) Professor R.G. Ballinger, L.W. Hobbs, R.C. Lanza and R.M. Latanision				
7. PERFORMING ORGANIZATION NAME(S) AND ADDRESS(ES) Dept of Materials Science and Engineering Nuclear Engineering Massachusetts Institute of Technology Cambridge, MA 02139			8. PERFORMING ORGANIZATION REPORT NUMBER	
9. SPONSORING/MONITORING AGENCY NAME(S) AND ADDRESS(ES) AFOSR/NE 110 Duncan Avenue Suite B115 Bolling AFB DC 20332-8050			10. SPONSORING/MONITORING AGENCY REPORT NUMBER F49620-93-1-0291	
11. SUPPLEMENTARY NOTES 19971003 067				
12. DISTRIBUTION/AVAILABILITY STATEMENT APPROVED FOR PUBLIC RELEASE: DISTRIBUTION UNLIMITED				
13. ABSTRACT (Maximum 200 words) A University Research Initiative, the objective of which was to develop a methodology for the detection, evaluation, and quantification of the effect of environmental degradation on the life of aircraft components. The program combined laboratory based methodology with field observations and data to develop predictive methodology for the initiation and propagation of localized corrosion damage. The focus of the program was in four major areas: (1) Non-destructive evaluation of environmental degradation, (2) Environmental degradation of structural materials, (3) High temperature environmental degradation of advanced engine materials, and (4) Predictive model development.				
14. SUBJECT TERMS Environmental Degradation, Corrosion, Oxidation, Fatigue			15. NUMBER OF PAGES	
			16. PRICE CODE	
17. SECURITY CLASSIFICATION OF REPORT UNCLASSIFIED	18. SECURITY CLASSIFICATION OF THIS PAGE UNCLASSIFIED	19. SECURITY CLASSIFICATION OF ABSTRACT UNCLASSIFIED	20. LIMITATION OF ABSTRACT	

Environmental Degradation and Fatigue in Aircraft Structures

The Relationship Between Environmental Duty and Component Life

Final Report

AFOSR Contract F49620-93-1-0291DEF

Principal Investigators

**R.G. Ballinger
L.W. Hobbs
R.C. Lanza
R.M. Latanision**

**Departments of:
Materials Science and Engineering
Nuclear Engineering**

**Massachusetts Institute of Technology
Cambridge, MA 02139**

May 30, 1997

DTIC QUALITY INSPECTED 3

Table of Contents

	Page
Table of Contents	1
1.0 Introduction & Background	4
2.0 Program Objectives	5
2.1 Non-Destructive Evaluation of Environmental Degradation	5
2.2 Environmental Degradation of Structural Materials	5
2.3 High-Temperature Environmental Degradation of Advanced Engine Materials	6
2.4 Predictive Model Development	7
3.0 Program Approach	7
3.1 Non-Destructive Evaluation of Environmental Degradation	7
3.1.1 Neutron Tomography/Radiography	7
3.2 Environmental Degradation of Structural Materials	8
3.2.1 Pitting	8
3.2.2 Crack Initiation	9
3.3 High Temperature Environmental Degradation of Advanced Engine Materials	9
3.4 Predictive Model Development	10
4.0 Program Element Progress	12
4.1 Non-Destructive Evaluation of Environmental Degradation	12
4.1.1 Task Element Accomplishments	12
4.1.2 Results & Discussion	13
4.1.2.1 Cooled CCD Camera	13
4.1.2.2 Low Fluence Processing Algorithms	21
4.1.2.3 Neutron Source	27
4.1.2.4 Experimental Results	37

4.1.3 Selected Publications	39
4.1.4 Theses	40
4.2. Environmental Degradation of Structural Materials	41
4.2.1 Electrochemistry of Pitting & Crack Initiation in Aluminum Alloys Under Static Load	41
4.2.1.1 Task Element Accomplishments	41
4.2.1.2 Literature Review	42
4.2.1.3 Experimental Procedures	56
4.2.1.4 Results	68
4.2.1.5 Discussion	117
4.2.1.6 Conclusions	134
4.2.1.7 References	136
4.2.1.8 Theses	141
4.2.2 Pitting and Crack Initiation Under Fatigue Loading	141
4.2.2.1 Physical Metallurgy	142
4.2.2.2 Experimental Procedures	143
4.2.2.3 Experimental Results	143
4.2.2.4 References	146
4.2.2.5 Theses	147
4.3 High-Temperature Environmental Degradation of Advanced Engine Materials	147
4.3.1 Task Element Accomplishments	148
4.3.2 Results & Discussion	150
4.3.2.1 Alloys Studied	150
4.3.2.2 Assessment of Morphology, Chemistry and Misostructure of High-Temperature Oxidation Scales and Substrates using Electron Microscopies	152
4.3.2.3 X-Ray Diffraction Studies of Scale Composition & Texture	160
4.3.2.4 In-Situ Determination of Stress in Oxide Scales and Substrates by X-Ray Diffraction	161
4.3.2.5 Oxidation Kinetic Measurements for Titanium Aluminides	171
4.3.3 Publications	173
4.3.4 Theses	174
4.3.5 References	174
4.4 Predictive Model Development	212
4.4.1 Task Element Accomplishments	212

4.4.2 Model of Corrosion Fatigue Life Prediction Applied to 2091-T351 Aluminum-Lithium Alloy in a Pitting Environment	213
4.4.2.1 Introduction	213
4.4.2.2 Propagation, Interaction and Coalescence of Semi-Elliptical Flaws	214
4.4.2.3 Simulation Results and Discussion	224
4.4.3 Fatigue Life and Pit Predictions	227
4.4.4 Mapping the Regimes of fatigue Crack Initiation in the $\Delta\sigma$ -f Space	232
4.4.5 Theses	236
4.4.6 References	236

1.0 Introduction & Background

The increasing demands to insure safety and reliability of major aircraft components require a much greater ability to predict the onset and the development of degradation and failure in structural and engine materials. The basis of any predictive capability is an understanding of the physics of failure and the way in which it is influenced by changes in materials properties with time and by the operating environment. Such understanding is defined by the constitutive equations for degradation and failure. In structural and engine alloy systems, accurate mathematical modeling of the processes is complex and difficult, but a framework can be defined which enables bounding conditions to be estimated. Along with empirical data from operating airplanes and from laboratory experiments, which can now be carried out in much more representative test facilities, the constitutive equations can be developed into an effective tool.

An important element in the evaluation of structural integrity is the assessment of the current state of the component. This is especially true when environmental degradation, due to general corrosion and/or pitting is occurring in airframe applications or when oxidation and high temperature gas reactions are occurring in engine applications. The initiation of and subsequent propagation of pits in hard to inspect regions in airframes presents special difficulties for NDE. However, the initiation of the final component failure by fatigue crack initiation and propagation from these pits makes the characterization of this damage of critical importance to the evaluation of reliability.

In response to the above needs a University Research Initiative (URI) was initiated at MIT. The program combines the expertise of faculty and students from several Departments; Materials Science and Engineering, Nuclear Engineering, and several disciplines; Materials Engineering, Aqueous Corrosion, High Temperature Corrosion, Physics, Mechanics, and Fatigue & Fracture.

This is the Final Report for the program

2.0 Program Objectives

The objective of the program was to develop a methodology for the detection, evaluation, and quantification of the effect of environmental degradation on the life of aircraft components. Further, the objective of this program was to combine laboratory based methodology with field observations and data to develop predictive methodology for the initiation and propagation of localized corrosion damage.

The focus of the program was in four major areas: (1) Non-destructive evaluation of environmental degradation, (2) Environmental degradation of structural materials, and (3) High temperature environmental degradation of advanced engine materials, and (4) Predictive model development.

2.1 Non-Destructive Evaluation of Environmental Degradation

The objective of this task was the identification and quantification of corrosion related damage. Damage, for purposes of this program is defined as any form of general or localized environmental degradation including general corrosion, pitting, or crack initiation. The program focused on the use of neutron radiography and tomography for the detection of corrosion damage.

The use of neutron radiography (two dimensional imaging) and neutron tomography (three dimensional imaging). More specifically the goals of this task were as follows:

- Demonstration of the ability to detect aluminum corrosion with spatial dimensions of the order of 50 μm .
- Demonstration of the use of both two and three-dimensional imaging methods for the detection of corrosion.
- The development of an appropriate non-reactor based neutron source to permit such imaging in the field.

2.2 Environmental Degradation of Structural Materials

The objective of this task element was to understand the process of crack initiation from pitted surfaces on the aluminum alloys currently in use or projected to become important for newer designs. The program combined fundamental studies concerning the identification and quantification of damage due to corrosion, the physics and mechanics of the initiation and propagation of cracks from corrosion pits, the fundamental interaction between microstructural components (inclusions, grain boundaries, cladding, etc.) and the pitting process, with empirical data from the field to develop a model that will be directly applicable to the prediction of structural life. In addition, it was expected that the methods and analysis used and developed would result in a significant advance in our fundamental understanding of the environmental degradation processes in aluminum alloys and would therefore contribute to the development of advanced materials which are resistant to degradation.

2.3 High-Temperature Environmental Degradation of Advanced Engine Materials

Problems of localized corrosion leading to crack initiation and premature failure are endemic at high temperatures, as well as at low temperature, and are to be found in aircraft engine and supersonic vehicle components subject to service in elevated-temperature gaseous environments. The purpose of this program task was to pursue, in parallel with the analogous low-temperature pitting corrosion/crack initiation program, a study of the mechanisms and implications of crack initiation and propagation arising from environmental attack of alloy coatings at temperatures in the 1200-2000°F (650-1100°C) range where current and near-term developments in aircraft propulsion and supersonic vehicle design have encountered, or are destined to encounter, materials performance limitations. Pursuit of this task has required identification of the mechanisms and microstructures of the high-temperature corrosion products formed on alloys of interest, analysis of the stresses arising in corrosion scales and adjacent substrate alloy, and investigation of the loss of integrity in scales, adjacent alloy and at the scale/substrate interface.

2.4 Predictive Model Development

Corrosion damage detection and prediction is of paramount importance in the maintenance and life extension of airframes. The goal of this Objective was to develop a methodology which combines detection techniques, and degradation data from both laboratory and field to develop a predictive model that will allow for the assessment of corrosion damage in aircraft.

3.0 Program Approach

3.1 Non-Destructive Evaluation of Environmental Degradation

The program consisted of three major tasks: (1) damage identification and quantification, (2) basic studies of pit, crack initiation and other forms of environmental degradation, and (3) life prediction model building. Figure 3.1 shows a schematic of the methodology that was used. The damage identification and quantification task made use of potential drop and/or neutron radiography and tomography techniques, as appropriate, to identify and characterize environmental degradation of aircraft structures. The program focused on actual structures. After examination the structures were then destructively examined to fully characterize the environmental degradation process. We were thus be able to develop a relationship between the NDE results and the detailed distribution of, for example, pitting in terms of density, depth and pit aspect (depth/width).

The laboratory studies focused on the understanding of the mechanisms of environmental degradation leading to corrosion and subsequent crack initiation.

The data from the field were combined with the laboratory data to develop a model for the prediction of the initiation and propagation of environmental degradation.

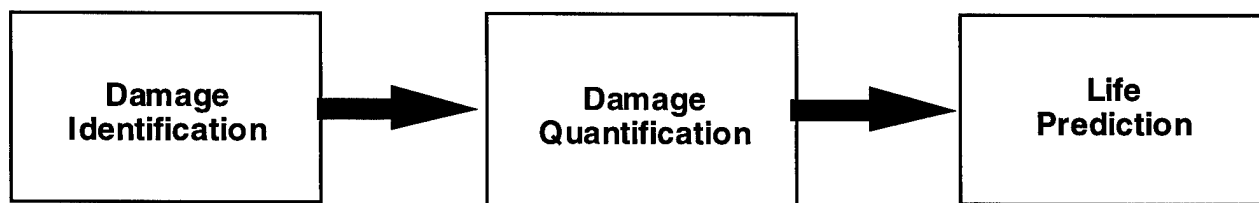


Figure 3.1.1 Schematic of methodology

3.1.1 Neutron Tomography/Radiography

The detection of corrosion products in aluminum is particularly well suited to the use of neutron radiography (two dimensional imaging) and neutron tomography (three dimensional imaging). The sensitivity of any radiographic system depends on both the quantity of corrosion and the attenuation characteristics of the corrosion to the probing radiation. The contrast between

corrosion products, typically aluminum hydrates, is far larger with thermal neutron than with low energy x-rays and is enhanced further if sub-thermal neutrons are used. Further, the use of a low noise electro-optical (CCD) imaging system permits imaging with spatial resolution as small as 50 μm . With this technique, the scale of the image is determined by the optics and can be scaled over a large range. The ultimate spatial resolution is determined by the scintillator thickness which can be as low as 25 to 50 μm . The upper limit to image size is determined by the size of the CCD and by optical losses. Using current single CCDs, upper limits of as large as 1m x 1 m are possible. Thus, a large area scan can be followed by a detailed scan of a selected small area with enhanced spatial resolution.

3.2 Environmental Degradation of Structural Materials

The approach to the understanding and characterization of pitting and crack initiation was a multidisciplinary one, combining mechanics, physical metallurgy, and electrochemistry. The necessity for this approach was dictated by the fact that the process of component failure by environmental degradation is, itself, multi-faceted.

3.2.1 Pitting

The pitting process is one of localized corrosion. In general, the materials of construction, aluminum alloys, consist of a solid solution matrix strengthened by precipitation of intermetallic and carbide phases which act as strengthening agents. The surface of the material, in the case of aluminum alloys, is generally protected by a passive layer of aluminum oxide. While the passive layer is generally protective the pitting process results in the local breakdown of the passive layer and the development of localized corrosion. While cladding of these alloys with pure aluminum has provided protection the requirement for assembly requires a riveted construction. In these regions, where the cladding is broken, pitting is a serious concern.

It is likely that the external environment will be very different from that within the pit. The external environment could be moist salt air, wet salt water, or either of these environments in combination with various contaminants which are present in industrial environments. For the pitting process to begin the external environment must be such that a pit is allowed to initiate. The occluded environment that can develop within a rivet hole between the rivet and the metal

surface is one example. Mass transfer must be possible in order that corrosion products can move in and out of the pit and for water to reach the pit/metal interface. Also, the pit enclave may become packed with corrosion product and further influence mass transport.

The program approach to understanding the pitting process was based on the requirement that pitting produced in laboratory experiments be the same, morphologically and produced in the same environment, as that which exists in the field. Pitting studies were conducted on aluminum alloys (7178-T6, and 7075-T651) which are characteristic of both current (7075) and older (7178) airframes and alloy 2091-T351 which is an advanced aluminum-lithium alloy.

3.2.2 Crack Initiation

The essential question to be answered in the development of life assessment is "will the pit become a crack?" The answer to this question will depend on the mechanical properties of the material, especially the threshold for stress corrosion crack or corrosion fatigue crack initiation, and the degree of and the nature of the pitting present in the material.

The program approach to understanding the process by which cracks initiate from pits was to insure that the laboratory conditions were representative, or overlapping, of the environment in the field. Further, crack initiation studies were conducted using the exact geometry which is used for fasteners and riveted joints.

3.3 High-Temperature Environmental Degradation of Advanced Engine Materials

The focus of this task was the study of the high-temperature failure of surface scales and alloy substrates of interest in advanced engine component materials, in particular oxide scales forming on aluminide intermetallics. Four principal approaches were utilized. The first was dynamic thermogravimetric study of the kinetics of high-temperature scaling of the alloys under consideration over long enough times to produce corrosion microstructures representative of probable in-service conditions. The second utilized the environmental scanning electron microscope (ESEM) and its associated straining hot stage to observe the dynamic development of corrosion microstructures *in situ*, and use of the ESEM and associated thin-window X-ray energy-dispersive spectrometry (XEDS) to provide information about scale morphologies and composition and fracture initiation in cross-sections through the scales and scale/substrate

interface. The third made use of scanning transmission electron microscopy (STEM), and associated windowless XEDS, to provide high-resolution information about microstructural and compositional developments in the scale and the adjacent substrate. The fourth technique used X-ray diffraction in a high-temperature environmental cell to provide information about scale phases present and measure *in situ* the stresses in scale and adjacent alloy substrate developing during growth of scales and as a consequence of differential thermal contractions during temperature cycling (and particularly including glancing-angle measurements that emphasize information in the scale and adjacent substrate near the scale/substrate interface).

3.4 Predictive Model Development

The ultimate goal of the research in this task element was the development of a predictive model for environmental degradation of airframe and engine structures. The program approach for this task was to combine deterministic laboratory modeling and data with field observations to develop a statistically verified model for the prediction of environmental degradation. Figure 3.4.1 shows a schematic of the model development process. In any complex process, airframe degradation included, there is often difficulty in making the connection between the laboratory and the field. At the same time, there is often a large amount of field observations which represents the “facts of the case” if you will. The objective of the program was to allow for prediction of airframe/engine condition.

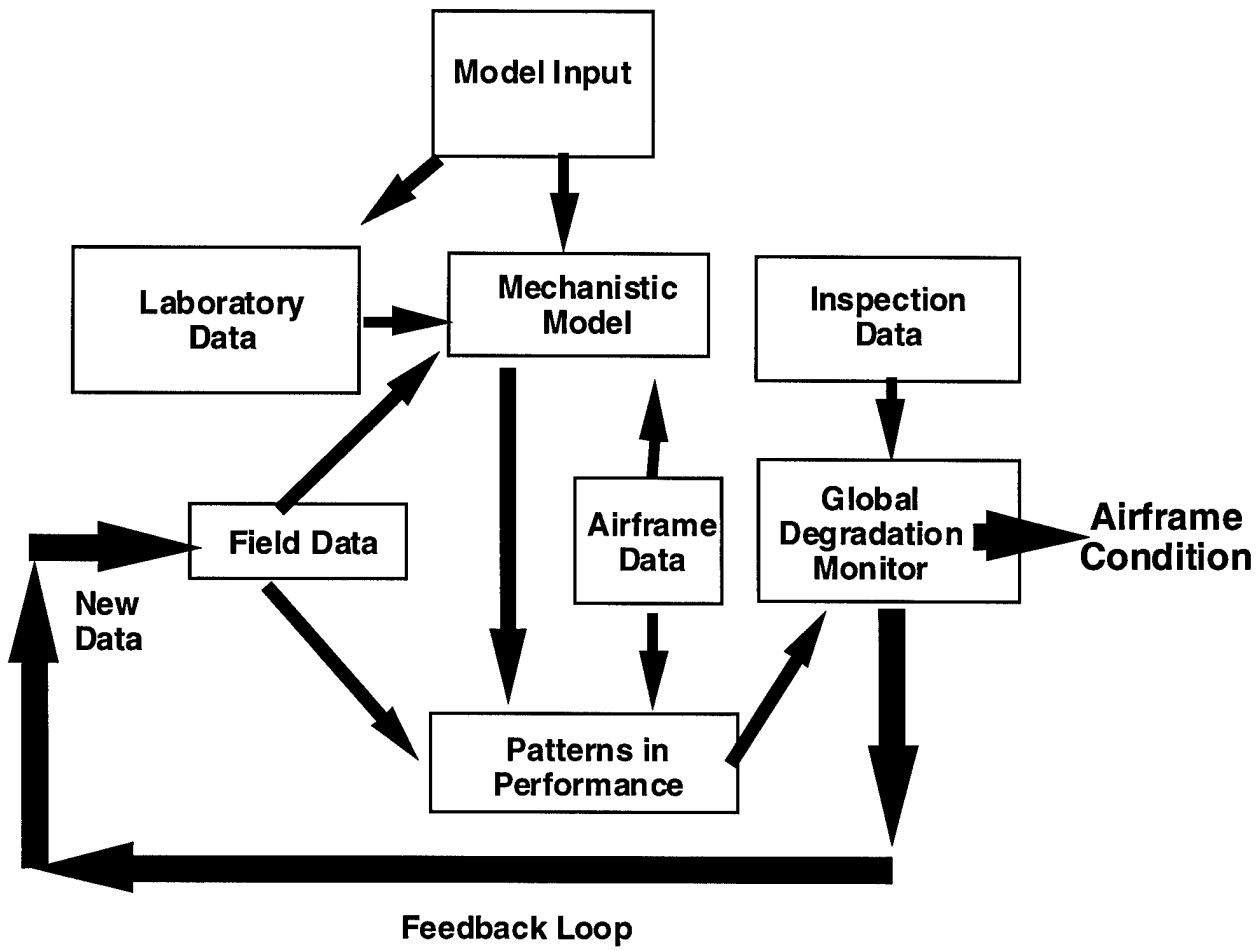


Figure 3.4.1 Schematic of model development effort

4.0 Program Element Accomplishments

4.1 Non-Destructive Evaluation of Environmental Degradation

Neutron tomographic imaging is the only non-destructive technique which permits the quantitative evaluation of hydrogen content and spatial distribution within metals. No other presently available non-destructive method of imaging can reliably detect hydrogen or other low atomic number atoms in thick metal components and in metal components whose geometry may be too complex for NDE techniques such as eddy current, ultrasound, or magnetic techniques. Unlike those techniques, the imaging performance of neutron tomography is not closely tied to the geometry of the object and the imaging does not require an *a priori* model for interpretation of the data.

4.1.1 Task Element Accomplishments

The neutron imaging work has:

- Developed a low noise high spatial resolution camera which is capable of imaging at very low neutron fluence rates
- Developed new algorithms for low fluence image processing with such cameras
- Demonstrated the use of compact ion accelerator based neutron sources for radiographic imaging
- Measured neutron production rates with such accelerators and discovered a new method for enhancing neutron output
- Redesigned moderators based on this new work

- Built a window-less gas target for accelerators which eliminates heating problems of solid metal targets

4.1.2 Results & Discussion

The neutron imaging work has had several significant technical accomplishments which were necessary to achieve the goal of development of a transportable radiography/tomography system. Our initial work was the design, construction and characterization of large area cooled CCD cameras for low fluence neutron imaging and the measurement of spatial resolution, efficiency, and noise characteristics. We have also developed algorithms for the processing of these images which enables us to detect single neutrons. Our accelerator, a 900 keV radio frequency quadrupole (RFQ) ion accelerator has been operated as a neutron source for radiographic imaging of aircraft components and has demonstrated the ability to detect lap joint corrosion. The spectrum of neutrons from the reaction $^9\text{Be}(\text{d},\text{n})^{10}\text{B}$ have been measured at 900 keV, the energy of our RFQ and also at higher energies using another accelerator. The higher energy measurements at 1.2 MeV showed an unexpected result: the production of large numbers of low energy neutrons below 100 keV, an effect not previously observed. This result implies that a small *increase* in our accelerator energy would lead to greatly enhanced thermal neutron output and thus to enhanced imaging capability. We have redesigned our moderator based on these new data and on a recent design method improvement. Finally, a new window-less gas target was constructed for the accelerator. With this, we are able to change to a deuterium gas target and to kinematically collimate the neutron beam. This new target is a major advance in accelerator target construction for high intensity neutron sources.

4.1.2.1 Cooled CCD Camera

The use of cooled CCD cameras for thermal neutron imaging provides substantial advantages over alternative technologies such as film, neutron image intensifiers, or multiwire proportional counters. When used as integrating, non-time resolved, detectors, they are capable of approaching operation as quantum limited detectors, that is, the noise is determined by neutron statistics rather than by intrinsic detector noise.

Since CCD imagers are generally smaller than the objects to be measured, they are operated in a minified mode, that is the image is reduced optically through either lenses or tapered fiber optic

couplers. The use of lens coupled scintillation screens provides a simple and flexible approach to imaging with thermal neutrons as compared to alternatives such as fiber optic coupled systems or large intensifier tubes. A wide range of imaging screen sizes can be operated and tradeoffs made between resolution and noise. In thermal neutron screens based on Li⁶F, the neutron interaction with the Li produces ³H and ⁴He which subsequently deposit their energy in the surrounding ZnS, producing light. The equivalent energy deposited is of the order of 3.5 MeV and thus the light output is substantially larger than for typical medical x-rays. With NE 426, the light output per stopped neutron is 8.5×10^4 photons/neutron and detection efficiency is 15%. In our case, the ZnS is activated with Cu rather than the usual Ag to shift the light further toward the green to improve CCD efficiency. When compared to conventional x-ray imaging with scintillation screens, thermal neutron imaging is considerably easier for comparable fluxes. The reason for this lies in the details of the interactions with the screen. For conventional x-rays in the diagnostic range, typically 60 keV, the light emitted per stopped x-ray is typically 10^3 photons/x-ray. In practice of course, the flux from x-ray sources is much larger and such images are often limited by other factors besides quantum noise. Figure 4.1.1 shows the arrangement of components in the camera.

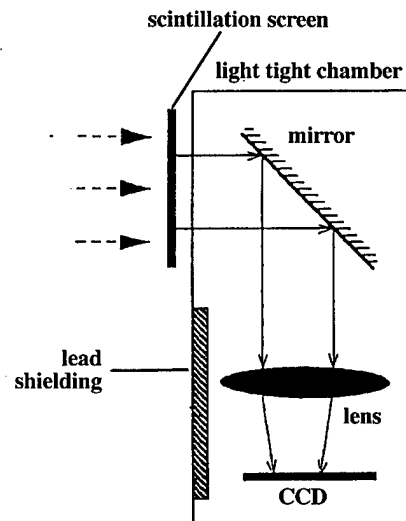


Figure 4.1.1. CCD camera system

For a Lambertian light source typical of a scintillation screen, the CCD signal in electrons per neutron is given by:

$$n_e = \frac{\eta_{sc}\eta_{ccd}\eta_o}{[2F(m+1)]^2} \quad (4.1.1)$$

n_e photoelectrons/neutron produced in CCD

η_{sc} screen detection efficiency

η_{ccd} quantum efficiency of CCD

η_o optical efficiency of lens (transmission)

η_γ photons/neutron produced in screen

F F/number of lens

m minification ratio ($A_{obj}/A_{ccd} = m^2$)

For our system, values are: $\eta_{sc}= 0.15$, $\eta_{ccd}=0.3$, $\eta_o = 0.85$, $\eta_\gamma= 8.5 \times 10^4$, and $F=0.9$. From this we get a simple relation between n_e and the minification:

$$n_e = \frac{6700}{(m+1)^2} \quad (4.1.2)$$

The factor of $[2F(m+1)]^2$ loss is the loss through the lens coupled system. Note that *any* optical system which produces an image smaller than the object will always reduce light by at least a factor of m^2 and this is the limit to the size of scintillation screen for a given CCD imager. A similar analysis can be done for other approaches such as tapered fiber optics or systems of lens/fiber optics combinations. The practical implication is that all other factors being equal, larger CCDs are better since the light loss due to optical reduction will be minimized. Of course, other factors such as readout noise and leakage current may not be equal and so a more detailed comparison will have to be made, particularly if different types of CCDs are being considered. The minimum value of n_e which is practical depends on the noise performance of the CCD and also on the statistical noise. For a quantum limited system, the noise should be limited by the variance in the number of detected neutrons. For cascaded events such as this, the $N^{1/2}$ variance for quantum limited system will be increased by a factor of $(1 + 1/n_e)^{1/2}$ so n_e should be $>>1$ to have a quantum limited system. If we assume that a 5% increase in noise is reasonable, then n_e must be greater than 10 per detected neutron. From this, the limits on minification and hence on screen size may be established using Equation 1, which gives a maximum value for m of about 18 for the system parameters of our camera. The CCD chip size

is approximately 28 mm which gives a maximum size of image of 50 cm.

For scintillation screens composed of Li⁶F-ZnS , typical of screens such as NE Technology NE 426, increased neutron detection efficiency can be obtained with increased LiF content, but this decreases the light output. For example, a screen similar to NE 426, with a mixture of 1 part of LiF to 3 parts of ZnS will produce 1.74×10^5 photons/n with a detection efficiency of 15% while a screen with 1 part of LiF to 2 parts of ZnS will produce 5.9×10^4 photons/n and 48% respectively. The original optimization of mixtures was for use with film where light output was maximized. For a CCD system, if n_e is sufficiently large even with the lower light output, then the increased screen efficiency will reduce the noise of the system. For our CCD camera, the effective optical minification is 7, which results in a calculated value of about 100 e/n *detected*. The size of the pixels on the CCD is 22.5 μm , 0.16 mm in object space, and therefore we have 4×10^3 pixels/cm². We measured thermal neutron fluxes using a GS-20 scintillator, and obtained 2×10^4 n/cm²/s at the screen position. Given the efficiency for detection in the screen of 15%, this gives 3×10^3 n/cm²/s *detected* or 0.75 n/pixel/s which we estimate to result in an average charge per pixel of 75 e/pixel/s compared to an average dark current of 10 e/pixel/s.

CCD Noise Sources

Although more detailed analysis can be made of the noise sources in CCDs, the most common noise sources are dark current noise and readout noise. The dark current is dependent on the CCD temperature and typically is reduced by a factor of 2 for every 7° C reduction in temperature. Readout noise is fixed and is usually most dependent on the readout rate of the CCD. A simple method for determining both these numbers, and also for calibrating the ADC converter in the camera, can be done by subtracting two images made under identical conditions and computing the average of the RMS value of the subtracted images computed per pixel. Using this method, calibration of the system gain in electrons/ADC count is straightforward. With no neutron signals, the dark current is integrated for varying time periods. For each image, the signal in electrons, N_{ij} , is given by:

$$N_{ij} = n_{ij} + n_{read} \quad (4.1.3)$$

where $n_{ij} = idct$, is true dark current signal and n_{read} the readout noise. The associated variance is then just

$$\sigma^2 = \sigma_{ij}^2 + \sigma_{read}^2 \quad (4.1.4)$$

and since σ_{ij}^2 is just equal to n_{ij} , we get

$$\sigma^2 = n_{ij} + \sigma_{read}^2 \quad (4.1.5)$$

If we subtract two frames, then the mean value of any pixel in the difference image is 0 and the variance in the difference is just twice the individual values:

$$\sigma_{diff}^2 = 2\sigma_{ij}^2 + 2\sigma_{read}^2 \quad (4.1.6)$$

The ADC reading, A, is given by:

$$A = GN_{ij} \quad (4.1.7)$$

Using σ to represent values in electrons and Σ values in ADC counts, we can compute the variance in the count, Σ_A^2 which is:

$$\Sigma_A^2 = G^2 \sigma^2 = G^2 (n_{ij} + \sigma_{read}^2) = G^2 (N_{ij} - n_{read} + \sigma_{read}^2) \quad (4.1.8)$$

which reduces to:

$$\Sigma_A^2 = GA - GA_{read} + \Sigma_{read}^2 \quad (4.1.9)$$

where G is the gain in counts/electron and A_{read} is the fixed offset, the signal for zero integration time. The average value for A_{read} can be determined by fitting data for A versus time and computing the intercept or by direct measurement at $t = 0$. Figure 4.1.2 shows data taken with an 1242 x 1152 pixel (27.9 x 25.9 mm) EEV 05-30 CCD operating at -50C, using a

Princeton Instruments ST-138 controller. The intercept is at 78.97 ADC counts, slightly below the measured value of 82.4 for $t = 0$.

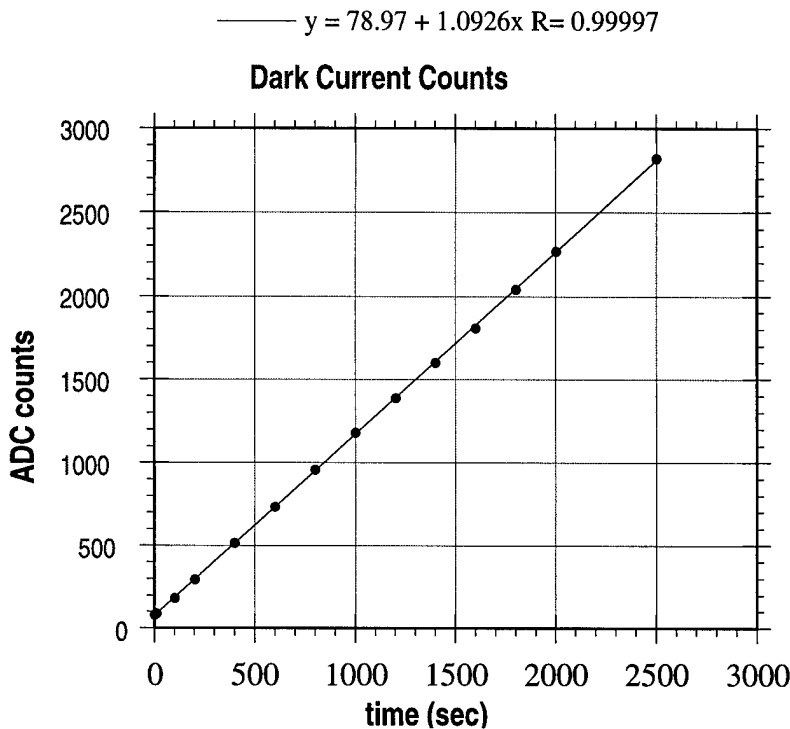


Figure 4.1.2. Determination of A_{read}

If we then plot the variance of the difference between two images versus the average ADC reading, the slope directly gives the gain of the system in electrons/ADC count and from the intercept, the read noise can be determined using the measured value of A_{read} , 82.4, and Equation 4.1.7. From Figure 4.1.3, the gain is 0.097 ADC counts/electron or 10.3 electrons/ADC count and $\Sigma_{read} = 0.56$ ADC counts, or 5.8 electrons.

From Figure 4.1.2, the slope of the dark current is 1.09 counts/s or 11.2 e/s, giving for the dark current noise:

$$\sigma_{dc}^2 = n_{dc} = 11.2t \quad (4.1.10)$$

and the read noise is:

$$\sigma_r^2 = (5.8)^2 = 33.6 \quad (4.1.11)$$

In this system, the variance noise from dark current will exceed that of the read noise for t greater than 3 s. Thus, the read noise contribution dominates for short integration times and the dark current noise will dominate for long integration times. From this, we can estimate a lower limit for neutron flux detectable by such a system, namely when the neutron signal is equal to the noise from dark current. From previous estimates of 100 e/n detected this would yield a lower limit of 0.1 n/s/pixel. Practically, the limit is higher, since light from a single event may be detected in more than one pixel and there may be other sources of background noise, such as gamma rays. The result of these experiments show however that CCD systems may be a viable alternative to imaging systems such as ${}^3\text{He}$ filled multiwire counters. We note also that the dark current noise can be reduced still further by reducing the temperature below -50° C.

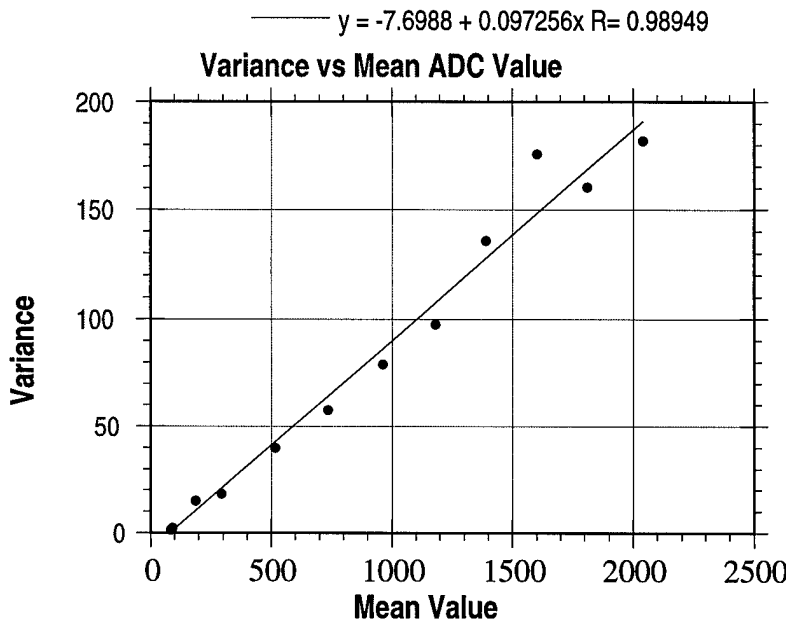


Figure 4.1.3. Determination of gain of camera

In order to compare different CCDs, we can estimate a lower limit for the neutron flux *independent of CCD size*. This can be done if we consider dark current per pixel to be proportional to the area of the pixel. The electron flux $\phi(\text{e}/\text{cm}^2/\text{s})$ produced at the CCD is given by:

$$\phi = \Phi_n n_e m^2 \quad (4.1.12)$$

where Φ_n is the number of detected neutrons/cm²/sec at the screen.

The factor of m^2 comes from the decrease in area due to minification. The factor of n_e computed previously for a Lambertian source is:

$$n_e = \frac{\eta_{ccd} \eta_0 \eta_\gamma}{[2F(m+1)]^2} \quad (4.1.13)$$

and thus:

$$\phi = \left(\frac{\Phi_n \eta_{ccd} \eta_0 \eta_\gamma}{4F^2} \right) \left(\frac{m^2}{(m+1)^2} \right) \quad (4.1.14)$$

which for large m gives:

$$\phi = \frac{\Phi_n \eta_{ccd} \eta_0 \eta_\gamma}{4F^2} \quad (4.1.15)$$

which is independent of CCD size. This allows us to compare CCDs easily since the dark current in CCDs scales as the area, i.e. is just given in e/cm²/sec and thus can be compared to the neutron fluence.

If, as before, we set a lower limit of detected neutron fluence as that where the neutron signal is just equal to N_{dc} , the dark current in e/cm²/s:

$$N_{dc} = \frac{n_{dc}}{A_{pixel}} \quad (4.1.16)$$

$$N_{dc} = \frac{\Phi_n \eta_{ccd} \eta_0 \eta_\gamma}{4F^2} \quad (4.1.17)$$

and finally:

$$\Phi_n = \frac{4F^2 N_{dc}}{(\eta_{ccd} \eta_0 \eta_\gamma)} \quad (4.1.18)$$

which yields approximately $500 \text{ n/cm}^2/\text{s}$ for $22.5 \mu\text{m}$ pixels; results comparable to our previous estimate.

Our measurements have demonstrated that even at low flux rates, cooled CCD cameras are limited primarily by neutron statistics rather than by camera noise. The use of simple lens coupled systems provides a flexible method for imaging large objects. Further, the performance of these systems is predictable and stable and makes use of readily available technologies, especially CCDs.

4.1.2.2 Low fluence Image Processing Algorithms

Most image processing algorithms have been developed for images in which all of the pixels have data and, in general, one can assume that these distributions are continuous. When cooled CCD cameras are used for neutron imaging at low fluence, the images may have large numbers of single neutron events. As we have shown earlier, cooled CCD cameras have noise levels which are compatible with the detection of single neutron events. Thus, with appropriate image processing techniques, the CCD can act almost as a counting detector, and thus extend the usefulness of the camera to very low fluences. By this we mean that each pixel is counted as 1 if there is a neutron event present and 0 otherwise, eliminating low-level noise. In order to investigate this possibility, we have made a detailed examination of the noise performance of neutron detection using CCD cameras.

Some initial analysis showed that the noise levels, both read noise and dark current, varied from pixel to pixel and had therefore to be accounted for on a pixel by pixel basis. This was done by taking multiple images and by measuring the distribution of noise on a pixel by pixel basis in a manner exactly analogous to the method described earlier for characterizing the entire array. We then exposed the camera to a low flux of neutrons and examined the distribution of pulse heights for an individual pixel. From these studies we were able to devise algorithms appropriate to the operating conditions of the CCD.

One possible approach to low noise imaging is in processing each event as it occurs, in effect implementing a counting technique in software. The following sections describe counting

algorithms tested by this project. The counting algorithms fall into three separate regimes depending on whether the spatial resolution of the detection system is limited by the CCD detection system, limited by the scintillation device, or, finally, when the resolution of the CCD detection system is approximately the same as that of the scintillation device. The ratio between the size of the light release from the scintillator screen per neutron event (object) and the resulting image projected on the pixel (image) is the minification. For a scintillator which is optically coupled to a light detector, the designer can change the relative size of the detector to the scintillator by changing the minification of the system. This gives the experimenter the capability to alter the spatial resolution of the system and in addition, to optimize the counting algorithm.

A simple model helps illustrate the difference between these three regimes. After detecting a neutron, the scintillator device gives off a flash of light, that when viewed from a distance, resembles a small area of light. The image of this flash, D_{Scint} is projected onto the CCD chip using lenses. We will define an image diameter which captures 99% out of the total light projected onto the CCD from a single event. This diameter is a measure of the projected scintillator resolution. CCD's are typically laid out in square or hexagonal close-packed arrays. We can model the CCD as a two dimensional array of squares of a given length (L_{Pixel})

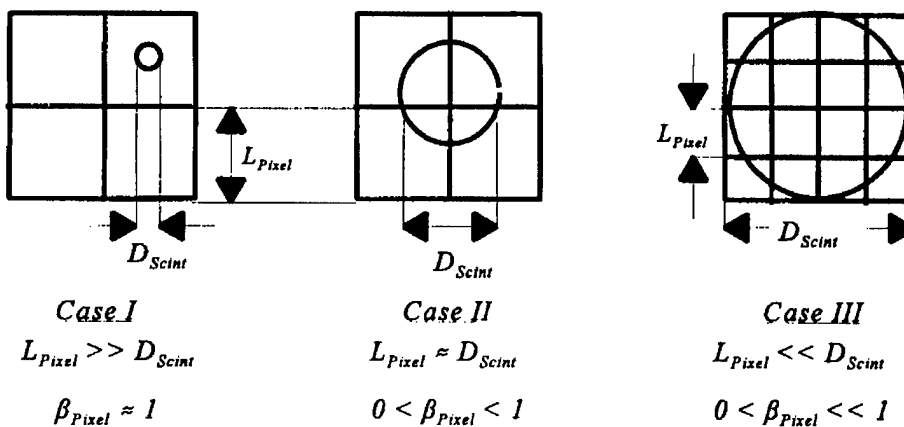


Figure 4.1.4. Relative Sizes of the Pixel and a Neutron Event from the Scintillator Screen

If the pixel is larger than the circle of light given off by the scintillator (Case I) the CCD pixel size limits the resolution of the detection system. In this case, all of the light from a neutron

event that is incident on the CCD falls into a single pixel. If all the light is collected within one pixel for most events, the CCD pixel acts as a single detector system and in this case, each CCD pixel acts independently of the other.

If the pixel size is on the same order of magnitude as the scintillator screen circle, it becomes much more likely that the light collected from a neutron event will be shared by more than one pixel. In this event, the CCD pixel array becomes a redundant detector system. Information from each neutron hit is deposited in multiple pixels. The extreme case of a redundant detector system is one in which the area of light from the scintillator is much larger than an individual pixel (Case III) In this case, the scintillator screen limits the spatial resolution of the detection system and the light will be distributed over many pixels .

Case I: Spatial resolution limited by the CCD spatial resolution

A very simple counting algorithm could be devised for the case when the spatial resolution of the system is limited by the CCD spatial resolution. In this case, the area of light projected onto the CCD from a neutron event is very small compared the CCD pixel. This means that all of the light from scintillator due to a neutron event that is incident on the CCD will be collected in a single pixel . A simple thresholding device could be used to check each pixel for neutron events by setting a threshold value for each detector device based on normal background levels. If the detector was over the threshold value, the detector can be assumed to have been hit by a neutron. A maximum value could then be set for a neutron event. If the detector value was greater than this maximum value, it can be assumed that the event was caused by another source of radiation.

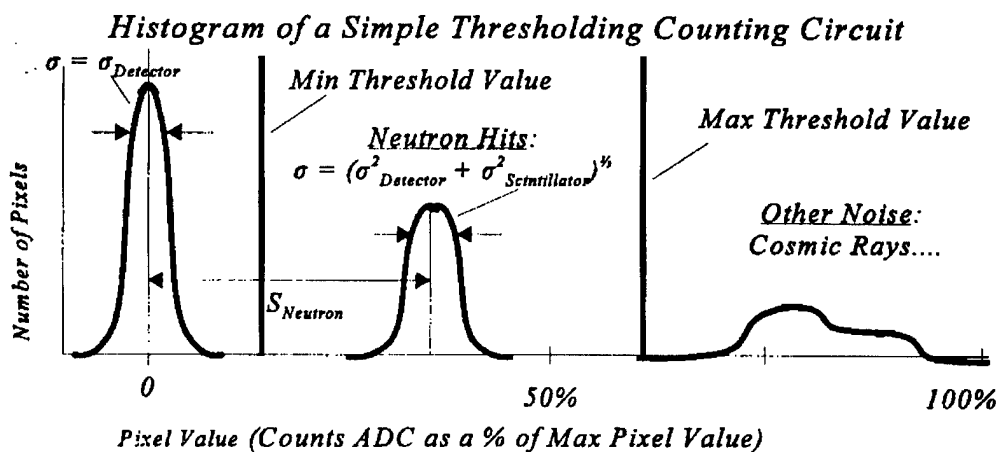


Figure 4.1.5. Case I $L_{\text{pixel}} \gg D$

The histogram for Case I shows the distribution of pixel values in a simple thresholding counting algorithm. The first peak represents pixels that have not been hit by neutrons. This peak can be modeled as a normal distribution with a standard deviation equal to the detector noise. The second peak represents pixels that have recorded neutron events. Again, this peak can be modeled as a normal distribution with a standard deviation equal to the summation of the detector noise and the scintillator noise . These noises are independent of each other and add in quadrature. The distance between the first and second peak is the average signal due to a neutron event and is controlled by the sensitivity of the detector device to a neutron event. The last peak represents large detector response to unwanted forms of radiation. Two thresholds have been set, representing the minimum and maximum value that a pixel with a neutron event may have. Therefore, any pixel falling within these two values could be recorded as a neutron event, and the rest can be discarded as noise.

It is possible that a single pixel could be "hit" by multiple neutrons. For example, if the exposure time and flux level were such that the 30% of the pixels have recorded a neutron hit, then $((.3)^2)/2 = (4.5 \%)$ of the pixels would have two neutron events. If the noise was low enough, and the gain high enough (i.e.: the S/N high enough), then a second peak would appear in the histogram for pixels that have been hit twice. Like the first peak, the standard deviation would be controlled by the detector and scintillator noises, and the distance between peaks would be controlled by the detector gain. The maximum number of neutron events that can be separated from the noise with certainty on an individual pixel establishes the limit for the neutron fluence for our system. The neutron fluence (controlled by the exposure time and the neutron flux) would have to be low enough to ensure that there was not a significant number neutron events that were lost due to our inability to separate out these multiple events on a single pixel from noise.

The criteria for use of a simple threshold counting algorithm are shown in Figure 4.1.5. The first criterion requires a detector with a high signal to noise. To distinguish an event, it is necessary to be able to pick out a single pixel that has been hit a neutron event, from those that have not been hit. The signal due to a neutron hit must be large enough and the noise small enough to statistically separate the two. If the scintillator or the detection system is too noisy or the signal due to a neutron event too low, the neutron peak will overlap with the peak from the system background. In other words, overlap will occur if either peak's width increases significantly, or if

the distance between the peaks decreases markedly. If the peaks overlap, it will be impossible to detect all the neutrons without getting noise from the system. If the threshold value is set conservatively to remove noise, not all of the events will be recorded. If an attempt is made to include these lost values, random system noise may be recorded as an event.

As already discussed, the criteria require that the resolution of the scintillator be much better than the detector array. This can be accomplished with optical coupling or by binning pixels together on the CCD.

Therefore, the efficiency of the simple counting algorithm is dependent on (1) minimization of the scintillator and (2) detector system noise (controls the width of the noise peak and the neutron peak), or (3) maximizing the signal due to a neutron event, and thus sensitivity of the detector (controls the spacing between the noise peak and the neutron event peak). This gives the designer of the algorithm three independent mean, to improve the of the counting algorithm.

Case II: CCD Resolution Equals Scintillator Resolution

If the CCD spatial resolution is approximately on the same order of magnitude as the scintillator spatial resolution, the system histogram is quite different. It is more likely that the light from a single neutron event will affect multiple pixels, each receiving a fraction of the total light.

Although the histogram of pixel values our experiment measured for Case II shows a peak for pixels involved in a neutron event, the peak was not be well separated from the peak of unaffected pixel. This is due to a number of reasons: (1) the signal from an affected pixel is much lower because it only collects a fraction of the light, (2) the fraction of light each pixel receives will vary widely, (3) multiple pixels are affected for each event, and (4) there are a large number of pixels hit with a very low percentage of light for each event which blurs the distinction between the two peaks. It should be noted that the upper threshold limit can still be used to remove unwanted radiation and noise that had a high detector response.

Although it is possible to use a counting algorithm to detect neutrons under these conditions, the efficiency of the algorithm is much lower than it was in Case I. It becomes difficult to detect neutron events with a simple thresholding technique even with an excellent signal to noise ratio for the system. If multiple pixels are affected by a neutron event, it is difficult to set a threshold value that will guarantee only one pixel is counted per event. An attempt to set a lower thresholding limit either resulted in a neutron events being recorded multiple times or in a

number of neutron events simply being discarded with the noise of the system. The first of these options no longer fits the definition of a counting algorithm. The second option results in a much lower detection efficiency for the system.

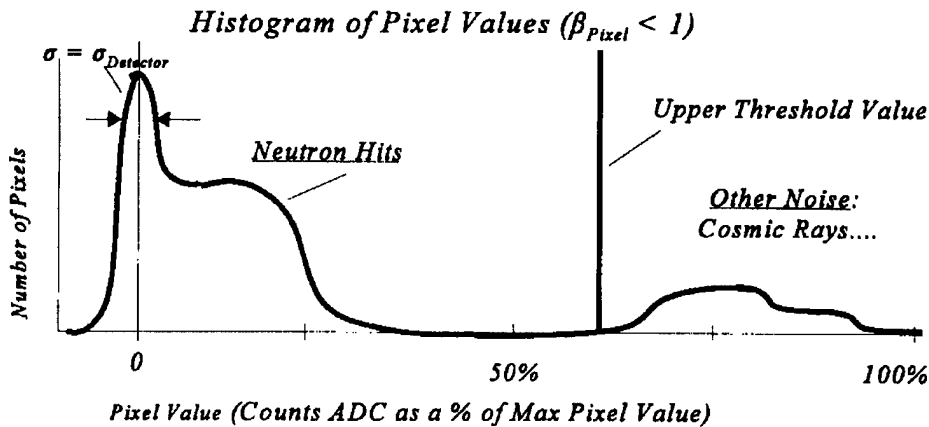


Figure 4.1.6. Case II $L_{pixel} \sim D$

A separate noise filter was developed to decrease the random noise of the CCD and the increased the reliability of our system in finding neutron events by removing unwanted detector noise. Because the fraction of light collected in each pixel is small, the signal strength is much lower for this detector collection technique. Therefore, it is critical that the noise of the system be minimized to maintain a reasonable signal to noise.

A number of noise filters were tested to see their effects on removing system noise. The first technique was the already mentioned thresholding techniques. The initial setting of a minimum threshold value removes much of the unwanted low pixel value noise. If the minimum threshold value is set too high, pixels that collected small fractions of light will be discarded, and this may affect the accuracy of the bubble recognition and centroid calculation. By setting a maximum threshold value, we can again discard the unwanted random noise and radiation noise for which our detection system gave a high pixel response.

The next variant of the noise filter was also able to remove noise based on the number of pixels involved in a given "event". Because a neutron event spans multiple pixels, it is possible to distinguish how many pixels were involved in an event. The number of pixels involved in a neutron event gave us another criteria for which we can filter out noise in the system. By only considering those "bubbles" that spanned a set number of pixels (the number of pixels involved

in a neutron event could be obtained through calculations or by empirical measurement), random pixel noise had much less of an effect on the system. Thus the improved noise filter drastically decreased the detectors sensitivity to random pixel noise, meaning that a more noisy, lower grade (and therefore cheaper) CCD camera could be used.

4.1.2.3 Neutron Source

The major single obstacle to fieldable neutron tomography remains the neutron source. We require collimated thermal neutron fluxes in the range of $10^5 \text{ n/cm}^2/\text{s}$ or greater. Most sources, whether isotopic (Cf-252) or accelerator based produce high energy neutrons which must be moderated to thermal energies. Since the goal is maximized thermal flux, the size of the moderator is important and smaller moderators are desired. The size of the moderator depends on the energy of the neutron source and thus lower energy sources are preferred; design of a system thus requires a balancing between neutron energy, intensity, and moderator design. For practical field use a source should have the following properties:

- Not based on the use of radioisotopes
- Capable of operation on a continuous basis
- Able to produce thermal neutron fluxes of $> 10^5 \text{ n/cm}^2/\text{s}$ with reasonable divergence
- Be compact and transportable

The most common accelerator based sources are those which use the D-T reaction to produce 14 MeV neutrons which then must be moderated to produce thermal neutrons. These sealed tubes generally can produce fluxes of approximately 10^8 to 10^9 n/s into 4π . Although systems exist which claim outputs of as much as $4 \times 10^{11} \text{ n/s}$, the lifetime is correspondingly lower and is measured in hundreds of hours before the tube must be replaced. Further, the source produces high energy neutrons which require larger moderators.

An alternative is the use of small, high current ion (D^+) accelerators based on the radio frequency quadrupole (RFQ) accelerator technology originally developed for the SDI program. The reaction ${}^9\text{Be}(d,n){}^{10}\text{B}$ is one of the most prolific reactions for low energy accelerators and published data (Figure 4.1.9) show that the neutron output from this reaction is second only to $\text{Li}(d,n)$ for incident particle energies between about 1 and 3 MeV. For these reasons this reaction is widely used for the generation of neutrons using small positive ion machines such as cyclotrons and RFQ accelerators. For this project, we have an AccSys technology Model DL-1 RFQ accelerator, part of another project at MIT sponsored by the FAA. This machine is similar to conventional particle accelerators and was designed for continuous operation in commercial applications. The original manufacturers specifications are shown in Table 4.1.1.

The energy spectrum of the neutrons from the accelerator is required to accurately design the moderator for producing thermalized neutrons. Our original designs were based on published neutron energy spectra for the reaction ${}^9\text{Be}(d,n){}^{10}\text{B}$, which showed a spectrum extending to approximately 5 MeV and, critically, *no neutrons below 1 MeV*. The manufacturers data were based on extrapolation of earlier experimental work and not on actual experiments at our accelerator energy of 0.90 MeV. A more critical analysis of the data showed a considerable discrepancy between the experiments, particularly with regard to the critical low energy end of the spectrum, where some experiments showed a larger than expected flux. If these data were valid, the amount of moderating material used in the design was larger than necessary and in fact leads to a *reduction* in the available neutron flux. We have investigated this process both theoretically and experimentally, including some later experiments which we performed at higher energies, and have now a clearer understanding of the physics of this process. Briefly, the neutron flux at low energies is greatly enhanced by a small *increase* in the energy of the incident D^+ beam.

This appears at first to be counterintuitive, however the physics of the compound nucleus formed in the reaction, shows that a new channel opens at 925 keV (25 keV over the nominal energy of the RFQ) and that this channel produces large numbers of low energy neutrons. Figure 4.1.7 shows the experimental results we have obtained at higher energies using time of flight for measurement of the neutron energy.

Table 4.1.1

Accelerated particle	d+
Beam energy (nominal, MeV)	0.9
Neutron yield (n/sec/ μ A)	7.8x10 ⁷
Beam current/pulse (mA)	8
Beam pulse width (μ sec)	30-100
Pulse repetition rate (Hz)	1-640
Maximum duty factor	2%
Maximum target current (μ A)	140
Maximum target yield (n/sec/4 π)	1x10 ¹⁰
Thermalization constant (cm ²)	200
Thermal flux (n/cm ² /sec)	5.0x10 ⁷
Collimated flux at L/D=24 (n/cm ² /sec)	5.4x10 ³
Accelerator length (m)	1.2
Accelerator weight (kg)	180
Electrical requirement (kVA)	12
Pulsed RF power (kW)	40

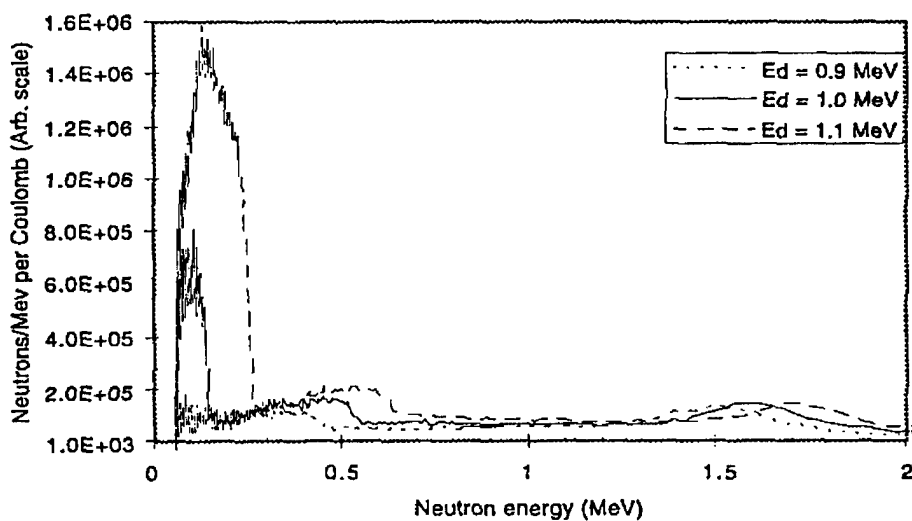


Figure 4.1.7. New data for neutron energy spectra (0 to 2 MeV only shown), for deuteron energies close to the threshold for excitation of the 5.11 MeV compound nucleus state and showing the relative intensity and growth of the low energy spectrum.

These results are very important for the design of a portable source for neutron radiography and tomography where the key parameter is not the total neutron flux at high energies but rather the thermal neutron flux available *after* moderation. The lower energy neutrons in this process are considerably easier to moderate and in addition, the ease of moderation means that the moderator size is smaller, approaching the ideal of a point-like source of thermal neutrons. The quality of the source will depend on the intensity of the thermal neutron flux and on its divergence at the specimen distance, conventionally expressed as the L/D ratio. For equal neutron fluxes at the specimen plane, a smaller moderator size will give a larger L/D, i.e. a smaller divergence. As a result, lower energy neutrons, which are more easily thermalized will provide a better quality, (i.e. brighter) source for thermal neutron radiography.

This is shown in Figure 4.1.8, which shows the results of a Monte Carlo study conducted with the program MCNP4a. It gives the flux at 30 cms from a point source of neutrons surrounded by a moderator of radius R (varying over range 0 to 10 cm), as a function of the neutron source energy and the radius. Note that for a true point source, the flux at 30 cm would be 8.84×10^{-5} n/cm² per source neutron. The small radius of moderator also implies a small loss of neutrons, hence moderation only results in a loss of about a factor of two over ideal. This preliminary design did not include any reflectors in the moderator, only a simple polyethylene sphere. The use of reflectors could increase the flux in the forward direction by a factor of three or more.

The results show clearly that the maximum neutron flux occurs for low energy neutrons with energies around a hundred keV. Note that when the energy of the deuteron beam is at 900 keV, corresponding to our RFQ accelerator, the spectrum of neutron energies is much higher and the efficiency for production of thermal neutrons is correspondingly lower. These are also thermalized efficiently in a small moderator, providing a beam with small divergence (high brightness). Thus, these new physics results provide the counter-intuitive result that the low energy neutron flux and hence the neutron flux for radiography or tomography can be increased if the energy of the beam is increased by 200 keV or so.

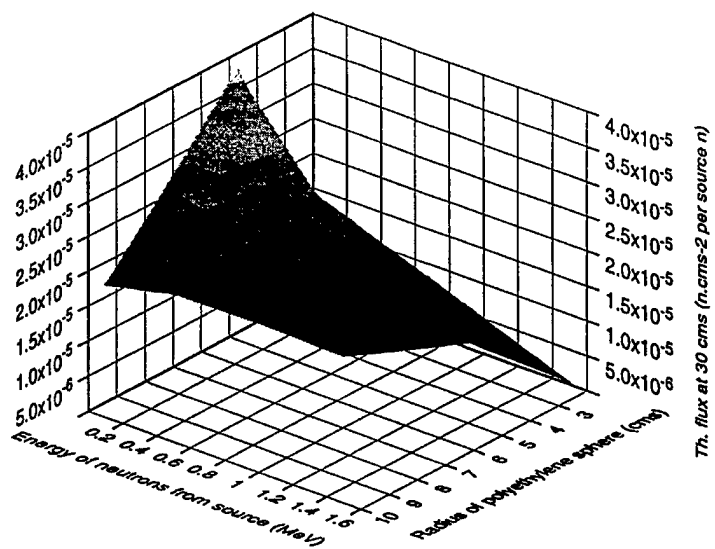


Figure 4.1.8. Thermal neutron flux at 30 cms as a function of moderator size and the neutron source energy. Results are from a Monte Carlo study using MCNP4a. Note that the radius of the moderator is only 5 cm if low energy neutrons are to be moderated.

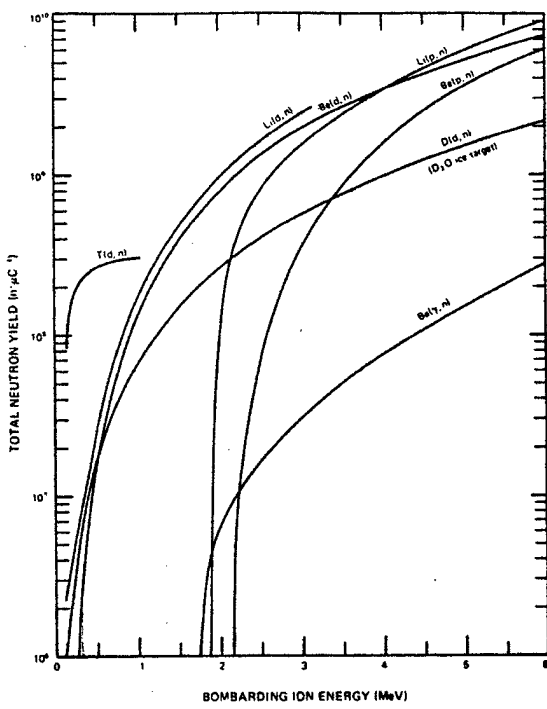


Figure 4.1.9. Neutron yield for various accelerator based reactions. Our present accelerator uses the Be(d,n) reaction at .9 MeV with a nominal yield of $7.8 \times 10^7 \text{ n/s}/\mu\text{A}$. We propose to operate at 1.2 MeV with a yield of about $3.5 \times 10^8 \text{ n/s}/\mu\text{A}$.

The increase in beam energy to 1.2 MeV may be accomplished by putting the target at -300 kV above ground or by changing the RFQ resonator. (RFQ accelerators are fixed in energy by the mechanical and electrical design of their internal RF structure). The increase in energy from .9 MeV to 1.2 MeV will also increase the total neutron yield by approximately a factor of four as shown in Figure 4.1.9.

Moderator Design

As shown in Figure 4.1.8, the thermal neutron yield depends quite strongly on the energy spectrum of the source neutrons. The factor which is often used to express this is the thermalization factor (TF) defined as the ratio of neutron source strength (n/s) to neutron flux ($n/cm^2/s$) (units are cm^2). Lower values of thermalization factor are preferred. Substantial improvements over simple polyethylene moderators can be obtained using lead or tungsten to modify the incoming neutron spectrum and also to act as a reflector. Figure 4.1.10 shows one of their designs based on use of a 14 MeV DT source which had a TF of more than 5 lower than simple polyethylene moderators. The TF for this design is 200 cm^2 for 14 MeV neutrons. An improved moderator with a predicted TF of 200 will produce a thermal flux of $5 \times 10^7\text{ n/cm}^2/s$ assuming a source strength of 10^{10} n/s from the unmodified accelerator.

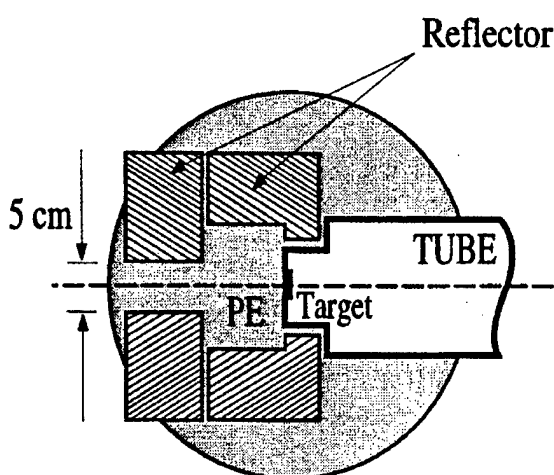


Figure 4.1.10. Improved moderator design.

Windowless Gas Target

One of the major limitations for accelerator based neutron sources is the design of the target.

Although many designs have contemplated high current ion beam accelerators, the heating of the target remains a major problem. In principle, beryllium metal is the best of the metal targets due to its high melting point and ease of fabrication and, as we have seen, the possibility of producing low energy neutrons suitable for thermalization. An alternative approach which has been examined is the use of gas targets rather than solid targets. However, the desirable properties of gas targets with respect to cooling and neutron kinematics are limited by the difficulties of passing any substantial beam current through a thin window without destroying the window in a short time.

In order to overcome these limitations, we have devised and tested a windowless gas target in which the pressure at the accelerator is in the 10^{-7} range and the target is at approximately one atmosphere without any intervening windows.

A windowless gas target for neutron production with low energy particle beams will allow beam currents higher than will a solid or windowed target, and thus will allow greater neutron yield. The primary characteristic of such a target is that there is a pressure change from the target to the accelerator covering several orders of magnitude. This pressure difference is supported by one or more stages of differential pumping through apertures with very small gas conductances.

We are examining a differentially pumped target system with three pumping stages for use with a 900 keV deuteron accelerator that produces a 6 mA (peak) beam with a duty factor of 2%. The beam admitted into the deuterium target has a "waist" of approximately .5-7 mm maximum width over a length of 400 mm. The target pressure is in the range 100-1000 mbar. We are conducting experiments to demonstrate the viability of a differentially pumped target system with a deuterium target pressure of greater than 150 mbar, for use with a beam of 5 mm footprint.

We have constructed the gas target system schematically shown in Figure 4.1.11. The system includes three vacuum pumps-a Balzers WKP 1000 roots blower (as part of a WOD 900 B pumping unit), a Balzers TMU 260 turbopump, and a Balzers TMU 520 turbopump. The pressure drops across the various apertures in this system have been measured for various

aperture dimensions with a Balzers IKR 050 cold cathode gauge, a Balzers TPR 010 Pirani gauge, and a Wallace & Tiernan FA 223 Bourdon gauge.

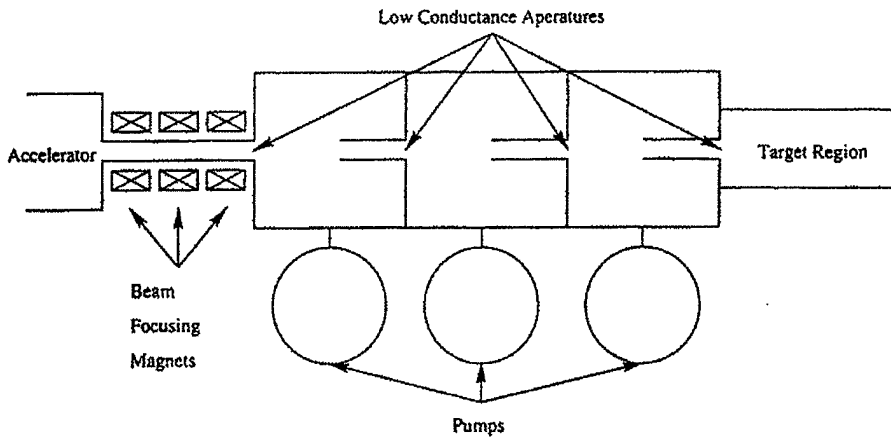


Figure 4.1.11 Gas target schematic.

The pressure drop supported across various apertures by the WKP 1000 blower appears in Figure 4.1.12, and is compared to the pressure drop predicted for viscous, turbulent, blocked flow through such apertures. The calculations were done for deuterium, although the numbers are identical for helium. All experiments were performed with helium. Similarly, the pressure drop supported by the TMU 260 turbopump appears in Figure 4.1.13, compared to the predictions based upon viscous, laminar, blocked flow. It is worth noting that the TMU 260 turbopump was unable to continue operation at inlet pressures greater than 0.05 mbar. This prevents operation with the first pumping stage pressure greater than 4 mbar, and thus the target pressure is limited to 100 mbar. Finally, the pressure supported by the TMU 520 turbopump appears in Figure 4.1.14, compared to predictions based on Knudsen flow. With the second pumping stage operating at 0.03 mbar, the third pumping stage maintains a pressure of approximately 2.0×10^{-6} mbar, which is low enough to prevent problematic gas fluxes into the accelerator system, as well as avoiding any difficulties with neutralization of the beam. Within the second pumping stage the space charge of the beam is advantageous, as it lengthens the waist of the beam.

As detailed in the previous section, operation of the gas target at target pressures greater than 100 mbar is problematic, due to limits on the intake pressure of the second stage turbopump. If one considers the definition of a differentially pumped target, one observes that the conductance of any given aperture can be reduced by blocking that aperture for that portion of the time during

which the beam is not being injected into the target. Thus, for a low duty factor system, the performance of the gas target can be enhanced by intermittently blocking the differentially pumped apertures.

We have constructed a rotating disk valve to be placed within the first pumping stage of the gas target system. This valve will block both the first and second apertures (that is, the one leading from the target to the first pumping stage, and the one leading from the first pumping stage to the second pumping stage) for 97% of the time. Preliminary measurements indicate that the gas flow through each aperture will be reduced by approximately a factor of ten, including the effect of leakage around the imperfectly sealed aperture..

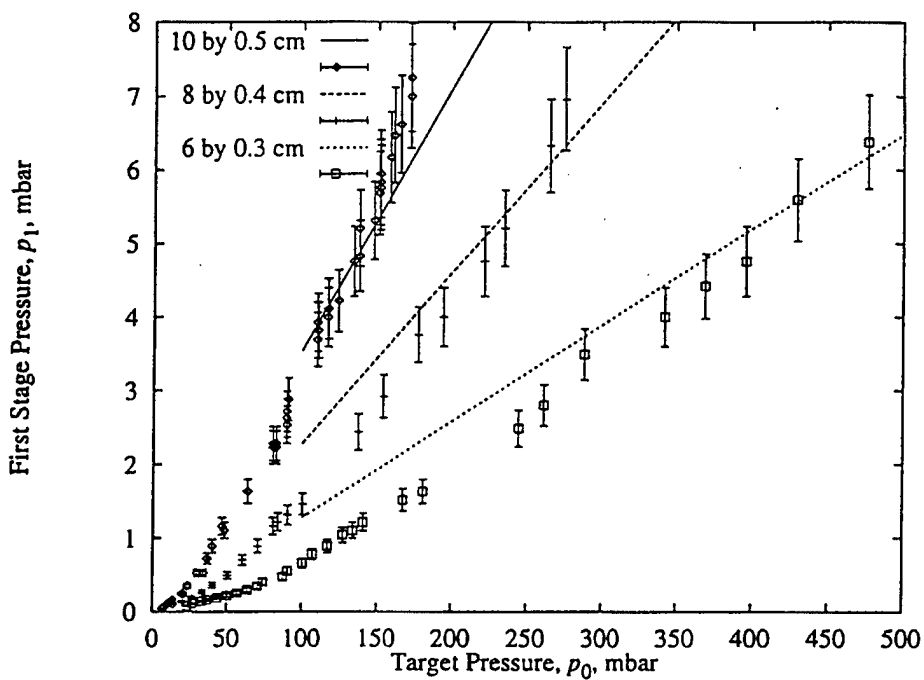


Figure 4.1.12: Comparison of the calculated pressure difference across the first aperture for a pumping speed of 278 Us to the measured difference for a WOD 900 B roots pumping unit.

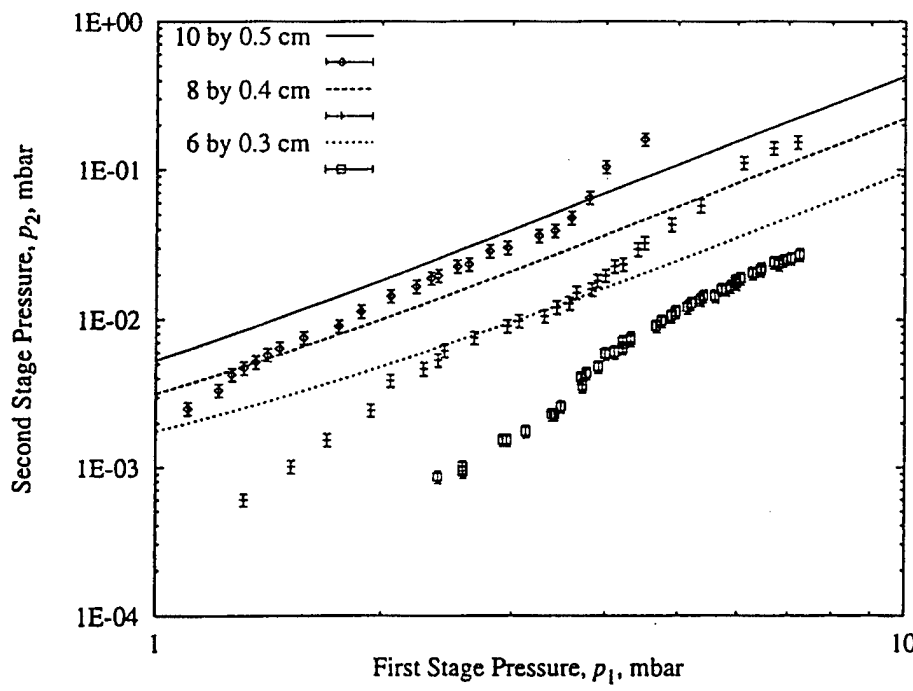


Figure 4.1.13: Comparison of calculated pressure difference across the second aperture to the measured pressure difference. The calculations were done for a pumping speed of 250 l/s, and the measurements were taken using a TMU 260.

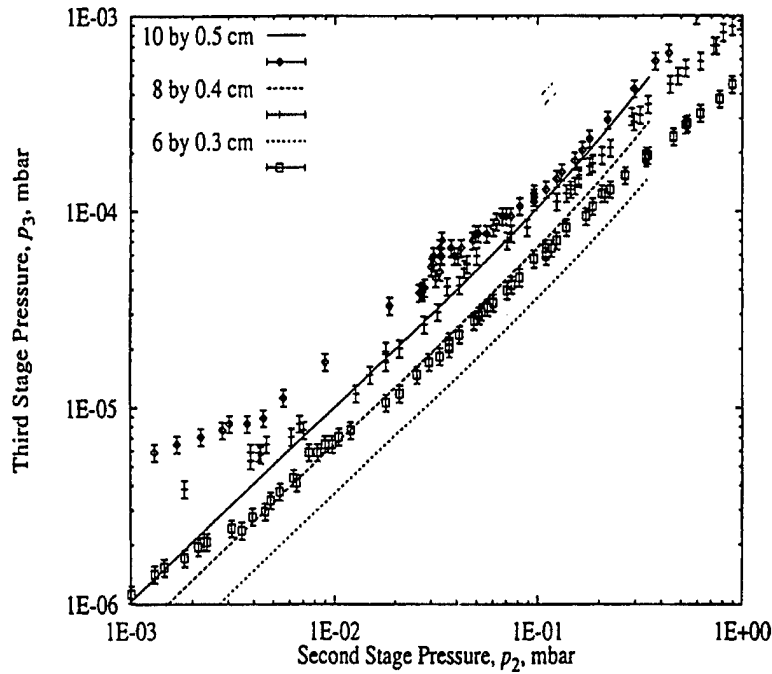


Figure 4.1.14: Comparison of calculated (helium) pressure difference for a 520 l/s pump across the third aperture to the measured pressure difference for a TMU 520.

4.1.2.4 Experimental Results:

The spatial resolution and modulation transfer function (MTF) of the camera system were measured using the edge response of the system to a cadmium edge. Two cases were measured, one with no collimation and another with crude collimation ($L/D = 4$) to reduce scatter.

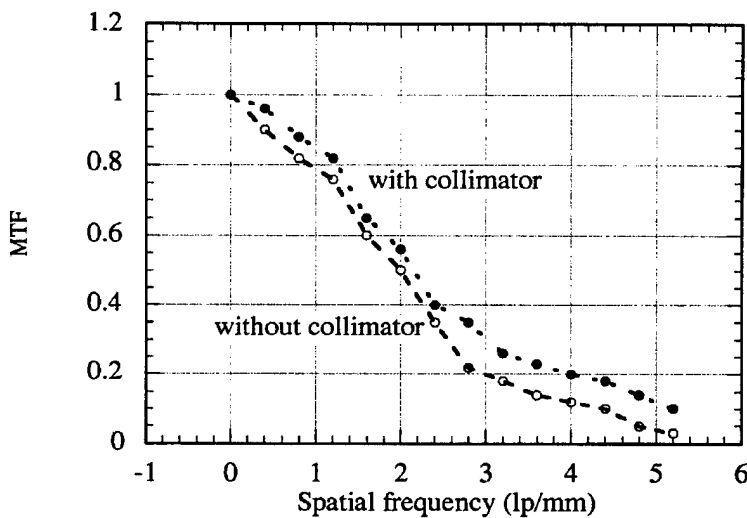


Figure 4.1.15. MTF of CCD camera system

The sensitivity of the system to corrosion detection can be estimated by assuming replacement of aluminum with an aluminum hydrate. For a transmission image, the linear absorption coefficient for pure aluminum is 0.0861 cm^{-1} and 2.4 cm^{-1} for the hydrate. The signal change expected, that is the change in the number of detected neutrons is $\Delta N = N \Delta \mu \Delta x$ which gives for the signal to noise ratio (SNR) a value of $N \Delta \mu \Delta x / N^{1/2}$ or a required number of detected neutrons of $(\text{SNR})^2 / (\Delta \mu \Delta x)^2$. The exact SNR required to establish the presence of some corrosion feature depends on the observer and the feature being detected. For example, using the criterion often used of an SNR of 5 requires 4.2×10^5 detected neutrons. In Figure 4.1.16 we show a neutron radiograph of the lap joint of a Boeing 737 aircraft. The neutron image estimated the amount of corrosion at approximately $100 \mu\text{m}$ thick and this was confirmed by subsequent measurements on the disassembled joint, shown in Figure 4.1.17, where the arrows show the corrosion. Figure 4.1.16 has been enhanced to show contrast more clearly, but quantitative measurements were made on the unenhanced images to determine corrosion thickness.

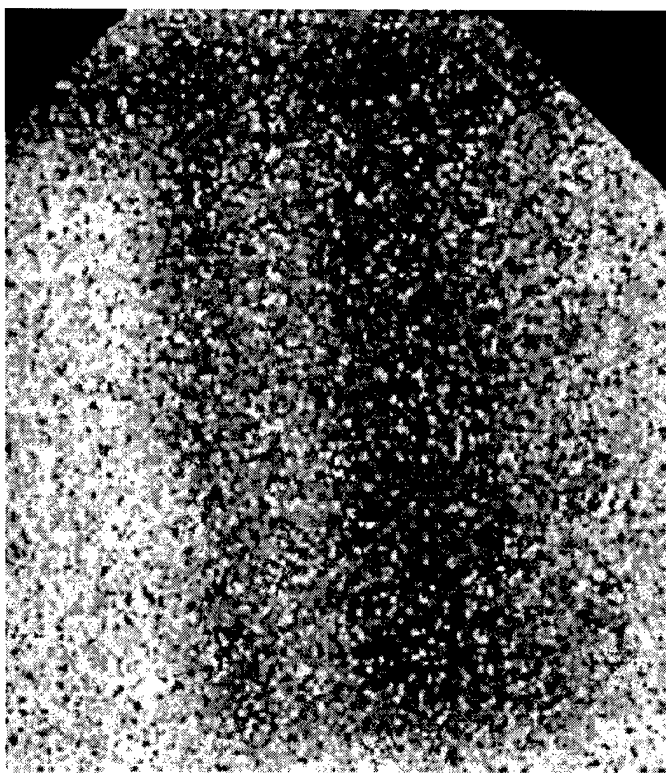


Figure 4.1.16. Neutron Radiograph of Boeing 737 lap joint

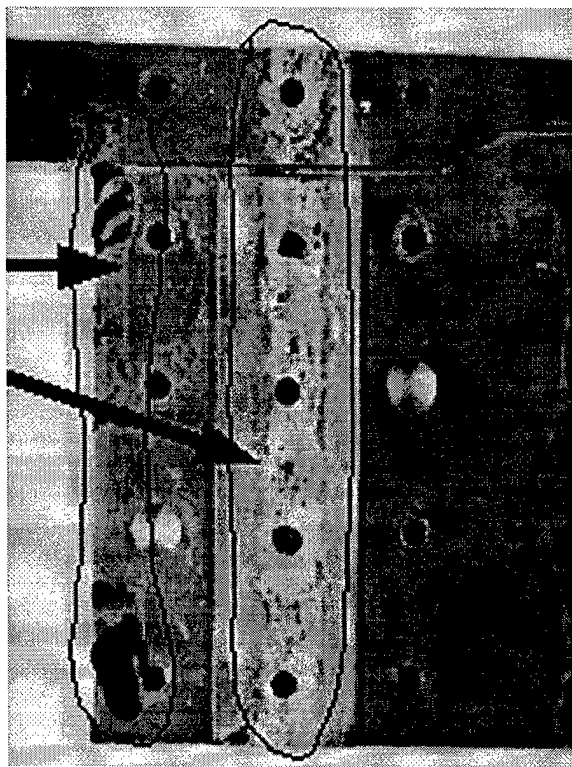


Figure 4.1.17. Photograph of disassembled lap joint

4.1.3 Selected Publications from This Task Element

R.C. Lanza, D.M. Fink, E.B. Iverson, E.W. McFarland, and S. Shi , "An RFQ Accelerator Based Neutron Radiography and Tomography System", 5th International Conference on Applications of Nuclear Techniques, Crete, 1996, G. Vourvopoulos, ed, "Neutrons in Resaerch and Industry",SPIE Proceedings Vol. 22867, SPIE Optical Engineering Press, Bellingham (1997) and Fifth World Conference on Neutron Radiography, Berlin, 1996 (accepted for publication 1996)

J.I.Watterson, R.C. Lanza, J. Guzek, U.A.S. Tapper, W.R. McMurray and E. Iverson, "The Small Deuteron Accelerator as a Source of Slow Neutrons", 5th International Conference on Applications of Nuclear Techniques, Crete, 1996, G. Vourvopoulos, ed, "Neutrons in Resaerch and Industry",SPIE Proceedings Vol. 22867, SPIE Optical Engineering Press, Bellingham (1997)

R.C. Lanza, S. Shi and E.W. McFarland, "Cooled CCD and Amorphous Silicon based Neutron Imaging Systems for Low Fluence Neutron Sources", 5th International Conference on Applications of Nuclear Techniques, Crete, 1996, G. Vourvopoulos, ed, "Neutrons in Resaerch and Industry",SPIE Proceedings Vol. 22867, SPIE Optical Engineering Press, Bellingham (1997) and Fifth World Conference on Neutron Radiography, Berlin, 1996 (accepted for publication 1996)

E.B. Iverson, R.C. Lanza, and L.M.Lidsky, "A Windowless Gas Target Neutron source", 5th International Conference on Applications of Nuclear Techniques, Crete, 1996, G. Vourvopoulos, ed, "Neutrons in Resaerch and Industry",SPIE Proceedings Vol. 22867, SPIE Optical Engineering Press, Bellingham (1997) and Fifth World Conference on Neutron Radiography, Berlin, 1996 (accepted for publication 1996)

J.I.W. Watterson, J. Guzek, U.A.S. Tapper, W.R. McMurray, R.C. Lanza, and E.B. Iverson, "The Reaction $^9\text{Be}(\text{d},\text{n})^{10}\text{B}$ as a Source of Slow Neutrons for Thermal Neutron Radiography", Fifth World Conference on Neutron Radiography, Berlin, 1996 (accepted for publication 1996)

R. C. Lanza, S.Shi, and E.W. McFarland, "A cooled CCD based Neutron Imaging System for Low Fluence Neutron Sources, IEEE Nuclear Science Symposium 1995

R. C. Lanza, "The Use of Neutron Tomographic Techniques for the Detection of Corrosion Damage in Aircraft Structures", pp 253-259 C.I. Chang and C.T. Sun, eds., AD v 47 Structural Integrity in Aging Aircraft, ASME (New York) 1995

R.C. Lanza, S.Shi, and E.W. McFarland, "A cooled CCD based Neutron Imaging System for Low Fluence Neutron Sources, IEEE Trans. Nucl. Sci., v 43, no. 3, pt.2, pp 1347 - 1351 (1996)

E.W. McFarland, J. Leigh, H. Dai, R. C. Lanza, and R. Odette, "Heterogeneous distribution of hydrogen in titanium compressor blades: detection and characterization by neutron computed tomography", presented at 1993 European Optical Society/SPIE Conference on Active Probe Technologies, L. Myers, P. Young, R. Lanza, and G. Harding, eds., Substance Detection Systems, SPIE Proceedings Vol. 2092, SPIE Optical Engineering Press, Bellingham (1995)

E.W. McFarland, J. Leigh, H. Dai, and R. C. Lanza, "Non-destructive Imaging of Hydrogen in High Performance Titanium Jet Engine Components with Neutron Computed Tomography", presented at 1993 IEEE Nuclear Science Symposium

E. McFarland, H. Dai, H. Na and R. Lanza, Segmented Array Reconstructions for Tomographic Imaging of Large Objects: Theory and an Application to Neutron Computed Tomography, IEEE Trans. Nucl. Sci. v 40, pp 1275 - 1281, (1993)

4.1.4 Theses from This Task Element

Barritt, Andrew Stephen, "Detection of hydrogen embrittlement in steel and steel alloys using method of neutron radiography," S.M. Thesis, MIT Dept. of Nuclear Engineering, 1994.

Godin, Michael A., " Mobile Neutron Sources for Residual Stress Measurement", S.M. Thesis, MIT Dept. of Nuclear Engineering, February 1994

Puffer, Donald B., "Moderator Design for Accelerator Based Neutron Radiography and Tomography Systems", S.M. Thesis, MIT Dept. of Nuclear Engineering, August 1994

Fink, David W., "Detecting Corrosion in Aircraft Components Using Neutron Radiography", S.M. Thesis, MIT Dept. of Nuclear Engineering, February 1996

Klein, Dennis , "Low Fluence Neutron Radiography Techniques", S.M. Thesis, MIT Dept. of Nuclear Engineering, January 1997

Shi, Shuanghe, "Neutron Tomography and Radiography for Corrosion Detection in Aircraft", PhD Thesis, MIT Dept. of Nuclear Engineering, May 1995

Iverson, Erik , "Windowless Gas Targets for Neutron Production", PhD Thesis, MIT Dept. of Nuclear Engineering, January 1997

4.2 Environmental Degradation of Structural Materials

4.2.1 Electrochemistry of Pitting & Crack Initiation in Aluminum Alloys Under Static Load

Stress corrosion cracking which often initiates from the bottom of pits has been observed on aircraft components where corrosive environment and tensile stresses are present simultaneously. This form damage was observed on the wing box lower panel of a fighter aircraft which was fabricated from 7075-T6 aluminum alloy.[1] The predominant damage was pitting in the bores and countersink area of the fastener holes. Extensive intergranular cracking was observed to originate from these pits. “Several surface connected cracks can be seen running between fastener holes. Metallographic examinations showed that substantial intergranular cracking was associated with the surface connected cracks.”[1] The failure of the trailing edge flap hinge lug in an F/A-18 has also been attributed to corrosion accelerated cracking.[2]

This task concentrated on crack initiation from pits in thick gauge, high strength aluminum alloys used for wing applications. Alloy 7178 is a high strength variant of alloy 7075. Many older aircraft, with structural components manufactured from alloy 7178, are still in active service. The relationships between structural as well as microstructural material heterogeneity and the localized corrosion behavior in these aluminum alloys used for older and newer generation airframes are explored. In particular, the effect of the variables on pitting have been examined. Since cracks most often initiate from pits in these structures, the control of this form of localized corrosion is critical to life extension.

The effort in this task element has been approached from the standpoint of electrochemistry. Passive film formation and its breakdown, pitting, are electrochemical processes. It is the local electrochemistry that determines the local environment. This environment, in turn, determines the stability of the protective film. Additionally, the dominant environmental factors such as the presence or absence of oxygen and chloride ions in the electrolyte determine the stability of surface films.

4.2.1.1 Task Element Accomplishments

As a result of this task element, the following key findings have been made.

- A detailed and fundamental understanding of the source of pits and intergranular attack initiation in aluminum alloys 7178 and 7075 has been developed.
- A fundamental understanding of the role of the constituent particles in pit initiation has been developed.
- The electrochemical properties of the constituent particles in alloys 7178 and 7075 have been studied in detail.
- The mixed potential theory has been applied to model the role of environment and microstructural features in the pit initiation process.
- The results of this research have been applied to actual riveted joints to rationalize the observed corrosion behavior.
- While alloy 7178 is more susceptible to pitting and intergranular attack than 7075, both of these materials can be expected to degrade with time.

4.2.1.2 Literature Review

Physical Metallurgy

Aluminum alloys are widely used in the aerospace industry, in part, due to their high strength to weight ratio. The highest strength aluminum alloys are based on the Al-Zn-Mg-Cu system (7xxx series alloys). Typical composition and mechanical properties for some of these alloys are listed in Tables 4.2.1.1 and 4.2.1.2

The 7xxx series aluminum alloys are precipitation strengthened. The most common heat treatments involve a solution treatment, quench, followed by an aging cycle. Table 4.2.1.3 shows some of the heat treatment practices used for these alloys. At the solution treatment temperature, most of the alloying elements are in solid solution. However, manganese rich intermetallics, often present in these alloys, may not be soluble and thus help to retard the movement of grain boundaries. As a result, the elongated shapes of cold worked grains are retained after heat treatment. It has been shown that the elongated grain shape reduces stress corrosion cracking (SCC) susceptibility.[3] Rapid cooling from the solution treatment temperature results in a homogeneous supersaturated matrix. With cooling rates slower than 1000⁰F/sec, heterogeneous nucleation of copper rich precipitates at grain boundaries can occur. This can result in copper

depleted zones adjacent to the grain boundaries. The presence of these depleted zones is often proposed as the source of increased susceptibility to environmental degradation.[4]

The source of strengthening in age hardenable aluminum alloys is the precipitation of Guinier-Preston (GP) zones and derivative equilibrium phases. For the Al-Zn-Mg-Cu alloy system, the precipitation sequence at elevated temperature depends on the zinc to magnesium ratio.

Spherical GP zones precipitate first followed by transformation to η' , then to η ($MgZn_2$) in high zinc-magnesium ratio alloys. η' is a transitional phase which has a hexagonal structure. Its basal planes are coherent with {111} planes of the alloy matrix while the interfaces in its c axis are incoherent. The equilibrium h phase forms at longer aging time. At lower zinc to magnesium ratios, T ($Mg_3Zn_3Al_2$) replaces h as the equilibrium phase. A transition phase T' has also been observed.[4] Table 4.2.1.4 summarizes the characteristics of these strengthening phases found in Al-Zn-Mg alloys.

Heterogeneous nucleation and growth of η along the grain boundaries is often observed in under aged and peak aged material. A solute depleted region, called the precipitate free zone (PFZ) is created adjacent to the grain boundaries due to this precipitation process. Figure 4.2.1.1 shows a TEM micrograph of a grain boundary decorated with coarse $MgZn_2$ particles. The PFZ adjacent to the grain boundary is clearly evident. Further aging leads to the diffusion of solute elements back into the PFZ eliminating the chemical heterogeneity. The presence of these PFZ is often cited as the cause of intergranular corrosion susceptibility.

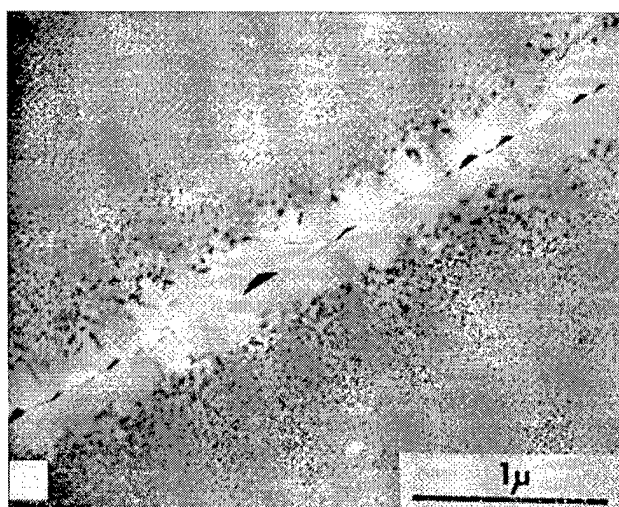


Figure 4.2.1.1. TEM picture showing the coarse $MgZn_2$ particles in the grain boundary and the adjacent precipitate free zone (PFZ) in Al-Zn-Mg alloy. [5]

**Table 4.2.1.1. Chemical composition limits of commercial aluminum alloys (in wt. %
maximum unless shown as a range [6]**

Alloy	Zn	Mg	Cu	Fe	Si	Mn	Cr	Ti
7049	7.2-8.2	2.0-2.9	1.2-1.9	0.35	0.25	0.20	0.10-0.22	0.10
7050	5.7-6.7	1.9-2.6	2.0-2.8	0.15	0.12	0.10	0.04	0.06
7075	5.1-6.1	2.1-2.9	1.2-2.0	0.50	0.40	0.30	0.18-0.35	0.20
7178	6.3-7.3	2.4-3.1	1.6-2.4	0.50	0.40	0.30	0.18-0.35	0.20
7079	3.8-4.8	2.9-3.7	0.40-0.80	0.40	0.30	0.10-0.30	0.10-0.25	0.10

Localized Corrosion

The effect of copper on the corrosion properties of aluminum was recognized as early as the 1940's. Brown et al.,[10] for example, produced a series of Al-Cu binary alloys which were solution treated for long periods of time at 525°C. These alloys were then quenched rapidly in cold water. The free corrosion potential of these alloys in the NaCl – H₂O₂ environment is made more noble (less negative) as increasing amount of copper is placed in solid solution. This is shown by the sloping curve in Figure 4.2.1.2. The break in the curve followed by the horizontal section indicates the solubility limit for copper at 525°C has been reached. Increasing the Cu content beyond the solubility limit has little effect on the solution potential of the alloy in the chloride environment examined.

Dix [11,12] measured the open circuit potential between the matrix and grain boundaries of Al - 4% Cu in the same NaCl – H₂O₂ environment. Precipitates, presumably CuAl₂, were found along the grain boundaries. Copper depleted zones were observed adjacent to the grain boundaries. The corrosion potential of these copper depleted zones were found to be 0.044V more active than the grain matrix. Dix thus concluded that the intergranular corrosion susceptibility of the material is caused by the difference in the corrosion potential between these regions.

Table 4.2.1.2. Mechanical and fracture properties for several aluminum alloys [7]

Alloy-Temper	Thickness (in.)	Axis of specimen	Minimum Tensile Strength		Elong (%) in 2in)	Range in plane strain fracture toughness, K_{IC} (ksi \sqrt{in})		
			UTS (ksi)	0.2% YS (ksi)		Long.	Long trans	Short trans
7049-T73	2.000-3.000	LT	70	60	3	32-34	—	18-29
7050-T7351	—	—	—	—	—	36	30	26
7075-T651	0.500-1.000	LT	78	68	7	25-33	19-31	15-20
7075-T7651	0.500-1.000	LT	71	60	6	31	23-26	22
7075-T7351	0.250-1.000	LT	69	57	7	30-41	24-35	19-21
7079-T651	0.250-1.000	LT	74	65	8	25-34	22-28	15-18
7178-T651	0.500-1.000	LT	84	73	6	21-27	18-23	14-21
7178-T7651	0.500-3.000	LT	73	62	6	26-30	21-28	17-19

Table 4.2.1.3. Heat Treatments for Commercial Aluminum Alloys.[8]

Alloy	Temper	Solution Treatment ($^{\circ}$ F)	Artificial aging treatment
7178	T6, T651*	875	24hr 250 $^{\circ}$ F
	T76, T7651*	875	3-5hr 250 $^{\circ}$ F + 15-18hr 325 $^{\circ}$ F
7075	T6, T651*	900	24hr 250 $^{\circ}$ F or 4hr 205 $^{\circ}$ F + 8hr 315 $^{\circ}$ F
	T7, T7351*	900	6-8hr 225 $^{\circ}$ F + 24-30hr 325 $^{\circ}$ F or 6-8hr 225 $^{\circ}$ F + 14-18hr 335 $^{\circ}$ F

* Stress relieved by cold stretching (to produce permanent set of 1.5% to 3% for sheet and plate) after solution heat treatment and prior to any elevated-temperature precipitation treatment.

The effect of other principal alloying elements on the corrosion potential of aluminum binary alloys are summarized in Figure 4.2.1.3. Manganese has a similar effect as copper. Namely, increasing the Mn content increases the corrosion potential to more noble values. Zinc and magnesium have the opposite effect. The corrosion potential becomes more active when the Zn and Mg content is increased.

Table 4.2.1.4. Characteristics of strengthening phases in Al-Zn-Mg alloys [9]

	GP Zones	h'	h	T
Stoichiometry	α	MgZn ₂	MgZn ₂	(Al,Zn)49Mg32
Shape	Spherical	Platelets	Rods, plates	Irregular
Structure	Alternate layers of Mg, Zn	HCP, $a = 4.96\text{\AA}$ $c = 8.68\text{\AA}$	HCP, $a = 5.21\text{\AA}$ $c = 8.60\text{\AA}$	BCC $a = 14.16\text{\AA}$
Coherency	Yes	Semi	No	No
Size	35 \AA	200 \AA long 50 \AA wide	500 \AA	α
Transition				
temperature (C)	120 - 160	120	200 - 250	190
Solvus				
temperature (C)	150	250	370	190

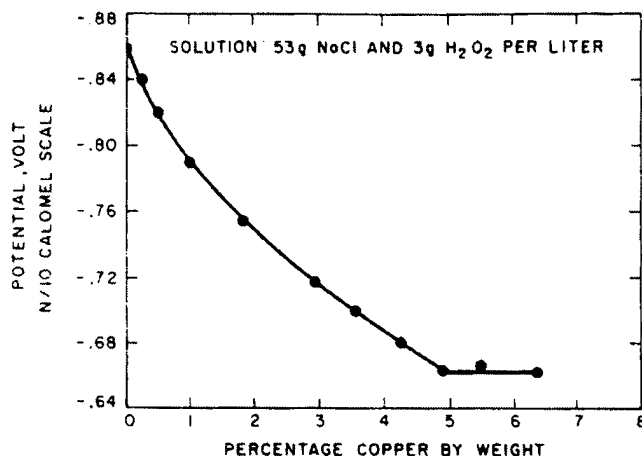


Figure 4.2.1.2. Plot of the solution potential for Al-Cu binary alloy in NaCl – H₂O₂

environment as a function of Cu content. The break in the sloping curve indicates the solubility limit has been reached.

The mechanism proposed by Dix however, does not explain why halide ions are necessary for intergranular corrosion. Galvanic corrosion should occur in any conductive electrolyte. As a result, Galvele et al. [14, 15] proposed that intergranular corrosion susceptibility resulted not from the difference in corrosion potential, but from the difference in the film breakdown potential of these materials in halide environments. Figure 4.2.1.4 shows the anodic polarization behavior of pure aluminum in deaerated NaCl solution. The film breakdown potential is defined

as the potential where there is a marked increase in the current density and is labeled as E_p in Figure 4.2.1.4.

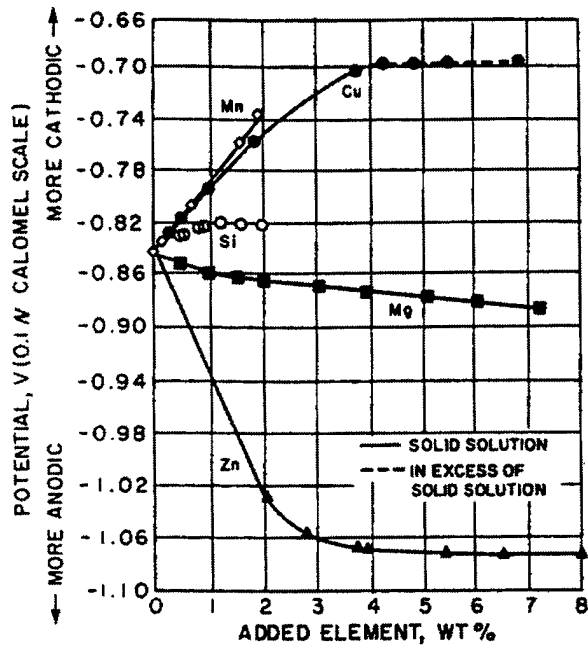


Figure 4.2.1.3. Effects of principal alloying elements on the solution potential of Al binary alloys in NaCl – H₂O₂ solution at 25°C [13]

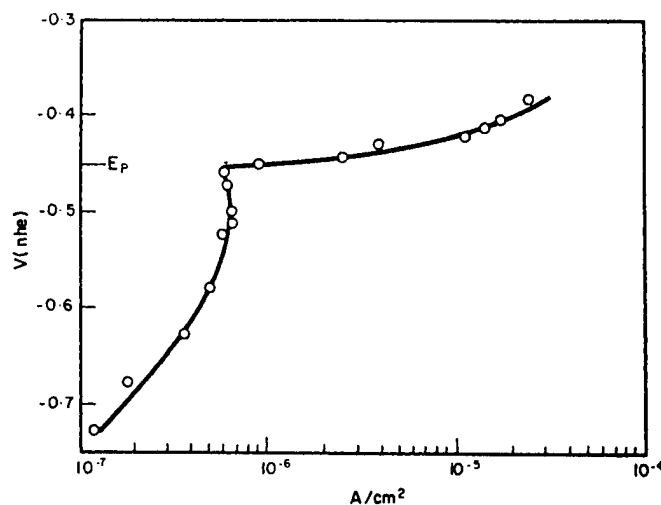


Figure 4.2.1.4. Anodic polarization curve of 99.99% Al in deaerated 0.1M NaCl solution. The breakdown potential (E_p) is the potential at which there is a marked increase in current density and signifies the onset of pitting [14]

Although pure aluminum is a highly reactive metal, the formation of a surface film often results in passivity. Figure 4.2.1.5 shows a phase stability diagram (Pourbaix diagram) for the aluminum system. $\text{Al}_2\text{O}_3 \cdot 3\text{H}_2\text{O}$ is the thermodynamically stable phase in aqueous environments with pH of roughly 4 to 10.[16] This oxide is stable to very noble (positive) potentials. The stability of this film however, is strongly influenced by the presence of halide ions. When aluminum alloys are polarized to potentials more noble than the film breakdown potential in halide environments, corrosion pits are observed on the surface of the alloy. The film breakdown potential, in this case, is therefore labeled as the pitting potential (E_{pit}). In other words, pits will form when the potential become more noble than E_{pit} .

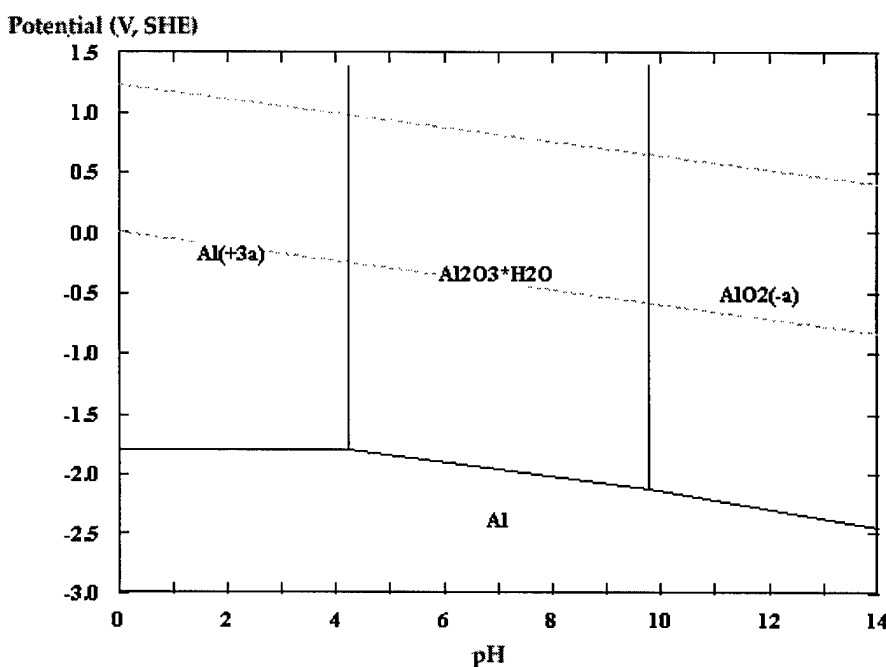


Figure 4.2.1.5. Pourbaix diagram showing regions of stability, passivity, and general corrosion for aluminum in aqueous environment at 25°C

Acidification and enrichment of chloride ions are often observed within active pits.[17] During localized corrosion in chloride environments, hydrolysis of metal ions by reactions such as



can cause the pH to drop to 3.5 at the bottom of a pit. Chloride ions then migrate into the pit in order to maintain charge neutrality.[17] The pit, in essence, is filled with hydrochloric acid. Repassivation of the active pit becomes impossible because the oxide is no longer the

thermodynamically stable phase in this aggressive environment. Active dissolution therefore continues. The process can become autocatalytic as increased dissolution occurs with decreasing pH.

The pitting potential for numerous alloy systems are often found to have a logarithmic dependence on the chloride ion concentration or activity.[18, 19, 20] The data reported in the literature are usually in the form of:

$$E_{pit} = A + B \log[Cl^-] \quad (4.2.1.2)$$

and B is found to depend on the composition of the supporting electrolyte, the measurement technique, and the metal involved.[21] In the case of aluminum alloys, B has been reported to be in the range of 0.05 to 0.13V.[14, 22]

The effects of principal alloying elements on the film breakdown potential of aluminum have been studied. Nilsen and Bardal [23] reported that the additions of magnesium (0.95, 2.7, and 4.5% Mg), manganese (0.8%), or silicon (0.83%) does not significantly affect the film breakdown potential of aluminum alloys in artificial sea water. The addition of tin, however, dramatically lowers the film breakdown potential. The potential drops 0.5V when 0.1% Sn is added.[24]

Wood et al. [25] observed that the surface oxide films on all aluminum, whatever the surface finish, contain sufficient flaws to provide sites at which pits may initiate. Similarly, Szklarska-Smialowska [26] proposed that aluminum oxide film is not an effective barrier against the penetration of water and chloride ions to the metal surface. She suggested that the rate determining step for stable pit growth, is not the diffusion of aggressive species in the environment through the oxide film, but the development of a stable aggressive environment which allows the continuous dissolution of the metal. These flaws in the film are more severe near copper or iron rich segregates because these precipitates interfere with the oxide growth above and around them. More recently, Seri [27] studied the corrosion behavior of a Al-1.4%Fe alloy in NaCl solutions and proposed that the oxide film in the aluminum matrix adjacent to FeAl₃ particles is weak. Pits then initiate at such weak spots and propagate by metal dissolution into the material and by undermining of the oxide film.

Exfoliation refers to the observed corrosion damage which consists of layers of corroded and uncorroded metal. Selective strata of material are corroded forming wedges of corrosion products. The corrosion products then forces the uncorroded layers upward giving rise to a blistered appearance.[28] Exfoliation has been observed in AlMg, AlZnMg, and AlZnMgCu systems of alloys.[29] Manganese depleted regions, which have a more active corrosion potential, have been reported as the sites of corrosion.[29]

Constituent Particles

Iron and silicon are the dominant impurities in commercial grade aluminum alloys. Although iron is highly soluble in molten aluminum, the solubility of iron in solid aluminum is very low (~0.04%).[30] Similarly, the solubility of silicon decreases from 12.6% in molten aluminum to 1.65% in solid aluminum.[30] Most of the iron will therefore precipitate out during solidification forming large second phase particles. These particles are usually in the order of 10 mm in diameter and are labeled as constituent particles. Depending on the purity of the aluminum alloy, the volume fraction of constituent particles can range from 0.1% to roughly 3%. The large second phase constituent particles in aluminum alloys are often cited as the initiation sites of localized corrosion. Elevated iron contents have been reported to increase the pitting susceptibility of Al alloys in halide environments.[17, 31, 32] Hübner et al. [17] suggested the FeAl₃ precipitates act as cathodes in local cells on the metal surface resulting in the increased pitting susceptibility.

Gehring and Peterson [33] found that pits tend to initiate from constituent particles in 5456-H137 Al alloys in sea water. The composition of the particles, based on EDX analysis, roughly conformed to (Cr,Fe,Mn)Al₆. They suggested that pits initiate around an intermetallic particle due to galvanic interaction between the matrix and the particle.

It is obvious that the large second phase constituent particles play a significant role in the initiation of localized corrosion in aluminum alloys. It is therefore useful to review the possible phases that can be present in the Al-Zn-Mg-Cu alloy system. No element is known to have complete miscibility with aluminum in the solid state.[34] Constituent particles can form from the melt when the concentration of the alloying element exceeds its solubility in solid aluminum.

Table 4.2.1.5 lists the solubility limits for various binary aluminum alloys in both the liquid and solid state while Table 4.2.1.6 lists the phases that have been observed in the Al-Cu-Mg-Zn-Fe-Si-Cr system. Depending on the cooling rate during solidification, and the subsequent heat treatments, not all the phases mentioned in Table 4.2.1.6 may appear simultaneously in the alloy.

Table 4.2.1.5 Solubility limits for various binary aluminum alloys.[34]

Element	Temp. ^{0C}	Liquid	Solid
		Solubility (wt.%)	Solubility (wt.%)
Cu	550	33.15	5.67
Cr	660	0.41	0.77
Fe	655	1.87	0.052
Mg	450	35.0	14.9
Si	580	12.6	1.65
Zn	380	95.0	82.8

Table 4.2.1.6 Possible phases in the Al-Cu-Mg-Zn-Fe-Si-Cr alloy system [34]

Alloy system	Alloy examples	Alloy form	Phases
Al-Cu-Mg-Zn-Fe-Si-Cr	7075, 7178	Ingot	(Fe,Cr)Al ₃ , (Fe,Cr) ₃ SiAl ₁₂ , Mg ₂ Si, Mg(Zn ₂ AlCu), CrAl ₇
		Wrought	(Fe,Cr)SiAl ₁₂ , Cu ₂ FeAl ₇ , Mg ₂ Si, CuMgAl ₂ , Mg(Zn ₂ AlCu), Cr ₂ Mg ₃ Al ₁₈

Stress Corrosion Cracking

Stress corrosion cracking (SCC) is the synergistic interaction between tensile stress and corrosion acting on a susceptible material in a specific environment. SCC crack velocity for Al-Zn-Mg-Cu alloys is strongly influenced by their copper content and heat treatment conditions.[35] Figure 4.2.1.6 shows that increasing the copper content above 1% and overaging the material can reduce the SCC crack growth rate by several orders of magnitude. The relation between SCC susceptibility and the microstructure for the 7xxx series aluminum alloys can be summarized as follows:[36]

Microstructure

- Solution treated, no grain boundary precipitation
 - Underaged
 - Peak aged
 - Overaged
- | | |
|-----------------------|----------------------|
| <u>Susceptibility</u> | Immune |
| | Maximum |
| | Susceptible |
| | Decreases with aging |

Although many mechanisms have been proposed for the initiation and growth of intergranular stress corrosion cracking (IGSCC) in high-strength aluminum alloys, two basic theories have evolved: stress assisted anodic dissolution (active path), and a hydrogen embrittlement based mechanism. The anodic dissolution mechanism suggests that a highly localized form of anodic attack occurs along grain boundaries which is aided by tensile stress. The hydrogen embrittlement mechanism, on the other hand, emphasizes the ingress of aggressive hydrogen atoms which leads to a general loss of ductility.

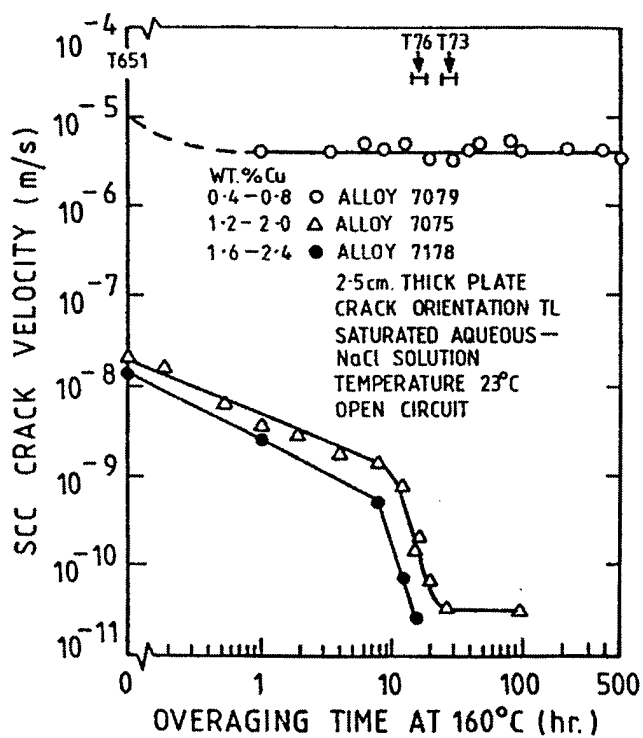


Figure 4.2.1.6. Influence of copper content on SCC performance as a function of aging time at 160°C [37]

Anodic Dissolution

Stress assisted anodic attack is favored by some researchers as the mechanism of IGSCC in the Al-Zn-Mg-Cu alloys. The dissolving phase is either the grain boundary region or the precipitates. For example, Maitra and English [38, 39] studied the corrosion behavior of 7075-T651 and -T7351 in 3.5% NaCl solution. They found that the material is susceptible to both intergranular attack (IGA) and pitting when peak aged (T651), but only susceptible to pitting when overaged (T7351). They reasoned that in the peak aged material, heterogeneous nucleation and growth of η ($MgZn_2$) at the grain boundaries preferentially enriched these sites with Mg and Zn which leads to the increased intergranular corrosion susceptibility. Homogeneous nucleation of η within the matrix in the overaged condition reduces the corrosion potential gradient between the matrix and the grain boundary regions.[40] As a result, the material is no longer susceptible to IGA.

Sedriks et al. [5] studied the electrochemical properties of the intermetallic phase $MgZn_2$ and Al-Zn-Mg alloys in NaCl and $AlCl_3$ solutions. They found the intermetallics to be more anodic than the alloys in environments similar to those found in active crack tips. As a result, they concluded that pits are formed by the dissolution of $MgZn_2$ precipitates. A crack is then formed by the lateral coalescence of these pits due to the applied stress. The crack grows by either ductile fracture or active dissolution until the next particle is reached. Once the crack tip reaches the next $MgZn_2$ particle, the process is repeated again. These processes are illustrated in Figure 4.2.1.7.

Poulose et al. [41] on the other hand, found that the SCC crack velocity, with stress intensity factor taken into account, is inversely proportional to the volume of $MgZn_2$ in the grain boundary. They proposed that the grain boundary precipitates act as sacrificial anodes to retard IGSCC. However, they cautioned, “this advantage (of increasing the volume of $MgZn_2$ at the grain boundary) would have to be balanced against the possible disadvantage that having larger precipitates might contribute to crack initiation.”

Attempts to correlate the size of the precipitate free zone (PFZ) and SCC susceptibility has added to the confusion. Some researchers found that the width of the PFZ has no effect on SCC [42,

43]. Others, on the other hand, have detected increasing [44] as well as decreasing [45] susceptibility as the width of the PFZ is reduced.

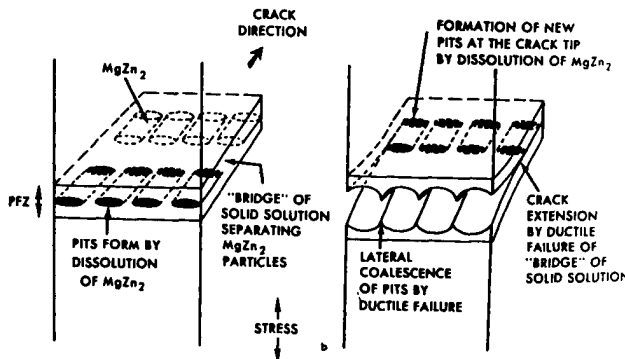


Figure 4.2.1.7. A schematic illustration of crack propagation mechanism involving the dissolution of $MgZn_2$ particles and ductile failure of the “bridge” material at the grain boundary [5]

Hydrogen Embrittlement

The presence of cathodically charged internal hydrogen has been linked to the loss of ductility in high strength aluminum alloys.[46-49] This is often demonstrated by a reduction of area in a tensile test and the occurrence of intergranular fracture. Lynch [50] suggested that hydrogen increases the plasticity in the material which leads to the loss of ductility. Brittle hydride formation [51, 52], crack blunting with hydrogen bubbles [53], reduction in cohesive strength [54], microvoid nucleation [55], and pressurization by hydrogen bubbles [56] have also been suggested as the cause of hydrogen embrittlement. Since hydrogen atoms are generated during corrosion in aqueous environment, hydrogen embrittlement is frequently quoted as the cause of intergranular stress corrosion cracking (IGSCC) in the Al-Zn-Mg-Cu system.

Hydrogen must be present ahead of an advancing crack tip for it to cause embrittlement. Volume diffusion of hydrogen in aluminum however, is extremely sluggish, usually orders of magnitude slower than the SCC growth rate. This led Albrecht et al. [57] to suggest that hydrogen is transported by mobile dislocations rather than bulk diffusion. They showed that straining plus cathodic charging of hydrogen embrittles the high purity underaged 7075 alloy more than charging alone. They also found that a notch accelerates the embrittlement process. As a result,

they concluded that hydrogen transport by mobile dislocations is not only possible, but is kinetically preferred to volume diffusion.

Gruhl [58], on the other hand, suggested that hydrogen transport is via the grain boundaries. He proposed that hydrogen solubility in the grain boundaries is influenced by the amount of Zn in solid solution at the grain boundaries, and the magnitude of the tensile stress normal to the boundaries. He showed a linear inverse correlation between the amount of Zn in solid solution and the time to failure. Grain boundaries, having a lower elastic modulus than the matrix, are preferentially opened up by the tensile stress. As a result, the ingress of atomic hydrogen is greatly accelerated when the grain boundaries are depleted in Zn and are opened up by the tensile stress which leads to IGSCC.

Thompson et al. [59] showed that the loading mode strongly affects the SCC susceptibility of 7075 aluminum alloy. The time to failure in AlCl_3 solution for materials under mode I loading (tension) was much shorter than that under mode III loading (torsion). The fracture surfaces from mode I failures were highly intergranular in nature while mode III fracture surfaces were predominantly transgranular ductile type failure. The triaxial stress state at crack tips in mode I can assist hydrogen cracking but cannot assist anodic dissolution. SCC which takes place by a hydrogen mechanism should therefore be more pronounced in mode I and slightly less or absent in mode III while SCC due to anodic dissolution should be similar in both loading modes. Thompson et al. therefore concluded that SCC propagated by a hydrogen embrittlement mechanism which led to the much greater SCC susceptibility in mode I loading.

Speidel [60] observed that when the material contains a high volume fraction of coherent particles, it is highly susceptible to SCC. When the material contains a high volume fraction of incoherent particles, on the other hand, it becomes highly resistant. A higher volume fraction of incoherent precipitates are formed for the copper rich alloys after the same heat treatment because copper accelerates the transformation kinetics from coherent GP zones to incoherent h phase. As a result, the copper rich alloys are less susceptible to SCC after a short heat treatment while alloys with less than 1 wt% copper required gross overaging before high resistance to SCC is achieved .[61]

Speidel [60] observed that alloys with very few active slip planes are more susceptible to SCC. Coherent particles which are usually sheared during deformation produce a highly localized

deformation structure. The shear stress at which a dislocation can shear a particle depends on the cross sectional area of the particle on the slip plane. As a particle is sheared, its cross sectional area on the active slip plane is reduced. Once a slip plane is activated, it therefore becomes the preferential slip system as the shear stress required for further deformation is reduced. When a particle is looped, as in the case of incoherent particles, no such reduction of shear stress occurs. Thus, other slip systems are just as likely to be active. That is, alloys with a high volume fraction of coherent particles have very few active slip systems; the deformation is highly localized. Large numbers of dislocations are therefore restricted to the few active slip planes which leads to large number of dislocations piled up at the grain boundaries. The stresses at the head of the pile up, and the height of the slip step is proportional to the number of the dislocations in the pile up. Thus, alloys with a large volume fraction of coherent particles have very localized deformation characteristics which in turn leads to very large dislocation pile ups at grain boundaries. Speidel attributed the increase susceptibility of these alloys to either the magnified stresses experienced at the head of a pile-up which aids in the nucleation of a crack, or the increased step height which makes repassivation of an exposed surface more difficult.

Researchers concentrating on the hydrogen embrittlement mechanism of SCC [57, 62, 63] also have made use of the deformation mode argument. They reasoned that if hydrogen is transported by mobile dislocations, the hydrogen concentration ahead of an advancing crack is going to be higher when the mobile dislocations are constricted to very few active slip planes. Hence, SCC susceptibility is higher for non-copper-containing alloys which have a very localized deformation characteristics. For these authors, matrix precipitates are their primary concern. These matrix precipitates exercise the most control on the deformation mode which in turn influences the rate of hydrogen transport to the crack tip. Grain boundary precipitates can only play a secondary role, probably via hydrogen trapping mechanisms and enhanced intergranular embrittlement. The presence and size of the precipitate free zones (PFZ) are of minor importance to these researchers.

4.2.1.3 Experimental Procedures

The corrosion properties of the alloys 7178-T6 and 7075-T651 were studied by potentiodynamic and potentiostatic techniques. Constituent particles were observed to be the initiation sites of pits for these alloys. The role of the constituent particles in corrosion processes was explored by galvanic studies where the intermetallic phases were electrically coupled to pure aluminum.

Galvanic experiments were also conducted on a disassembled riveted wing joint where steel rivets were used to fasten the aluminum panel. Controlled potential constant load and constant displacement stress corrosion cracking tests were conducted to reproduce the phenomenon of intergranular stress corrosion cracking initiating from corrosion pits.

Material

Commercial Materials

As discussed earlier, aluminum alloys 7178 and 7075 are the main focus of this research program. Alloy 7178 is a high strength variant of 7075 and was used in airframes such as the KC-135 and B52. An understanding of the behavior of this material will allow for better extrapolation of current airframe life predictions. Alloy 7075 has a higher fracture toughness and is less susceptible to environmental degradation due to SCC. However, the constituent particle chemistry is similar for both alloys.

Alloy 7178 material was obtained as part of a replaced wing panel from a KC-135 aircraft. The panel was obtained from the U.S. Air Force Air Logistic Center at Oklahoma City and contained obvious corrosion damage at rivet attachment points. The material was identified as being in the T6 condition. Alloy 7075 was obtained in plate form (38mm thick) from a commercial source in the T651 condition. The composition of these materials is listed in Table 4.2.1.7.

Table 4.2.1.7. Chemical composition (wt. %) of the plates used.

Sample	Al	Zn	Mg	Cu	Fe	Si	Cr	Ni	Mn	Ti
7178-T6	90.0	6.38	2.21	1.86	0.23	0.09	0.18	0.005	0.043	0.047
7075-T651	90.4	5.33	2.20	1.47	0.25	0.11	0.18	0.004	0.083	0.040

In addition to the KC-135 panel, a B52 wing panel section was obtained from Boeing - Wichita. The wing panel contained obvious corrosion damage associated with riveted joint areas. Two of the joints, where steel rivets were used to fasten the aluminum panel, were disassembled and used for electrochemical studies. These disassembled joints are presented in Figures 4.2.1.8 and 4.2.1.9. No corrosion was observed in joint #1 (Figure 4.2.1.8). Two areas of corrosion, labeled Area I and II, can be found on the plate from joint #2 (Figure 4.2.1.9 b, c, and d). Exfoliation and pits were observed on the countersink area of the aluminum panel. The rivet from joint #2,

however, was not corroded (Figure 4.2.1.9 a). Samples were cut from the plates and rivets for electrochemical studies. EDX analyses were conducted to identify the composition of the rivets and plates. The results of these analyses are tabulated in Table 4.2.1.8.

High purity aluminum (99.999%) was obtained in rod form for electrochemical studies. The labeling scheme used to identify the orientations and planes of the alloys is shown in Figure 4.2.1.10.

Intermetallic Phases

Five types of commonly occurring constituent particles in aluminum alloys were manufactured in bulk by the hot isostatic press (HIP) process. The composition of these phases was chosen based on analysis of precipitates in the 7178 and 7075 materials described above. High purity elemental powders were used as the starting material. The powders were consolidated in steel cans with 0.5" inside diameter, evacuated, sealed, and hipped. Each sample was then sectioned and polished. The finished products were fully dense. The extent of chemical homogeneity was established by energy dispersive X-ray spectroscopy (EDX) mapping of the polished surface. The target and actual composition of the hipped samples are listed in Table 4.2.1.9. X-ray diffraction was used for phase identification. The obtained spectra were compared to known data and the results are tabulated in Table 4.2.1.10. $\text{Al}_3\text{Fe} (\theta)$ is listed as a “very complex end-centered monoclinic” structure [64] with 100 atoms to the unit cell [65] and not enough is known about the phase to perform a rigorous calculation of the diffraction pattern from first principles.

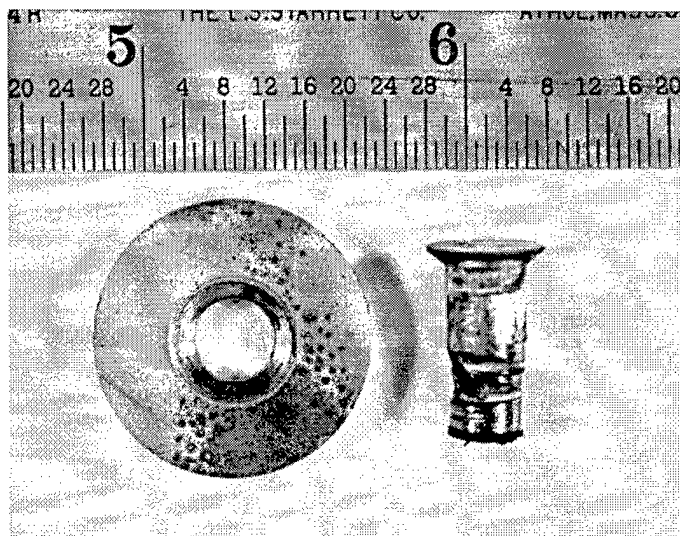


Figure 4.2.1.8. Picture showing rivet and plate from joint #1

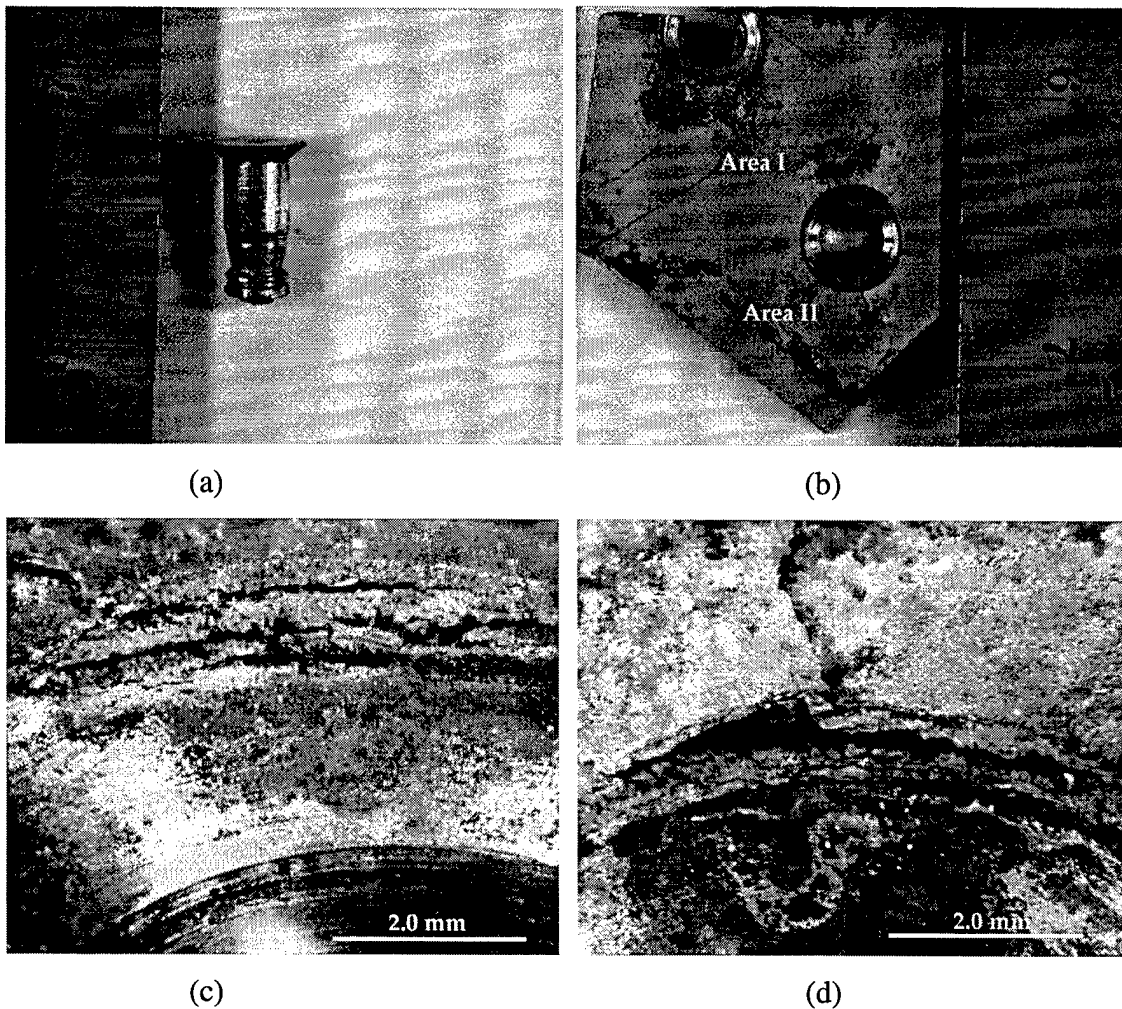


Figure 4.2.1.9. (a) Rivet and (b) plate from joint #2. Note extensive corrosion.

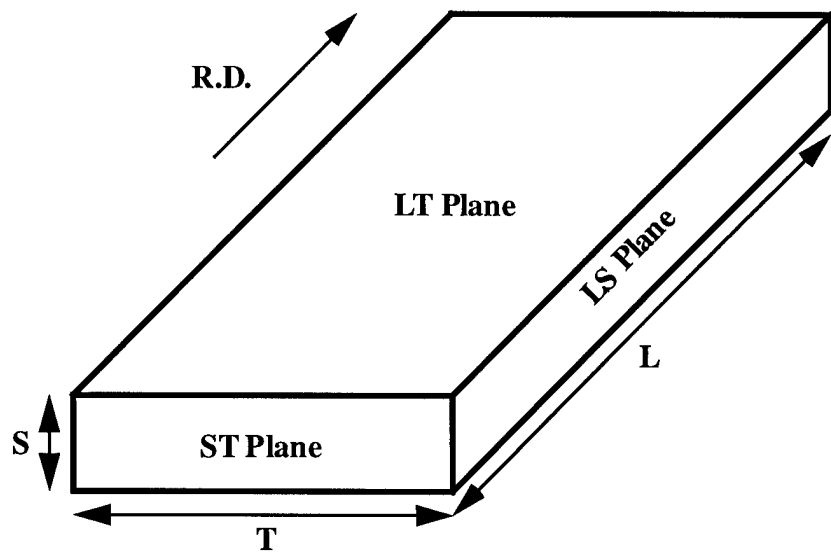


Figure 4.2.1.10. Labeling scheme used for directions and planes

Table 4.2.1.8. Composition (wt.%) of the plate and rivets from the dismantled joints

Material	Al	Cu	Zn	Mg	Fe	Si	Mn	Cr
Plate #2	89.3	2.1	7.1	1.5				
Rivet #1					98.3	0.3	0.8	0.6
Rivet #2					98.7	0.3	0.9	

Table 4.2.1.9. Actual and target compositions (wt%) of the five aluminum intermetallic samples.

Material	Al	Cu	Zn	Fe
Al ₂ Cu	51.9 (Bal)	48.1 (53-54)		
Al ₂ Cu + 1.5% Zn	50.8 (Bal)	48.5 (53-54)	0.7 (1.5)	
Al ₂ Cu + 2.5% Zn	50.2 (Bal)	48.2 (53-54)	1.6 (2.5)	
Al ₆ (Fe,Cu)	72.8 (Bal)	5.9 (7-8)		21.3 (22-25)
Al ₃ Fe	62.1 (Bal)			37.9 (39-41)

Table 4.2.1.10. Results of x-ray diffraction qualitative phase analysis of the intermetallic alloys.

Sample	Major Phase	Minor Phase
Al ₂ Cu	CuAl ₂ (Khatyrkite)	
Al ₂ Cu + 1.5% Zn	CuAl ₂ (Khatyrkite)	Cu ₂ AlZn
Al ₂ Cu + 2.5% Zn	CuAl ₂ (Khatyrkite)	Cu ₂ AlZn
Al ₆ (Fe,Cu)	Al ₇ Cu ₂ Fe	
Al ₃ Fe	N/A	N/A

Experimental Environments

The environments chosen for this research work were designed to: (1) simulate the possible ranges of oxygen and chloride concentrations likely to be seen in service, and (2) allow for comparison with other experimental data from the literature. The major environmental variables were the chloride concentration (0.1M, 0.3M, 1.0M, 3.0M and 5.0M) and oxygen concentration (deaerated with nitrogen gas and air saturated). Tests were also carried out in ASTM G69 (58.5 ± 0.1 g NaCl and 9 ± 1 mL of H₂O₂ per 1L of solution) and G34 (234g NaCl, 50g KNO₃, and 6.3ml of 70% HNO₃ per 1L of solution) environments. The G69 and G34 solutions are 1.0M and 4.0M with respect to NaCl concentration. The G34 solution has an apparent pH of 0.4. Some tests were conducted in sulfate solutions to evaluate the effect of chloride ions. Test temperature ranged from 298 to 323K.

The choice of chloride concentration range was based on a desire to simulate more relevant environments - appropriate to a marine source environment. It was felt that crevice chloride concentrations on the order of 0.1M were not unreasonable to expect in service. The chloride concentration plays a critical role in the pitting of aluminum alloys.

The choice of oxygen concentrations was based on a desire to simulate conditions of air exposure but to allow for crevice conditions where oxygen consumption would be expected. The role of the oxygen reduction reaction in polarizing the material above the pitting potential was felt to be a critical factor in the experimental program.

A standard G69 solution was used for some of the tests in order to allow for comparison with the data in published literature. However, for most of the electrochemical studies, the potential, as measured during a G69 exposure and achieved chemically, was achieved using potentiostatic methods. In this way, the condition of a G69 exposure could be duplicated in a less aggressive environment (chemically) that was more appropriate to actual service.

The temperature range was chosen to simulate actual service temperatures during non-flight conditions.

Microscopy

Optical Microscopy

Samples were cut from the 7075-T651 and 7178-T6 plate to confirm the orientation of the material. The samples were ground and polished with diamond paste. The grain boundaries were revealed by a modified Keller's reagent (2.5 ml HNO₃, 1.0 ml HCl, 1.0 ml HF, and 95 ml water).[66]

SEM Microscopy

The Topcon ABT-150S, equipped with a Noran Voyager II X-ray Quantitative Microanalysis System, was used for all scanning electron microscopy (SEM) work and energy dispersive X-ray (EDX) analysis. The accelerating voltage varied between 20 and 40kV. Secondary and back

scattered electron imaging modes were used.

Electrochemical Studies

Samples, approximately 1cm² in area, were cut from the aluminum alloy plates. In the case of the intermetallic alloys, a section roughly 1.5cm thick was first cut from the HIP can. A small cylinder approximately 0.8 cm in diameter was then removed by EDM. Electrical lead wires were attached to the samples and the samples were then mounted in resin.

Each specimen was ground and polished to a mirror finish. 3mm diamond paste was used for the final polish. The specimen was then rinsed with deionized water, cleaned in isopropanol alcohol, and masked along its edges with resin prior to testing. The exposed area on the sample was measured.

Electrolytes used in all the studies were made from reagent grade chemicals and deionized water. Unless stated otherwise, all electrolytes used were deaerated with nitrogen gas (less than 5ppm oxygen) for a minimum of 45 minutes before testing. In the case of aerated studies, a gas mixture of 20% oxygen in argon was bubbled through the electrolytes for a minimum of 1 hour prior to testing.

Two potentiostats, a EG&G 173 with a 276 interface and a EG&G 273, were used for all the experiments. A programmable electrometer (Keithley 617) was used as a high impedance voltmeter for free corrosion potential measurements.

All electrochemical potential measurements were made via Luggin probes. Saturated calomel electrodes (SCE) were used as the reference in chloride environments. In sulfate solutions, mercury / mercurous sulfate (Hg/Hg₂SO₄) electrodes served as the reference. The readings were then converted to the SCE scale.

Free Corrosion Potential Measurement

Experiments were conducted in accordance to ASTM G69 (“Standard Practice for Measurement of Corrosion Potentials of Aluminum Alloys”) and ASTM G34 (“Exfoliation Corrosion

Susceptibility in 2XXX and 7XXX Series Aluminum Alloys, EXCO Test"). The free corrosion potential was monitored continuously by the high impedance voltmeter and recorded by computer.

Potentiodynamic Experiments

Dynamic polarization scans were started within 5 minutes of immersing the specimen into the electrolyte. The scans were initiated from the open circuit potential and the potential was scanned in the noble direction at a rate of 10mV/min. When the current density reached 5mA/cm², the experiment was terminated. Experiments were also conducted at 1mV/min to study the effect of scan rate. Dynamic polarization studies were conducted in 0.1M, 0.3M, 1.0M, 3.0M, and 5.0M (saturation at 298K) NaCl solutions to study the effects of chloride ion concentration. Test temperature varied from 298, 308, 318 to 323K. Water baths were used to maintain the test temperature to within $\pm 0.5^{\circ}\text{C}$ of the target. The breakdown potentials reported are the averages of at least two experiments. The average scatter in the critical potentials reported is 4mV.

Cyclic polarization experiments were also conducted to examine the repassivation behavior of these materials. The initial conditions for cyclic polarization experiments were identical to those of dynamic polarization studies. In the case of cyclic polarization experiments, the direction of polarization was reversed when the current density reached 5mA/cm². The scan rate was maintained at 10mV/min. The test was terminated when the material had repassivated.

Potentiostatic Experiments

Potentiostatic experiments were conducted to identify the corrosion sites associated with a particular breakdown potential and environment. The potential was maintained constant until a charge density of approximately 3C/cm² was reached. This ensures significant corrosion had occurred and the breakdown sites could easily be identified. Energy dispersive x-ray spectroscopy (EDX) studies were conducted on various second phase particles found on the corroded surfaces.

Galvanic Corrosion Experiments

Two specimens were immersed into the corrosion cell approximately 2cm apart with the polished surfaces facing each other. The Luggin probe was positioned roughly in the middle of the two specimens. The potentiostat functioned as a zero resistance ammeter (ZRA) in these experiments and the galvanic current was recorded. Concurrently, the high impedance voltmeter monitored the free corrosion potential.

Mechanical & Environmental Behavior Testing

As discussed earlier, airframe degradation often occurs in the form of pitting / exfoliation attack in occluded area followed by crack initiation in stressed regions. Crack propagation can be either by static stress corrosion cracking or by fatigue (assisted by the environment). The role of the corrosion damage is often to provide both the aggressive environment and the stress concentrator required for crack initiation.

Mechanical/environmental behavior testing was conducted to characterize the initiation process. Two types of tests were employed, constant load and constant displacement. Additionally, tensile tests were performed to characterize the strength of the materials.

Tensile Tests

The configuration of the specimens used for tensile tests is depicted in Figure 4.2.1.11. It consists of a round bar with a square gage section. The sides of the square section correspond to the principal directions of the material. The 0.2% offset yield stress was computed for each specimen. At least two specimens were used for each material and orientation. Fracture surfaces were examined in SEM and representative fractographs obtained.

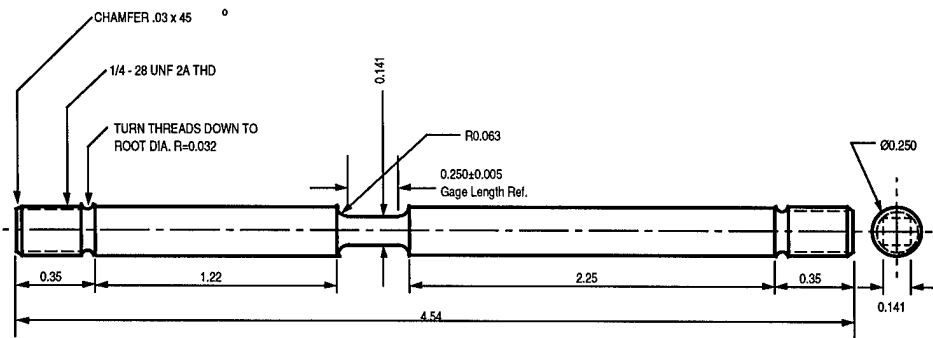


Figure 4.2.1.11. Sketch of specimens used for tensile tests and constant load SCC tests. The dimensions are in inches.

Stress Corrosion Cracking Tests

Constant Load

The specimens used for constant load SCC tests were identical to those used for the tensile tests. The dimensions of the specimens are shown in Figure 4.2.1.11 above. Most of the specimen was masked off with resin during SCC tests. Only the gage area was exposed to the environment. A gas tight 10 liter bottle was used as the electrolyte reservoir. The corrosion cell, which holds roughly 150cc of electrolyte, was machined from Lexan. The test cell is illustrated in Figures 4.2.1.12 and 4.2.1.13. A Cole Parmer Master Flex pump was used to circulate the electrolyte between the reservoir and the corrosion cell. Deaeration of the electrolyte was accomplished by bubbling nitrogen gas through the reservoir. A nitrogen gas cover inside the corrosion cell maintained the deaeration. A lever arm creep tester was used to apply the constant load. The electrochemical potential was maintained by a potentiostat during all tests. A Luggin probe, attached to the side of the corrosion cell, was used to measure the potential. A platinum foil, roughly 6cm^2 in area, served as the counter electrode.

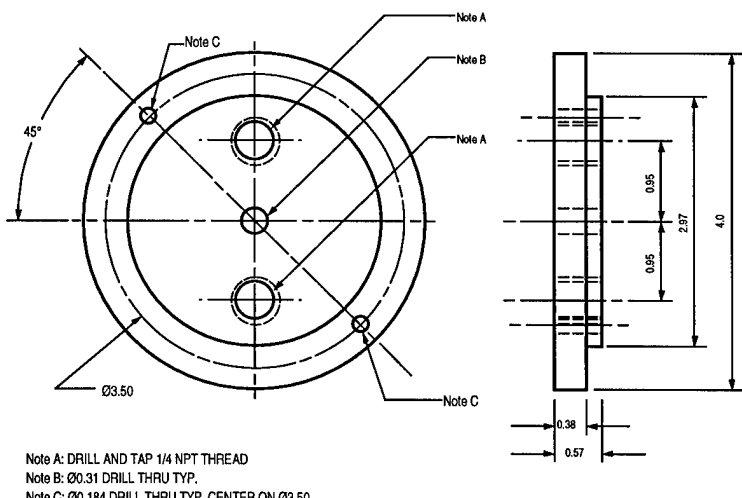


Figure 4.2.1.12. Corrosion cell lid used for constant load experiments.

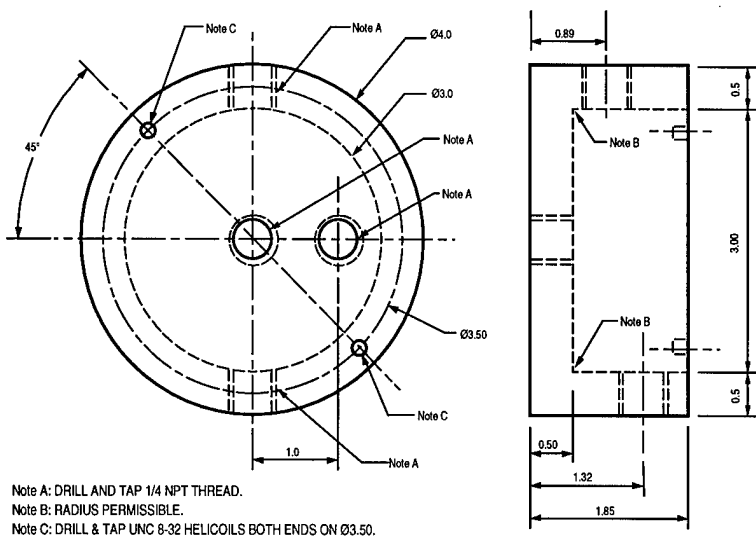


Figure 4.2.1.13. Corrosion cell bottom used for constant load experiments.

Electrolyte was first pumped into the cell. The constant electrochemical potential was established by the potentiostat and the load was finally applied.

Constant Displacement

The specimens used for constant displacement tests are 4.5" long 0.141" square bars. These tests were conducted in a 316 stainless steel four point bend fixture shown in Figure 4.2.1.14. The load was applied by adjusting a stainless steel screw on the bottom of the fixture. Only a small portion of the gage section was exposed to the environment; most of the specimen was masked off with resin. Strain gages were attached to the specimen surface under tension between the two inside supports. Two independent 1/4 bridge strain gage circuits were used for each specimen to assure the accuracy of the measurements.

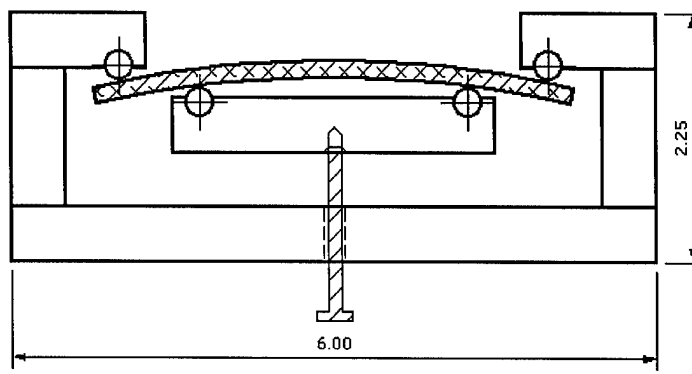


Figure 4.2.1.14. Schematic of a four point bend fixture. The dimensions are in inches.

Since the maximum stress never exceeded yield, Hooke's law for uniaxial stress applies. In the elastic range, the normal stress varies linearly with the distance from the neutral surface. [67]

This is shown schematically in Figure 4.2.1.15. The bending moment is calculated by:

Where

$$\sigma_m = \frac{M}{S} \quad (4.2.1.3)$$

σ_m : maximum absolute value of stress

M : bending moment

S : elastic section modulus

The elastic section modulus of a beam with rectangular cross sectional width b and depth h is:

$$S = \frac{1}{6}bh^2 \quad (4.2.1.4)$$

The tensile strain on the surface on the specimen was monitored by the strain gages. Since the stress never exceeded yield, the maximum stress (σ_m) can be obtained directly from these strain measurements. With b and h known, the bending moment, M can be calculated. The calculated bending moment is used for stress intensity factor calculations.

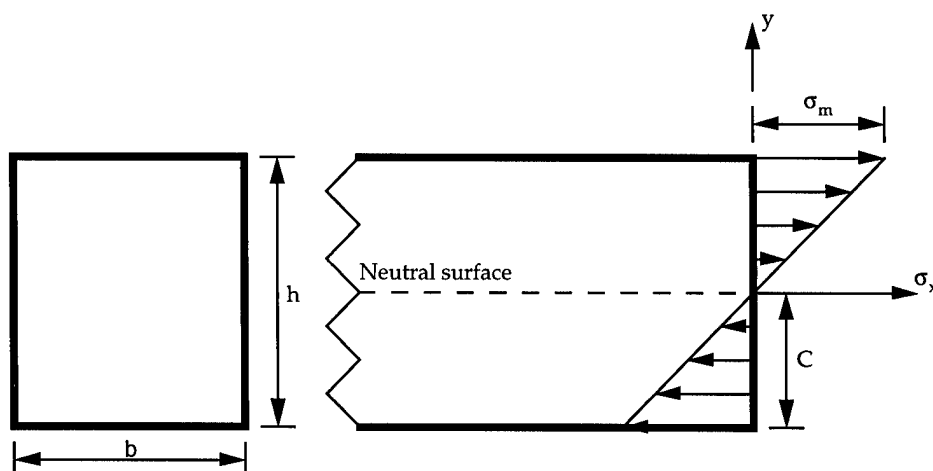


Figure 4.2.1.15. Schematic of the stress state for a bending specimen.

The corrosion cell used in the four point bend tests consisted of a 9.0"(L) x 7.5" (W) x 4.3" (H)

Lexan box. The electrolyte reservoir and circulation pump used for the constant load tests were also used in four point bend tests. Nitrogen cover gas, electrolyte circulation, and Luggin probe attachment were accomplished via various ports on the corrosion cell. Four test fixtures were attached to the perimeter of the corrosion cell which allowed four specimens to be tested simultaneously.

4.2.1.4 Results

Metallographic Results

Figures 4.2.1.16 and 4.2.1.17 show the strong grain shape anisotropy common in these materials. The grain boundaries are revealed by a modified Keller's etchant.

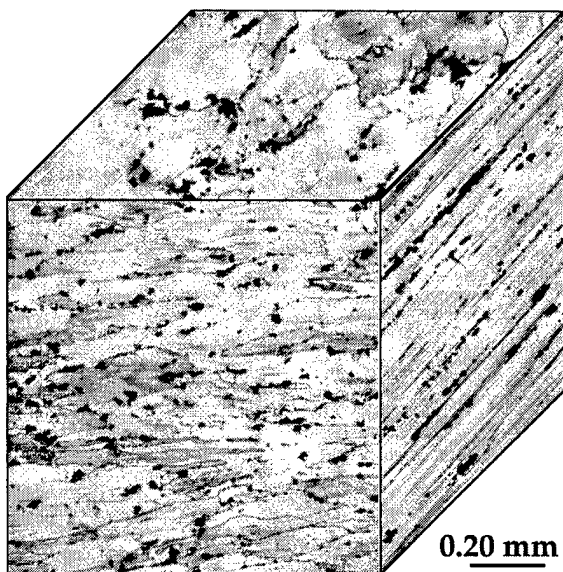


Figure 4.2.1.16. Optical micrograph showing the strong orientation effect in the 7075-T651 plate.

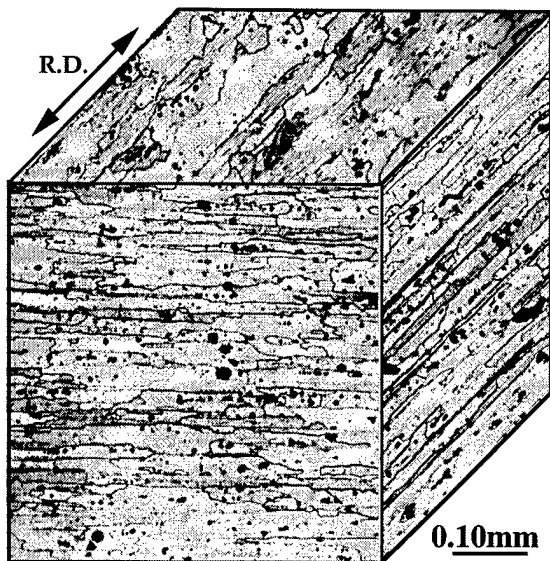


Figure 4.2.1.17. Metallograph of the 7178-T6 plate used. The arrow indicates the rolling direction of the plate.

Electrochemistry

Unless stated otherwise, all electrochemical potentials reported are referenced to the saturated calomel electrode (SCE) scale. Conversion to the standard hydrogen scale (SHE) can be accomplished by adding 0.2416V to the SCE readings.

$$E(V, \text{SHE}) = E(V, \text{SCE}) + 0.2416 \quad (4.2.1.5)$$

Corrosion Potential Measurements

Figure 4.2.1.18 shows the potential vs. time for a G69 exposure. The average corrosion potential for 7075-T651 and 7178-T6 in the last 30 minutes of an 1 hour ASTM-G69 test is -0.726 and -0.736V respectively. It is likely that the changes in potential with time is due to the deterioration in the strength of the hydrogen peroxide added to the electrolyte. In other words, the amount of dissolved oxygen in the solution decreased with time.

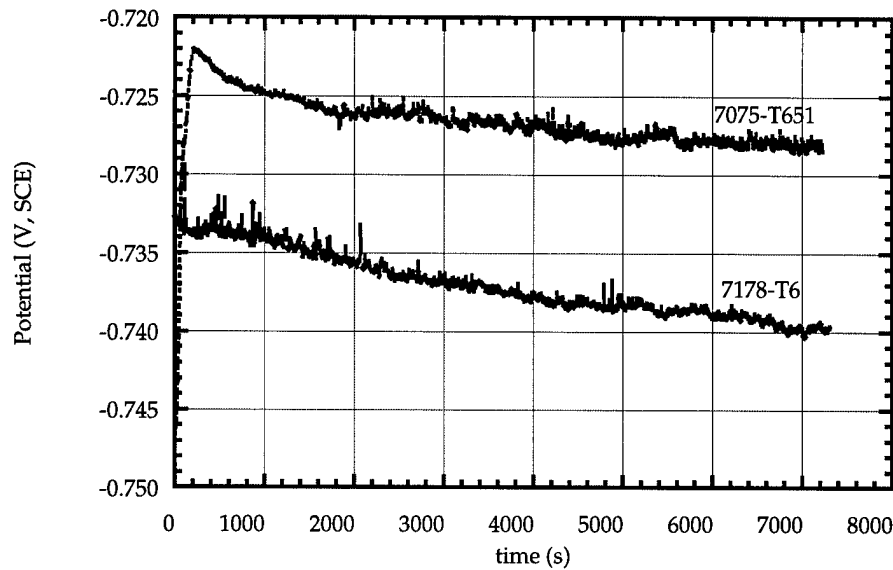


Figure 4.2.1.18. Changes in corrosion potential for 7075-T651 and 7178-T6 during ASTM G69 test.

The corrosion potential for these materials was also recorded during ASTM G34 exfoliation susceptibility tests. These are shown in Figure 4.2.1.19. The average of the free corrosion potential in the last hour of a 48 hr test is -0.704 and -0.713V for 7075-T651 and 7178-T6 respectively. The corrosion potential for 7178-T6 in both G69 and G34 tests are more active than that of 7075-T651.

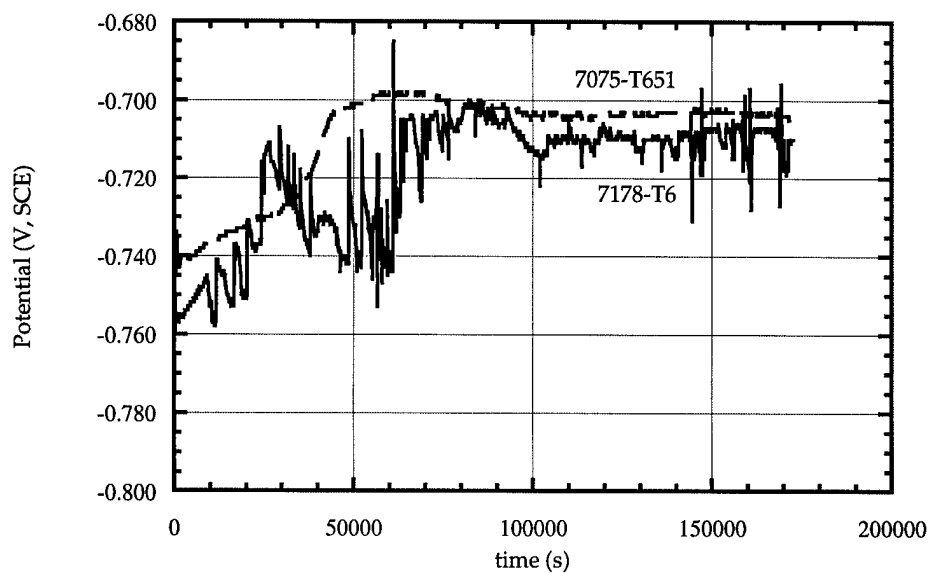


Figure 4.2.1.19. Free corrosion potential vs. time for 7075-T651 and 7178-T6 during ASTM G34 test.

The samples from both materials were sectioned after the exfoliation susceptibility test to determine the extent of exfoliation corrosion. Figures 4.2.1.20 and 4.2.1.21 show the results of this analysis. It is apparent that significant corrosion had occurred in these materials.

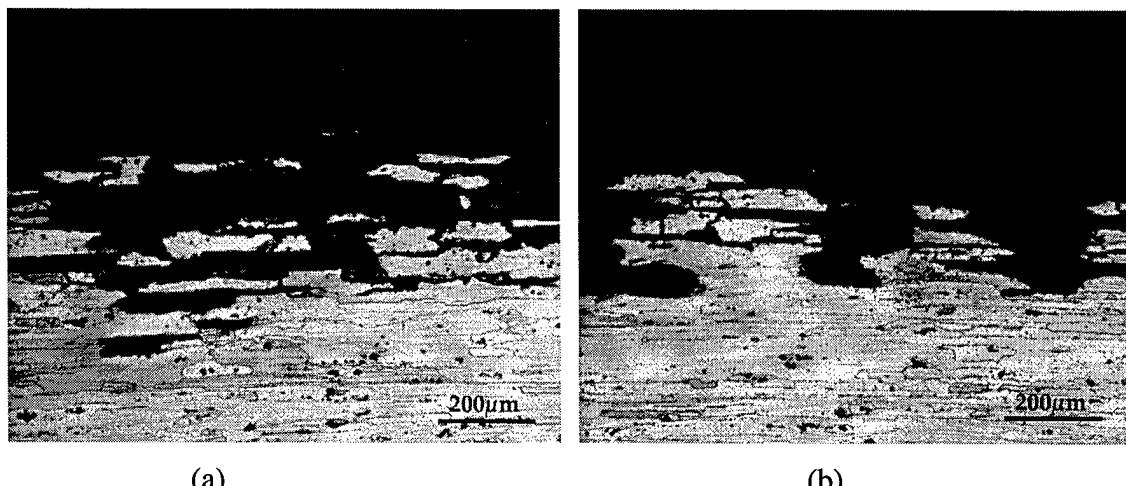


Figure 4.2.1.20. Cross section of 7178-T6 sample after ASTM G34 test.

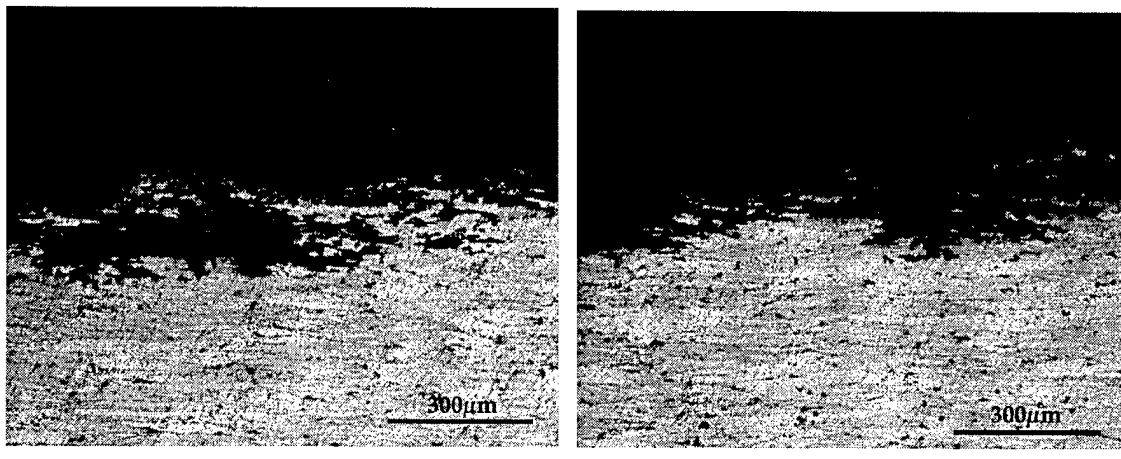


Figure 4.2.1.21. Cross section of 7075-T651 sample after ASTM G34 test.

Identification of Breakdown Potentials

Aluminum alloys are protected by a surface film in many environments. However, in the presence of chloride ions and/or at potentials more active than the critical “breakdown” potentials, film breakdown occurs locally and accelerated attack can occur. The accelerated attack can take the form of pitting and/or intergranular attack and was characterized by a potential above which a large increase in current density was observed. The type of the localized corrosion which was responsible for the current density increase was confirmed by metallographic analysis of the polarized sample.

7178-T6 Material

Figure 4.2.1.22 shows a typical polarization plot for 7178-T6 material in chloride environment. Two breakdown potentials, a “lower” and an “upper” breakdown potential, were identified. In Figure 4.2.1.22, the breakdown potentials are at -0.701V and -0.656V.

Static polarization experiments were conducted to identify the corrosion sites associated with the breakdown potentials. Figure 4.2.1.23 illustrates the typical response of 7178-T6 after static polarization at -0.670V. This potential is above the lower breakdown potential of -0.656V but below the upper breakdown potential of -0.701V. Two different types of second phase particles were observed. The particles shown in Figures 4.2.1.23 b and c are rich in copper while Figure 4.2.1.23 d shows a silicon rich particle. The arrow in the figures indicates the particle whose

EDX spectrum is shown. Because of their size and composition, these particles were classified as constituent particles. The interface between the copper rich particle and the matrix was corroded and is thus the source of the increased current density. In some cases, only dimples were observed. No corrosion was observed around silicon rich particles.

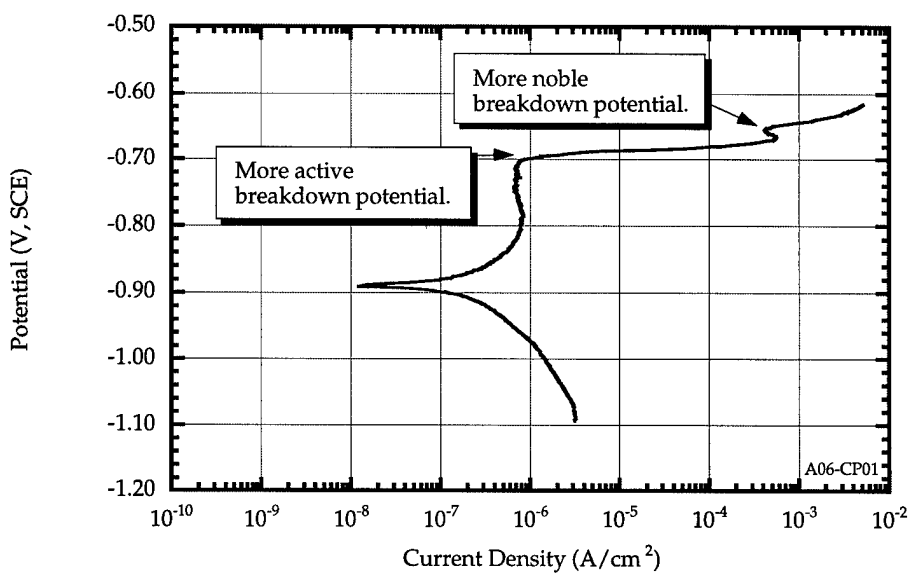
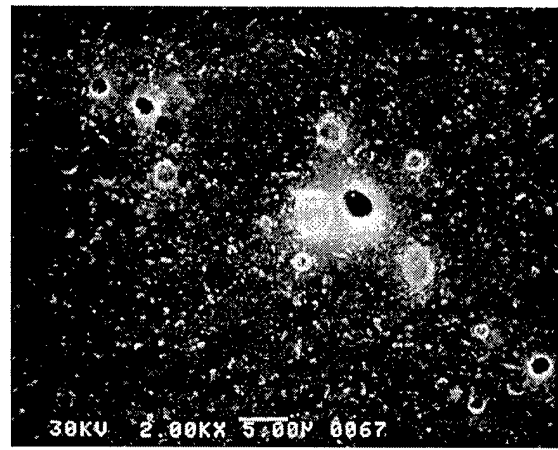
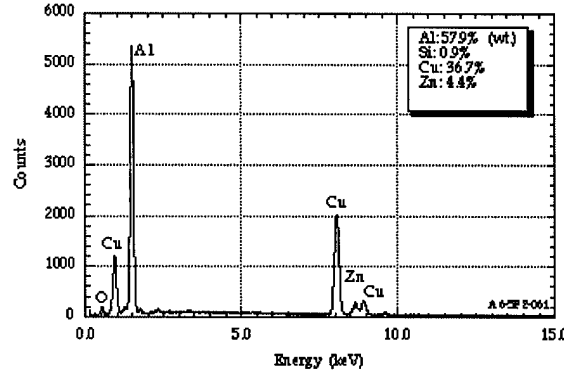
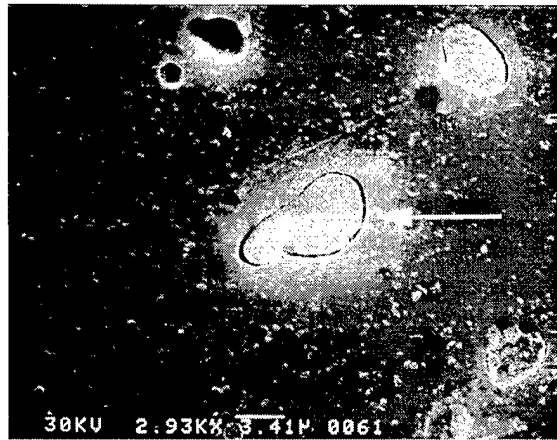


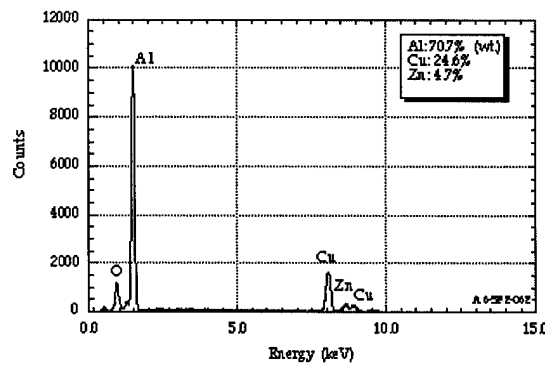
Figure 4.2.1.22. Dynamic polarization plot for 7178-T6 in 0.1M NaCl at 298K.



(a)

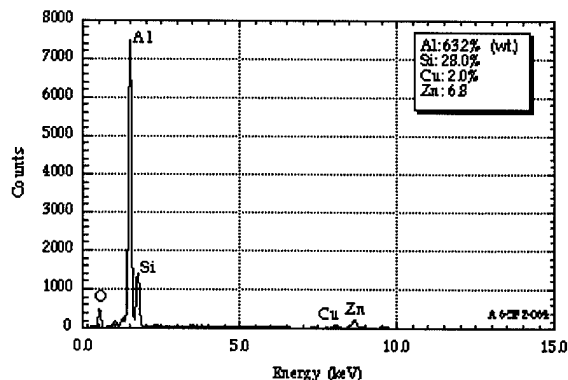
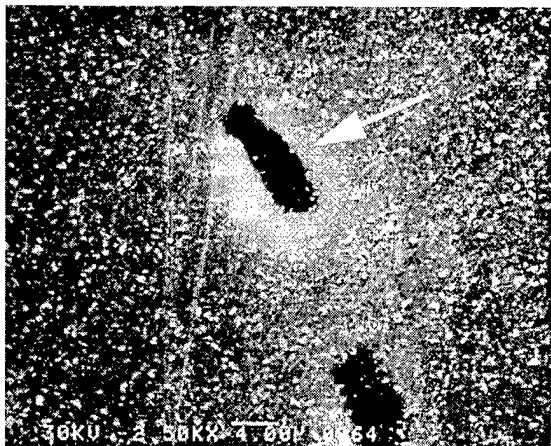


(b)



(c)

Figure 4.2.1.23. SEM images of corroded surface for 7178-T6 after static polarization at -0.670V in 0.1M NaCl at 298K. The arrow points to the particle whose EDX spectrum is shown.



(d)

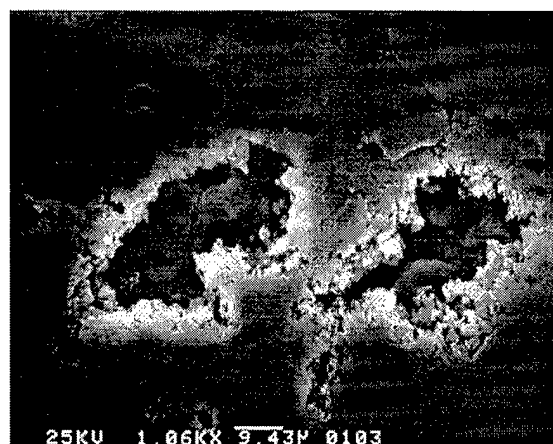
Figure 4.2.1.23 (Continued). SEM images of corroded surface for 7178-T6 after static polarization at -0.670V in 0.1M NaCl at 298K. The arrow points to the particle whose EDX spectrum is shown.

Intergranular attack (IGA) was the dominant form of corrosion for 7178-T6 after static polarization above the upper breakdown potentials at -0.650V. This is shown in Figures 4.2.1.24 and 4.2.1.25. Large scale pitting which originated from grain boundaries (Figure 4.2.1.24 a and b), and interface dissolution around second phase particles (Figure 4.2.1.24 c and 4.2.1.25 d) was also observed.

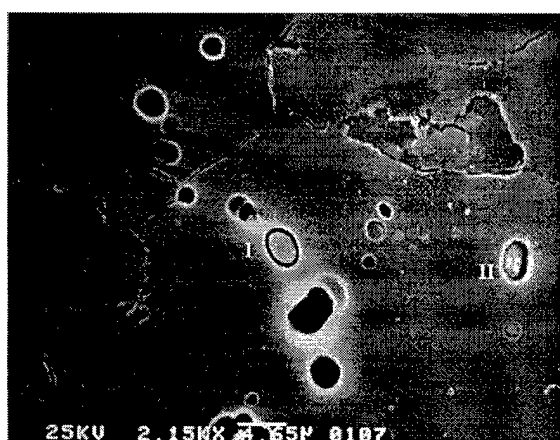
As with the 7178-T6 material, two breakdown potentials were observed, a more active breakdown at -0.691V and a more noble breakdown at -0.651V. Figures 4.2.1.26 and 4.2.1.27 show the surfaces of 7075-T651 after polarization above these potentials. The increase in corrosion current density at the more active breakdown potential is associated with interface corrosion of second phase particles in the matrix. The increase in current density above the more noble breakdown potential is associated with intergranular attack.



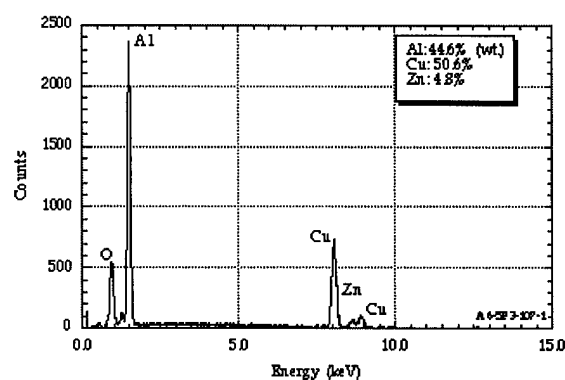
(a)



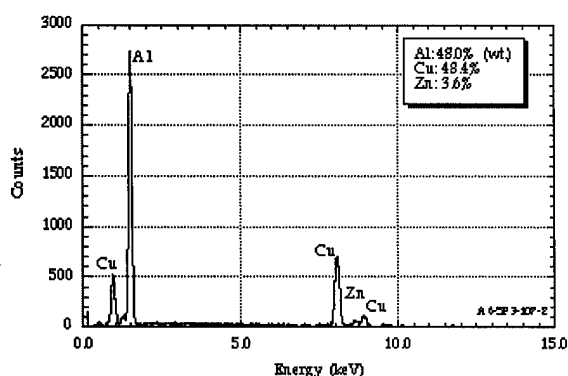
(b)



(c)

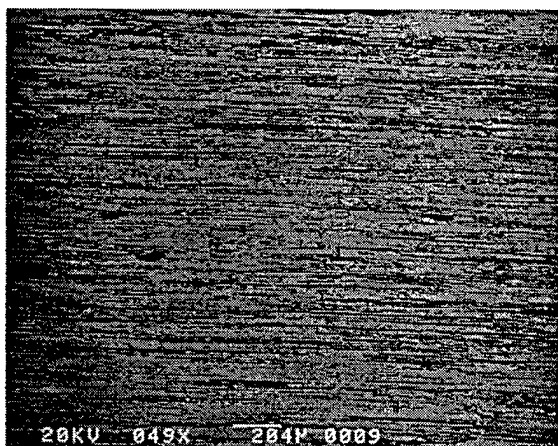


(d)

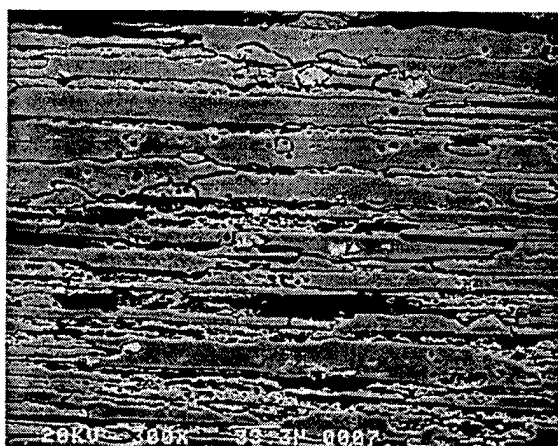


(e)

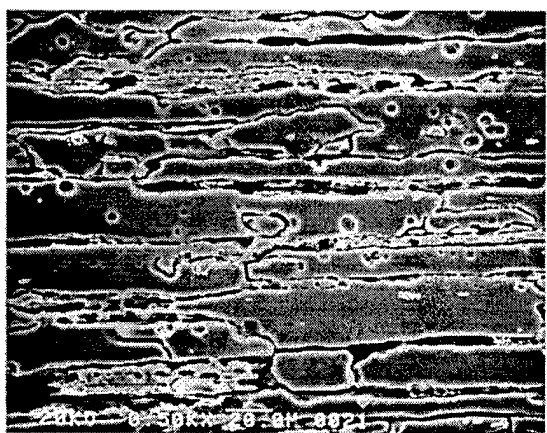
Figure 4.2.1.24. SEM micrographs of 7178-T6 after static polarization experiment at -0.650V in 0.1M NaCl at 298K. The EDX spectrums for the particles labeled I and II in (c) are shown in (d) and (e) respectively.



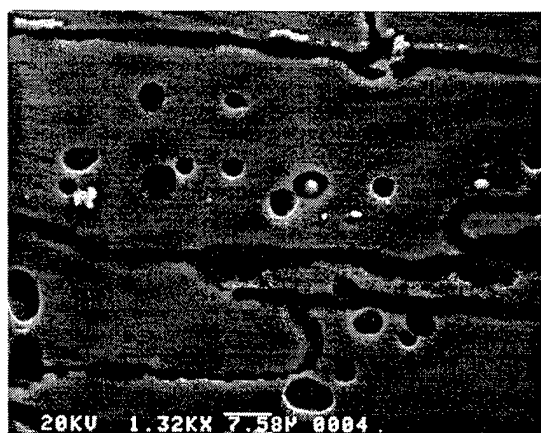
(a)



(b)

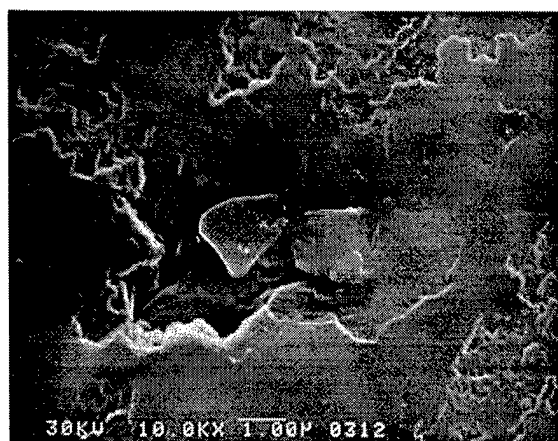


(c)

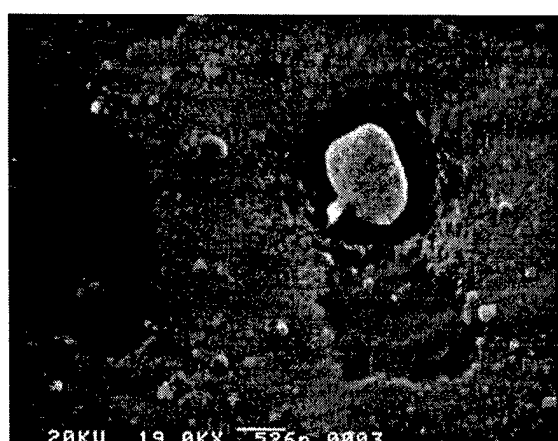


(d)

Figure 4.2.1.25. 7178-T6 ST plane after static polarization at -0.650V in 0.1M NaCl at 298K.
7075-T651 Material

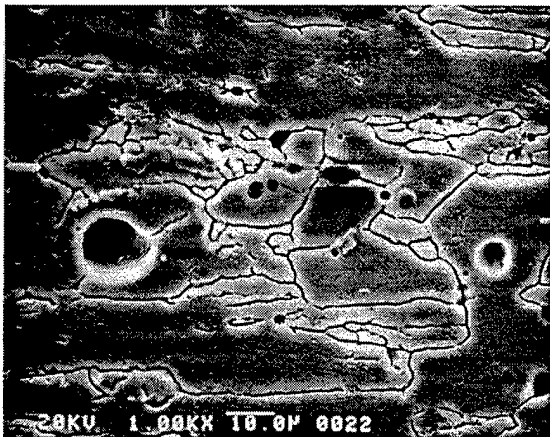


(a)



(b)

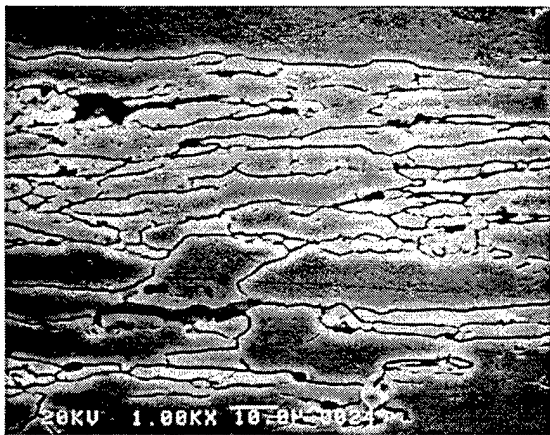
Figure 4.2.1.26. 7075-T651 maintained between the critical potentials, showing interface corrosion around second phase particles.



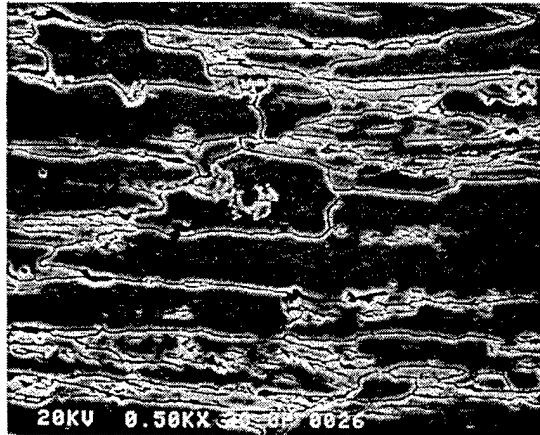
(a)



(b)



(c)



(d)

Figure 4.2.1.27. SEM micrographs of 7075-T651 after static polarization at -0.650V in 0.1M NaCl at 298K showing intergranular attack and dissolution around second phase particles.

It can therefore be concluded, for both 7075-T651 and 7178-T6, that the more active (more negative) breakdown potential is associated with interface corrosion around constituent particles which leads to pitting while the more noble breakdown potential is related to intergranular corrosion. For future reference, the lower (more active) breakdown potential will be referred to as E_{pit} while the upper (more noble) breakdown potential will be referred to as E_{iga} .

Figures 4.2.1.28 and 4.2.1.29 show the results of polarization in sodium sulfate solution for 7178-T6 and 7075-T651 respectively. In each case, the observed behavior is of a transition to passive behavior with no subsequent breakdown at noble potentials. These results confirm the role of chloride ion in the film breakdown process.

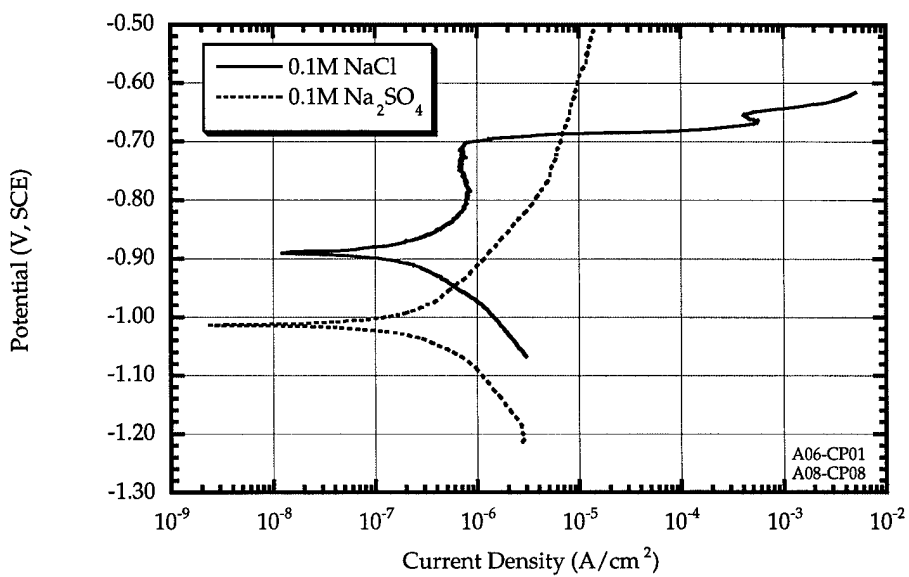


Figure 4.2.1.28. Comparison of polarization results of 7178-T6 in NaCl and Na₂SO₄.

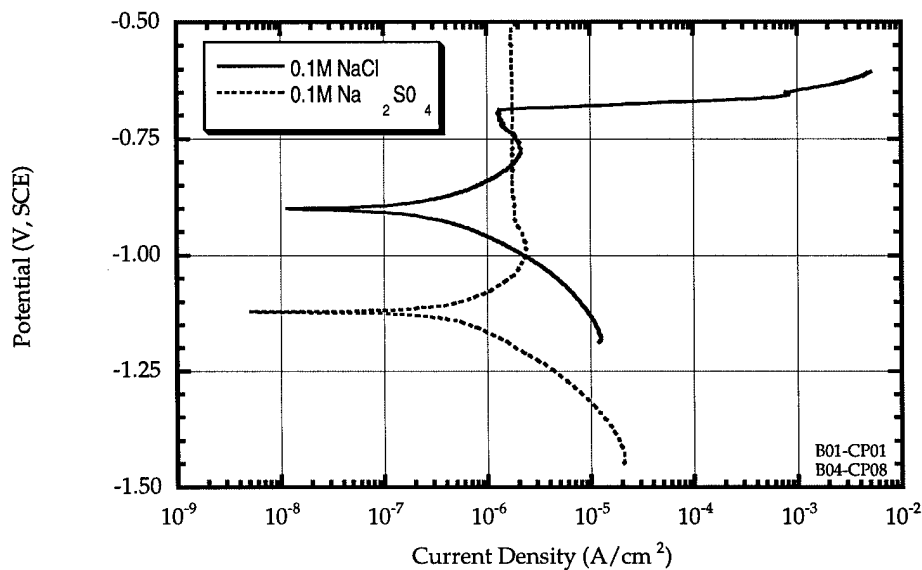


Figure 4.2.1.29. Comparison of polarization results of 7075-T651 in NaCl and Na₂SO₄.

Effect of Scan Rate on the Breakdown Potentials

Dynamic polarization experiments were conducted in 0.1M NaCl solutions at 298K with scan rates of 1mV/min and 10mV/min. The results are presented in Figures 4.2.1.30 and 4.2.1.31. The breakdown potentials for the two sets of experiments are virtually identical.

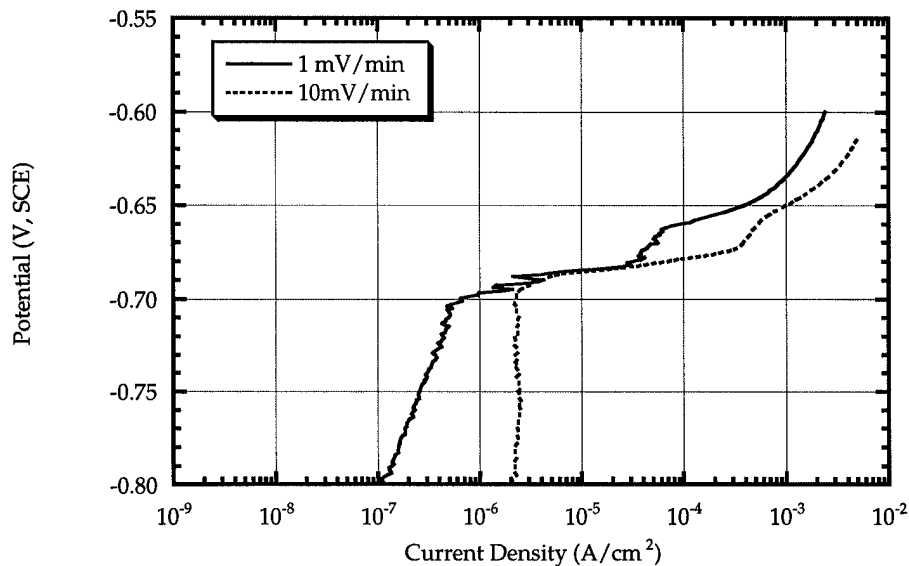


Figure 4.2.1.30. The effect of scan rate on the critical potentials for 7178-T6 in 0.1M NaCl at 298K is demonstrated.

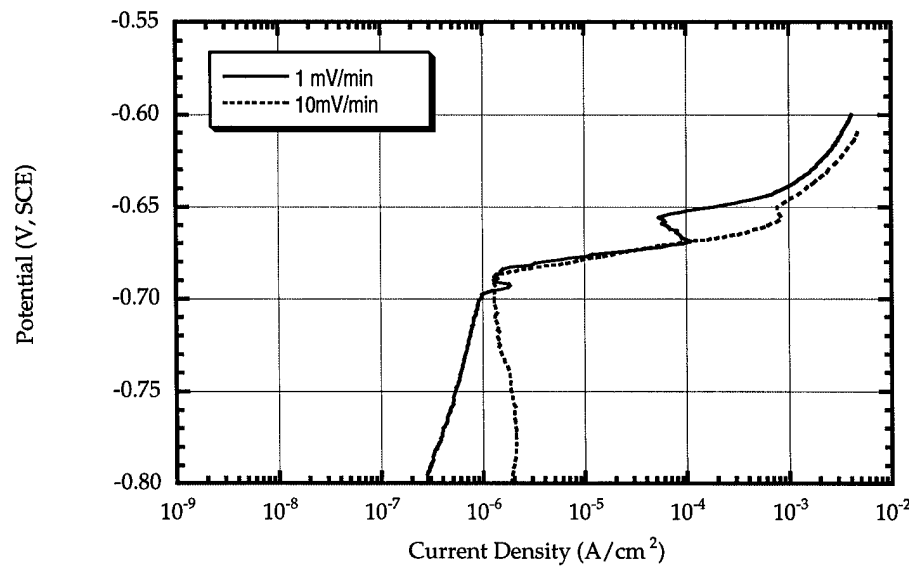


Figure 4.2.1.31. The effect of scan rate on the critical potentials for 7075-T651 in 0.1M NaCl at 298K is demonstrated.

Effect of Chloride Ion Concentration on the Breakdown Potentials

Dynamic polarization experiments were conducted at 298K as a function of orientation and material in 0.1M, 0.3M, 1.0M, 3.0M, and 5.0M (saturation at 298K) NaCl solutions. The chloride ion concentrations were converted to activities via the activity coefficients listed in Table 4.2.1.11.[68] The breakdown potentials (E_{pit} and E_{iga}) for 7075-T651 and 7178-T6 as a function of orientation and chloride ion activities are presented in Figures 4.2.1.32 and 4.2.1.33. In general, the values for E_{pit} and E_{iga} were more active for the 7178-T6 material at a given chloride ion concentration.

Table 4.2.1.11. Chloride ion activity coefficients used.[68]

Concentration (M)	0.10	0.30	1.0	3.0	5.0
Activity coefficient, γ	0.78	0.71	0.66	0.71	0.83
Activity	0.078	0.21	0.66	2.1	4.2

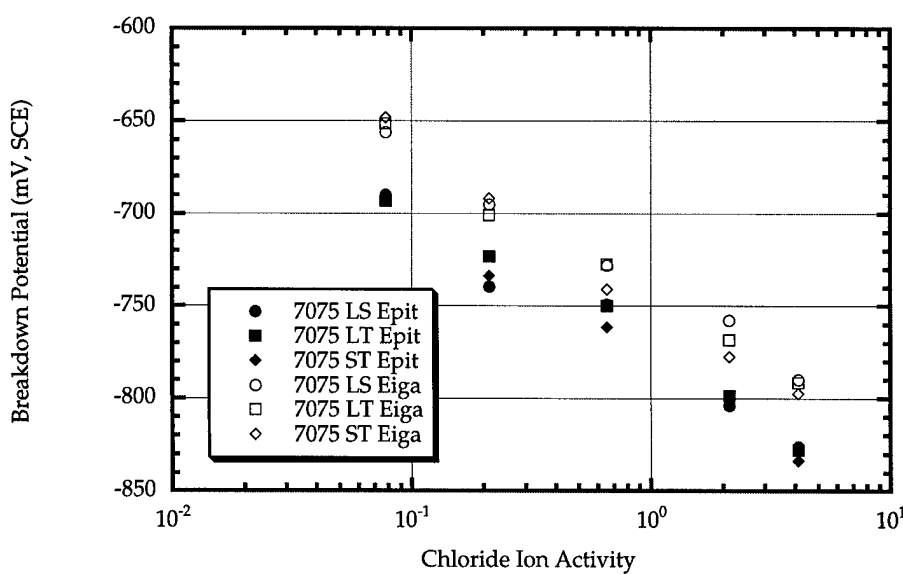


Figure 4.2.1.32. Plot of pitting potential (E_{pit}) and intergranular corrosion potential (E_{iga}) in 7075-T651 as a function of chloride ion activity and orientation.

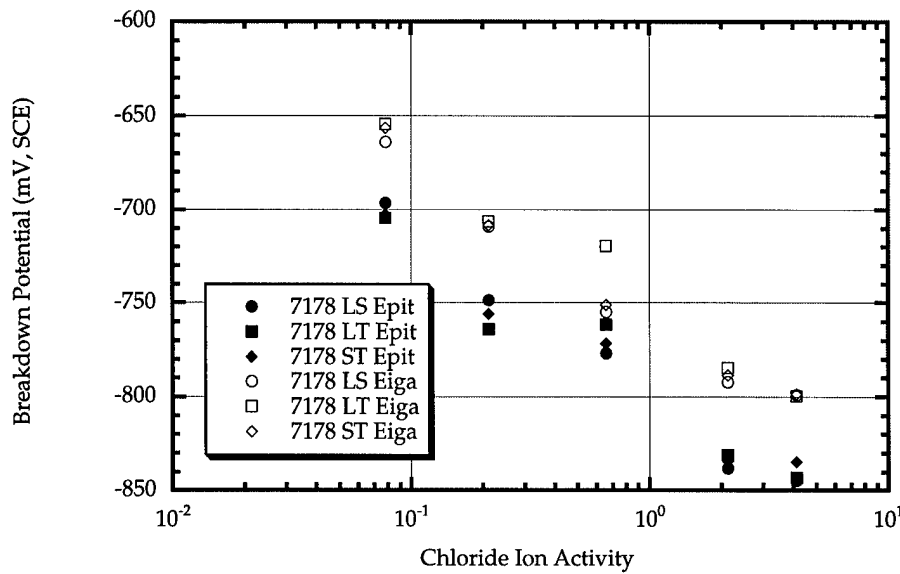


Figure 4.2.1.33. Plot of pitting potential (E_{pit}) and intergranular corrosion potential (E_{iga}) in 7178-T6 as a function of chloride ion activity and orientation.

Effect of Temperature on the Breakdown Potentials

Dynamic polarization experiments were conducted in 1.0M NaCl solutions at 298K, 308K, 318K, and 323K. The effect of temperature on the critical potentials (E_{pit} and E_{iga}) are presented in Figures 4.2.1.34 and 4.2.1.35. The critical potentials are found to be proportional to the reciprocals of the absolute temperature.

Repassivation Behavior

Cyclic polarization experiments were conducted in deaerated 1.0M NaCl solution at 298K to examine the repassivation behavior of 7178-T6 and 7075-T651. The results are presented in Figures 4.2.1.36 and 4.2.1.37. The arrows in the figures indicate the direction of polarization. The free corrosion potential after exposure to potentials above the breakdown potentials is lower (more active) than that for the unexposed material. Looked at in another way, after exposure above the breakdown potentials, the corrosion current density for a given fixed potential noble to the corrosion potential is higher (by several orders of magnitude). The magnitude of this difference is larger, both in terms of the potential difference and current density, for the 7178-T6

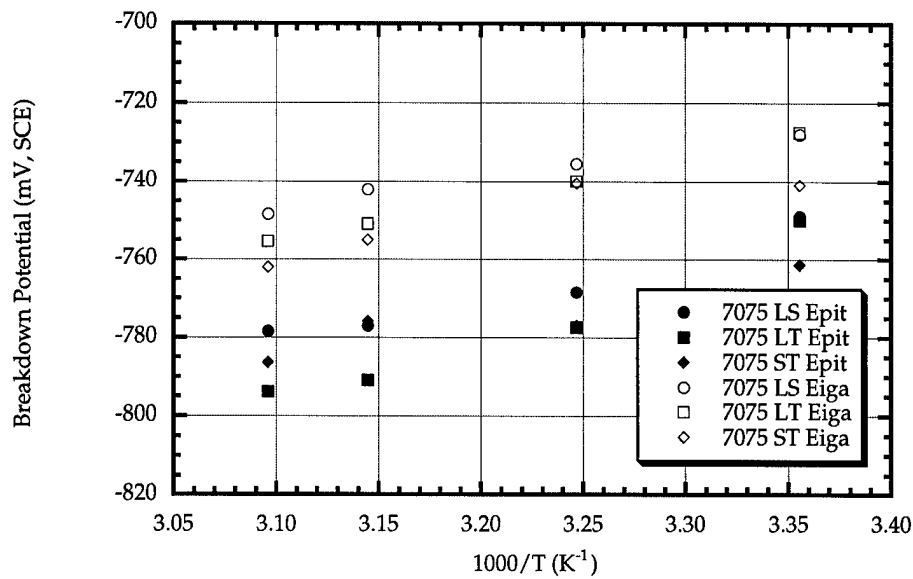


Figure 4.2.1.34. Plot of critical pitting potential (E_{pit}) and intergranular corrosion potential (Eiga) in 7075-T651 as a function of temperature and orientation in 1.0M NaCl solutions.

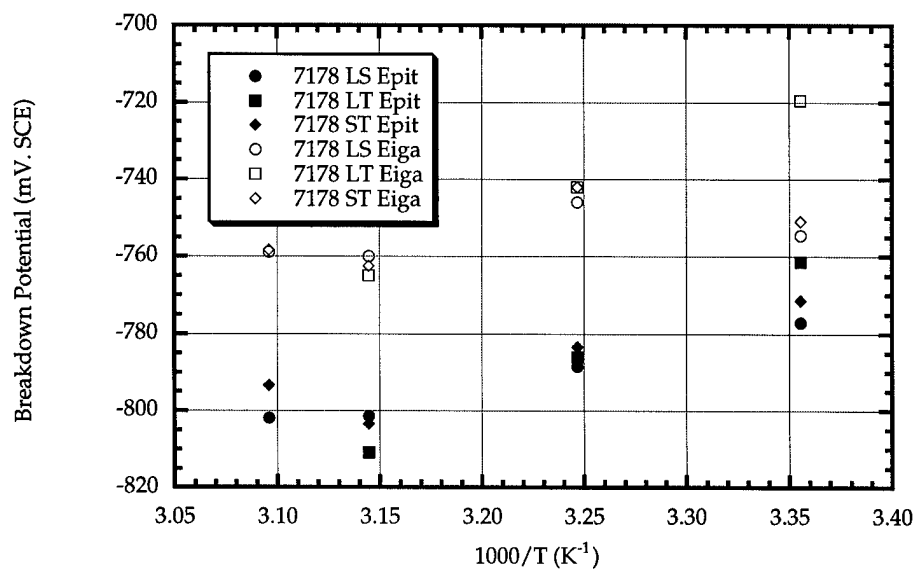


Figure 4.2.1.35. Plot of critical pitting potential (E_{pit}) and intergranular corrosion potential (Eiga) in 7178-T6 as a function of temperature and orientation in 1.0M NaCl solutions.

material. In a practical sense, this means that the 7178-T6 material is easier to pit and once pit has initiated, it is easier (less noble potential required) to maintain pit growth.

The average E_{corr} and E_{repass} are -0.91 and -0.95V SCE respectively for 7075-T651 while they are -0.90 and -0.96V SCE for 7178-T6. In other words, the difference between E_{corr} and E_{repass} is more pronounced for 7178-T6.

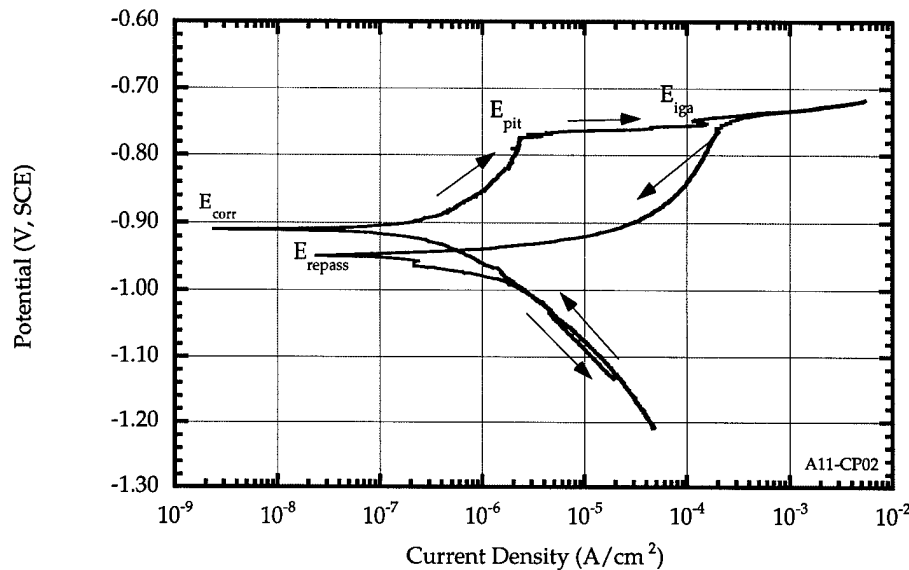


Figure 4.2.1.36. Cyclic polarization behavior of 7178-T6 in 1.0M NaCl at 298K. The arrows indicate the direction of polarization.

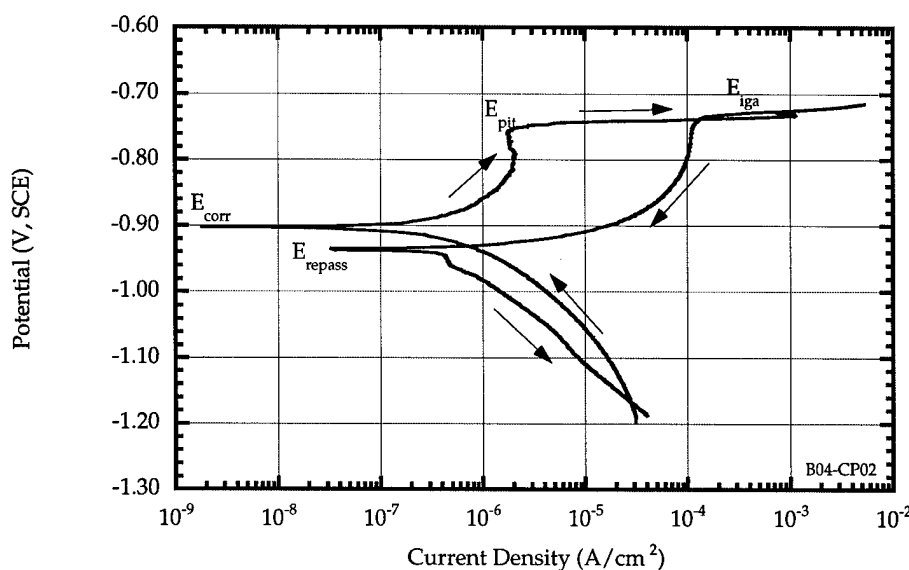


Figure 4.2.1.37. Cyclic polarization behavior of 7075-T651 in 1.0M NaCl at 298K. The arrows indicate the direction of polarization.

Polarization Behavior of the Intermetallic Alloys

Dynamic polarization experiments were conducted on the five intermetallic alloys and pure aluminum in 1.0M NaCl solution at 298K. The pH of the electrolyte was found to be 6.2. At least two experiments were conducted on each material to verify the accuracy and reproducibility of the data. Typical results are illustrated in Figures 4.2.1.38 through 4.2.1.43.

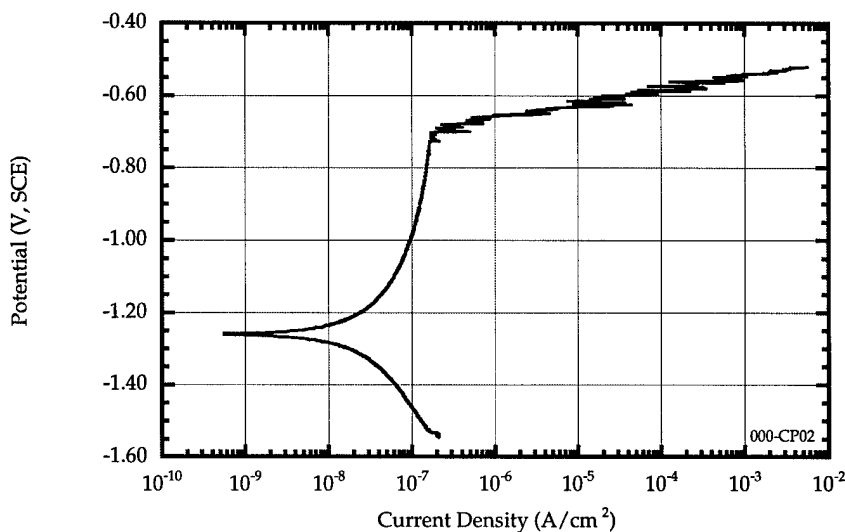


Figure 4.2.1.38. Typical polarization response of pure aluminum in 1.0M NaCl solution at 298K.

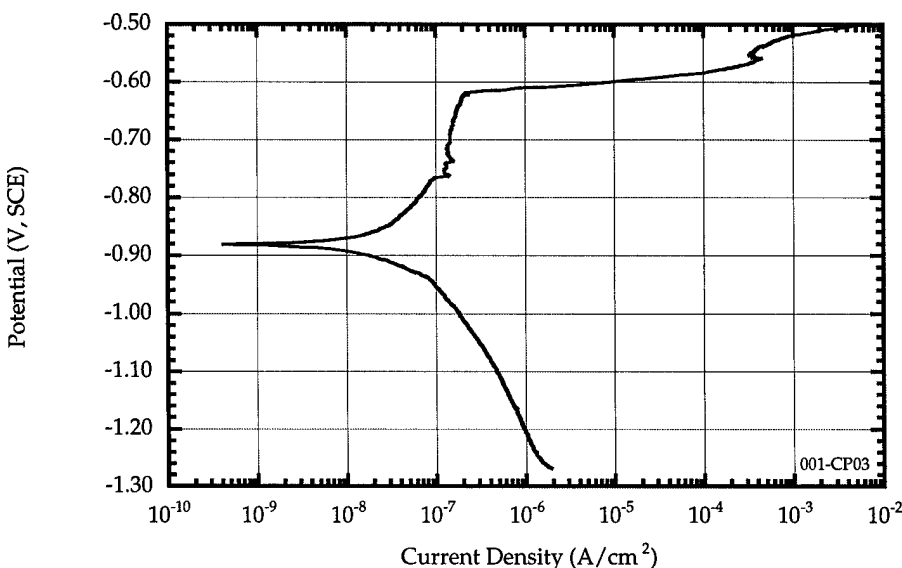


Figure 4.2.1.39. Polarization plot of Al₂Cu in 1.0M NaCl solution at 298K.

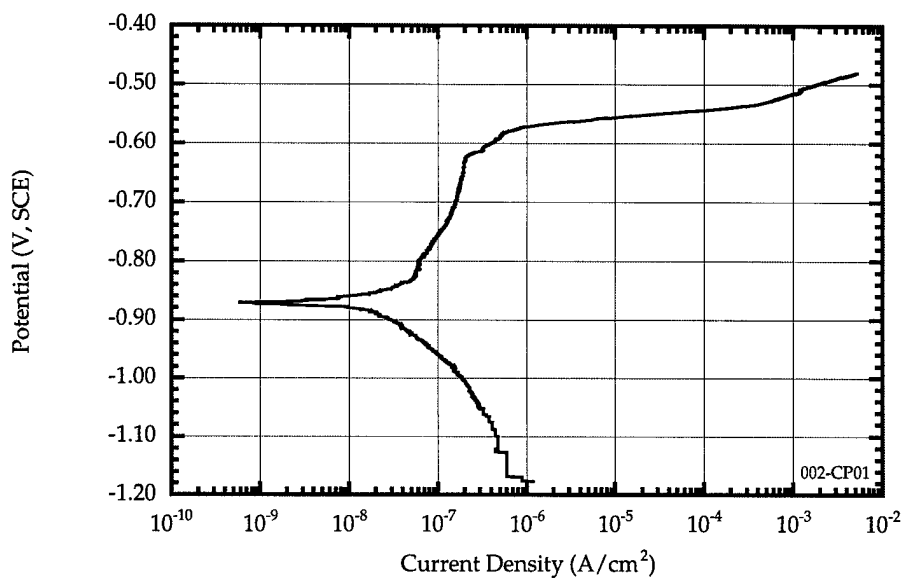


Figure 4.2.1.40. Polarization plot of Al₂Cu + 1.5% Zn in 1.0M NaCl solution at 298K.

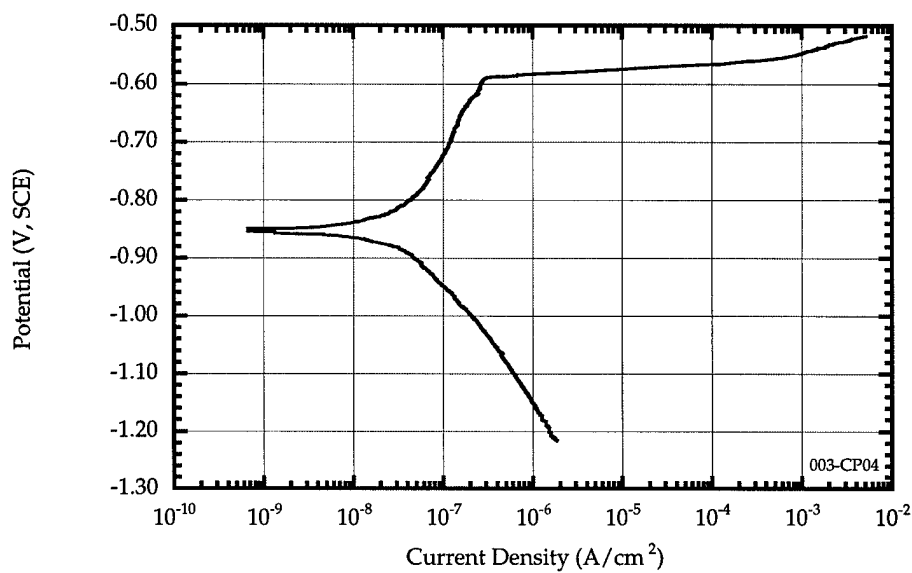


Figure 4.2.1.41. Typical polarization plot of Al₂Cu + 2.5% Zn in 1.0M NaCl solution at 298K.

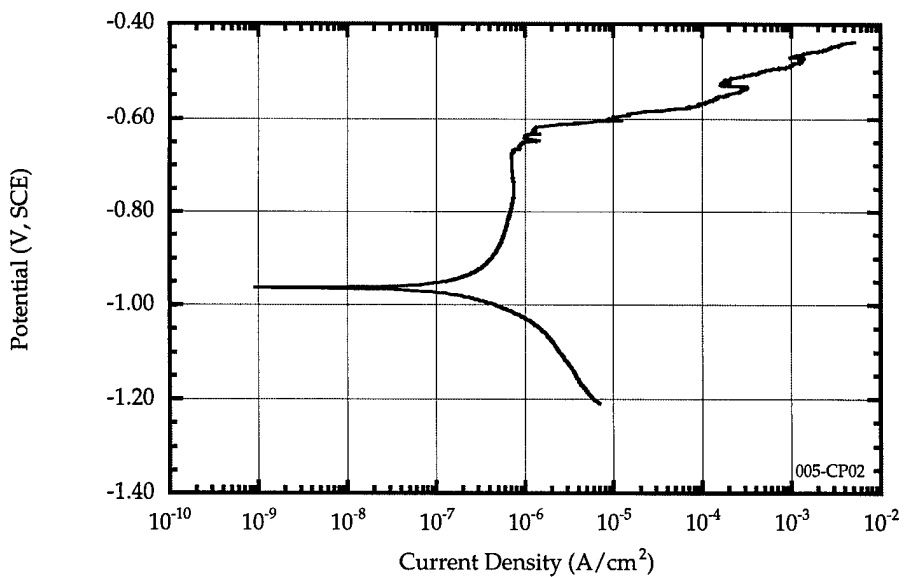


Figure 4.2.1.42. Typical polarization plot of Al₆(Fe,Cu) in 1.0M NaCl solution at 298K.

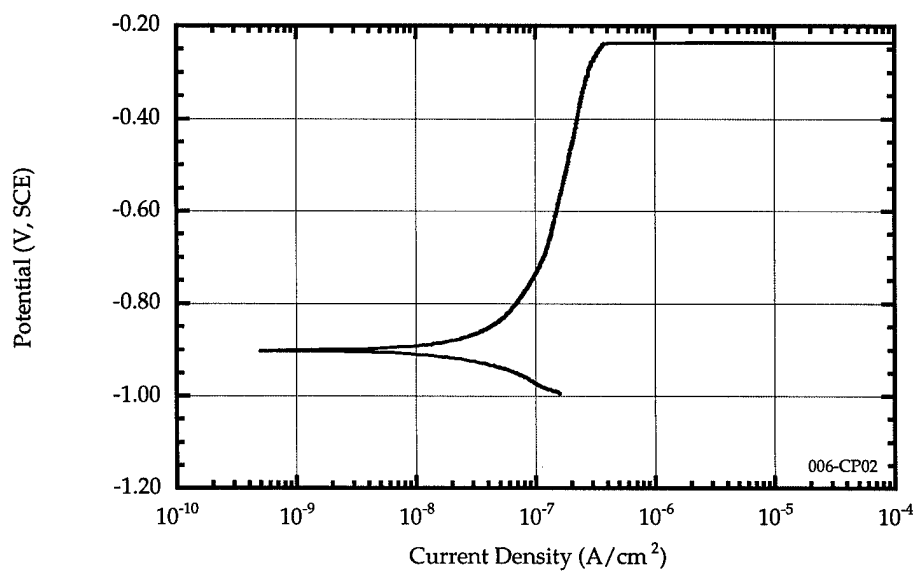


Figure 4.2.1.43. Typical polarization plot of Al₃Fe in 1.0M NaCl solution at 298K.

Effect of Oxygen

Polarization scans were conducted in aerated 1.0M NaCl solution at 298K. Figure 4.2.1.44 through 4.2.1.49 compares the polarization behavior of 7075-T651, 7178-T6, pure Al,

intermetallic alloys Al₂Cu + 2.5% Zn, and Al₃Fe in aerated and deaerated solutions. The corrosion potential in all cases is more noble (more positive) in the aerated environment. The cathodic current density is also higher in the aerated solution. The corrosion potential for 7075-T651 and 7178-T6 in aerated solutions is more noble than their pitting potential (E_{pit}). In other words, pits can form spontaneously on the surface of these alloys in aerated environments.

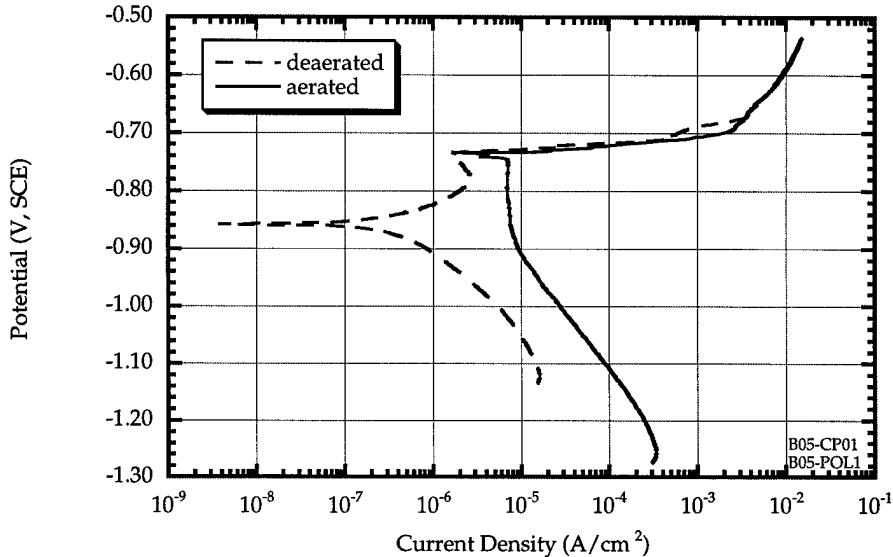


Figure 4.2.1.44. Comparison of polarization behavior for 7075-T651 in aerated and deaerated 1.0M NaCl solution at 298K.

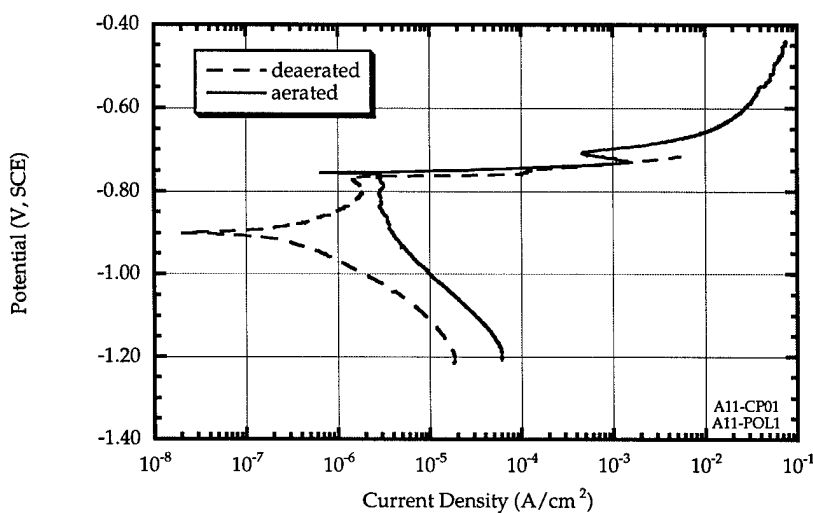


Figure 4.2.1.45. Comparison of polarization behavior for 7178-T6 in aerated and deaerated 1.0M NaCl solution at 298K.

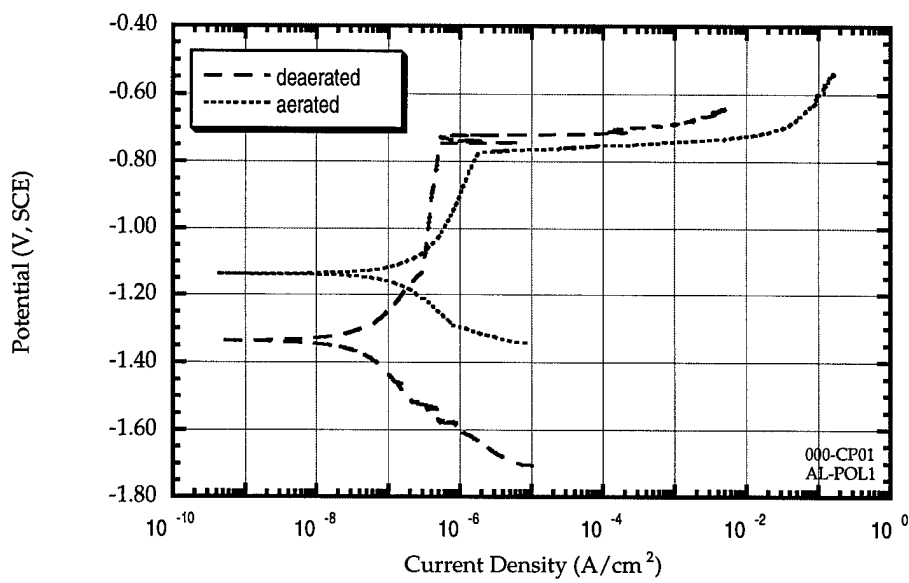


Figure 4.2.1.46. Comparison of polarization behavior for pure Al in aerated and deaerated 1.0M NaCl solution at 298K.

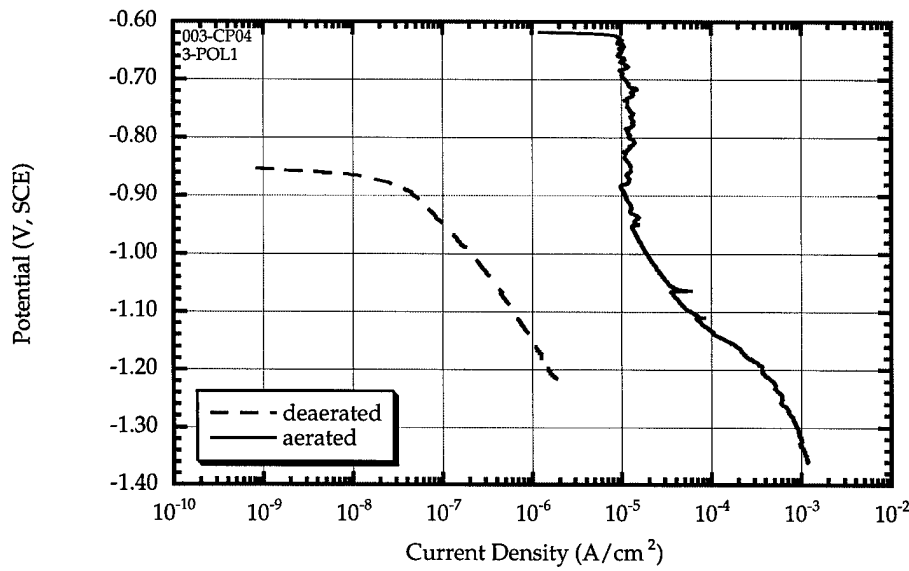


Figure 4.2.1.47. Comparison of cathodic polarization behavior for Al₂Cu + 2.5% Zn in aerated and deaerated 1.0M NaCl solution at 298K.

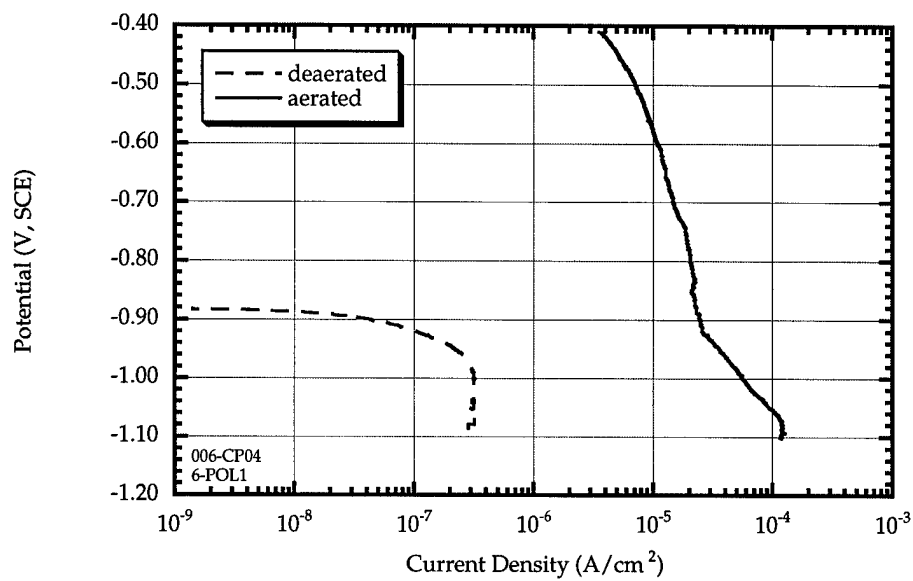


Figure 4.2.1.48. Comparison of polarization behavior for Al₃Fe in aerated and deaerated 1.0M NaCl solution at 298K.

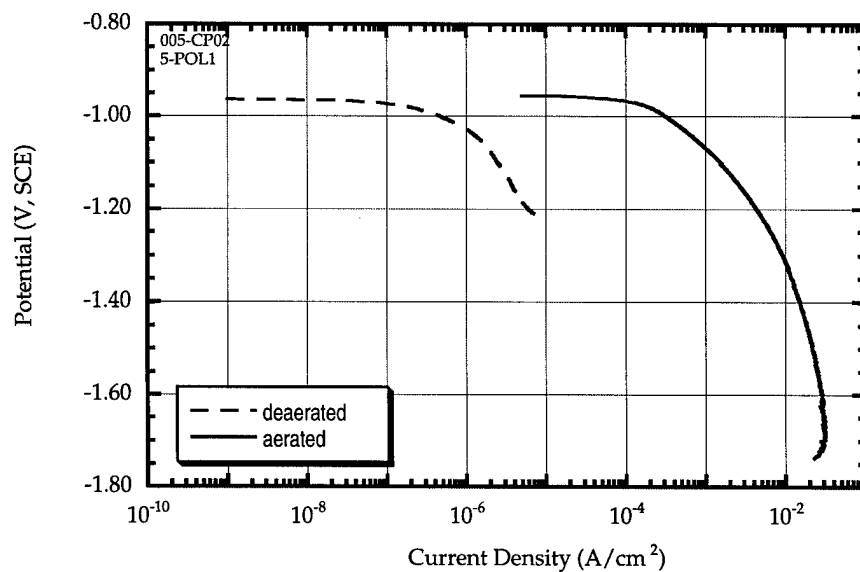


Figure 4.2.1.49. Comparison of cathodic polarization behavior for Al₆(Fe,Cu) in aerated and deaerated 1.0M NaCl solution at 298K.

Polarization Behavior of the Wing Joint

Dynamic polarization experiments were conducted on the rivets obtained from the dismantled joints. The results of this analysis are shown in Figure 4.2.1.50. Since the plate material used for the two joints are the same, only the plate material from joint #2 was tested. These results are shown in Figure 4.2.1.51. Polarization scans were conducted in deaerated 1.0M NaCl solutions.

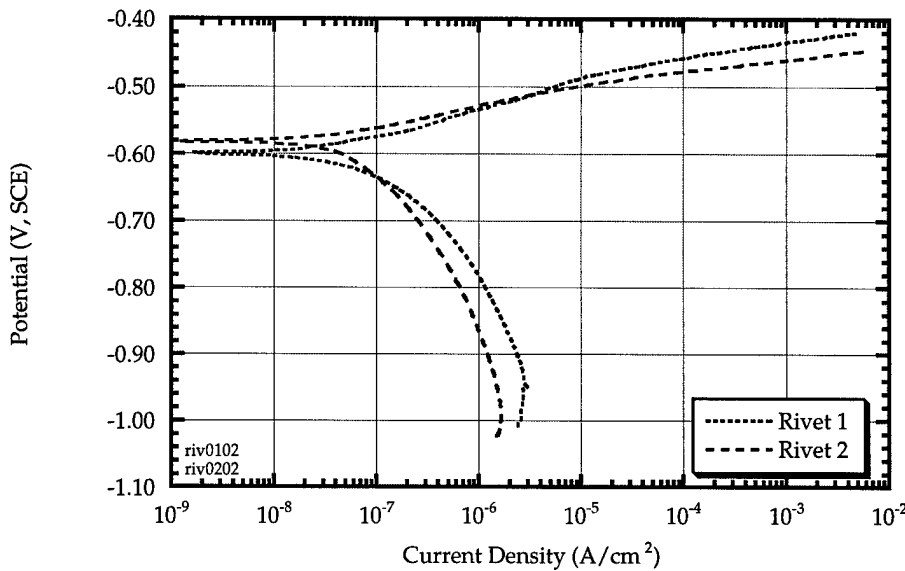


Figure 4.2.1.50. Dynamic polarization plots of the two rivets in 1.0M NaCl solution at 298K.

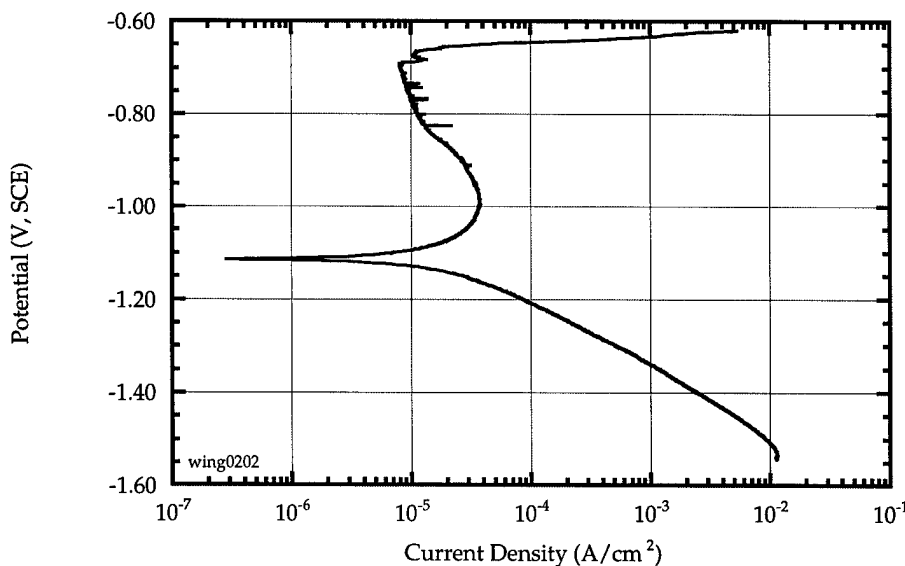


Figure 4.2.1.51. Dynamic polarization of plate material from joint #2 in 1.0M deaerated NaCl solution at 298K.

Effect of Oxygen

Dynamic polarization experiments were also conducted on the rivets and the alloy plate from joint #2 in aerated 1.0M NaCl solutions. The results from the cathodic scans are presented in Figures 4.2.1.52 and 4.2.1.53 below. The deaerated data is included for comparison purposes. The current density for the rivet is roughly two orders of magnitude higher in the aerated environment. The cathodic current density for the alloy plate is also higher in the aerated environment although the difference between the two environments is less pronounced. The corrosion potentials for both materials are more noble in the aerated environment.

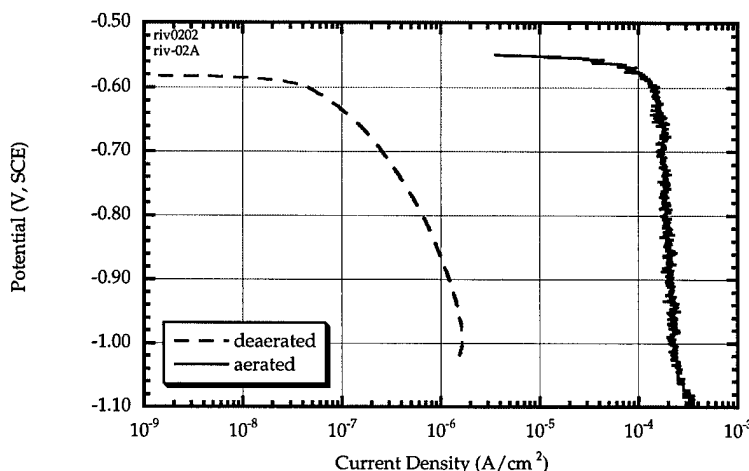


Figure 4.2.1.52. Comparison of the cathodic polarization behavior in aerated and deaerated 1.0M NaCl for the steel rivet.

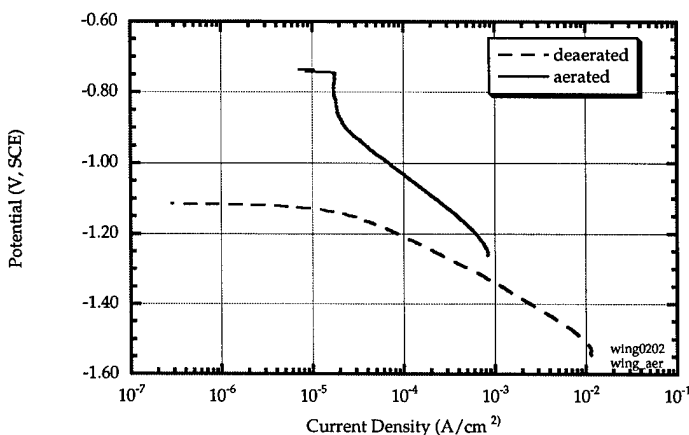


Figure 4.2.1.53. Comparison of cathodic polarization behavior for the alloy plate from joint #2 in aerated and deaerated 1.0M NaCl solution.

Galvanic Interaction

Constituent Particle / Matrix Interaction

In the deaerated solution, hydrogen reduction is the most likely cathodic reaction due to the slightly acidic pH of 6.2. The equilibrium potential for this reaction in the environment is:



$$E_{\text{eq}} (\text{V, SHE}) = -0.059 \text{ pH}$$
$$E_{\text{eq}} (\text{V, SCE}) = -0.61 \text{ V, SCE}$$

The cathodic and anodic polarization data for the intermetallics and pure aluminum in deaerated 1.0M NaCl is presented as Tafel plots in Figures 4.2.1.54 and 4.2.1.55. The exchange current densities and slopes were extracted by regression analysis on the linear portion of the plots. This information was converted to the more convenient form of:

$$E(V, \text{SCE}) = a + b \log(i) \quad (4.2.1.7)$$

and is summarized in Tables 4.2.1.12 and 4.2.1.13.

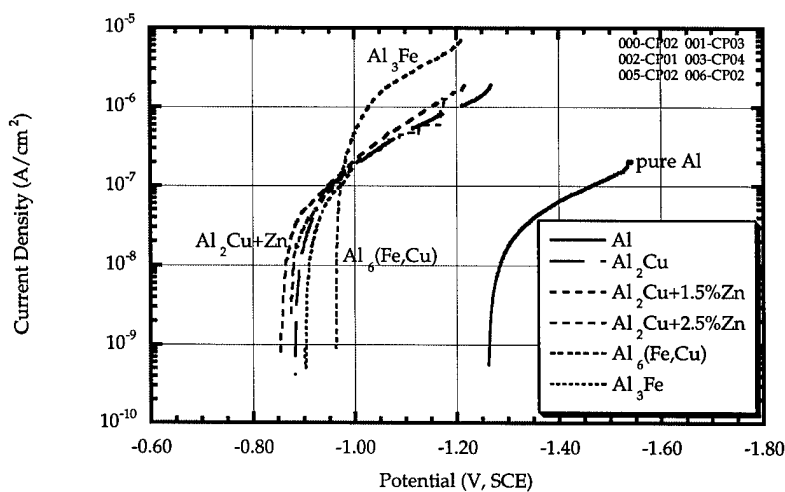


Figure 4.2.1.54. Tafel plot showing the cathodic polarization data for pure aluminum and the intermetallic alloys in deaerated 1.0M NaCl at 298K.

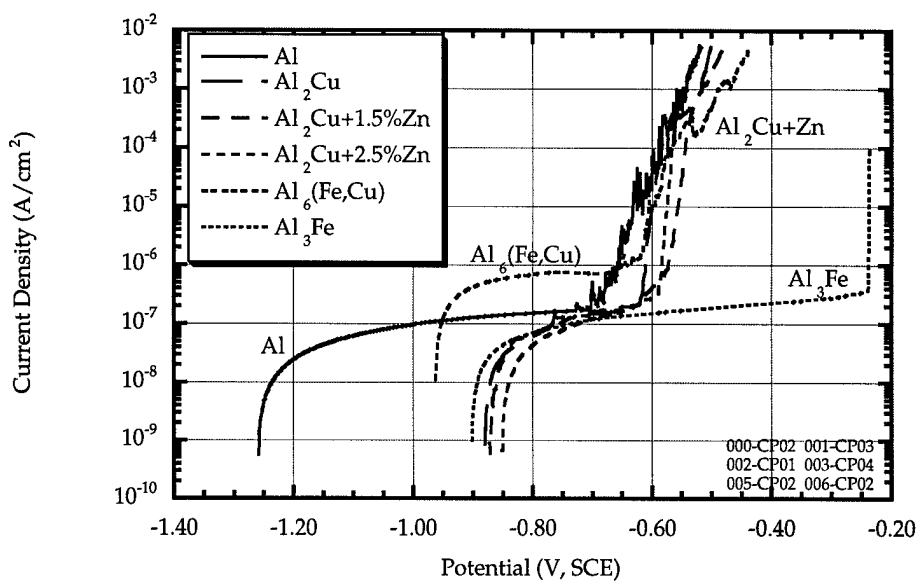


Figure 4.2.1.55. Tafel plot of the anodic polarization data for pure aluminum and the intermetallic alloys in deaerated 1.0M NaCl at 298K.

Dynamic polarization experiments were also conducted in aerated 1.0M NaCl solutions. In addition to the hydrogen reduction reaction, reduction of dissolved oxygen can take place. The equilibrium potential for the oxygen reduction reaction for the pH range studied is 0.62V SCE. The cathodic polarization data for pure aluminum, Al₂Cu + 2.5% Zn, Al₃Fe, and Al₆(Fe,Cu) in aerated environment are presented in Figure 4.2.1.56. The data is summarized in Table 4.2.1.12.



$$E_{eq} (V, SHE) = 1.228 - 0.059 \text{ pH}$$

$$E_{eq} (V, SCE) = 0.62 \text{ V, SCE}$$

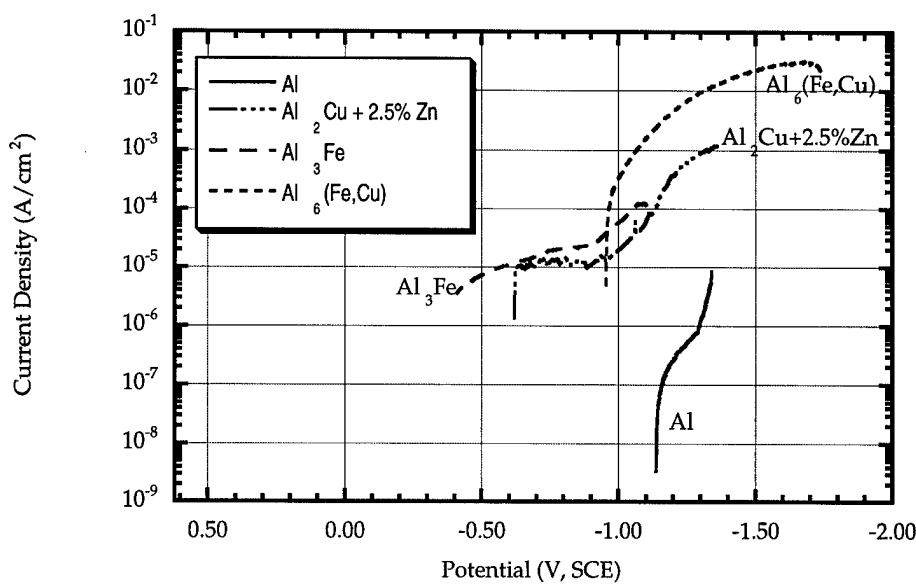


Figure 4.2.1.56. Tafel plot showing the cathodic polarization data for pure Al, $\text{Al}_2\text{Cu} + 2.5\%$ Zn, Al_3Fe , and $\text{Al}_6(\text{Fe},\text{Cu})$ in aerated 1.0M NaCl solution.

Table 4.2.1.12. Cathodic polarization kinetics parameters for the intermetallics and pure aluminum in aerated and deaerated 1.0M NaCl

Material	Deaerated			Aerated		
	a	b(V)	$i_0(\text{A}/\text{cm}^2)$	a	b (V)	$i_0(\text{A}/\text{cm}^2)$
Pure Al	-3.38	-0.27	7.4×10^{-11}	-2.27	-0.22	1.4×10^{-13}
Al_2Cu	-2.89	-0.28	8.0×10^{-9}			
$\text{Al}_2\text{Cu} + 1.5\%$ Zn	-2.55	-0.23	3.5×10^{-9}			
$\text{Al}_2\text{Cu} + 2.5\%$ Zn	-2.35	-0.20	2.1×10^{-9}	-1.77	-0.25	1.9×10^{-15}
$\text{Al}_6(\text{Fe},\text{Cu})$	-2.54	-0.26	2.8×10^{-8}	-1.98	-0.30	2.9×10^{-9}
Al_3Fe	-1.82	-0.12	3.7×10^{-10}	-3.16	-0.51	3.9×10^{-8}

Table 4.2.1.13. Anodic polarization parameters for the intermetallics and pure aluminum in deaerated 1.0M NaCl at 298K.

Material	a	b (V, SCE)
Pure Al		
E > -0.69V	-0.43	0.039
E < -0.69V	7.57	1.23
Al ₂ Cu		
E > -0.62V	-0.54	0.012
E < -0.62V	3.41	0.60
Al ₂ Cu + 1.5% Zn		
E > -0.58V	-0.48	0.014
E < -0.58V	1.66	0.35
Al ₂ Cu + 2.5% Zn		
E > -0.59V	-0.53	0.0092
E < -0.59V	1.31	0.29
Al ₆ (Fe,Cu)		
E > -0.63V	-0.44	0.032
E < -0.63V	3.55	0.70
Al ₃ Fe		
E > -0.24V	-0.23	0.00058
E < -0.24V	7.23	1.15

With the data in Tables 4.2.1.12 and 4.2.1.13, the net current density for intermetallic - pure aluminum couples can be computed by applying the mixed potential theory (equations 1.12 through 1.14). The α and β phases in this case are pure aluminum and the intermetallics.

The free corrosion potential is defined as the potential where the net current is zero. Since the anodic and cathodic currents have opposite signs, the free corrosion potential can be found by equating the sum of all cathodic currents to the negative sum of all anodic currents.

$$\sum i_c = -\sum i_a \quad (4.2.1.9)$$

$$f_{Al} i_{a,Al} + f_{int} i_{a,int} = -(f_{Al} i_{c,Al} + f_{int} i_{c,int}) \quad (4.2.1.10)$$

where

- f_{Al} : area fraction of pure Al in the coupled sample
- f_{int} : area fraction of the intermetallics in the coupled sample
- $i_{a,Al}$: anodic current density on pure Al
- $i_{a,int}$: anodic current density on the intermetallics
- $i_{c,Al}$: cathodic current density on pure Al
- $i_{c,int}$: cathodic current density on the intermetallics

The free corrosion potential for the intermetallic - pure Al couples were calculated as a function of the area fraction of the intermetallic alloy; that is, f_{int} is the independent variable in these calculations. The calculation for Al-Al₂Cu couple ($f_{int} = 0.50$) in deaerated environment is demonstrated in Figure 4.2.1.57. The variation of the coupled free corrosion potential in deaerated and aerated solutions as a function of the area fraction of intermetallic particle are presented in Figures 4.2.1.58 and 4.2.1.59 respectively. Figures 4.2.1.58b and 4.2.1.59b are magnified views of these calculations near the pure aluminum end of the spectrum. Galvanic coupled experiments were conducted to verify these calculations. The results of these experiments are shown in Figures 4.2.1.60-4.2.1.62.

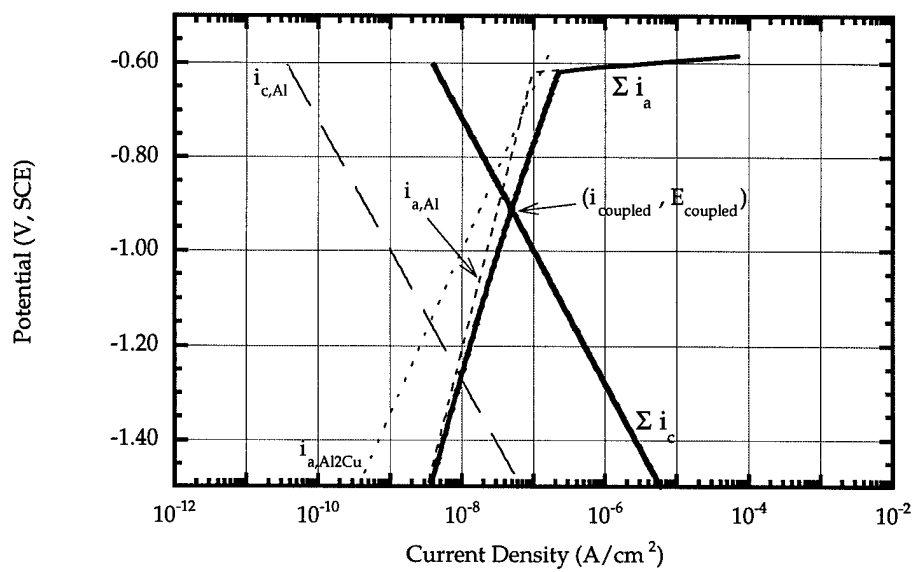
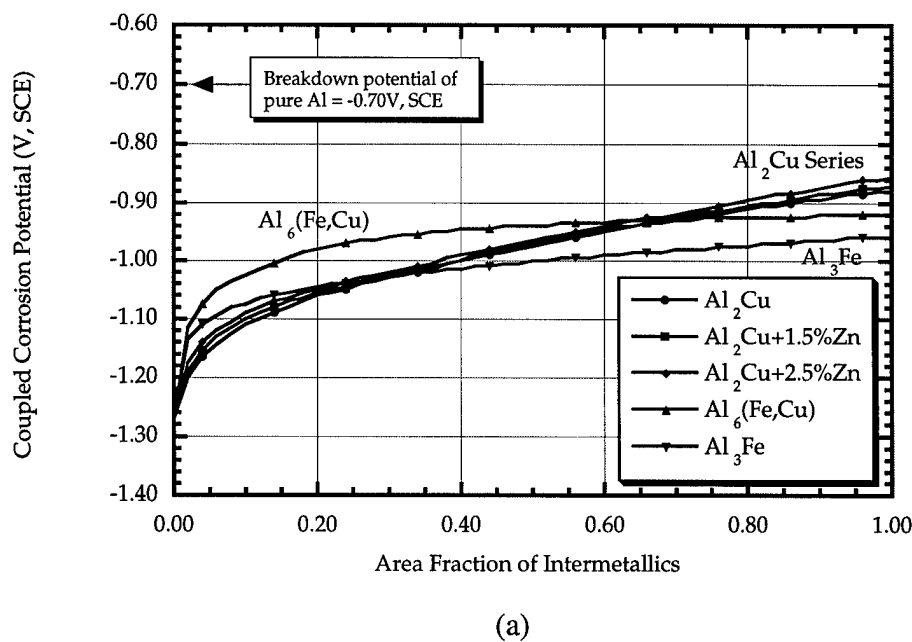
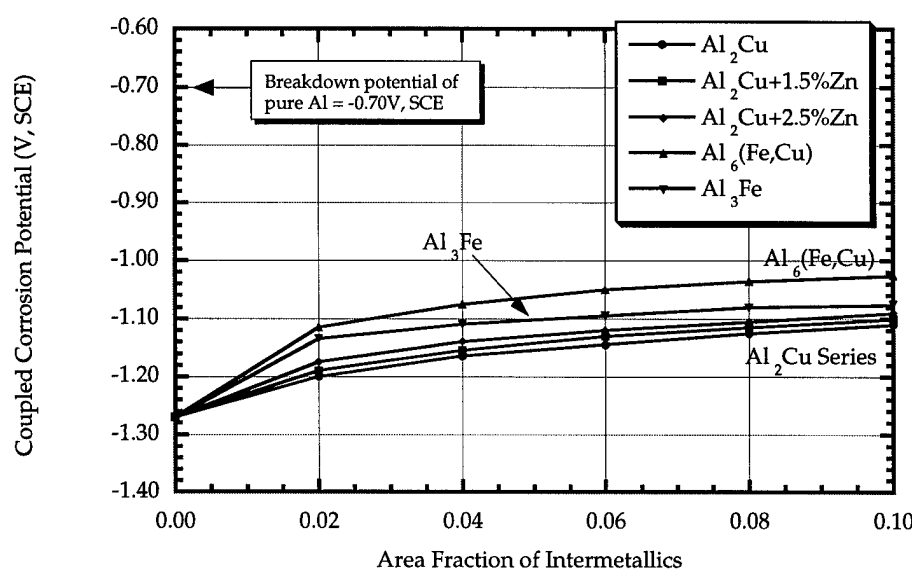


Figure 4.2.1.57. Calculation of free corrosion potential of coupled Al and Al₂Cu in deaerated 1.0M NaCl solution at 298K (Area fraction of Al₂Cu = 0.5)

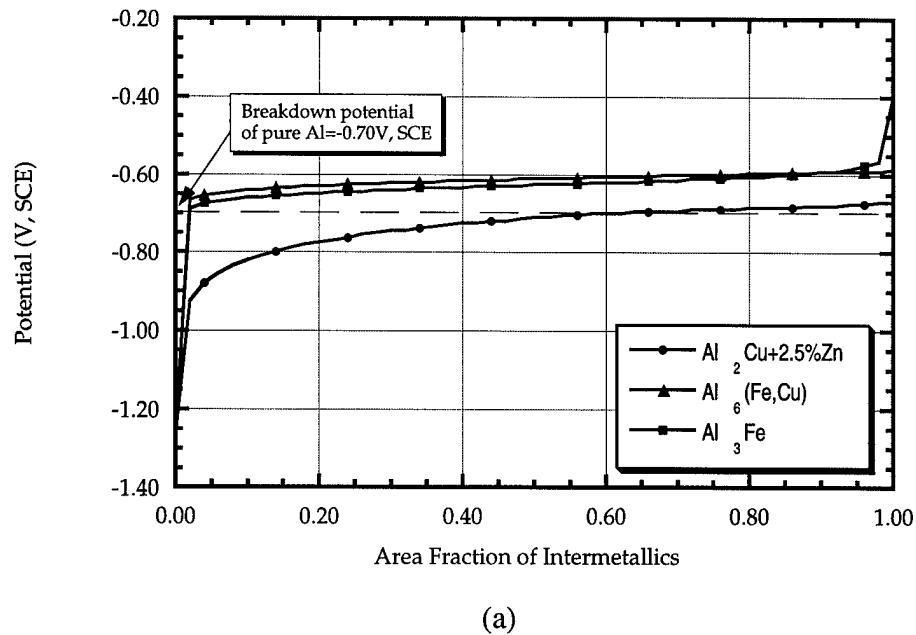


(a)

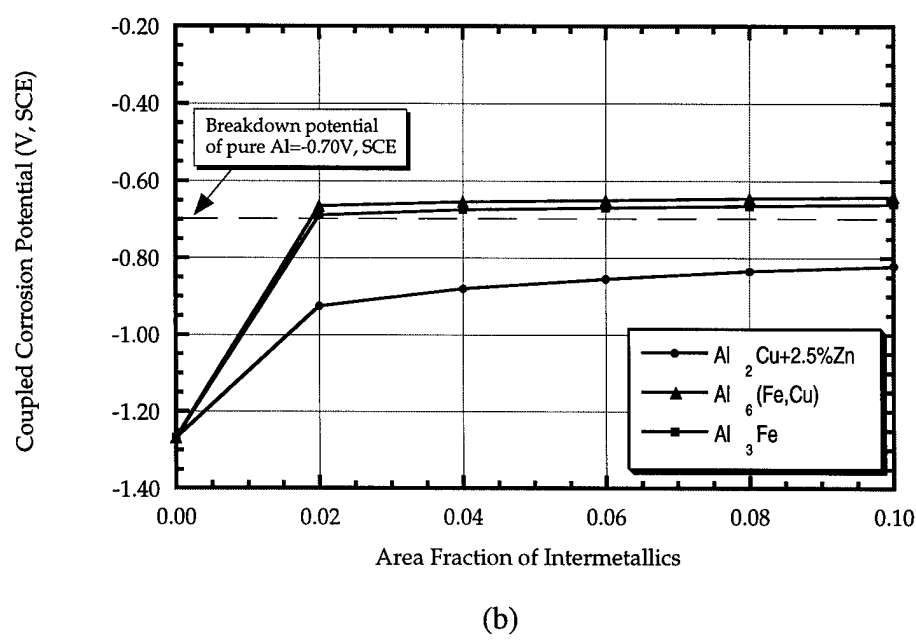


(b)

Figure 4.2.1.58. Calculated corrosion potential of intermetallic - pure Al couples in deaerated 1.0M NaCl solution at 298K. Figure b is a magnified view of these calculation when the couples are predominantly aluminum.



(a)



(b)

Figure 4.2.1.59. Calculated corrosion potential of intermetallic - pure Al couples in aerated 1.0M NaCl solution at 298K. Figure b is a magnified view of these calculations when the coupled samples are predominantly aluminum.

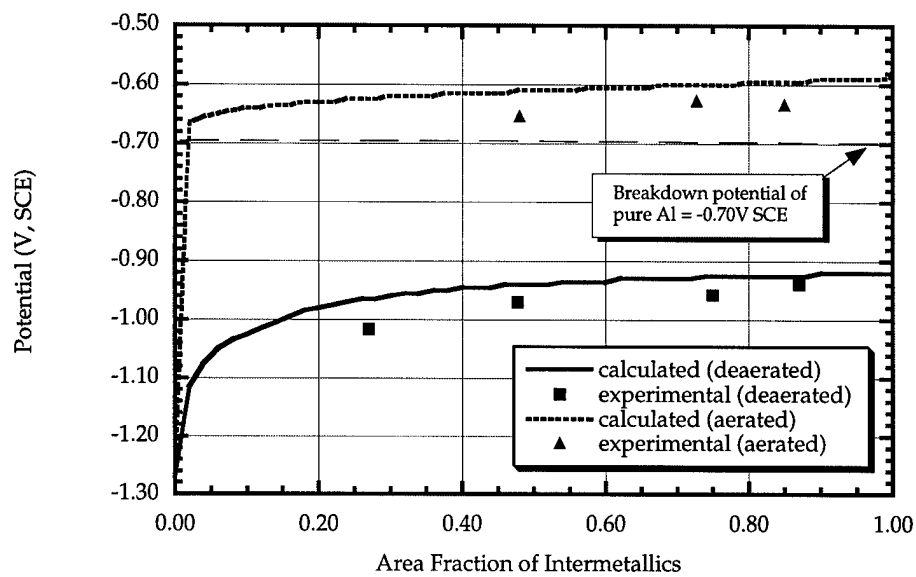


Figure 4.2.1.60. Comparison of calculated and experimental coupled corrosion potential in aerated and deaerated environments for $\text{Al}_6(\text{Fe},\text{Cu})$ - Al samples.

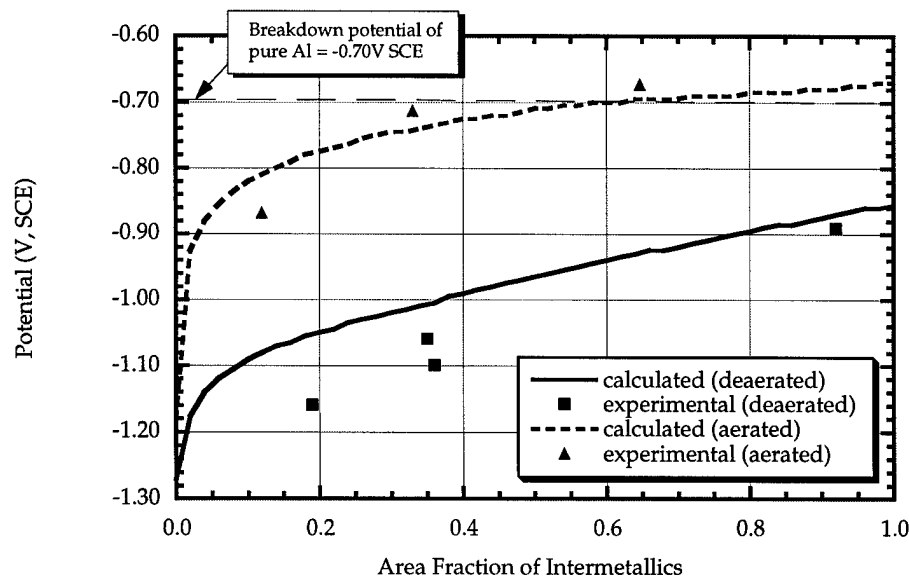


Figure 4.2.1.61. Comparison of calculated and experimental coupled corrosion potential in aerated and deaerated 1.0M NaCl for $(\text{Al}_2\text{Cu} + 2.5\%\text{Zn})$ - Al samples.

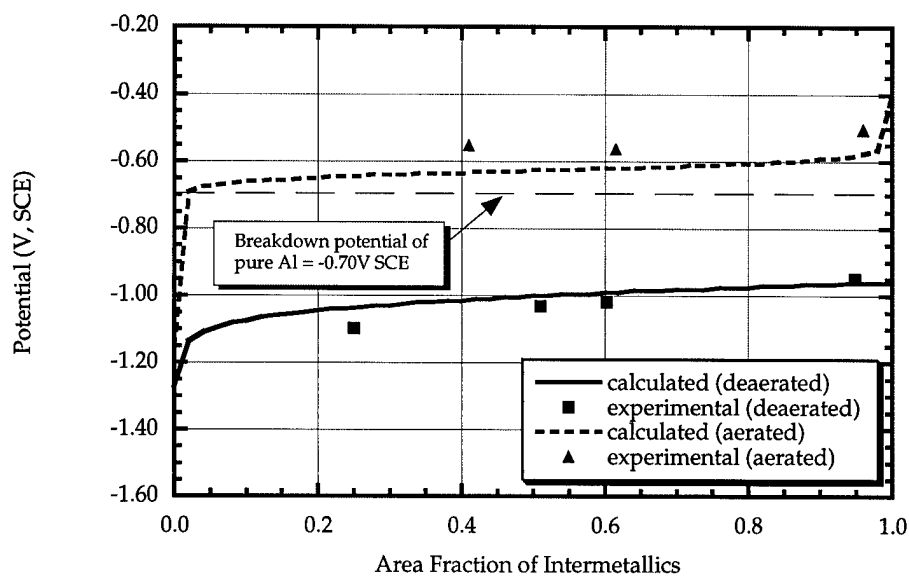


Figure 4.2.1.62. Comparison of calculated and experimental coupled corrosion potential in aerated and deaerated 1.0M NaCl for Al_3Fe - Al samples.

Rivet / Alloy Plate Interaction

The cathodic polarization data for the rivets, wing panel, 7075-T651, and 7178-T6 in aerated and deaerated 1.0M NaCl are presented as Tafel plots in Figures 4.2.1.63 and 4.2.1.64. Similarly, the anodic polarization data for these materials in deaerated 1.0M NaCl solution are presented in Figure 4.2.1.65. The cathodic and anodic reaction kinetics parameters are summarized in Tables 4.2.1.14 and 4.2.1.15 respectively. It is obvious from Figure 4.2.1.64 that the rivet is very effective at reducing oxygen. The exchange current density in aerated solutions on the rivet is on average three orders of magnitude higher than that of the aluminum alloys.

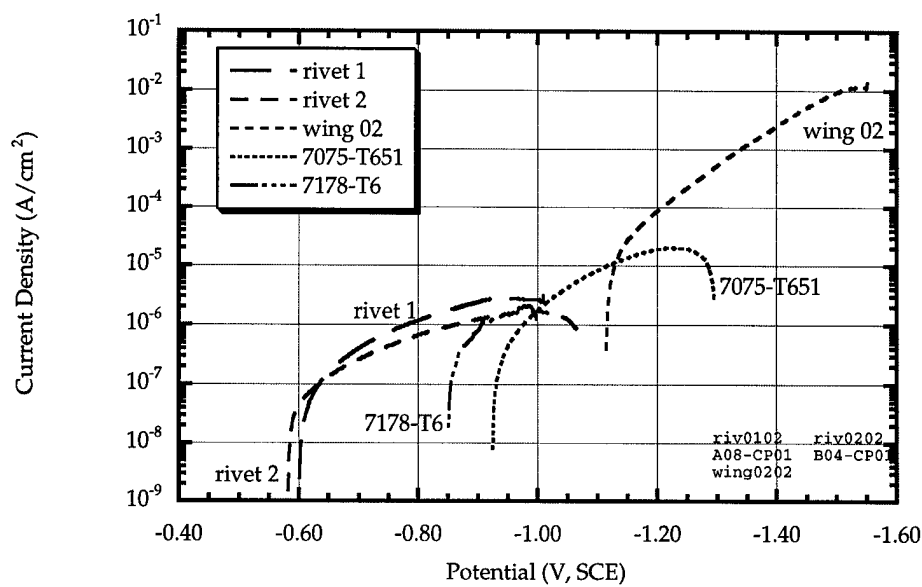


Figure 4.2.1.63. Tafel plot of the cathodic polarization data for the rivet from joints #1 and #2, and the wing panel #2 in deaerated 1.0M NaCl solution.

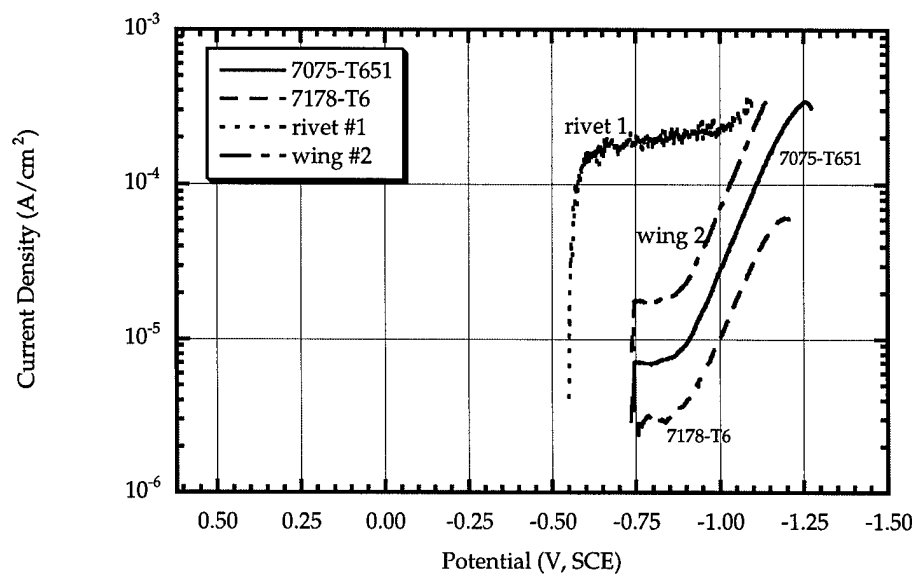


Figure 4.2.1.64. Tafel plot of the cathodic polarization data for the rivet, 7178-T6 and 7075-T651 in aerated 1.0M NaCl solution.

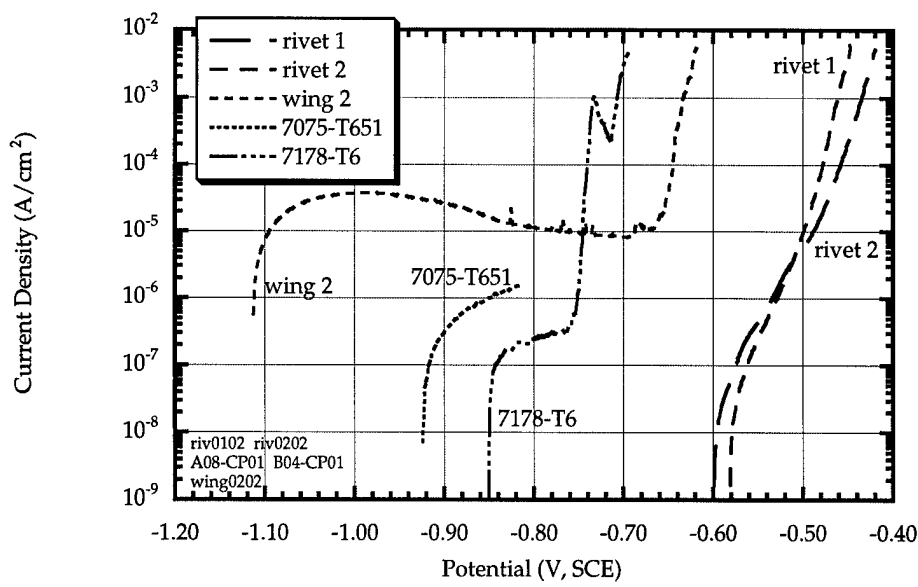


Figure 4.2.1.65. Tafel plot presenting the anodic polarization data of rivets from joints #1, #2, and wing material from joint #2. Representative data from 7075-T651 and 7178-T6 is also included.

Table 4.2.1.14. Cathodic reaction kinetics parameters extracted from Tafel plots.

Material	Deaerated			Aerated		
	a	b (V)	i_0 (A/cm ²)	a	b (V)	i_0 (A/cm ²)
Rivet #1	-2.29	-0.25	1.1×10^{-7}	-7.23	-1.73	1.7×10^{-8}
Rivet #2	-2.72	-0.31	9.4×10^{-8}			
Plate #2	-1.76	-0.14	1.9×10^{-9}	-2.01	-0.25	3.0×10^{-11}
7178-T6	-1.69	-0.12	5.9×10^{-10}	-2.25	-0.24	1.1×10^{-12}
7075-T651	-1.82	-0.15	4.8×10^{-9}	-1.91	-0.20	2.2×10^{-13}

Table 4.1.2.15. Anodic reaction kinetics parameters in deaerated 1.0M NaCl extracted from Tafel plots.

Material	a	b (V, SCE)
Rivet #1	-0.29	0.040
Rivet #2	-0.33	0.032
Plate #2	-0.59	0.014
7178-T6		
E > -0.77V	-0.69	0.015
E < -0.77V	-0.015	0.14
7075-T651		
E > -0.74V	-0.72	0.0052
E < -0.74V	-0.47	0.066

The free corrosion potential of coupling the rivets to the plate from joint #2, 7178-T6, and 7075-T651 was calculated by applying the mixed potential theory with the kinetics parameters listed above. The results of these calculations in both aerated and deaerated environments are presented in Figures 4.2.1.66 through 4.2.1.68.

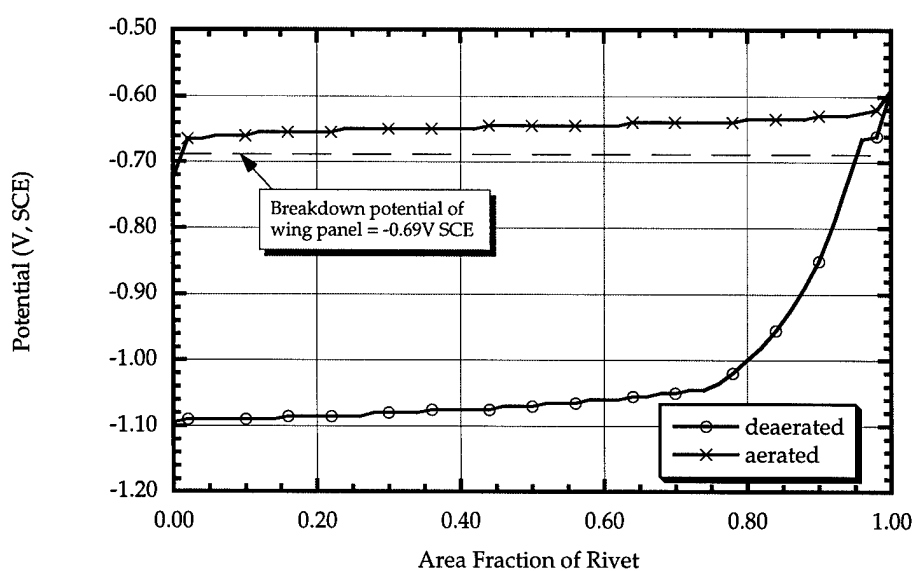


Figure 4.2.1.66. Plot showing the calculated corrosion potential of the coupled rivet - wing panel in aerated and deaerated 1.0M NaCl solutions.

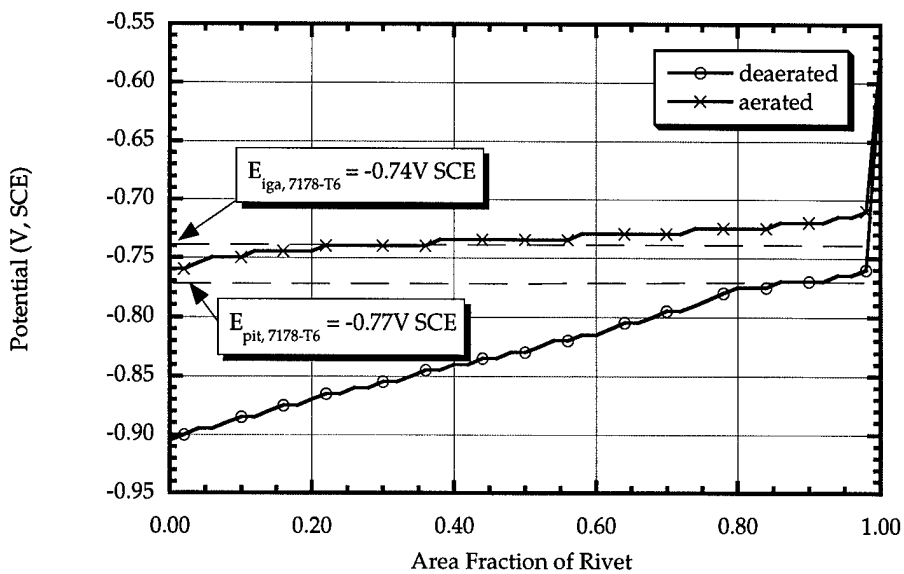


Figure 4.2.1.67. Plot showing the calculated corrosion potential of the coupled rivet - 7178-T6 in aerated and deaerated 1.0M NaCl solutions.

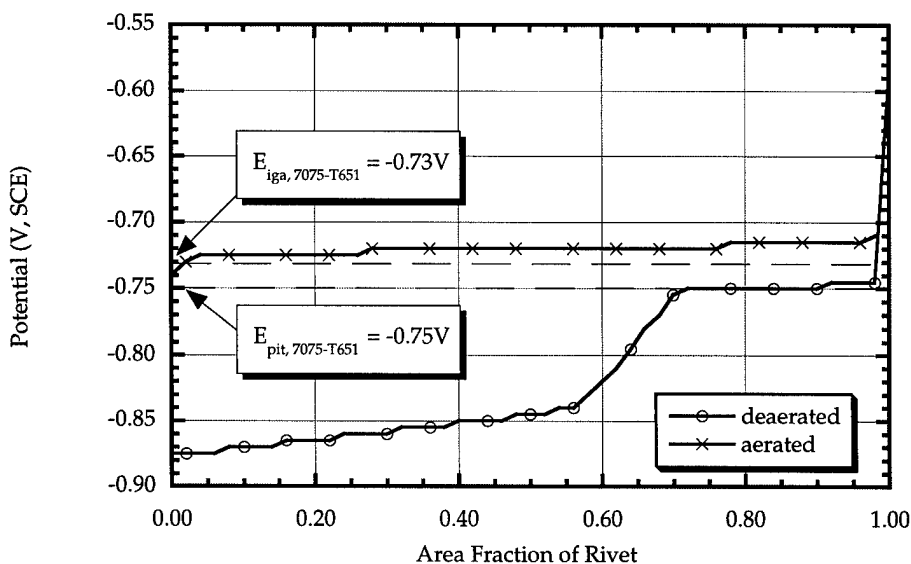


Figure 4.2.1.68. Plot showing the calculated corrosion potential of the coupled rivet - 7075-T651 in aerated and deaerated 1.0M NaCl solutions.

Experiments were conducted in 1.0M aerated and deaerated NaCl solutions to verify the calculations above. Comparisons between the experimental results and calculations are

presented in Figures 4.2.1.69 to 4.2.1.71 below. There is in general good agreement between the calculated and observed results.

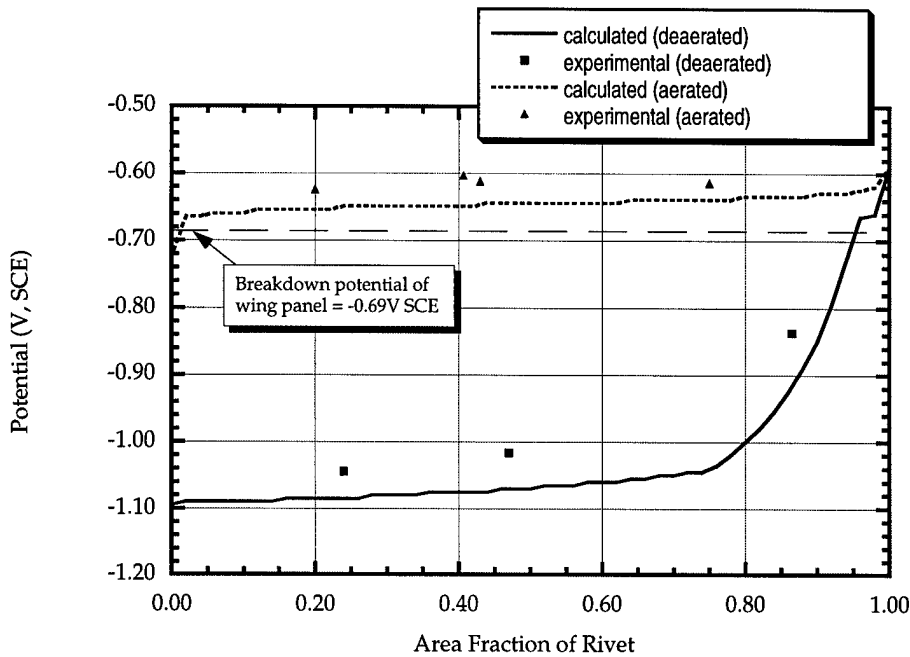


Figure 4.2.1.69. Comparison of calculated and experimental coupled corrosion potential in aerated and deaerated 1.0M NaCl for rivet - wing panel samples.

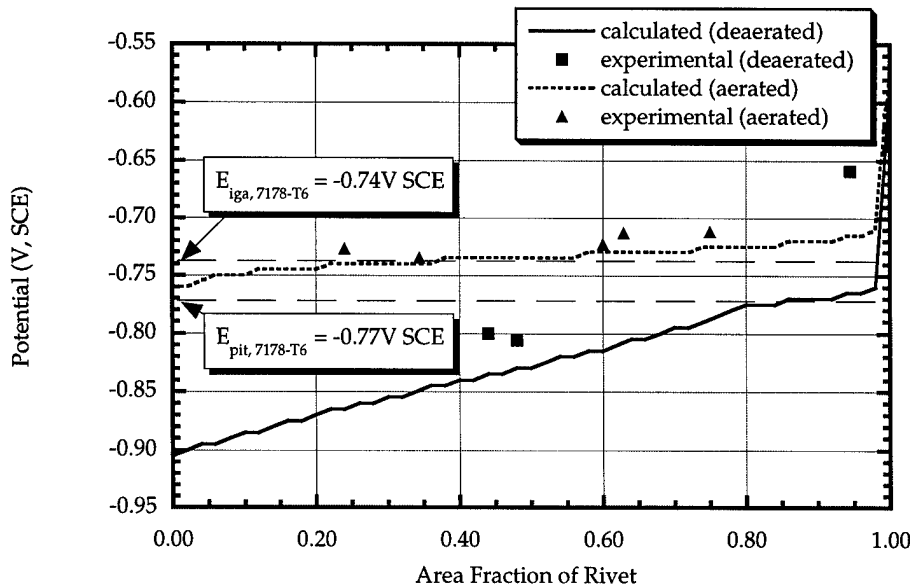


Figure 4.2.1.70. Comparison between experimental and calculated coupled corrosion potential between the steel rivet and 7178-T6 plate.

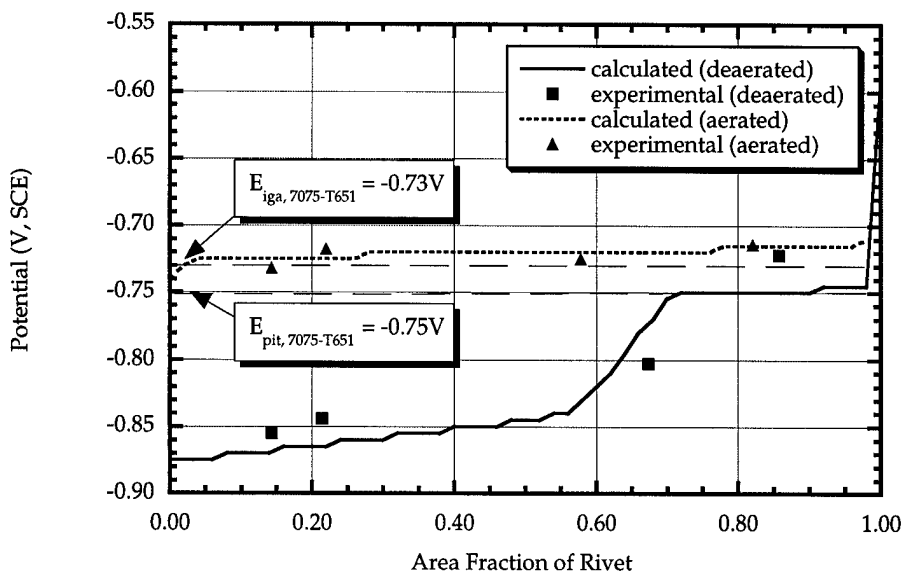


Figure 4.2.1.71. Comparison between experimental and calculated coupled corrosion potential between the steel rivet and 7075-T651 plate.

The important electrochemical potentials for 7178-T6 and 7075-T651 are summarized in Figures 4.2.1.72(a) and (b) respectively. The properties of the alloy are denoted in bold. The terms used in these figures are explained below.

- Ecorr, dea.** : Corrosion potential of the alloy in deaerated environment
- Ecorr, aer.** : Corrosion potential of the alloy in aerated environment
- Eiga** : Critical potential for the initiation of intergranular attack
- Epit** : Critical potential for the initiation of pitting
- Ecorr, int, dea.** : Corrosion potential of the intermetallics in deaerated environment
- Ecorr, int, aer.** : Corrosion potential of the intermetallics in aerated environment
- Ecorr, riv.** : Corrosion potential of the rivet in both aerated and deaerated environment

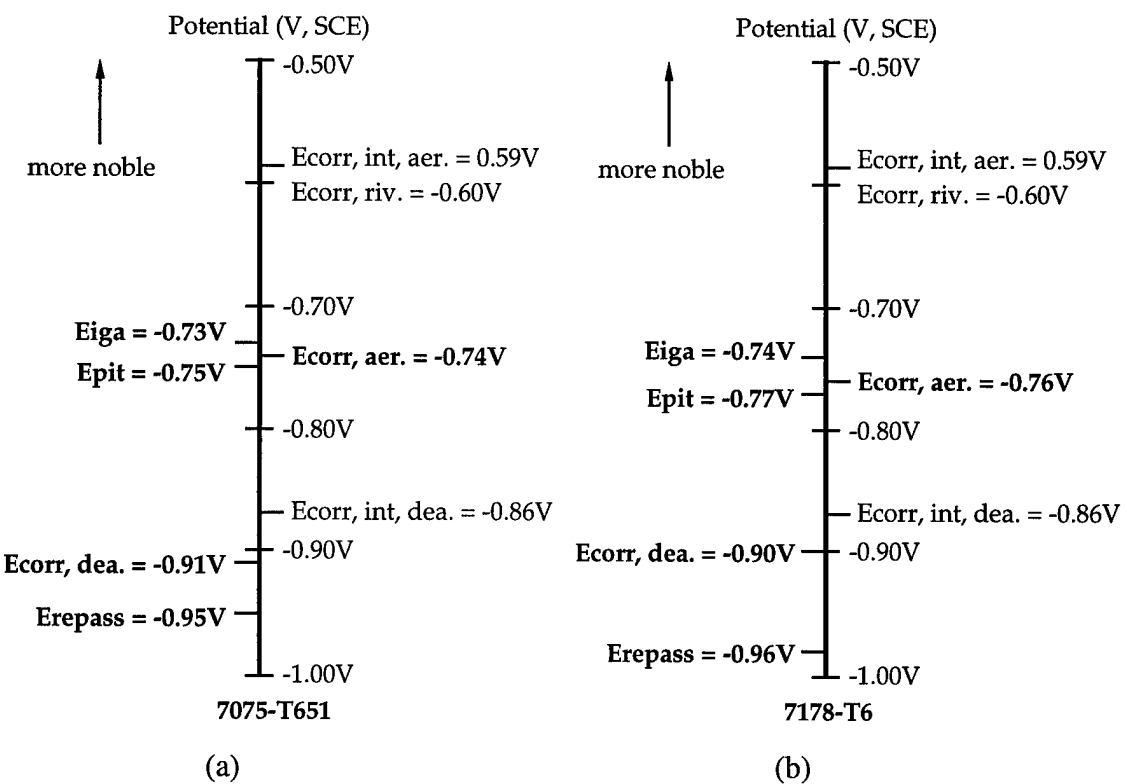


Figure 4.2.1.71. Schematic summary of the important electrochemical potentials for (a) 7075-T651 and (b) 7178-T6.

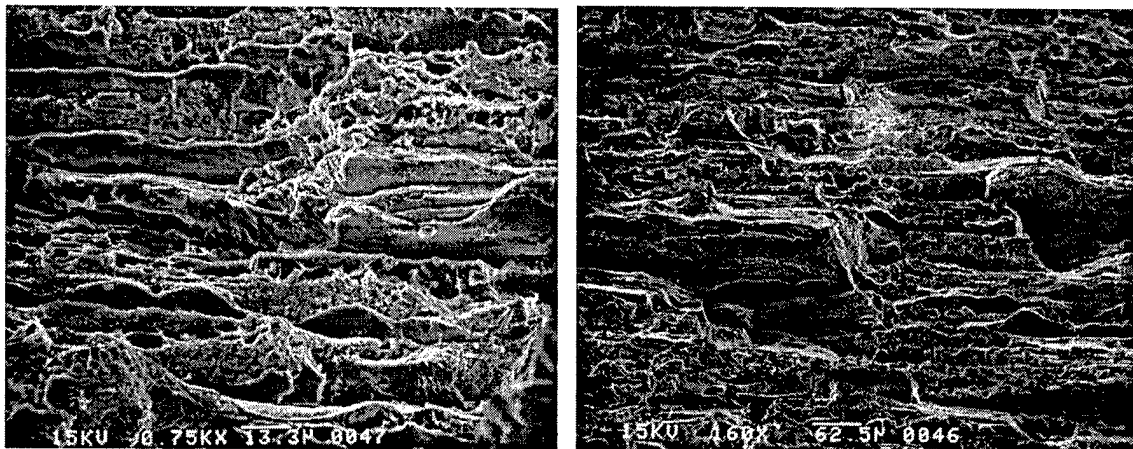
Mechanical & Environmental Behavior Testing

Tensile Tests

Tensile tests were conducted to obtain the 0.2% yield stress of the material. The results presented in Table 4.2.1.16 are the averages of at least two tests. The fracture surfaces for the two materials are shown in Figures 4.2.1.72 and 4.2.1.73.

Table 4.2.1.16. Tensile properties of the materials used

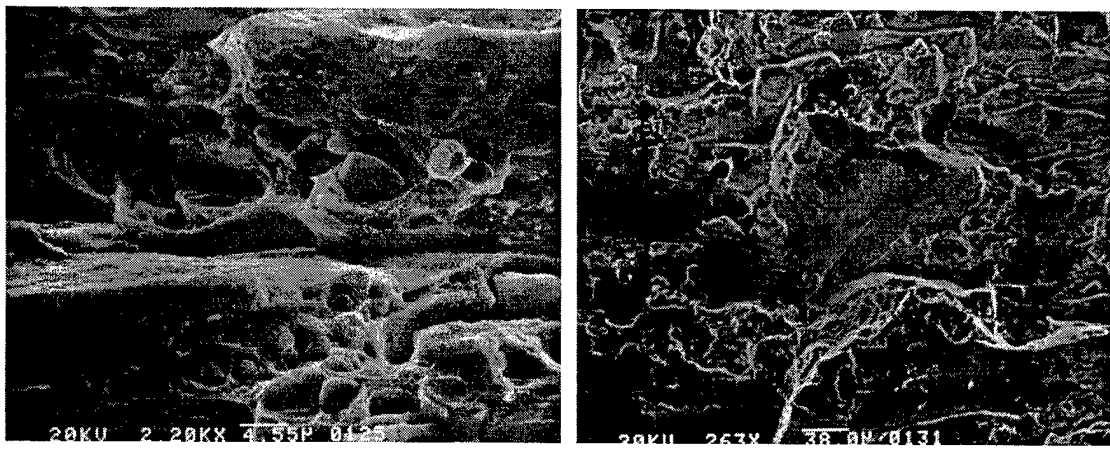
Material	Orientation	Yield Stress (MPa)
7075-T651	Longitudinal	561
7075-T651	Transverse	571
7178-T6	Longitudinal	575
7178-T6	Transverse	598



(a)

(b)

Figure 4.2.1.72. Fracture surfaces from 7075-T651 tensile samples along the (a) longitudinal, (b) transverse direction.



(a)

(b)

Figure 4.2.1.73. Fracture surfaces from 7178-T6 tensile samples along (a) longitudinal, (b) transverse direction.

Stress Corrosion Cracking Tests

Stress corrosion cracking studies were conducted in 1.0M NaCl solution at 298K. The material was loaded to approximately 65% of yield. A potentiostat was used to maintain the potential above the lower breakdown potential, E_{pit} , but below the upper breakdown potential, E_{iga} . Hence, pitting was the only form of corrosion on these specimens. Figure 4.2.1.74 shows a 7075-T651 sample tested to failure in 1.0M NaCl solution under a constant tensile load of 3,540kg. This is equivalent to an initial tensile stress of 379 MPa. Only one longitudinal surface (the surface on the right of Figure 4.2.1.74 a) was exposed. All other surfaces were masked off

with resin. High magnifications of the fracture surface (Figure 4.2.1.74 b and c) show little sign of ductility.

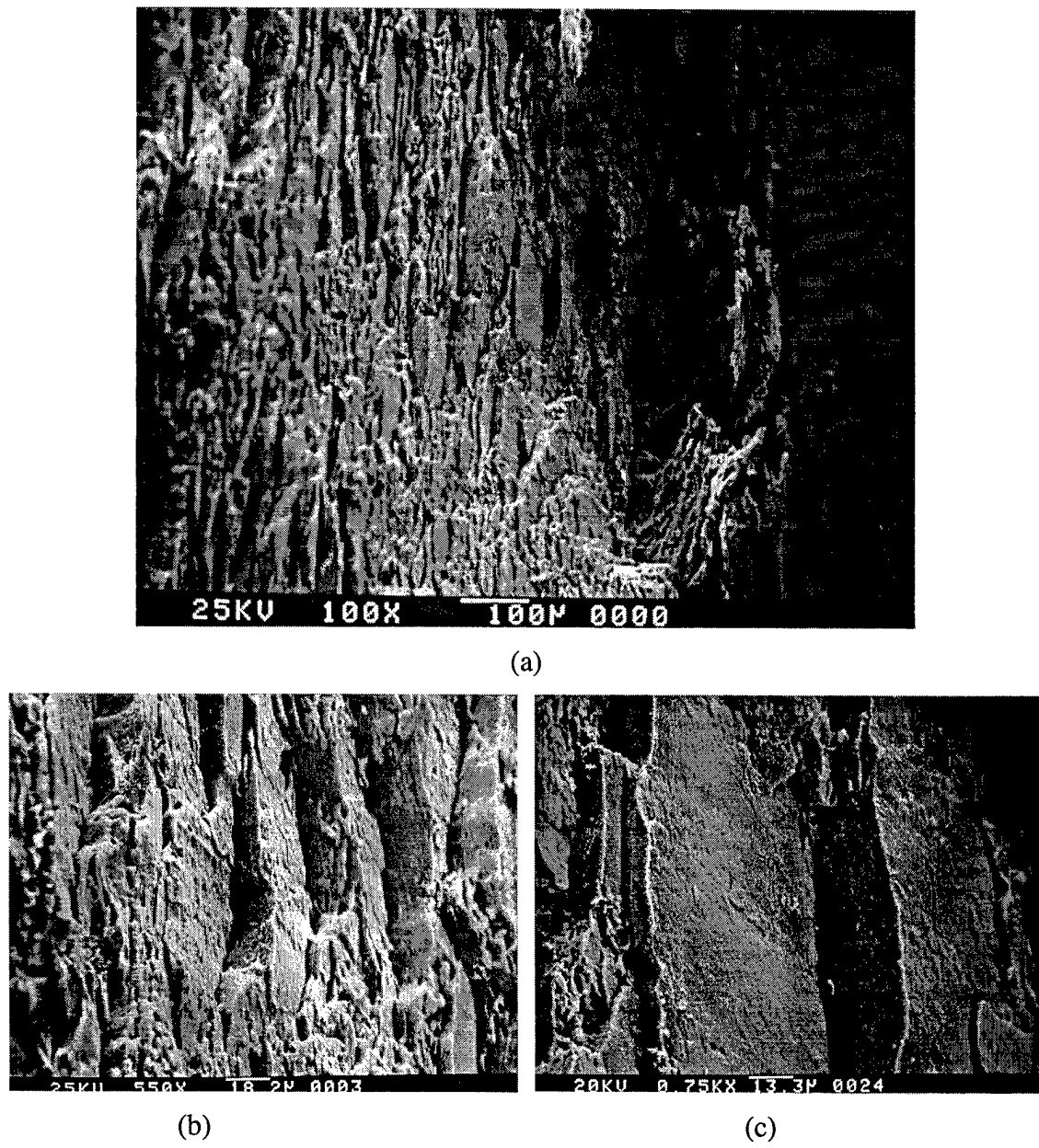


Figure 4.2.1.74. Fractograph of 7075-T6 in 1.0M NaCl solution under a constant tensile load of 3,540 kgf.

A 7178-T6 4-point bend sample was tested in 3.0M NaCl solution at 298K. The potential was maintained at -0.810V SCE which is between the critical potentials in this environment. Only one surface of the specimen was exposed to the environment. The maximum tensile stress was 448 MPa (76% of 0.2% yield stress). After 48 hours, the test was stopped and the exposed surface examined. Figure 4.2.1.75 shows the surface examined. Pits were observed on the specimen surface. There was no sign of intergranular corrosion. The specimen was then pulled

to failure in air and the fracture surfaces examined. Figure 4.2.1.76 and 4.2.1.77 show tensile fracture initiating from corroded areas. The elliptical corroded sites are easily distinguishable from the subsequent tensile fracture. IGSCC was not observed in either one of these sites. Figure 4.2.1.77, on the other hand, shows a corroded site where IGSCC was observed. Facets similar to those depicted in Figure 4.2.1.77 b and c can be observed. Figure 4.2.1.78 shows the transition zone between IGSCC and subsequent tensile failure.

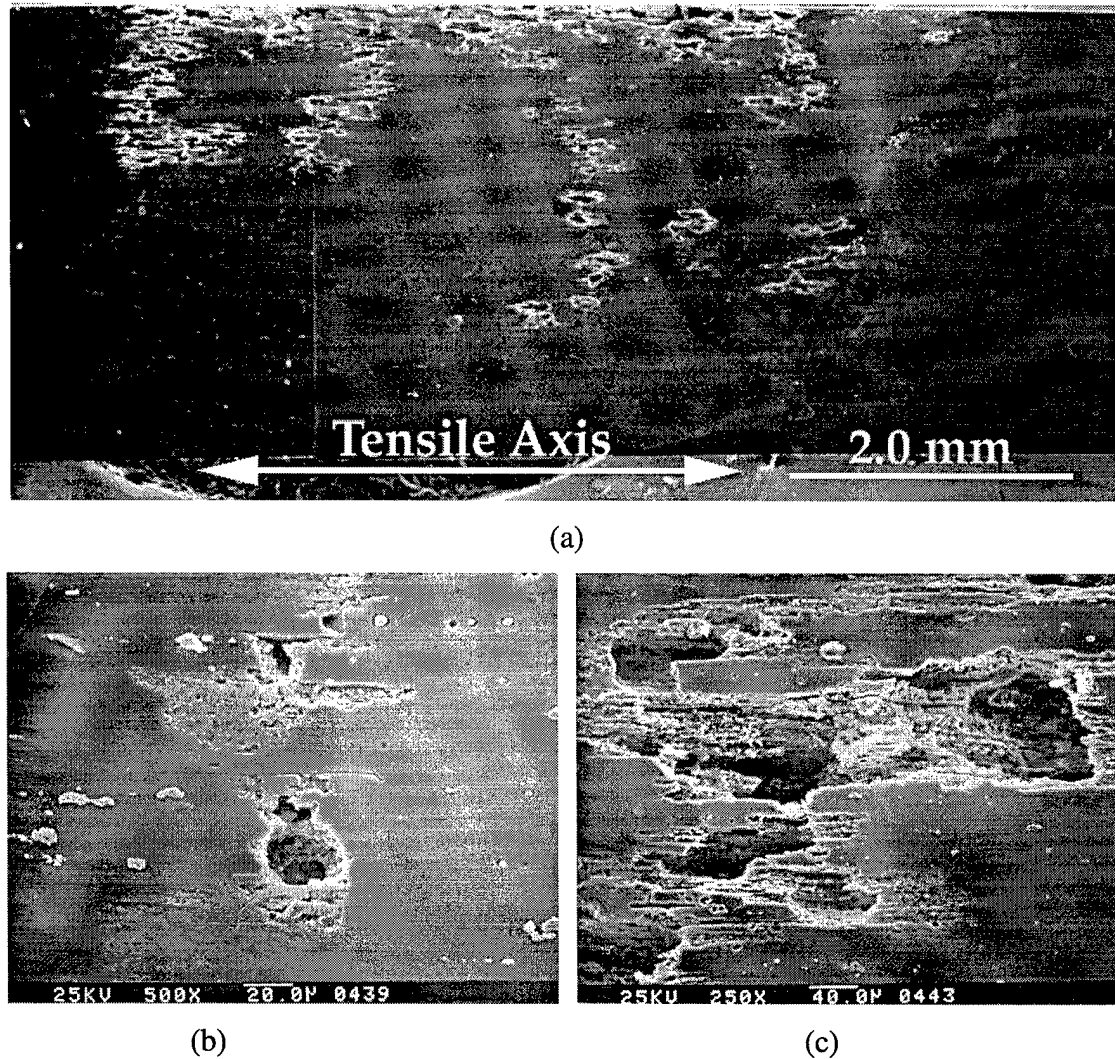
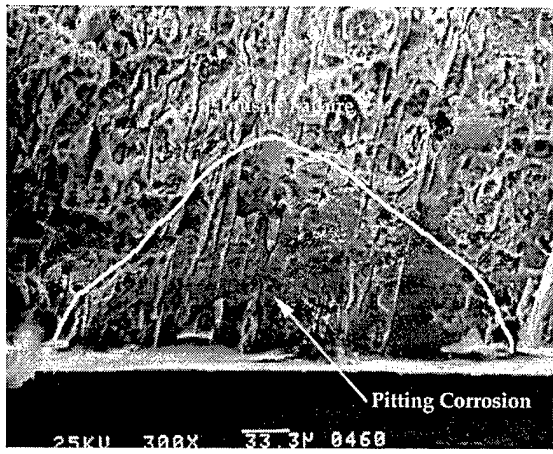
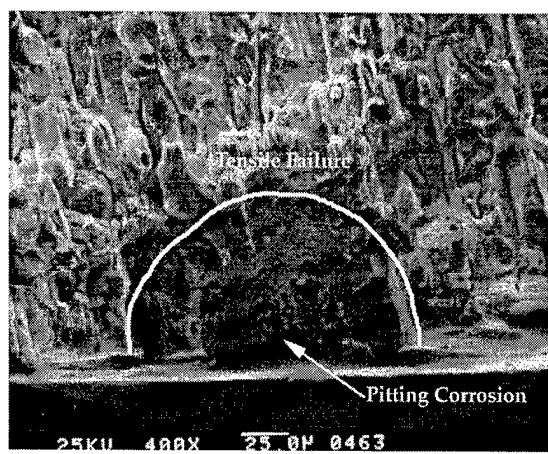


Figure 4.2.1.75. Examination of 7178-T6 4-point bend specimen tested in 3.0M NaCl solution for 48 hours. Figures b and c are high magnification images of typical corrosion observed on the exposed surface.



(a)



(b)

Figure 4.2.1.76. Fracture surfaces of the same specimen depicted in Figure 4.61 after being pulled to failure in tension. (a) and (b) show tensile fracture along corroded sites. No SCC was observed in these areas.

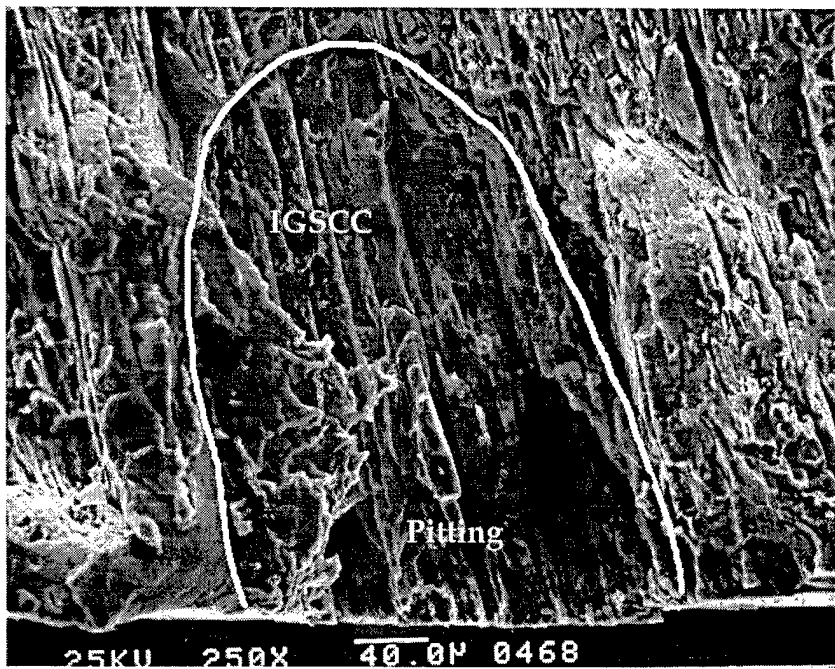


Figure 4.2.1.77. Fracture surface showing a pitted site. IGSCC and the subsequent tensile failure can be seen originating from the pit.

One half of the broken specimen was then mounted and polished for examination and is shown in Figure 4.2.1.79. Two cracks can be seen emanating from the pitted area. Figure 4.2.1.79 b shows the polished surface after etching. The cracks clearly follow the grain boundaries confirming the intergranular nature of these cracks. Figure 4.2.1.80 shows the same area under higher magnification.

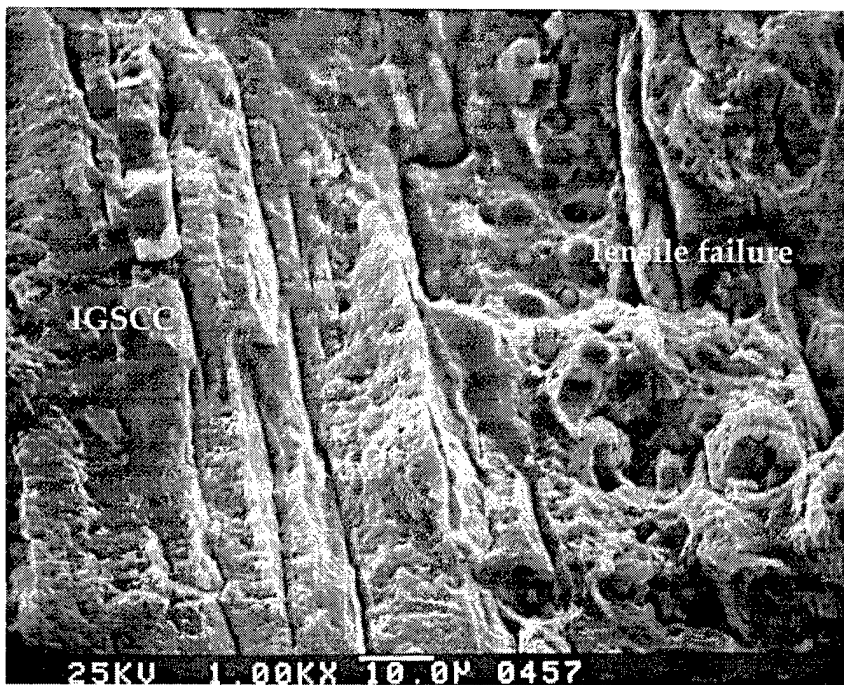


Figure 4.2.1.78. Micrograph showing the transition between IGSCC and tensile fracture.

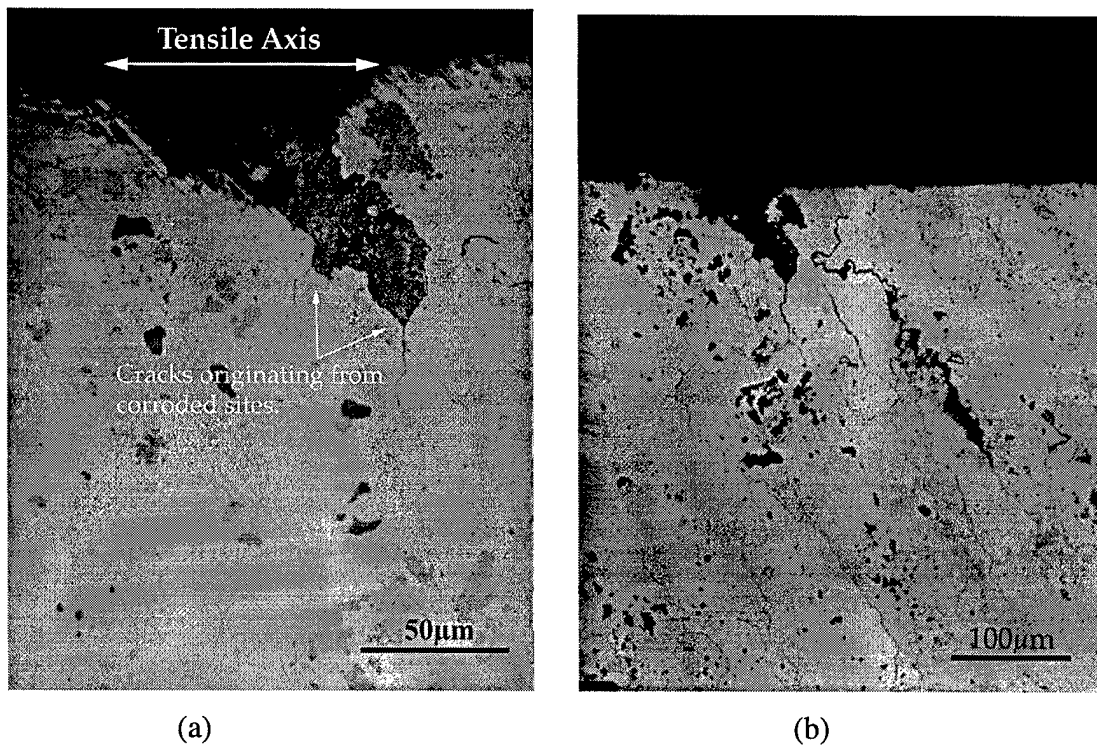
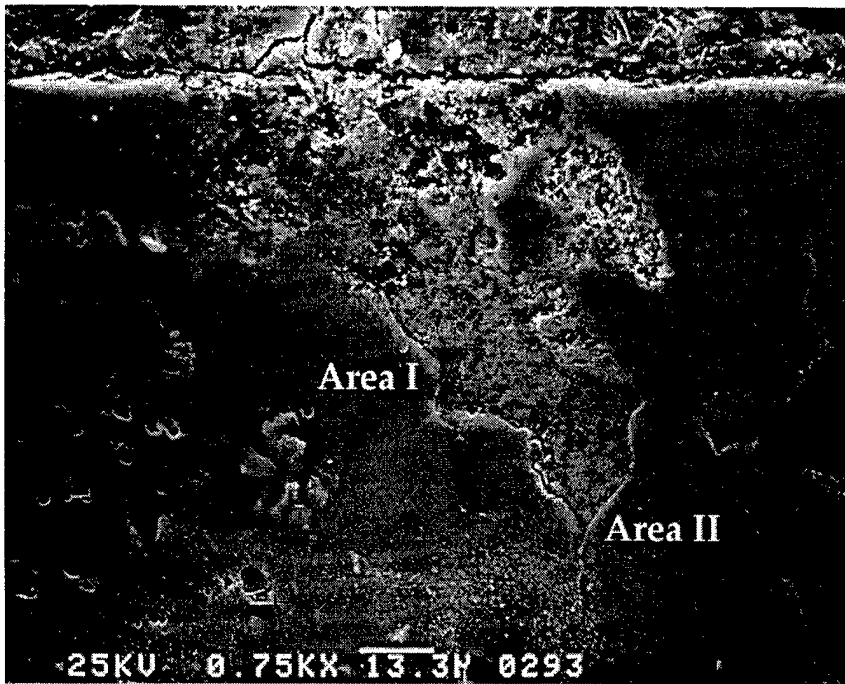


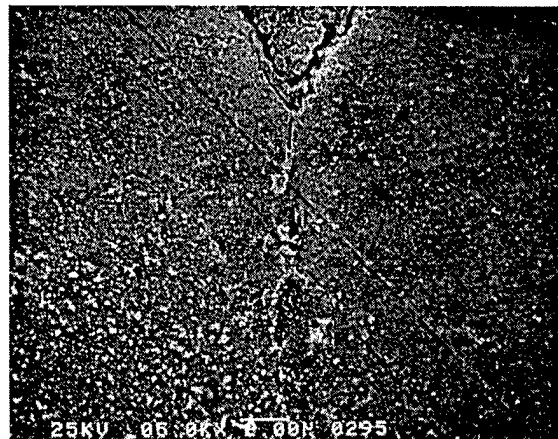
Figure 4.2.1.79. Cross section of 7178-T6 fracture surface. The etched surface (b) indicates that cracking is intergranular. Note that only pitting occurred on the surface - no iga was observed.



(a)



(b)



(c)

Figure 4.2.1.80. SEM micrographs of the sectioned fracture surface. Figures (b) and (c) are close ups of areas I and II in (a) respectively.

Stress Intensity Factor Calculations

The corroded areas in Figures 4.2.1.76 a, b and 4.2.1.77 were modeled as elliptical surface cracks. The stress intensity factor for this crack configuration under bending was calculated using the formulas presented by Newman and Raju [69]. The idealized pit shape of an elliptical surface crack configuration is presented in Figure 4.2.1.81. The stress intensity factors were calculated as a function of position along the crack front and the definition of the parametric

angle used is given in Figure 4.2.1.82. Only half of the crack needs to be considered because of symmetry. The parameters used for the calculations are listed in Table 4.2.1.17.

Figure 4.2.1.83 shows the stress intensity factor as a function of the parametric angle for the three pits portrayed in Figures 4.2.1.76a, b, and 4.2.1.77. The stress intensity factors for the pits depicted in Figures 4.2.1.76a and 4.2.1.77 are above K_{ISCC} for this material.

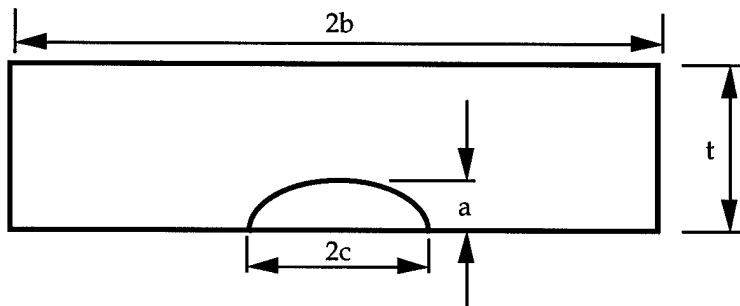


Figure 4.2.1.81. Schematic of an elliptical surface crack.

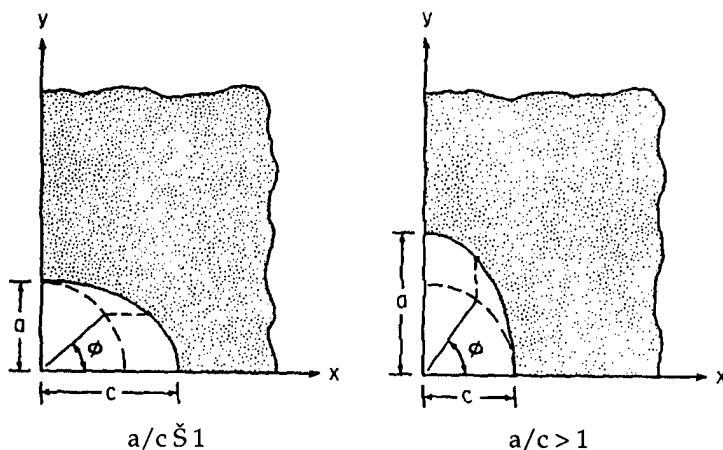


Figure 4.2.1.82. Coordinate system used to define the parametric angle, f.[69].

Table 4.2.1.17. Parameters used to calculate stress intensity factors. The bending stress is 448 Mpa.

Pit depicted in	a (mm)	c (mm)	c/a	t (cm)	b (cm)
Figure 4.2.1.76a	132	145	0.92	0.36	.15
Figure 4.2.1.76b	89	56	1.59	0.36	.15
Figure 4.2.1.77	135	150	0.91	0.36	.15

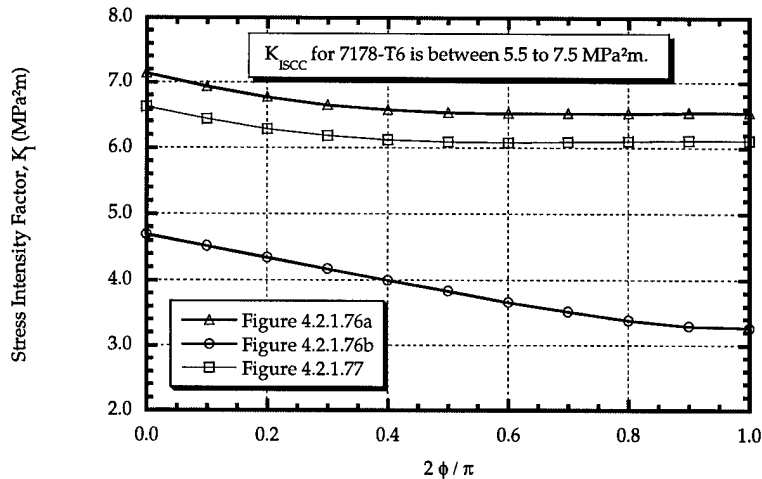


Figure 4.2.1.83. Plot of stress intensity factor as a function of the parametric angle for the three pits observed on the fracture surface.

4.2.1.5 Discussion

Polarization Behavior of the Alloys

Both 7075-T651 and 7178-T6 exhibit localized film breakdown in NaCl environments. Film breakdown leads to intergranular attack (IGA) and/or pitting. Breakdown however was not observed in 0.1M Na₂SO₄ solution. This lends support to Galvele et al.'s argument [14] that the breakdown is not simply the results of a galvanic cell but is related to the stability of the passive film on aluminum. Chloride ions play a critical role in establishing film stability. It is important to first understand the significance of the film breakdown potentials at potentials more noble than the corrosion potential. The breakdown potential is defined as the potential where there is a significant increase in the current density. Since the film formed on individual phases (or even regions) in a material will differ in stability and hence, response to its environment differently, these phases/regions will exhibit distinct breakdown potentials. Indeed, while pitting and IGA are the consequences of breakdown in the materials studied, this need not be the case for other systems. If there are more than one metallurgical phase in the material and the phases are in significant quantity, there may be a distinct breakdown potential for each of these phases. This is in fact the case for the alloys 7178-T6 and 7075-T651 studied: corrosion

around second phase particles (Epit) and intergranular attack (Eiga) each has a unique initiation potential in the chloride environments examined. For both materials, Epit is approximately 30mV more active than Eiga regardless of orientation, test temperature, and chloride ion concentration.

The breakdown potentials for 7178-T6 are consistently more anodic than that of 7075-T651 in the same environment. Epit and Eiga, in various chloride ion concentrations at 25⁰C, are on average 19mV and 9.3mV respectively more active in 7178-T6. This is also reflected in the corrosion potential measurements during ASTM G69 tests. The corrosion potential for 7178-T6 was 11mV more active than that of 7075-T651. These measurements are in accordance with the data reported by Burleigh et al.[70] Alloying elements, when they are in solid solution, can have large effects on the corrosion potential of aluminum alloys. This is especially true for copper and zinc [70] and is illustrated in Figure 4.2.1.84. Increasing the zinc content lowers the corrosion potential to more active values while copper has the opposite effect. The zinc content in the 7178-T6 alloy is 1% higher than that of the 7075-T651 (6.4% vs. 5.3%). At the same time, the copper content in 7178-T6 is only slightly higher than that of 7075-T651 (1.9% vs. 1.5%). It is therefore reasonable to expect the net effect of these compositional differences is the lowering of the potentials in 7178-T6 to more active values due to its higher zinc content.

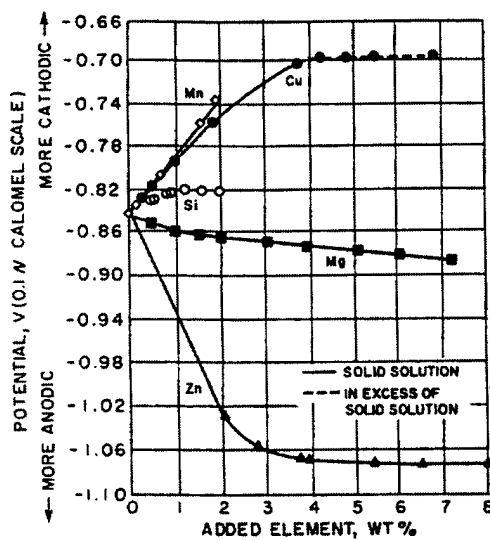


Figure 4.2.1.84. Effects of principal alloying elements on the solution potential of Al binary alloys in NaCl – H₂O₂ solution at 25⁰C [13]

For the alloys studied, the polarization behavior is not strongly influenced by the scan rate. The critical potentials (E_{pit} and E_{iga}) obtained from tests with a scan rate of 1mV/min is virtually identical to those from 10mV/min experiments. As a result, a scan rate of 10mV/min was used for all dynamic polarization experiments. The breakdown potentials were then obtained as a function of orientation, chloride ion concentration, and test temperature.

The critical pitting potential for numerous alloy systems are often found to have a logarithmic dependence on the chloride ion concentration or activity.[18, 20, 71] The data reported in the literature are usually in the form of:

$$E_{pit} = A + B \log[Cl^-] \quad (4.2.1.11)$$

and B is found to depend on the composition of the supporting electrolyte, the measurement technique, and the metal involved.[21] In the case of aluminum alloys, B has been reported to be in the range of 0.05 to 0.13V.[14, 22] This is true for the alloys examined in this study. The pitting potential shows a logarithmic dependence on the chloride ion activity and B is found to be on average 0.077 and 0.081V for 7075-T651 and 7178-T6 respectively. This is well within the range of values found in published literature.

The breakdown potentials for both materials are linearly dependent on the reciprocal of the absolute test temperature. An increase of 25°C shifts the breakdown potentials roughly 30mV in the active direction. This indicates that pitting and intergranular corrosion resistance of these materials decreases with increasing temperature.

There does not appear to be a strong correlation between the critical potentials and orientation. The variations in critical potentials between the different orientations is well within the scatter of experimental measurements.

With the knowledge that the critical potentials follow a logarithmic relationship with chloride ion activity and are linearly dependent on the reciprocal of the absolute temperature, E_{pit} and E_{iga} can be predicted in various environments. An understanding of the conditions necessary for pitting/IGA has both practical as well as scientific implications. Since stress corrosion cracking (SCC) is often preceded by pitting (cracks initiate from pits), preventing pitting will significantly

improve a material's response to stress corrosion cracking. On the scientific (fundamental) side, the ability to reproduce these conditions in a laboratory setting allows one to study the initiation process in a more controlled environment. The ability to control the form of localized breakdown is crucial to the task of reproducing stress corrosion cracks which originate from pits in a laboratory setting. With a thorough understanding of the interactions between these environmental parameters and the corrosion behavior of the alloys, it is possible to generate materials with pits and no intergranular corrosion. For example, the material can be polarized to a potential above E_{pit} but below E_{iga} . As a result, only pits can form. In the presence of a tensile stress, SCC may initiate from these pitted sites. Hence, this understanding of the interactions between the macroscopic parameters and the corrosion properties of these materials forms the back bone of the SCC studies.

In a deaerated environment, neither pit nor IGA can occur spontaneously on 7178-T6 and 7075-T651 because the corrosion potential for these materials in deaerated conditions ($E_{corr, dea}$) are more active than the corresponding breakdown potentials. This is illustrated in Figure 4.2.1.85 a and b where $E_{iga} > E_{pit} > E_{corr, dea}$. In an aerated environment, the cathodic current density for these materials increases by approximately one order of magnitude. This is caused by the added oxygen reduction reaction in the aerated environment. The anodic reaction rate, on the other hand, is not affected by the addition of oxygen. As a result, the corrosion potential of the alloys is more noble in the aerated environment. The corrosion potential of 7178-T6 increases from -0.90V to -0.76V SCE when oxygen is present. Similarly, the corrosion potential of 7075-T651 increases from -0.91V in the deaerated case to -0.74V in aerated conditions. The increase in corrosion potential in the presence of oxygen results in a potential that is noble to the pitting potential for both alloys while still being active to the IGA potential. This is shown in Figure 4.2.1.85 a and b where the corrosion potential in the aerated environment ($E_{corr, aer.}$) is in between their corresponding breakdown potentials (E_{pit} and E_{iga}). That is, $E_{iga} > E_{corr, aer.} > E_{pit}$. This implies that pits can form spontaneously on both materials in aerated chloride environments while IGA cannot occur. In other words, neither pitting nor IGA should be observed on 7178-T6 and 7075-T651 in deaerated environments while the addition of oxygen to the electrolyte can cause pits to form spontaneously.

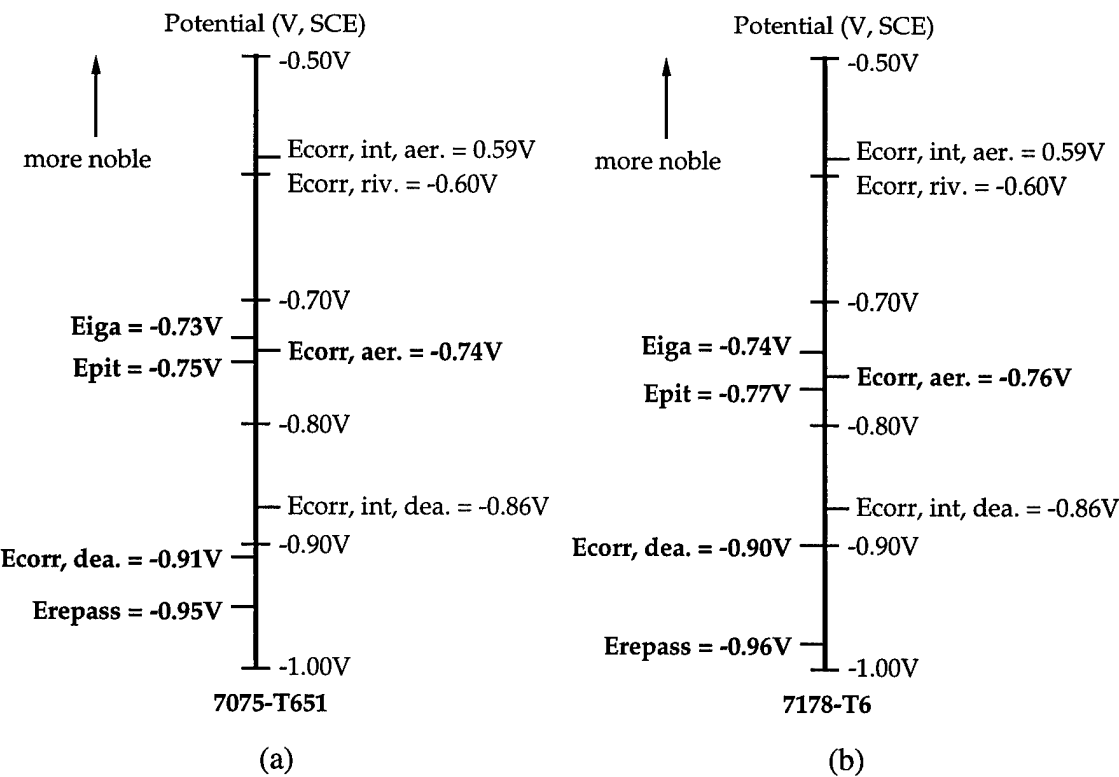


Figure 4.2.1.85. Schematic summary of the important electrochemical potentials for (a) 7075-T651 and (b) 7178-T6

Once localized breakdown has occurred, the potential must decrease beyond (more active than) the repassivation potential (E_{repass}) before repassivation can occur. The repassivation potential for both 7178-T6 and 7075-T651 are more active than their corresponding free corrosion potential in both aerated and deaerated solutions ($E_{corr,aer.}$ and $E_{corr,dea.}$). This is demonstrated in Figure 5.2 where $E_{corr, aer.} > E_{corr,dea.} > E_{repass}$. In other words, once localized breakdown has occurred, active dissolution continues because none of these materials can repassivate spontaneously. This is especially troubling in aerated solutions where pits can form spontaneously on both materials. The difference between E_{corr} and E_{repass} is less pronounced in 7075-T651. This suggests that 7075-T651 may have a better chance of repassivation than 7178-T6. Even if repassivation can occur, the large hysteresis loop in the repassivation behavior of both materials implies that significant corrosion can occur before repassivation.

Constituent Particles

Based on the static polarization experiments, it is obvious that second phase particles play a significant role in localized corrosion of aluminum alloys. Epit, for example is related to the dissolution of the matrix at the interface between the matrix and the constituent particles. In order to gain an insight into the role of these particles, five intermetallic alloys that are representative of the constituent particles found in commercial grade aluminum alloys were produced in bulk for this thesis work. The composition and crystal structure of these alloys were confirmed by EDX and X-ray diffraction phase analysis. In the case of Al₃Fe, the crystal structure could not be confirmed due to a lack of information in the published literature. The chemical composition however, is well within the specified limit. It can therefore be concluded that the intermetallic alloys produced are representative in both chemical composition and crystal structure of the constituent particles found in commercial grade aluminum alloys.

The polarization behavior of these alloys was studied in both aerated and deaerated chloride solutions. Results from these experiments provided the much needed electrochemical data of these alloys. The corrosion properties of CuAl₂ have been studied before. It has been reported that CuAl₂ is cathodic in relation to the Cu depleted zones in aged Al-4%Cu alloys.[14] It has also been reported that CuAl₂ can dissolve up to 2-3% of Zn.[65] Since Zn can drastically lower the corrosion potential of aluminum alloys, it is worthwhile to investigate the effect of Zn on the corrosion properties of CuAl₂ itself. Hence, three intermetallics were produced with varying amounts of Zn (from 0 to 1.6%). The free corrosion potential for these materials in deaerated 1.0M NaCl at 298K varied from a high of -0.85V to a low of -0.88V SCE. This is well within the scatter of corrosion potential measurements. The polarization behavior of these materials are also indistinguishable from each other. Furthermore, the cathodic polarization behavior of CuAl₂ in aerated 1.0M NaCl published by Galvele et al. [14] is identical to that of Al₂Cu+Zn from this work. It can therefore be concluded that Zn addition does not significantly alter the electrochemical properties of the phase CuAl₂.

The corrosion properties of aluminum alloys can be modeled as a combination of the electrochemical behavior of the constituent particles and pure aluminum. Once the electrochemical properties of individual components are known, mixed potential theory can be applied to predict the behavior of the alloy as a whole. The intermetallics were manufactured to simulate the composition as well as the crystal structure of the constituent particles. Dynamic polarization scans were then conducted on pure aluminum and the intermetallics in both aerated and deaerated chloride solutions. The potential - current relations for these materials are

extracted from the Tafel plots. This data are then combined in accordance with the mixed potential theory and used to predict the corrosion behavior of aluminum alloys.

Aluminum is protected by an oxide film in the pH and potential range of interest. The current density is therefore virtually independent of the potential. This is reflected by the steep slope in the anodic polarization behavior for aluminum before the breakdown. Hydrogen reduction on the surface of the intermetallics, on the other hand, is not hindered. Slight cathodic polarization produces a relatively large increases in the cathodic current. In other words, the cathodic polarization plot has a very shallow slope while the anodic polarization curve has a very steep slope. This is consistent with the development of an anodically controlled system where polarization occurs mostly at the anode and the corrosion potential is close to the open circuit potential of the cathode. Thus, the corrosion potential of a couple between aluminum and the intermetallic phase quickly approaches the open circuit potential of the intermetallics.

The corrosion potential for all the intermetallics are above (more noble than) -0.9V SCE while the corrosion potential for pure aluminum is roughly -1.3V SCE. In other words, the corrosion potentials of all the intermetallic alloys in 1.0M NaCl at 298K are more noble than that of pure aluminum. Furthermore, hydrogen ion reduction is accelerated on the surface of these intermetallics. Table 4.2.1.12 shows that the exchange current density of hydrogen reduction for the intermetallics is on average two orders of magnitude higher than that of pure aluminum (3×10^{-9} vs. 7×10^{-11} A/cm²). Since the reduction of hydrogen ions is more rapid on the intermetallics, and the free corrosion potential of the intermetallics are more noble than that of aluminum, it is clear that the intermetallics will act as cathodes when they are coupled with pure aluminum. Figure 4.2.1.86 shows that when the samples are electrically coupled, the cathodic current on the intermetallics is roughly two orders of magnitude higher than that of pure aluminum (10^{-7} vs. 10^{-9} A/cm²). The anodic dissolution rate on aluminum increases accordingly (from 10^{-8} to 10^{-7} A/cm²) as the coupled system must remain electrically neutral. These predictions are verified by the galvanic experiments where increasing the area fraction of the intermetallics polarizes the pure aluminum to more noble potentials.

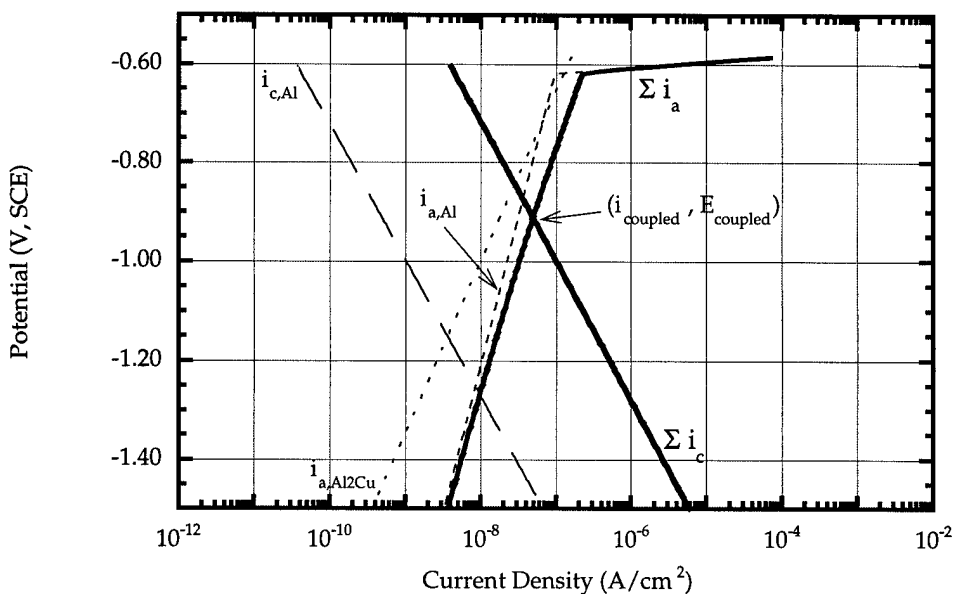


Figure 4.2.1.86. Calculation of free corrosion potential of coupled Al and Al₂Cu in deaerated 1.0M NaCl solution at 298K. (Area fraction of Al₂Cu = 0.5)

The mixed potential theory does not take into account the possibility of secondary reactions between the cathode and the anode, such as the formation of a protective oxide film. In other words, the corrosion potential calculated from the mixed potential theory is bounded by the free corrosion potential of the components. In this case, the calculated free corrosion potential for these couples are between that of pure aluminum and the intermetallics. There is good agreement between the calculated corrosion potential and that from galvanic experiments. It can therefore be concluded that no secondary reaction occurred between the alloy systems and the mixed potential theory is successful in predicting the corrosion behavior of pure aluminum - intermetallics couples.

Although Al₂Cu + Zn alloys have the most noble corrosion potentials among all the intermetallics, their corrosion potentials in deaerated 1.0M NaCl environment are over 0.15V more active than the breakdown potential of aluminum. In other words, the corrosion potential of Al - intermetallics couples are more active than the breakdown potential of Al regardless of the area fraction of the intermetallics. This is illustrated graphically in Figure 4.2.1.87 where the coupled potential is always more active than -0.70V SCE, the breakdown potential of Al. This

implies that the intermetallics cannot cause localized breakdown in aluminum under deaerated conditions. In aerated environments, the corrosion potential of pure aluminum and the intermetallics become more noble because of the added oxygen reduction reaction. As demonstrated in Figure 4.2.1.88, the corrosion potential of Al - intermetallics couples can become more active than the breakdown potential of aluminum. In other words, when the intermetallics are electrically coupled to aluminum in aerated electrolytes, localized breakdown can be expected.

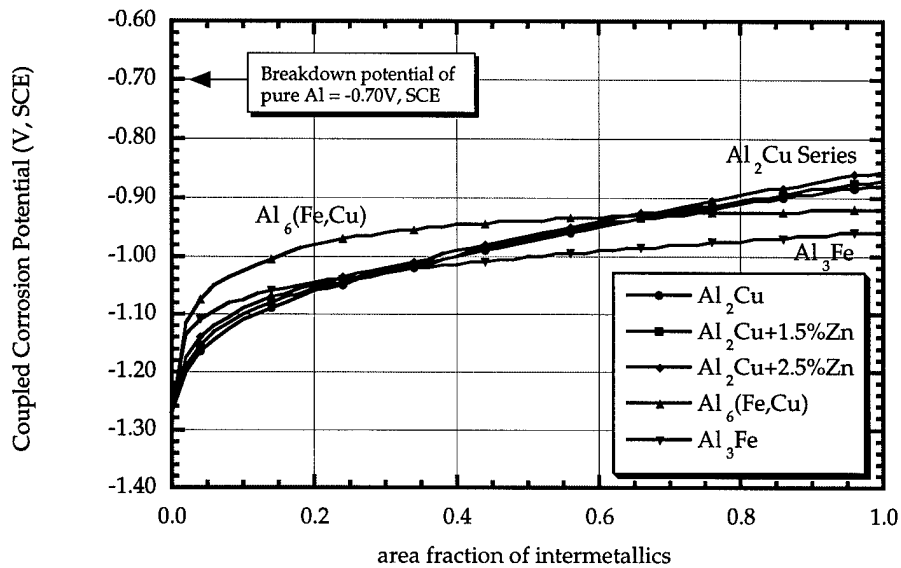
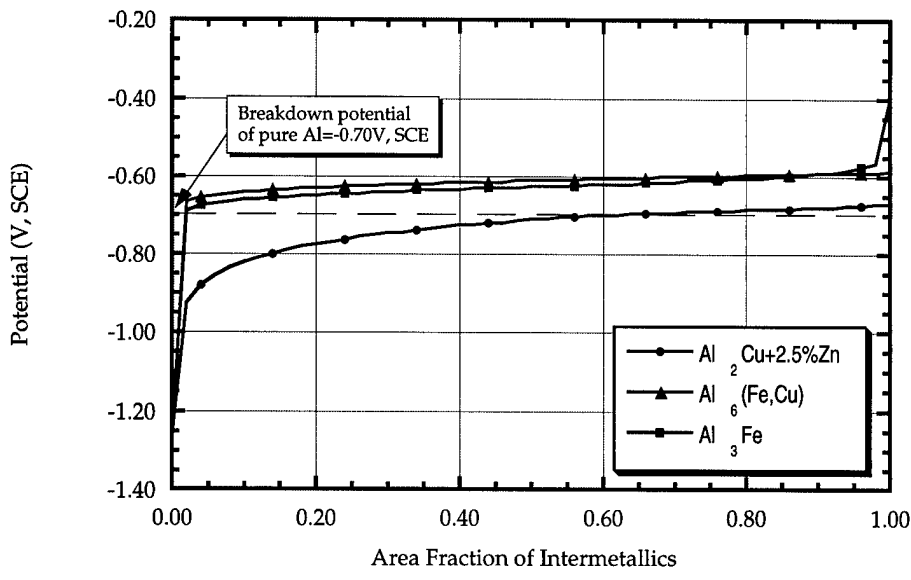
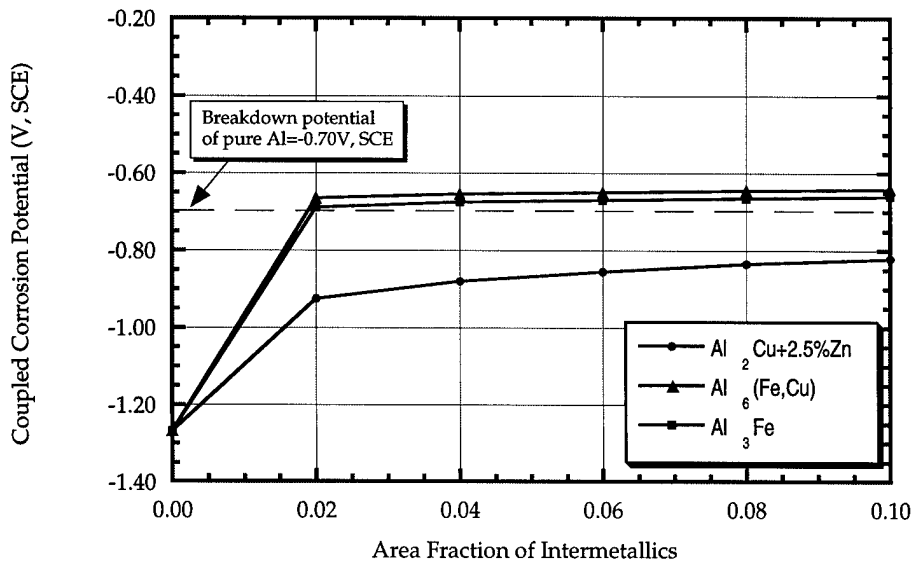


Figure 4.2.1.87. Calculated corrosion potential of intermetallic - pure Al couples in deaerated 1.0M NaCl solution at 298K.



(a)



(b)

Figure 4.2.1.88. Calculated corrosion potential of intermetallic - pure Al couples in aerated 1.0M NaCl solution at 298K. Figure b is a magnified view of these calculations when the couples are predominantly aluminum.

Figure 4.2.1.88b is a magnified view of the calculated corrosion potential of aluminum - intermetallics couples when the coupled samples are predominantly aluminum. This reflects the condition found in commercial aluminum alloys where the volume fraction (area fraction) of constituent particles ranges from 0.1% to 3%. The benefit of improving the purity of aluminum alloys is clearly demonstrated. When the area fraction of intermetallics is less than 2%, the Al-intermetallics coupled corrosion potential is more active than the breakdown potential. In other words, localized corrosion around constituent particles can be prevented if the volume fraction of the constituent particles is less than 2%.

Hübner et al. [17] observed that the electrolyte must contain dissolved oxygen for pits to initiate in commercial aluminum alloys. Hydrogen reduction by itself cannot cause localized breakdown. They reported that once pitting has begun however, hydrogen reduction is enough to sustain the dissolution reaction. The results from this work provide a mechanistic explanation to Hübner's observation. Recall that the pure aluminum - intermetallics studies indicate that the intermetallics by themselves cannot polarize the matrix above the breakdown potential in deaerated environments. The intermetallics, however, can cause localized breakdown in aerated solutions. This is the exact observation reported by Hübner et al. In other words, the matrix adjacent to the constituent particle is polarized above the breakdown potential and pitting can therefore occur. Once breakdown has begun, the potential must be lowered beyond E_{repass} (more active than E_{repass}) before repassivation can occur. The cyclic polarization data for 7178-T6 and 7075-T651 indicates that the corrosion potential of these materials are more noble than E_{repass} . This is summarized in Figures 4.2.1.85 a and b where the corrosion potential in both aerated and deaerated conditions are more noble than the repassivation potential ($E_{corr, aer.} > E_{corr, dea.} > E_{repass}$). In other words, these materials will not spontaneously repassivate in either aerated or deaerated environments and active dissolution continues. Hence, hydrogen reduction alone is enough to sustain the pitting reaction after pitting has initiated. Recall the objective of the pure aluminum - intermetallics experiments is to model the corrosion properties of aluminum alloys according to the mix potential theory as a combination of the electrochemical behavior of the constituent particles and pure aluminum. Considering the good fit between Hübner's observation on commercial aluminum alloys and the prediction made from the pure aluminum - intermetallics studies, it can be concluded that modeling the corrosion behavior of aluminum alloys as a combination of the constituent particles and pure aluminum is not only a valid approach, but also a successful and useful one.

Riveted Joints

Steel rivets are often used in wing joints because of the higher strength requirements. This configuration presents the situation of electrically coupling two dissimilar metals: the steel rivet and the aluminum panel. In deaerated conditions, the corrosion potential of the steel rivet is roughly 0.5V more noble than that of the wing panel, the 7178-T6, and the 7075-T651 plates. Furthermore, the exchange current density for the hydrogen reduction on the steel rivet is on average one order of magnitude higher than that of the aluminum alloys (1.1×10^{-7} vs. 2.5×10^{-8} A/cm², Table 4.2.1.14). In other words, not only is the steel rivet more noble than the aluminum alloys, it is also more effective at reducing hydrogen ions. The steel rivet will therefore act as the cathode when it is electrically coupled to the aluminum alloys while the aluminum alloys will be the anode. The cathodic current density of the coupled sample is higher than that of the aluminum alloy by itself because of the steel rivet's higher capacity for hydrogen reduction. The anodic current density in the coupled sample must increase accordingly as the coupled sample must remain electrically neutral. As a result, the aluminum alloy is polarized to more noble potentials when it is electrically coupled to the steel rivet. The amount of polarization increases as the area fraction of the rivet in the coupled sample increases. In other words, the corrosion potential of the coupled sample in deaerated environments approaches that of the steel rivet as the area fraction of the rivet increases.

Mixed potential calculations suggest that when the area fraction of the rivet exceeds approximately 0.9, the corrosion potential of the coupled sample in deaerated environments will be more active than the breakdown potentials (E_{pit} and E_{iga}) of the aluminum alloys. Pitting and intergranular corrosion can therefore occur in the immediate vicinity of the steel rivet in deaerated chloride environments. As pointed out earlier, these materials cannot repassivate spontaneously. Once localized breakdown has occurred, active dissolution continues. When the electrolyte is aerated, in addition to the hydrogen reduction reaction, the reduction of oxygen becomes possible. Compared to the aluminum alloys, the steel rivet is much more effective at reducing oxygen. The exchange current density for oxygen reduction on the rivet is on average three orders of magnitude higher than that of the aluminum alloys (1.7×10^{-8} vs. 1×10^{-11} A/cm²). In other words, the steel rivet remains as the cathode in the rivet - aluminum panel coupled sample. Because of the added oxygen reduction reaction, the corrosion potential of the rivet and the aluminum alloys assume more noble values as compared to the deaerated situation.

The corrosion potentials of the aluminum alloys, in aerated environments, are more noble than their E_{pit} but more active than E_{iga} . In other words, pits can form spontaneously on these alloys while intergranular attack cannot occur when the electrolyte is aerated. When these alloys are electrically coupled to the steel rivet, they are polarized to more noble values because of the added oxygen reduction capacity on the steel rivet. As a result, the corrosion potential of the coupled sample becomes more noble than the E_{iga} of the aluminum panel. That is, when the aluminum alloy is by itself in aerated electrolytes, only pits can form. When it is electrically coupled to the steel rivet however, both pitting and intergranular corrosion can occur.

The results from these steel rivet - aluminum alloy coupled experiments provide an explanation for the type and the extent of corrosion observed on the two dismantled joints from a replaced B52 wing panel discussed earlier. The steel rivets in both joints were not corroded. Pitting and intergranular corrosion was observed on the countersink area of one of the aluminum panels while the other was intact. These observations are consistent with the laboratory results. The steel rivet, acting as the cathode in the rivet - aluminum panel coupled system, should not be corroded. The aluminum panel, on the other hand, is the anode. Because of the polarizing effects of the steel rivet, the corrosion potential in the vicinity of the rivet can be more noble than both E_{pit} and E_{iga} of the aluminum alloy. Localized breakdown can therefore occur spontaneously when a conductive electrolyte penetrates the joint. As a result, it is not surprising to see pits and IGA at the countersink area of the steel riveted joint.

The results of electrically coupling pure aluminum or aluminum alloys to the constituent particles and the steel rivet are summarized in Table 4.2.1.14.

Table 4.2.1.14. Summary of the results when aluminum alloys are electrically coupled to constituent particles and the steel rivet used in wing joints

	Dearerated environment	Aerated environment
Coupled with constituent particles	No localized breakdown	Localized breakdown
Coupled with steel rivet	Pitting and IGA	Pitting and IGA
Spontaneous repassivation	No	No

SCC Initiation from Pits

Numerous SCC studies have been conducted on these high strength aluminum alloys using either the ASTM G69 solution (58.5 ± 0.1 g NaCl and 9 ± 1 ml of 30% H₂O₂ per 1 L of aqueous solution, this solution is 1M with respect to concentration of NaCl) or the 3.5% NaCl solution. Both these electrolytes rely on chemical means to maintain the electrochemical potential. The hydrogen peroxide in the ASTM G69 solution, for example, increases the cathodic reaction kinetics by raising the level of dissolved oxygen in the electrolyte. As a result, the potential is raised to more noble values. There are several drawbacks in applying this method to SCC tests. First, the electrochemical potential cannot be maintained for long periods of time by chemical means. As the solution ages, the electrochemical potential will vary. The corrosion potential of 7178-T6, for example, dropped roughly 7mV during the two hour ASTM G69 test when the added hydrogen peroxide was gradually consumed by the cathodic reaction. Typical SCC test can last for hours, if not days. Continuous maintenance of the electrochemical for the duration of SCC tests by chemical means is therefore unfeasible. Second, the electrochemical potential cannot be controlled precisely by chemical means. In order to reproduce the phenomenon of IGSCC initiating from pits, it is critical to be able to generate corroded surfaces with only pits and no intergranular attack. This implies that the potential must be more active than E_{iga} but more noble than E_{pit}. In other words, the potential must be controlled within roughly a 20mV range. This is not possible by chemical means. As a result, all the SCC tests conducted in this work were done with a potentiostat where the electrochemical potential could be maintained precisely and indefinitely.

Stress corrosion cracking is the synergistic interaction between tensile stress and corrosion acting on a susceptible environment in a specific environment. In the case of these high strength aluminum alloys, stress corrosion cracks propagate along the grain boundaries. Intergranular stress corrosion cracks (IGSCC) have been observed to initiate from pitted sites on the countersink and bore area of wing joints.[1] The goal of the SCC tests in this thesis work was to reproduce and understand the phenomenon IGSCC initiating from pits.

A thorough understanding of the interaction between the macroscopic environmental variables and the corrosion behavior of 7075-T651 and 7178-T6 is made possible by the results of the dynamic polarization studies. This enables one to generate samples with only pitting corrosion but no intergranular attack. Figure 4.2.1.89 demonstrates that this goal was successfully

accomplished as the sample was pitted only and no sign of intergranular corrosion was observed. Concurrent to the corrosion reaction, a bending load was applied to the sample. As a result, tensile stresses were generated on the top surface of the specimen. After being in this configuration for 48 hours, the test was terminated and the specimen was then pulled to failure in air. The fracture surfaces indicate that IGSCC has initiated at some of the corroded sites.

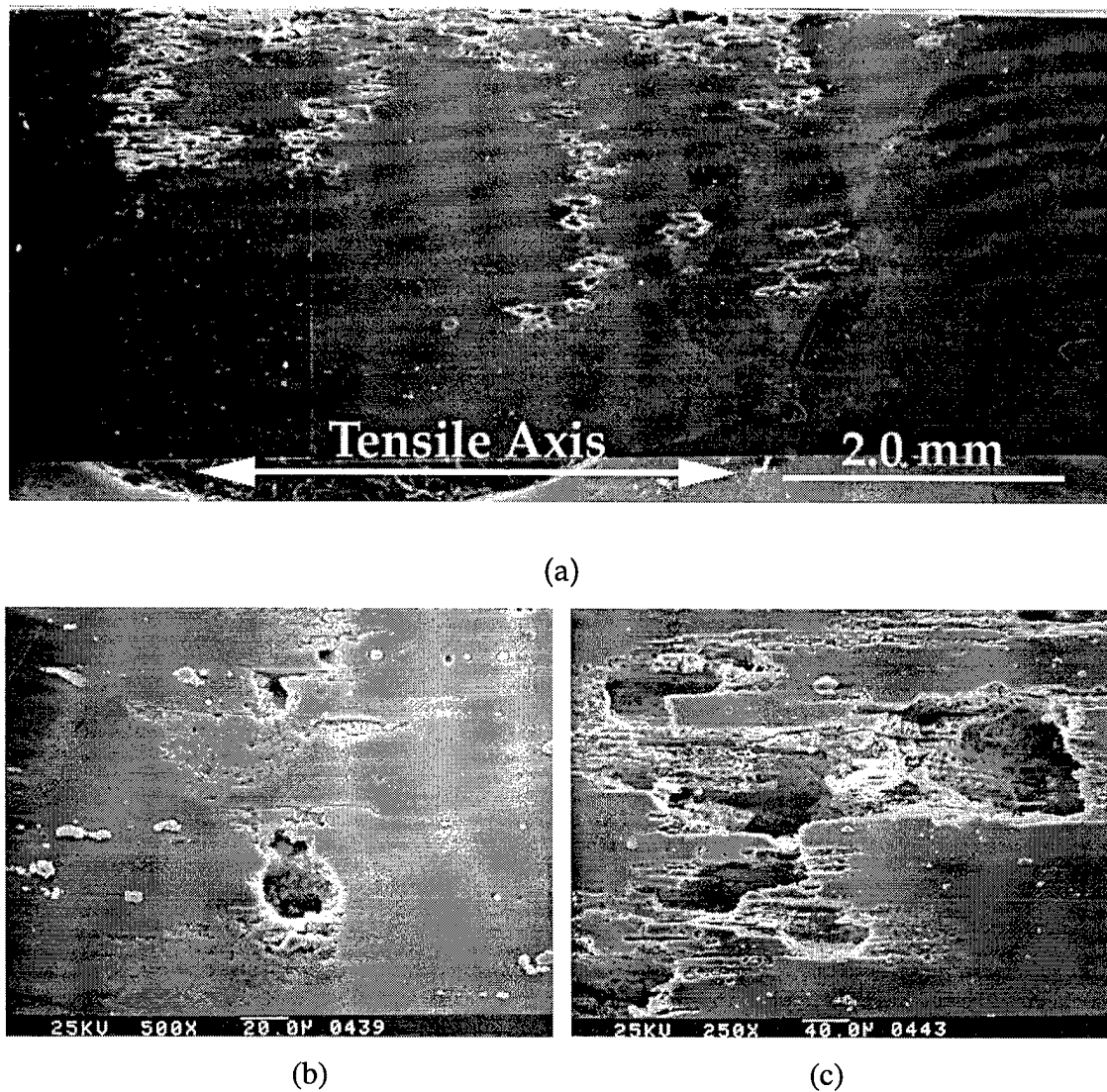


Figure 4.2.1.89. Examination of 7178-T6 4-point bend specimen tested in 3.0M NaCl solution for 48 hours. Figures b and c are high magnification images of typical corrosion observed on the exposed surface.

The goal was then to understand why IGSCC has formed in only some of the pitted sites and not in others. It is important to first understand the sequence of events leading up to IGSCC. When the stress intensity factor at the corroded site exceeds a threshold (K_{ISCC}), the stress corrosion

crack can be expected to grow at an appreciable rate. The pitting process however, is still active. In other words, pitting and crack growth are competitive processes and the one with a higher growth rate will dominate. The kinetics of pit growth usually diminishes with time. The pit depth is often fitted to a power growth equation where

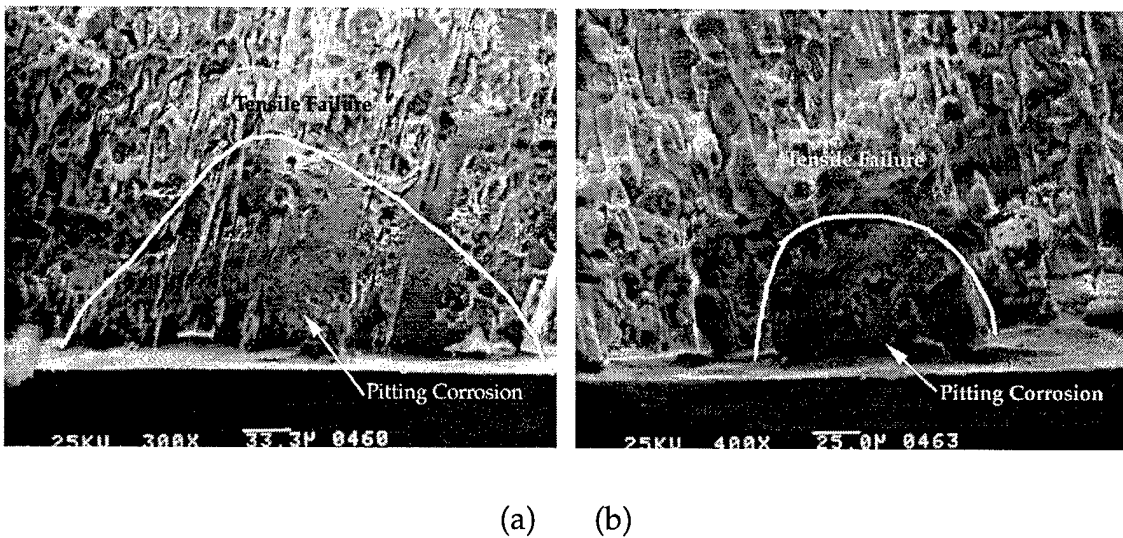
$$d = kt^n \quad (4.2.1.12)$$

where

- d : pit depth at time t
- k : kinetics constant
- t : time
- n : coefficient of power law (less than 1, in the order of 1/3)

Crack growth rate, on the other hand, accelerates as the stress intensity factor increases. In other words, pitting has a higher growth rate in the early stages and SCC dominates at a later time. A transition from pitting to SCC can therefore be expected. Based on the above discussion, several events must occur before this transition can be observed. Since the stress corrosion crack is intergranular in nature for these alloys, the corroded site where IGSCC may initiate must be in the vicinity of a grain boundary. This allows a growing pit to come into contact with a grain boundary. If the stress intensity is high enough such that the IGSCC growth rate is higher than the corrosion rate, a transition from pitting to IGSCC can be observed. When the crack growth rate is too low, or when the corroded site is not in the vicinity of a grain boundary, this transition from pitting to IGSCC will not occur.

Figure 4.2.1.90 a and b show two corroded sites where the transition from pitting to IGSCC has not occurred. Calculations show that the stress intensity factor for the pit shown in Figure 4.2.1.90b is below K_{ISCC}. Hence, corrosion should be the only form of damage. In the case of the pit depicted in Figure 4.2.1.90a, the stress intensity factor is above K_{ISCC} but no IGSCC was observed. One possible explanation is that the corroded site has not reached a grain boundary and therefore, the transition from corrosion to IGSCC cannot occur. A pitted site where IGSCC was observed is depicted in Figure 4.2.1.91. The stress intensity factor for this corroded site is above K_{ISCC}. It is therefore not surprising to observe the transition from pitting to IGSCC in this area.



(a) (b)

Figure 4.2.1.90. Fractographs showing that the transition from pitting to IGSCC has not occurred in these corroded sites.

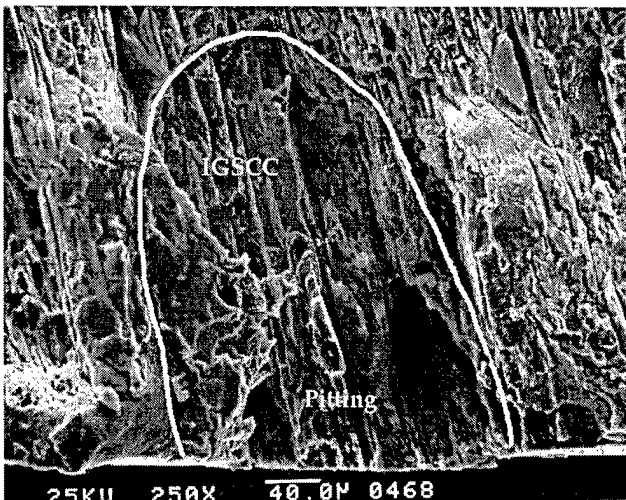


Figure 4.2.1.91. Fracture surface showing a pitted site. IGSCC and the subsequent tensile failure can be seen originating from the pit.

Practical Implications

A mechanistic model can be proposed to explain the observed corrosion and the subsequent formation of intergranular stress corrosion cracks around steel riveted wing joints. Mechanical wear, for example, can form a crevice between the steel rivet and the aluminum panel. This allows a chloride containing conductive electrolyte to seep into the joint. It has been demonstrated that the constituent particles in 7075-T651 and 7178-T6 can polarize the matrix above the pitting potential when the electrolyte is aerated. These constituent particles however, are unable to cause intergranular attack (IGA). The steel rivet, on the other hand, can polarize

the aluminum panel above both Eiga and Epit in either deaerated or aerated solutions. In other words, the constituent particles can only cause pitting but not IGA in aerated solutions while the steel rivet can cause both pitting and IGA in either aerated and deaerated conditions. Hence, localized breakdown occurs spontaneously on the aluminum panel where it is electrically coupled to the steel rivet. This explains the fact that corrosion often occurs on the aluminum alloy in the countersink and shank area of riveted joints and that the corrosion is much more extensive if the rivet is made from steel.

The oxygen in the electrolyte is consumed by the cathodic reaction as dissolution continues. Mass transport to the corroding area is limited because it is in an occluded region. As a result, the oxygen content in the electrolyte drops as the corrosion reaction continues. The corrosion potential of 7075-T651 and 7178-T6, in either aerated or deaerated solutions, are more noble than the repassivation potential. Thus, these materials cannot spontaneously repassivate. Once breakdown has occurred, active dissolution continues. Hydrolysis of the dissolved metal ion can lower the pH to 3.5 at the bottom of a pit. Aluminum ions, rather than aluminum oxide, becomes the thermodynamically stable product in this environment. Repassivation is therefore impossible at these actively corroding sites. The corrosion process can become autocatalytic as increased dissolution rate occurs with decreasing pH. This explains the severity and rapidity of corrosion damages observed around steel riveted wing joints.

When the wing panel is under a tensile load, and the corroded site is in the vicinity of a grain boundary, intergranular stress corrosion cracks may develop. If the crack growth rate is smaller than the corrosion rate, pitting remains the dominant form of damage. When the crack growth rate exceeds the corrosion rate, IGSCC can be observed.

4.2.1.6 Conclusions

A study of the fundamental mechanisms of localized corrosion has been conducted for two aluminum airframe structural materials, 7178-T6 and 7075-T651. Alloy 7178 represents a higher strength material used in airframes such as the KC-135 and B-52. Alloy 7075 has a higher fracture toughness and is used in more recent airframes.

The dynamic and cyclic polarization behavior of aluminum alloys 7178-T6 and 7075-T651 was investigated in aerated and deaerated chloride environments. Two breakdown potentials were observed for these materials. The more noble breakdown potential is related to corrosion around constituent particles while the more active breakdown potential is associated with the dissolution of grain boundaries. These potentials are associated with the initiation of pitting and intergranular attack respectively. The breakdown potentials follow the logarithmic relationship with chloride ion activity and are linearly dependent on the reciprocal of the absolute temperature. The repassivation potential for these materials were found to be more noble than the corrosion potential in either aerated or deaerated environments. In other words, these materials cannot spontaneously repassivate. Once localized breakdown has occurred, active dissolution continues.

Constituent particles have often been found to be the site of localized breakdown in these alloys. In order to understand the fundamental role of these particles, five intermetallics were produced in bulk to simulate the constituent particles found in commercial aluminum alloys. Three of the alloys produced are variants on the phase Al₂Cu with different concentrations of Zn (0 - 1.6 wt.%). The other two are Al₆(Fe,Cu) and Al₃Fe. The chemical compositions and crystal structures of these alloys were verified and are found to be similar to those of the constituent particles.

Dynamic polarization studies were conducted on all the intermetallics. Experiments were also conducted on pure aluminum for comparison purposes. The results indicate that Zn does not have a strong influence on the corrosion properties of the phase Al₂Cu. The corrosion potential and polarization behavior of the three alloys with varying amount of Zn are virtually identical. All the intermetallics were found to be more noble than aluminum. The hydrogen and oxygen exchange current density on these intermetallics are several orders of magnitude higher than that on aluminum. The particles are all cathodic in relation to aluminum. As a result, aluminum will be polarized to more noble potentials when it is electrically coupled to these alloys. In deaerated conditions, the constituent particles cannot polarize aluminum above its breakdown potential. In aerated solutions however, localized breakdown can be expected. These observations are in accordance with the published literature. It is reported that the electrolyte must contain dissolved oxygen for localized breakdown to occur. Modeling the corrosion behavior of aluminum alloys

as electrically coupled samples of pure aluminum - constituent particles is both valid and successful.

Two riveted joints from a replaced wing panel were dismantled and examined for corrosion damage. The electrochemical behavior of the steel rivet and the wing panel was obtained independently via potentiodynamic experiments. The data were then combined in accordance with the mixed potential theory and used to predict the corrosion behavior of the joint assembly as a whole. The results indicate that the steel rivet is cathodic in relation to the aluminum alloys. The steel rivet can cause both pitting and intergranular attack on the aluminum panel in either aerated and deaerated solutions. Since the aluminum alloys cannot spontaneously repassivate, active dissolution continues. This provides an explanation to the fact that severe corrosion damage is often observed in the countersink and shank area of riveted joints.

Intergranular stress corrosion cracks which initiate from pits have been successfully reproduced in the laboratory.

4.2.1.7 References

1. W.W. Wallace, D.W. Hoeppner, AGARD Corrosion Handbook, Volume 1, Aircraft Corrosion: Causes and Case Histories, 1985, pp. 101-102.
2. S. Barter, P.K. Sharp, and G. Clark, "The Failure of an F/A-18 Trailing Edge Flap Hinge", Engineering Failure Analysis, vol. 1, 1994, pp. 255-266.
3. M.O. Speidel, M.V. Hyatt, "Stress-Corrosion Cracking of High-Strength Aluminum Alloys", Advances in Corrosion Science and Technology, Volume 2, eds. M.G. Fontana and R.W. Staehle, Plenum Press, New York, 1972.
4. J.E. Hatch, Aluminum: Properties and Physical Metallurgy, American Society for Metals, Metals Park, 1984, p.143-147.
5. A.J. Sedriks, J.A.S. Green, and D.L. Novak, "Corrosion Processes and Solution Chemistry Within Stress Corrosion Cracks in Aluminum Alloys", Localized Corrosion, B.F. Brown, J. Kruger, and R.W. Staehle, eds., 1971, National Association of Corrosion Engineers, Houston, Texas, pp. 569-575.
6. Registration Record of Aluminum Association Alloy Designations and Chemical Composition Limits for Wrought Aluminum Alloys, The Aluminum Association.
7. M.O. Speidel, M.V. Hyatt, "Stress-Corrosion Cracking of High-Strength Aluminum Alloys", Advances in Corrosion Science and Technology, Volume 2, eds. M.G. Fontana and R.W. Staehle, Plenum Press, New York, 1972, p.121.

8. M.O. Speidel, M.V. Hyatt, "Stress-Corrosion Cracking of High-Strength Aluminum Alloys", Advances in Corrosion Science and Technology, Volume 2, eds. M.G. Fontana and R.W. Staehle, Plenum Press, New York, 1972, p. 119.
9. J.J. Thompson, E.S. Tankins, and V.S. Agarwala, "A Heat Treatment for Reducing Corrosion and Stress Corrosion Cracking Susceptibilities in 7XXX Aluminum Alloys", Material Performance, vol. 26, 1987, pp. 45-52.
10. R.H. Brown, W.I. Fink, and M.S. Hunter, "Measurement of Irreversible Potentials as a Metallurgical Tool", Trans. AIME, 1941, pp. 115-123.
11. E.H. Dix, R.H. Brown, and W.W. Binger, "The Resistance of Aluminum Alloys to Corrosion", Metals Handbook, 8th edition, vol. 1, Metals Park, Ohio, pp. 916-928.
12. E.H. Dix, "Acceleration of the Rate of Corrosion by High Constant Stress", Trans. AIME, 1940, pp. 11-40.
13. Metals Handbook, 9th edition, vol. 13, 1987, p.584.
14. J.R. Galvele, and S.M. De De Micheli, "Mechanism of Intergranular Corrosion of Al-Cu Alloys", Corrosion Science, vol.10, 1970, pp. 795-807.
15. J.R. Galvele, S.M.de De Micheli, I.L. Mueller, S.B. de Wexler, and I.L. Alanis, "Critical Potentials for Localized Corrosion of Aluminum Alloys", Localized Corrosion, NACE 3, R. Staehle, B. Brown, J. Kruger, A. Agrawals, Eds., National Association of Corrosion Engineers, Houston, Texas, 1974, pp. 580-599.
16. M. Pourbaix, Atlas of Electrochemical Equilibria in Aqueous Solutions, National Association of Corrosion Engineers, Houston, 1974.
17. W. Hübner, G. Wranglen, "Studies on the Mechanism of the Pitting Corrosion of Aluminum", Current Corrosion Research in Scandinavia, Lectures held at the Fourth Scandinavian Corrosion Congress, 1964, Helsinki, J. Larinkari, eds., pp.60-69.
18. G. Sussek, and M. Kestern, "Eine Charakterisierung der Lochfrabkorrosion des Nickels - I. Die Bestimmung der Lochfrabpotentiale in Neutralen und Alkalischen Lösungen" (Abstract), Corrosion Science, vol. 15, 1975, pp.225-238.
19. H.H. Strehblow, and B. Titze, "Pitting Potentials and Inhibition Potentials of Iron for Different Aggressive and Inhibiting Anions", Corrosion Science, vol. 17, 1977, pp. 461-472.
20. Z.A. Foroulis, and M.J. Thubrikar, "On the Kinetics of the Breakdown of Passivity of Preanodized Aluminum by Chloride Ions", J. Electrochem. Soc., vol. 122, 1975, pp. 1296-1301.
21. Z. Szklarska-Smialowska, Pitting Corrosion of Metals, National Association of Corrosion Engineers, Houston, Texas, 1986, pp. 203-205

22. H. Bohni, and H.H. Uhlig, Corrosion Science, vol. 9, (1969) p.353.
23. N. Nilsen, and E. Bardal, "Short Duration Tests and a New Criterion for Characterization of Pitting Resistance of Al Alloys", Corrosion Science, vol. 17, 1977, pp. 635-646.
24. D.S. Keir, M.J. Pryor, P.R. Sperry, "Galvanic Corrosion Characteristics of Aluminum Alloyed with Group IV Metals", J. Electrochem. Soc., vol. 114, 1967, pp. 777-782.
25. G.C. Wood, W.H. Sutton, J.A. Richardson, T.N.K. Riley, and A.G. Malherbe, "The Mechanism of Pitting of Aluminum and Its Alloys", Localized Corrosion, NACE 3, R. Staehle, B. Brown, J. Kruger, A. Agrawals, Eds., National Association of Corrosion Engineers, Houston, Texas, 1974, pp. 526-539.
26. Z. Szklarska-Smialowska, "Insight into the Pitting Corrosion Behavior of Aluminum Alloys", Corrosion Science, vol. 33, 1992, pp. 1193-1202.
27. O. Seri, "The Effect of NaCl Concentration on the Corrosion Behavior of Aluminum Containing Iron", Corrosion Science, vol. 36, 1994, pp. 1789-1803.
28. ASTM G34-90, "Standard Test Method for Exfoliation Corrosion Susceptibility in 2XXX and 7XXX Series Aluminum Alloys (EXCO Test)".
29. D.G. Evans, P.W. Jeffrey, "Exfoliation of AlZnMg Alloys", Localized Corrosion, NACE 3, R. Staehle, B. Brown, J. Kruger, A. Agrawals, Eds., National Association of Corrosion Engineers, Houston, Texas, 1974, pp. 614-622.
30. "Effects of Alloying Elements and Impurities on Properties", Aluminum: Properties and Physical Metallurgy, J.E. Hatch, Eds., American Society for Metals, Metals Park, Ohio, 1984, pp. 230-231.
31. G.A.W. Murray, H.J. Lamb, and H.P. Godard, "Role of Iron in Aluminum on the Initiation of Pitting in Water", Brit. Corros. J., vol. 2, 1967, pp. 216-218.
32. P.M. Aziz, and M.S. Walker, "Pitting Corrosion Characteristics of Aluminum", Corrosion, vol. 10, 1954, pp. 269-279.
33. G.A. Gehring, and M.H. Peterson, "Corrosion of 5456-H117 Aluminum in High Velocity Sea Water", Corrosion, vol. 37, (1981), pp. 232-242.
34. Aluminum and Aluminum Alloys, J.R. Davis, and Davis & Associates, eds., ASM, Metals Park, Ohio, 1993, pp. 31-33.
35. M.O. Speidel, and M.V. Hyatt, "Stress-Corrosion Cracking of High-Strength Aluminum Alloys", Advances in Corrosion Science and Technology, vol.2, M.G. Fontana, and R.W. Staehle, eds., Plenum Press, New York, 1972, pp.299-305.
36. N.J.H. Holroyd, "Environment-Induced Cracking of High-Strength Aluminum Alloys", Environment-Induced Cracking of Metals, Proceedings of the First International Conference on Environment-induced Cracking of Metals, R.P. Gangloff, M.B. Ives, Eds., National Association of Corrosion Engineers, Houston, 1988, pp. 311-345.

37. M.O. Speidel, and M.V. Hyatt, "Stress-Corrosion Cracking of High-Strength Aluminum Alloys", Advances in Corrosion Science and Technology, vol.2, M.G. Fontana, and R.W. Staehle, eds., Plenum Press, New York, 1972.
38. S. Maitra, and G.C. English, "Mechanism of Localized Corrosion of 7075 Alloy Plate", Met. Tran. A, vol. 12A, 1981, pp.535-541.
39. S. Maitra, and G.C. English, "Environmental Factors Affecting Localized Corrosion of 7075-T7351 Alminium Alloy Plate", Met. Tran. A, vol. 13A, 1982, pp.161-166.
40. S.C. Byrne, "Effect of Microstructure on Stress-Corrosion Cracking in 7075-T7", Aluminum Alloys - Physical and Mechanical Properties, T.H. Sanders, and E.A. Starke, eds., 1986, pp.1095-1107.
41. P.K. Poulose, J.E. Morral, and A.J. McEvily, "Stress Corrosion Crack Velocity and Grain Boundary Precipitates in Al-Zn-Mg Alloy", Met. Tran., vol. 5, 1974, pp.1393-1400.
42. P.N. Adler, R. De Isai, G. Geschwind, "Influence of Microstructure on the Mechanical Properties and Stress Corrosion Susceptibility of 7075 Aluminum Alloy", Met. Trans., 3 (1972), p.3191.
43. A.J. De Ardo, R.D. Townsend, Met. Trans., vol. 1, 1970, p.2573.
44. I.J. Polmear, J. Aust. Inst. Metals, vol. 89, 1960, p.193.
45. A.J. Sedriks, P.W. Slattery, E.N. Pugh, Trans. ASM, vol. 26, 1969, p.238.
46. R.M. Pelloux, and J.A. Van den Avyle, Hydrogen in Metals, I.M. Bernstein, and A.W. Thompson, eds., ASM, Metals Park, Ohio, 1974, pp. 275-276.
47. J.A. Albrecht, B.J.M. McTiernan, I.M. Bernstein, and A.W. Thompson, "Hydrogen Embrittlement in High-Strength Aluminum Alloys", Scripta Met., vol. 11, 1977, pp. 893-897.
48. T.F. Klimowicz, and R.M. Latanision, "On the Embrittlement of Aluminum Alloys by Cathodic Hydrogen: The Role of Surface Films", Met. Trans. A, vol. 9A, 1978, pp.597-599.
49. I.M. Bernstein, and A.W. Thompson, "An Evaluation of Hydrogen Embrittlement Mechanism", Mechanisms of Environment Sensitive Cracking of Materials, Swann, Ford, and Westwood, eds., 1977, Metals Society, London, pp. 412-491.
50. S.P. Lynch, "Environmentally Assisted Cracking: Overview of Evidence for an Adsorption Induced Localized-Slip Process", Acta Met., vol. 36, 1988, pp. 2639-2661.
51. G.M. Scamans, N.H.J. Holroyd, and C.D.S. Tuck, "The Role of Magnesium Segregation in the Intergranular Stress Corrosion Cracking of Aluminum Alloys", Corrosion Science, vol. 27, 1987, pp.329-347.

52. S.W. Ciaraldi, J.L. Nelson, R.A. Yaske, and E.N. Pugh, "Studies of Hydrogen Embrittlement and Stress-Corrosion Cracking in an Aluminum-Zinc-Magnesium Alloy", Hydrogen Effects in Metals, I.M. Bernstein, and A.W. Thompson, eds., Metallurgical Society of AIME, 1981, Warrendale, Pennsylvania, pp.437-447.
53. K. Rajan, W. Wallace, and J.C. Beddoes, "Microstructural Study of a High Strength Stress-Corrosion Resistant 7075 Aluminum Alloy", J. Materials Science, vol. 17, 1982, pp. 2817-2824.
54. Z.X. Tong, Si Lin, and C.M. Hsiao, "The Influence of Hydrogen on Atomic Binding Energy, Critical Slip Shear Stress, and Fatigue Crack Propagation Rate of Aluminum Single Crystals", Met. Trans. A, vol. 20A, 1989, pp. 921-924.
55. C.P. You, M. Dollar, A.W. Thompson, and I.M. Bernstein, "Microstructure Property Relationships and Hydrogen Effects in a Particulate-Reinforced Aluminum Composite", Met. Tran. A, vol. 22A, 1991, pp. 2445-2450.
56. H.P. Van Leeuwan, "A Quantative Model of Hydrogen Induced Grain Boundary Cracking", Corrosion, vol. 29, 1973, pp.197-204.
57. J. Albrecht, I.M. Bernstein, and A.W. Thompson, "Evidence for Dislocation Transport of Hydrogen in Aluminum", Met. Trans. A, vol. 13A, 1982, pp. 811-820.
58. W. Gruhl, "Stress Corrosion Cracking of High Strength Aluminum Alloys", Z. Metallkd, vol. 75, 1984, pp.819-826.
59. A.W. Thompson, M.A. Mueller, and I.M. Bernstein, "Stress-Corrosion Cracking in Equiaxed 7075 Aluminum under Tension and Torsion Loading", Met. Tran. A, vol. 24A, 1993, pp.2569-2575.
60. M.O. Speidel, "Interaction of Dislocations with Precipitates in High Strength Aluminum Alloys and Susceptibility to Stress Corrosion Cracking", Fundamental Aspects of Stress Corrosion Cracking, R.W. Staehle, eds., 1967, pp.561-579.
61. F.S. Lin, E.A. Starke, "The Effect of Copper Content and Degree of Recrystallization on the Fatigue Resistance of 7XXX Type Aluminum Alloys. I. Low Cycle Corrosion Fatigue", Mater. Sci. Eng., 39 (1979), pp.27-41.
62. D.A. Hardwick, A.W. Thompson, and I.M. Bernstein, "The Effect of Copper Content and Microstructure of the Hydrogen Embrittlement of Al-6Zn-2Mg Alloys," Met. Trans. A, vol. 14A, 1983, pp. 2517-2526.
63. J. Albrecht, A.W. Thompson, and I.M. Bernstein, "The Role of Microstructure in Hydrogen-Assisted Fracture of 7075 Aluminum", Met. Trans. A, vol. 10A, 1979, pp.1759-1766.
64. P. Villars, and L.D. Calvert, Pearson's Handbook of Crystallographic Data for Intermetallic Phases, Volume 2, ASM, Metals Park, OH, 1985, p.973.

65. L.F. Mondolfo, Aluminum Alloys: Structure and Properties, Butterworths, Boston, 1976, p.284.
66. G.F. Vander Voort, Metallography Principles and Practices, McGraw-Hill, 1984, p.610.
67. F.P. Beer, and E.R. Johnston, Jr., Mechanics of Materials, McGraw-Hill Book Company, New York, 1981, pp.156-158.
68. H.H. Uhlig, and R.W. Revie, Corrosion and Corrosion Control, John Wiley & Sons, New York, NY, 1985, pp. 406-408.
69. J.C. Newman, Jr., and I.S. Raju, "Stress-Intensity Factor Equations for Cracks in Three-Dimensional Finite Bodies Subjected to Tension and Bending Loads", Computational Methods in the Mechanics of Fracture, eds. S.N. Atluri, Elsevier Science Publishers, 1986, pp. 318-321.
70. T.D. Burleigh, R.C. Rennick, and F.S. Bovard, "Corrosion Potential for Aluminum Alloys Measured by ASTM G69," Corrosion, 1993, Vol. 49, pp.683-685.
71. H.H. Strehblow, and B. Titze, "Pitting Potentials and Inhibition Potentials of Iron for Different Aggressive and Inhibiting Anions", Corrosion Science, vol. 17, 1977, pp. 461-472.

4.2.1.8 Theses Published Based on This Task Element

Au, H. K., "Pitting and Crack Initiation in High Strength Aluminum Alloys for Aircraft Applications", January 1996

4.2.2 Pitting and Crack Initiation Under Fatigue Loading

During this reporting period we have developed an understanding of the fundamental nature of the crack initiation process in aluminum alloys. While there is ample literature on pitting and crack initiation **SEPERATELY** there has been very little work done to establish the details of the connection between the two and to model this process. During this project we have developed this connection. In the process we have established quantitatively the details of the transition between pit growth and crack initiation. For this task we have chosen an aluminum-lithium alloy (2091-T351). This alloy is one of several advanced alloys that have been proposed as replacements for current structural alloys. Work focused on 2024 and 7075 alloys. In this section we present results that have been generated to serve as the basis for the modeling effort to be discussed in Section 4.4.

4.2.2.1 Physical Metallurgy

Specimens were machined from a 1.6 mm thin sheet of 2091-T351 Alclad manufactured by CEGEDUR. The 2091 alloy nominal composition is displayed in Table 4.2.2.1. The microstructure of the material is illustrated in Figure 4.2.2.1. Etching reveals an elongated grain structure along the rolling direction. Grains were more recrystallized near the surface of the sheet. The average grain shape near the surface was approximately to 25 μm wide x 35 μm in length. The cladding thickness was 100 μm on each side of the sheet. The heat treatment consisted of a solutionization followed by 2-3% deformation and a natural age to a substantially stable condition. This heat treatment resulted in a yield strength of 260 MPa and an Ultimate Tensile Strength (UTS) is of 360 MPa.

Table 4.2.2.1: Nominal composition in wt% of alloy 2091.

Elements	Li	Cu	Mg	Fe	Si	Mn	Cr	Zn	Zr
2091 (wt%)	1.7-2.3	1.8-2.5	1.1-1.9	0.3	0.2	0.1	0.1	0.25	0.04-0.16

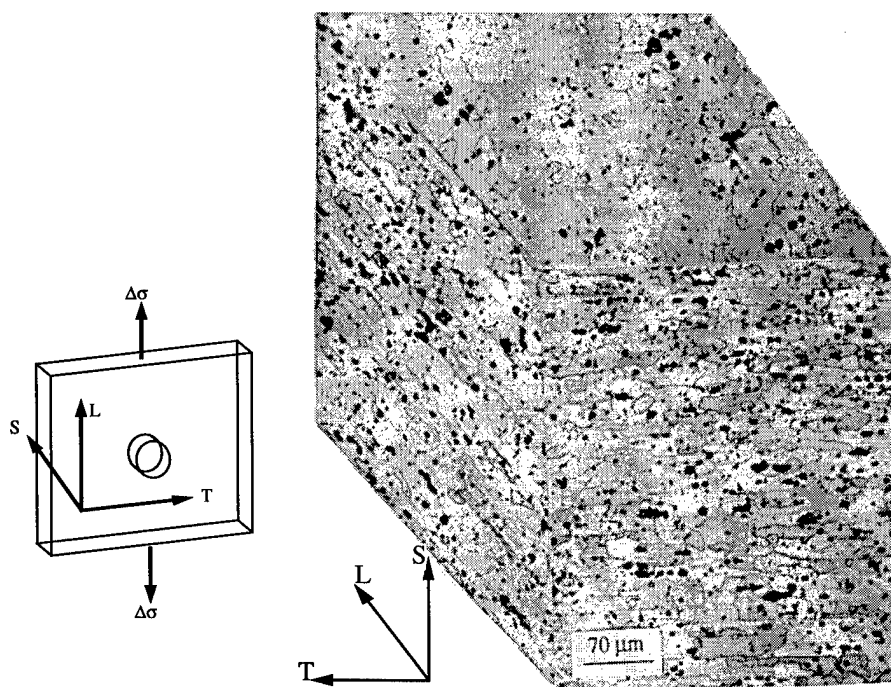


Figure 4.2.2.1: 2091-T351. Effect of orientation on the grain structure close to the specimen surface. Keller's etch.

4.2.2.2 Experimental Procedures

Fatigue specimens were fabricated which simulated an aircraft fuselage skin with an open rivet hole. Specimens were cut from 1.6 mm thin gauge material. The cross-section dimensions were 1.6mm x 44.45 mm. An open hole, 4 mm in diameter was drilled in the center. Prior to testing, machining marks were removed by grinding and polishing the hole inner surfaces down to a three μm diamond paste. Specimens were maintained in the test grips by a row of three bolts. The stress axis was parallel to the rolling direction. An R-ratio (P_{\min}/P_{\max}), of 0.05 was used to simulate pressurization cycles in a fuselage skin. Five stress levels were chosen. They were 65, 80, 100, 120 and 140 MPa. Test frequency ranged from 0.1 Hz to 10 Hz.

When it was necessary to control the electrochemical potential, a recirculation loop containing deaerated 1M NaCl was used. A 10 liter water tank was used to minimize bulk concentration changes during the experiment. Prior to and during testing, the NaCl solution was deaerated by nitrogen bubbling. A Schlumberger Model 1286 potentiostat was used to control the potential. Two platinum counter electrodes were positioned in the corrosion cell, one on each side of the specimen. The Luggin probe was located in front of the open hole. A traveling microscope (x50) was used to monitor crack initiation and crack length.

4.2.2.3 Experimental Results

Fatigue Crack Growth Rates

Figure 4.2.2.2 shows a $\text{da}/\text{dN}-\Delta K$ curve derived experimentally. The crack growth rates have been established in 1M NaCl, at room temperature, for a potential of -750 mV(SCE), under constant amplitude and under a R-ratio of 0.05.

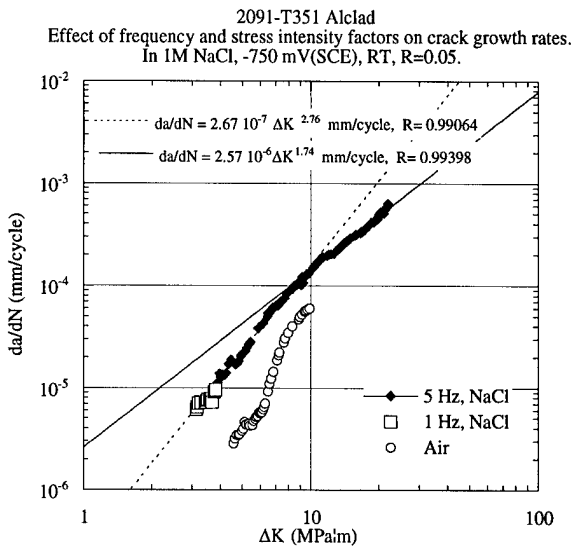


Figure 4.2.2.2: 2091-T351 Alclad. Effect of test frequency on fatigue crack growth rates.

The seven point polynomial method [1] was used to process the data from a center cracked sheet. A change in slope is observed around $9 \text{ MPa}\sqrt{\text{m}}$.

For ΔK less than $9 \text{ MPa}\sqrt{\text{m}}$:
$$\frac{da}{dN} = 2.67 \cdot 10^{-7} \Delta K^{2.76} \text{ mm/cycle} \quad (4.2.2.1)$$

For ΔK greater than $9 \text{ MPa}\sqrt{\text{m}}$:
$$\frac{da}{dN} = 2.57 \cdot 10^{-6} \Delta K^{1.74} \text{ mm/cycle} \quad (4.2.2.2)$$

S-N curves

Results for fatigue initiation and fatigue failure are shown in Figures 4.2.2.3.a (Initiation) and 4.2.2.3.b (Failure). Fatigue initiation was defined as the number of cycles necessary for a surface crack to reach a length of $400 \mu\text{m}$.

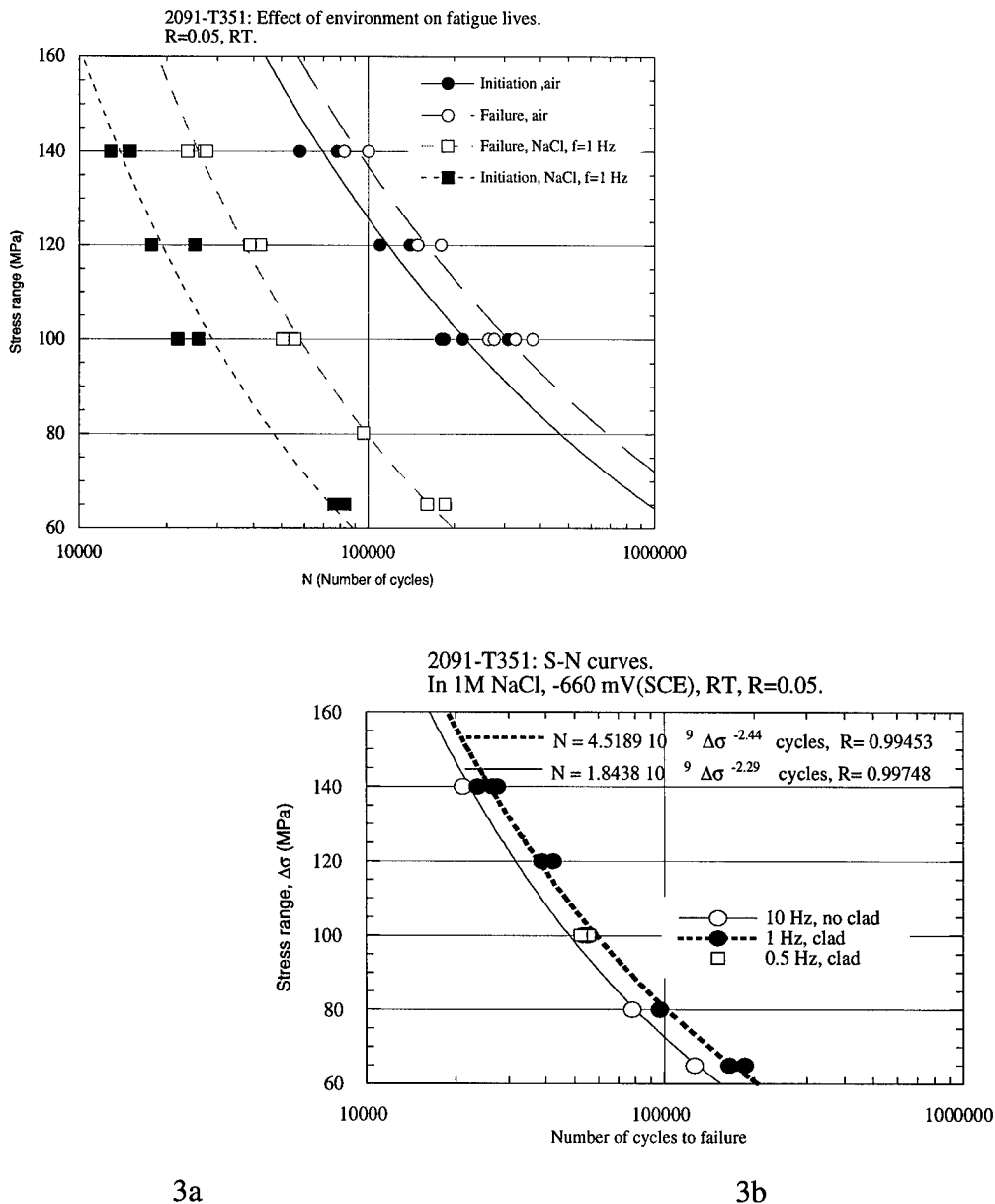


Figure 4.2.2.3: 2091-T351. Effect of the environment on fatigue lives. Initiation is defined as the number of cycles necessary to grow a fatigue crack, 400 μm in length.

Specimens tested at 10 Hz were unclad and specimens tested at 1 Hz were clad. In the latter case, fatigue crack initiation was delayed by approximately 10,000 seconds due to a potential drop introduced by the very high dissolution rate of the cladding at a potential of -660 mV(SCE). In terms of fatigue life, there is very little difference between tests at 1 Hz (clad) and 10 Hz (unclad). In both cases, 1 and 10 Hz, the scatter in fatigue life was minimal, especially when compared to fatigue life in air. The harmful effect of the environment is obvious. The minimal

scatter in 1M NaCl at -660 mV(SCE) supports a deterministic process, such as pure propagation. The initiation time for pitting is close to zero in this very severe environment.

Pitting Rates

A maximum pit depth curve is shown in Figure 4.2.2.4. A linear regression on the logarithm of the data has shown that the pitting curve can be approximated by two power laws, one for short times with an exponent of 2/3 and one for long times for an exponent close to 1/3.

$$\text{For short times } (t < 24,400 \text{ seconds}) \quad c = 0.74 \cdot t^{2/3} \text{ } \mu\text{m s}^{-1} \quad (4.2.2.3)$$

$$\text{For long times } (t > 24,400 \text{ seconds}) \quad c = 25 \cdot t^{1/3} \text{ } \mu\text{m s}^{-1} \quad (4.2.2.4)$$

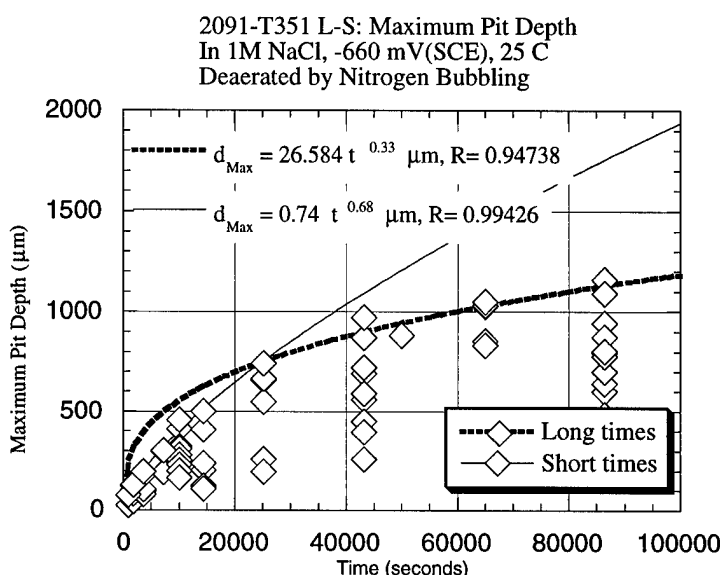


Figure 4.2.2.4: 2091-T351 Bare. maximum pit depth as a function of the immersion time. In 1M NaCl, -660 mV(SCE), RT, deaerated.

4.2.2.4 References for This Task Element

- ASTM E647-88a, Standard Test Method For Measurement of Fatigue Crack Growth Rates, ASTM, Philadelphia PA, 1989.

4.2.2.5 Theses Published Based on This Task Element

Genkin, Jean-Marc P , "Corrosion Fatigue Crack Initiation in 2091 Aluminum-Lithium", June 1996.

4.3 High-Temperature Environmental Degradation of Advanced Engine Materials

Problems of localized corrosion leading to crack initiation and premature failure are endemic at high temperatures, as well as at low temperature, and are to be found in aircraft engine and supersonic vehicle components subject to service in elevated-temperature gaseous environments. The purpose of this program task was to pursue, in parallel with the analogous low-temperature pitting corrosion/crack initiation program, a study of the mechanisms and implications of crack initiation and propagation arising from environmental attack of candidate alloys and alloy coatings at temperatures in the 1200-2000°F (650-1100°C) range where current and near-term developments in aircraft propulsion and supersonic vehicle design have encountered, or are destined to encounter, materials performance limitations. Pursuit of this task has required identification of the mechanisms and microstructures of the high-temperature corrosion products formed on alloys of interest, analysis of the stresses arising in corrosion scales and adjacent substrate alloy, and investigation of the loss of integrity in scales, adjacent alloy and at the scale/substrate interface.

The focus of this task is the study of the high-temperature failure of surface scales and alloy substrates of interest in advanced engine component materials, in particular oxide scales forming on aluminide intermetallics. Four principal approaches have now been utilized. The first is dynamic thermogravimetric study of the kinetics of high-temperature scaling of the alloys under consideration over long enough times to produce corrosion microstructures representative of probable in-service conditions. The second utilizes the environmental scanning electron microscope (ESEM) and its associated straining hot stage to observe the dynamic development of corrosion microstructures *in situ*, and use of the ESEM and associated thin-window X-ray energy-dispersive spectrometry (XEDS) to provide information about scale morphologies and composition and fracture initiation in cross-sections through the scales and scale/substrate interface. The third is scanning transmission electron microscopy (STEM), and associated windowless XEDS, to provide high-resolution information about microstructural and compositional developments in the scale and the adjacent substrate. The fourth is X-ray diffraction in a high-temperature environmental cell to provide information about scale phases

present and measure *in situ* the stresses in scale and adjacent alloy substrate developing during growth of scales and as a consequence of differential thermal contractions during temperature cycling (and particularly including glancing-angle measurements that emphasize information in the scale and adjacent substrate near the scale/substrate interface).

4.3.1 Program Element Accomplishments

It has been shown that the ESEM can be used to study oxidation phenomena. The observation of initial and complex layers, followed by growth and spallation of duplex scales, indicates that the ESEM environment can sufficiently model high temperature oxidation. The entire sequence of oxidation can be observed, especially the cooling phase, and the precise position and temperature of oxidation events can be determined which are not accessible in conventional furnaces.

Phenomena such as buckling and cracking in oxide layers are visible in the ESEM.

The X-ray stress measurements have been made in parallel with the ESEM observations and provide a useful complement to the ESEM study of imposed external stress, since only the externally-imposed stress and not the internal stresses generated by oxidation processes are quantifiable during ESEM observations.

Assuming a plane stress equiaxial condition is operative in the oxide and metal, the application of the conventional $\sin^2\gamma$ is greatly simplified. Under these assumptions, the in-plane stress can be determined from a simple strain measurement. The compressive residual oxide strains measured at room temperature are consistent with the superposition of the compressive thermal stress onto growth stress. The departure from the plane stress equiaxial condition can be ascribed to the anisotropic behavior of individual grains of the metal. The in-situ results indicated that the strains in the metal and oxide are established almost immediately upon introduction of air and remain constant over the duration of the oxidation period. The constant strain suggests that the elastic limit is quickly reached in the metal.

The growth mode of NiO at 1000°C in room air produced the duplex oxide morphology.

The results of Cr/Cr₂O₃ are similar to those for Ni/NiO in the sense that high temperature growth strains are observed and the maximum strains in the oxide appears to be limited by the plastic

deformation (creep + yield strength) of the metal. There are some important differences in Cr/Cr₂O₃ results compared to those previously discussed for Ni/NiO. The thermoelastic behavior of chromia is more complicated than that of NiO because of its rhombohedral symmetry. The thermal expansion of Cr₂O₃ is anisotropic, with the a-axis direction being about 40% more expandable than the c-axis direction. This means that diffraction planes such as (110) in Cr₂O₃ will serve as more sensitive strain gauges than will reflections such as (116) and (104). This behavior has important consequences for the development of thermal stresses upon cooling to room temperature because the (Cr) has a value between the a-direction and c-direction expansivities of the oxide.

If one wishes to calculate the thermal stress in either the oxide or the metal using the Tien-Davidson formulation, the sign can be either positive or negative, meaning the thermal stress can be either compressive or tensile depending on lattice orientation of the oxide. From a practical standpoint, Cr₂O₃ scales which grow with their c-axes normal to the metal interface should have a minimal in-plane stress and should be more resistant to failure. The final residual stresses observed in Cr and Cr₂O₃ are a combination of the stresses developed during growth at high temperature and the stresses that develop during cooling.

The reproducibility of the thermogravimetric experiments is good, considering the extremely low weight gains and the non-isotropic substrates .

The structure of super- α_2 Ti₂NbAl is similar to the alpha two structure., yet super- α_2 Ti₂NbAl typically has a kinetic rate or weight gain intermediate between γ -TiAl and α_2 -Ti₃Al .

The presence of nitrogen in the gas lowers the oxidation rates in the titanium aluminides.

There are some environments where super- α_2 Ti₂NbAl experiences higher oxidation rates than α_2 -Ti₃Al: in pure oxygen environments and in some argon-oxygen mixes.

Lowering the temperature to 700°C reduces the amount of spallation observed in these alloys, but α_2 -Ti₃Al spalls in some environments even at 700°C, specifically at higher oxygen contents and longer times.

There remains high temperature applications of interest for titanium aluminides.

4.3.2 Results & Discussion

4.3.2.1 Alloys Studied

We have focused our study on alumina-forming alloys, as represented in current use by MCrAlY compositions used as oxidation resistant overlay coatings on superalloys, but with more emphasis on intermetallic aluminides of titanium and nickel where future applications lie. Aluminides are favored because of the formation of protective Al_2O_3 scales, stable to temperatures at least as high as 2750° F (1500° C) [1], which exhibit low permeability for oxygen and alloy cations. Adherence of scale to alloy during thermal cycling is the principal difficulty and is found to improve with the addition of oxygen active elements, such as Y and Zr (so-called reactive elements, RE) to the alloy, just as in chromia formers, though there is much less effect of such additions on the oxidation kinetics [2]. The MCrAlY alloys investigated were mechanically alloyed Inco MA754 (Ni-20wt%Cr-0.52t%Ti-0.3wt%Al-0.05wt%C-0.6vol% Y_2O_3) and Inco MA 956 (Fe-20wt%Cr-4.3wt%Al-0.36wt%Ti-2vol% $\text{Y}_2\text{O}_3/\text{Al}_2\text{O}_3$) and oxide-dispersion strengthened alloys with yttrium additions (Ni-10wt%Cr-10%Al and Ni-20wt%Cr-10%Al). Some initial studies of pure Ni, pure Cr and the chromia former Ni-17.6wt%Cr were made for comparison purposes, because the behavior of the NiO and Cr_2O_3 oxides formed on these alloys substrates is fairly well understood.

β -NiAl (Ni-30wt%Al) is the common constituent of aluminide diffusion coatings on Ni-base superalloy, exhibits excellent cyclic high-temperature oxidation resistance, and is a potential lighter replacement for high-temperature structural materials; it was therefore studied, with and without RE additions. During oxidation, the θ - Al_2O_3 phase forms first and may later transform to the stable α - Al_2O_3 phase; above 2200° F (1200° C), only α -alumina forms. The phase change is accompanied by a change in the mechanism for oxide formation: θ -alumina grows parabolically with time at the scale-gas interface predominantly by outward diffusion of Al cations [3], while α -alumina without the addition of a RE grows parabolically by a mixed diffusion mode of simultaneous Al and O transport. RE additions stabilize θ -alumina and

notable segregate to alumina scale grain boundaries where they reduce Al grain-boundary diffusion, resulting in scales which grow primarily by inward oxygen transport [4]. Both single-crystal and polycrystalline substrates were employed. NiAl single crystals of dimensions approximately 1.5x2.4.75 in (38x50x120) were grown by General Electric-Evendale using a floating-zone method at two compositions, Ni-50.6at%Al and Ni-48.4at%Al (nominally Ni-30wt%Al). The as-grown ingots were homogenized at 2400° F (1315° C) for 50 hours and subsequently cooled down slowly inside the furnace at approximately 270° F (150° C)/h to room temperature; samples with surfaces parallel to (100) were spark cut from the ingots.. Polycrystalline NiAl from the same source was recrystallized at 2100° F (1150K C) for 6 hours in argon before oxidations.

Ni₃Al, though containing sufficient Al to form protective alumina scales [5] , confers no weight benefit and was not chosen for study.

Ti-based alloys are potentially useful in advanced aircraft engine applications because of their low specific weight and high strength at elevated temperature, for example in high performance, lightweight compressor structures operating in engines with fewer compressor stages doing more work at higher rotation speeds. Advanced compressor designs specify exit temperatures of 1200-1650° F (650-900° C) , but the poor oxidation resistance of Ti alloys above 1300° F (700° C) has impeded their further application in such designs above a current temperature of about 1100° F (600° C). γ -titanium aluminides, for example, despite their high aluminum content, do not form slowly-growing protective alumina scales, but grow layered scales comprising alternation of TiO₂ and Al₂O₃ phases resulting from local depletion of aluminum from the alloy [6]; furthermore, the alumina layer is not stable over long oxidation times [7]. Al depletion additionally results in formation of a Ti-rich cubic phase in the alloy adjacent to the scale/substrate interface [8]. The presence of nitrogen in the atmosphere leads to still further complications, because of the potential for formation of (Ti,Al) nitrides and oxynitrides in regions of low oxygen activity and high titanium activity near the scale/substrate interface [9]. Additions of ternary elements such as Nb to γ -TiAl have been shown to retard Al loss near the interface and maintain a sufficiently high Al activity [10,11].

The α_2 -Ti₃Al intermetallic composition has insufficient aluminum to form protective alumina scales, but again additions of β -stabilizing elements such as Nb have resulted in better oxidation resistance [12]. Adding sufficient Nb to replace one-third of the Ti results in the ordered orthorhombic "super- α_2 " Ti₂NbAl alloy phase [13], whose oxidation resistance has been little explored. Sufficient oxidation resistance is obtained from TiAl (γ phase) which contains just enough Al to form protective alumina scales, at least in air in the 1500-1800°F (800-1000°C) range, though problems are encountered with Ti nitride formation in air. The extreme brittleness of this material has limited its successful use as components; instead such low ductility materials are typically used as coatings. TiAl was thus a principal alloy in this study, unmodified and near-stoichiometric and modified by small additions of Nb, Si, Mn, Cr and B. Ti₃Al (α_2 phase), though *not* containing sufficient Al to form alumina scales, is nevertheless currently the best alloy-base candidate titanium aluminide for jet engine applications, particularly in the Nb-modified form (Ti₂NbAl, a phase in the super- α_2 alloys) and was therefore studied. Two suites of titanium-aluminum alloys were obtained from Wright Patterson Air Force Base. The alloys compositions specifically selected for oxidation comparisons were Ti-47.9at% (γ -TiAl), Ti-25at%Al (α_2 -Ti₃Al) and Ti-25at%Nb-23.5at%Al (super- α_2 Ti₂NbAl).

All the intermetallic alloys exhibit brittle fracture (though there has been limited success in partially-ductilizing them with alloy additions and two-phase microstructures), and the alumina scales that form on them are also brittle and readily crack and spall. Cracks in brittle scales can propagate into brittle substrates and *vice versa*, compromising substrate strength and accelerating environmental degradation. Experimental approaches have thus focused on observations of scale morphological development and on observations of crack initiation and propagation in scale, substrate and at their interface, using so far as possible *at-temperature* dynamic observations of these phenomena, or *at-temperature* measurements of the stress states in both substrate and scale.

4.3.2.2 Assessment of Morphology, Chemistry and Microstructure of High-Temperature Oxidation of Scales and Substrates using Electron Microscopies

Electron microscopy has been used extensively in the study of surface morphology and microstructure of high-temperature oxidation scales in order to aid in understanding the mechanisms of oxide growth and failure. Both scanning and transmission electron microscopies, coupled with analytical methods, can provide critical information about the microstructures and chemistries and scales and scale/substrate interfaces. Our observations of the systems studied, and particularly the titanium aluminides, using conventional SEM and STEM techniques are documented below.

These studies are, nonetheless, limited by the fact that oxidized samples can be examined microscopically only after oxidation is complete, so that important changes in scale and substrate morphology that occur during scale growth and cool down go unobserved. The recent development of the environmental scanning electron microscope (ESEM) has provided an additional observational tool which permits actual *in-situ* observation of the evolution of scales, coatings and substrates *during* oxidation, offering the prospect of better understanding of the detailed mechanisms of scale growth and failure of protective scales and coatings. Such *in-situ* studies have the potential to clarify existing theories about growth mechanisms in oxide scales and to help identify the type of stresses (differential thermal stresses, oxide growth stresses, externally-imposed stresses) which principally contribute to the cracking and spallation of scales, coatings and substrates during high-temperature service. In addition, the ESEM has provided a microscopical tool, with elemental analysis capability, for examination of oxide scale morphologies in plan view, in fracture sections and in polished cross-sections with a minimum of specimen preparation and no required application of conductive coatings. Since the application to oxidations studies is relatively new, we have chosen to discuss the technique and our results with it in a little greater detail.

The Electroscan ESEM is the development of a conventional scanning electron microscope design (Figure 4.3.1a) fitted with a novel environmental secondary electron detector (ESD) integral to the objective lens pole piece (Figure 4.3.1b). The detector utilizes the environmental gaseous environment in the specimen chamber as the detector ionization gas. The microscope is capable of imaging in almost any gaseous environment at pressures ranging from high vacuum to about 250 Pa (20 Torr). This pressure range is maintained through a differential pumping system built into the column. Secondary electrons generated at the specimen near-surface by an incident 20-30 keV scanned electron probe are accelerated toward the ESD by an imposed electric field and in transit collide with local gas ions, liberating even more electrons and causing a current

cascade within the gas. The positive gas ions provide an additional benefit in that they neutralize the build up of excess electron charge on specimen surfaces and allow observation of uncoated insulating samples, in our case the oxide scales grown on metals and alloys.

Best resolution and contrast are achieved when the imaging is done with a LaB₆ electron source and the specimen is in a water-vapor environment. However, we have demonstrated that other gas environments, such as air, argon, and oxygen mixtures can also yield good images if all the operating conditions, including accelerating voltage, current, projection aperture, *etc.* are carefully optimized. Because the ESEM was initially a new instrument and most imaging experience had been in water-vapor environments, considerable effort was expended in optimizing imaging conditions for our dry specimens in oxygen-bearing environments at high temperature. The ESEM also turns out to be limited in several fundamental respects. For example, the incident electron probe is broadened by scattering from the environment gas molecules, lowering the overall resolution of the microscope. The differential pumping aperture limits the detector field of view to about 0.25 mm² at the specimen at the lowest magnifications. Finally, although X-ray energy-dispersive spectrometry (XEDS) is available for element identification, the XEDS detector is configured geometrically in such a way that the technique cannot be used with heating or heating/straining stages in place. It is also presently better suited to obtaining qualitative X-ray spectra and mapping than to quantitative analysis.

In-situ Oxidation in the ESEM

The ESEM comes equipped with a heating stage that can nominally reach a temperature of 1800°F (1000°C). Samples were placed into 5 mm-diameter alumina crucibles which sit directly above the heating element and thermocouple, and the entire heating block is water-cooled. Preliminary tests were designed simply to determine if studying oxide growth was feasible in the ESEM. Initially, commercially pure metal powders were chosen to determine if indeed the progression of oxide growth could be followed in-situ. Cu, Ni, and Fe powders were sealed into the crucibles with a Aremco Ceramabond™ alumina ceramic bonding agent, and the crucibles were then sealed to the furnace with the same bonding material. The samples were heated in 2-4 Torr air (≈ 400 Pa, P_{O₂} = 7x10⁻⁴ atm) to temperatures ranging from 1100-1500°F (600-800°C), and all three metals underwent observable surface changes at high temperatures. The Cu particles sintered and grew a rumpled oxide, while the Ni powder particles developed a smooth,

continuous oxide layer. Fe powder particles grew whiskers, a characteristic hematite (Fe_2O_3) growth morphology. All oxide morphologies, in fact, resembled those grown under similar conditions in a laboratory furnace, giving initial confidence that the investigating electron beam in the ESEM did not have a significant effect on the oxidation processes.

Research was next expanded to oxidation of flat, polished metal surfaces, using pure Ni, pure Cr, and Ni-Cr alloy substrates. Samples were ground through 600-grit SiC (about 12 μm particles), polished to 0.3 μm γ -alumina, degreased with acetone, and ultrasonically cleaned in methanol. It was found that the surfaces of thicker samples took significantly longer to reach oxidation temperatures, so specimens were ground to thicknesses between 100 and 200 μm (0.004-0.008 in) and cemented to the heating element with Ceramabond. Thin samples can pose problems for oxidation of alloys over long periods of time because of eventual depletion of the more active alloying elements; however, such depletion was not considered significant in the present experiments carried out over periods of only a few hours.

Flat polished samples were oxidized in wet air, dry air and argon-oxygen mixtures. There was little development of surface morphological features associated with oxide growth in any of the alloys before reaching temperatures of 750° F (400° C). Figure 4.3.2 shows the initial growth of oxide on mechanically-polished γ -TiAl and α_2 - Ti_3Al substrates in dry air at higher temperatures after nucleating on polishing scratches. Oxide scales grown in the presence of water vapor grew with different morphologies from those grown in air or Ar-20%O₂ gas mixtures. For example, Ni-17.6wt%Cr alloy grew a faceted scale in air and Ar-20%O₂ and a heavily-whiskered scale in water vapor, indicating that the presence of water vapor in the specimen chamber accelerates whisker growth mechanisms (in this case, of Cr₂O₃). At low temperatures, water vapor is the superior imaging environment, but all gases utilized appear to have equal efficacy at high temperatures. Images improved in contrast greatly at temperatures above 600°F (300°C), but their contrast degraded somewhat at temperatures greater than 1700°F (900°C), probably due to thermal emission of electrons from samples at the highest temperatures. Scale growth was recorded on video prints and on Polaroid prints at selected intervals and continuously on videotape in real time. XEDS was performed on the alloys after oxidation to identify oxide phases grown.

The most interesting morphological results came from the development of oxide scales on pure Cr, Ni-17.6wt%Cr and α_2 -Ti₃Al. Pure Ni and Ni-5%Cr grew continuous oxide layers as well, but with no notable surface features apparent during the growth and cooling of these scales, as was expected based on our earlier transmission electron microscope (TEM) studies of oxide development on these substrates [14,15]. The early stages of oxide growth on high-purity polycrystalline Cr, oxidized in air and Ar-20%O₂ mixtures, are shown in Figure 4.3.3. The first development, occurring at 1300°F (700°C), was growth of oxide islands which covered the surface. These were followed by the development of whiskers which grew into a continuous scale upon holding the sample at 1750-1800°F (950-1000°C) for several hours. The chromia scales grown on pure Cr frequently spalled upon cooling, as shown in Figure 4.3.4a. Growing oxide layers on Ni-17.6wt% Cr alloy featured distinctive stages of growth, as well as cracking and spallation after only a few hundred degrees of cooling. Surface morphologies for three of these stages are in shown Figure 4.3.5a-c and cracking of the oxide layer upon cooling in Figure 4.3.4b.

Oxide whiskers notably grew on α_2 -Ti₃Al substrates also during *in-situ* oxidation in moist air. Figure 4.3.6 illustrates the morphological development for oxidation after 1 and 2 hours at 1500°F (800°C); the oxide needles were identified as the rutile phase of TiO₂ by XEDS and *ex-situ* XRD. Figure 4.3.7a shows slower development of the same morphology at 1300° F (700° C) and Figure 4.3.7b an earlier stage of TiO₂ nodule formation in dry air at the same temperature. Figure 4.3.8 shows crazing of the thin oxide scale formed on α_2 -Ti₃Al at 1230° F (665° C) in dry air. Nodules were also observed (Figure. 4.3.9) to grow on γ -TiAl at 1300° F (700° C). Oxide nucleation on super- α_2 Ti₂NbAl was observed at temperatures as low as 750° F (400° C), but at higher temperatures the thin scale formed was featureless and uniform.

Imposed Strain During In-Situ Oxidation

An initial objective in the initial phase of this project was to test the capabilities and limitations of the ESEM in high temperature corrosion studies, and to investigate the development and failure of protective scales and coatings. To this end, a high-temperature heating-straining stage was developed with a manufacturer for installation in the Electro-Scan ESEM. Construction of

the stage was commissioned from Messrs. Ernest F. Fullam, Inc., Latham, NY, who had considerable experience building specialty stages for SEM instruments. The final design realized, illustrated in Figure 4.3.10, features a twin-screw driven straining platform, suspending the specimen over a Pt-alloy heating element embedded in a ceramic block and fitted with a thermocouple and temperature controller and capable of temperatures up to 2200°F (1200°C). 100-lb and 1000-lb load cells are available, and both load and elongation are read-out digitally. The maximum sample dimensions are 0.3 in width \times 1.0 in length (8 mm \times 25 mm); sample thickness is limited to about 0.040 in (1 mm).

Initial investigations to demonstrate feasibility focused on the morphological development of chromia scales on pure Cr and chromia-forming alloys, because the behavior of these scales was relatively well understood and because the maximum specimen temperature in the ESEM was initially limited to about 1800°F (1000°C), marginal for the study of alumina scales forming on nickel aluminides with which we have considerable experience already at much higher temperatures from *ex-situ post-facto* studies [4]. Special emphasis was given to two alloys with nominal composition Ni-20wt%Cr, which are important both from an engineering and a scientific standpoint. Cracking of adherent alumina scales under externally-imposed stress was studied using a commercial FeCrAlY alloy (Inco MA956) initially oxidized outside the ESEM.

Figure 4.3.11 shows application to a 0.004 in (0.1 mm)-thick specimen of Inco's mechanically-alloyed FeCrAlY alloy MA956, which had been pre-oxidized in pure oxygen at 2200°F (1200°C) for 24 hours. Initial examination in the ESEM showed that a continuous, adherent aluminum oxide scale had formed on the alloy surface, just as deduced previously from our TEM oxidation study of this alloy [2]. The sample was clamped in the load cell, and simultaneous heating and straining imposed in laboratory air at a chamber pressure of approximately 5 Torr (650 Pa, $P_{O_2} = 1 \times 10^{-3}$ atm). The temperature of the sample (as measured at the point where the bottom of the sample touched the heating element) was initially raised to 930°F (500°C) at a rate of 45°F(25°C) per minute. At this point, a constant rate of tensile strain was imposed on the sample, while the temperature continued to be raised at a rate of about 5°F (3°C) per minute. After approximately 40 minutes, at a temperature of 1150°F (620°C), numerous parallel cracks rapidly propagated across the entire width and through the oxide scale, roughly regularly spaced with periods of 0.001-0.002" (20-40 mm) and aligned normal to the tensile axis (Figure 4.3.11a). The onset of scale fracture can be recorded both on videotape and in Polaroid micrographs.

Post-experiment examination of the fractured oxide layer showed regions of spallation along the edges of the sample. In these regions, cross sections of the oxide layer could be examined; the cracks were observed to have propagated all the way through the columnar-grained oxide layer and in some cases (but, significantly, not all) even into the alloy substrate below (Figure 4.3.11b). The latter is an important observation, which suggests that fracture of the oxide scale may initiate crack propagation into alloy substrate surfaces at low stresses.

ESEM Examination of Oxide Scales Grown Ex-Situ

Dynamic observations of ESEM oxidations were, of course, limited to several hours and provided no information about oxide thickness or internal microstructure or chemistry. Fracture cross-sections of scales grown both *in situ* and *ex situ* were therefore made. Figure 4.3.12 shows fracture cross-sections for α_2 -Ti₃Al substrates oxidized in moist air at 1300° F (700° C) and 1475° F (800° C); oxide thickness was easily measured, and morphological developments--such as the whisker growth at the higher temperature but not at the lower--readily noted. A fracture cross-section of the oxide scale grown on super- α_2 Ti₂NbAl (Figure 4.3.13) at 1300° F (700° C) confirmed the conclusion from the dynamic ESEM oxidations that the scale was morphologically unremarkable. Polished cross-sections across scales were also prepared (Figure 4.3.14a) to facilitate thickness measurements for comparison to thermogravimetric measurements §4.4), but fracture cross-sections proved preferable for chemical analysis by XEDS to avoid contamination of the cross-section with polishing agents. An XEDS map of the scale grown on α_2 -Ti₃Al at 1300° F (700° C) in Ar-20%O₂ for 3.5 hours (Figure 4.3.14b) shows a mixed composition in most of the scale, with some enhancement of Al content near the scale/substrate interface.

ESEM observations were also made of scales grown on Ti aluminide substrates for long times during thermogravimetric measurements. For example, ESEM observations of super- α_2 Ti₂NbAl oxidized at 1300° F (700° C) for 100 hours in N₂-5% O₂ and Ar-5% O₂ (Figures 4.3.15a and b respectively) revealed no difference in scale surface morphologies with or without the presence of nitrogen in the gas environment, complementing glancing-angle XRD measurements which revealed no difference in the scale phases present in 20 hour oxidations in the two gas mixtures. ESEM images of the scale surface on super- α_2 Ti₂NbAl oxidized at 1300°

F (700° C) in Ar-20% O₂ for 3.5 hours in the XRD hot stage and subsequently cooled to room temperature did reveal cracking of the scale and regrowth of oxide under the scale (Figure 4.3.16).

A modification of the TEM and STEM sample preparation has been explored using nickel plating over an oxidized sample. This plating has three advantages: a) clarifies scale thickness by providing a marker for the oxide/gas interface, b) illuminates the cracks and porosity in the oxide and substrate, and c) reduces the detachment of the scale, especially in cases of multilayered, complex scales. Figure 4.3.17 shows an example of this preparation on a γ -TiAl sample oxidized in air.

Analytical STEM of TEM Cross Sections

It became clear from the XEDS composition maps in ESEM observations of fracture cross-sections, as well as from recent TEM results on γ -TiAl scales [7,8], that the oxide scales on Ti-Al are complex on a scale that can be investigated only by using transmission electron microscopy. The instrument of choice for sorting out the elemental distributions in the various oxide phases observed is the analytical scanning transmission electron microscopy (STEM), but no STEM work had been previously reported for oxidation of Ti-Al alloys. TEM cross-sections of super- α_2 Ti₂NbAl alloy samples, oxidized for 100 hours at 1300° F (700° C) in N₂-5%O₂, were therefore prepared, using the techniques developed in Professor Hobbs laboratory for prior oxidation studies of NiAl and other Ni-based superalloys, and examined by STEM and TEM [9]. The super- α_2 Ti₂NbAl alloy was particularly chosen for the purpose of learning more about the effects of Nb and a nitrogen-containing environment on the oxide phase assemblage.

The STEM image and accompanying XEDS maps, Figure 4.3.18 and the synthesized colored map, Figure 4.3.19, revealed a complex, multilayered corrosion scale with overall thickness of order 0.5 mm. A thin, well-delineated layer of alumina was seen at the outermost observable surface, which the Nb added to the super- α_2 alloy has appeared to stabilize. Underneath this was an oxynitride containing mainly Ti and Nb cations and relatively small amounts of Al. The layer sequence is then repeated; such repeat layering on a larger scale has been reported in the development of other Ti-Al alloy oxidations at higher temperatures. Beneath the second

oxynitride layer was a layer of marked Al depletion, followed by a mixed oxides and oxynitrides of Ti and Nb, and then a Nb oxide (probably the NbO_2 detected in the glancing-angle XRD analysis). At the scale/substrate interface, nitrogen was found to be clearly enriched, as was found also for air-oxidized γ -TiAl [16,17] where TiN and ALON were identified.

TEM revealed a very fine-grain scale structure [18]. Adhesion of the outer oxide layers was not that strong, as evidenced by the frequent (and annoying) spallation of the outer-layer portions during cross-section preparation. It is clear from the STEM results that the oxidation process and the oxidation products of these alloys, and particularly the super- α_2 Ti_2NbAl , is very complex. A unresolved question for future investigation by TEM techniques is whether the oxygen-stabilized "new cubic phase" alloy phase (possibly the sub-oxide $\text{Ti}_5\text{Al}_3\text{O}_2$), reported in γ -TiAl oxidations adjacent to the scale/substrate interface, forms in oxidized super- α_2 Ti_2NbAl .

4.3.2.3 X-ray Diffraction Studies of Scale Composition and Texture

Conventional and glancing-angle (GA) XRD measurements were made on scales grown on both NiAl and Ti aluminide substrates. These utilized a Rigaku RU-200 12-kW rotating anode $\text{Cu}-\text{K}_\alpha$ source and automated powder diffractometer operating in standard Bragg configuration.

Conventional, though not GAXRD, measurements could be made *in situ* in the high-temperature environmental cell, described in §4.5, up to temperatures of 2550° F (1400° C). Figure 4.3.18 shows GAXRD spectra from the polycrystalline α_2 - Ti_3Al and super- α_2 Ti_2NbAl starting alloy substrates, which were remarkably similar, with some peak shifts due to the Nb substitution, confirming that our super- α_2 material retained the α_2 structure.

In-situ oxidations in the XRD hot stage in Ar-20% O_2 atmosphere confirmed the XEDS findings for the oxides respectively formed in the three substrates. As well as rutile TiO_2 , GAXRD measurements revealed the presence of $\alpha-\text{Al}_2\text{O}_3$ in all three scales, most prominently for the γ -TiAl; Figure 4.3.20 shows the result for α_2 - Ti_3Al at 1475° F (800° C) Figure 4.3.21 shows the development of the (110) rutile peak with oxidation time for α_2 - Ti_3Al at 700°C (1300°F); texture analysis, Figure 4.3.22, revealed a very weak (110) fiber texture. For the case of super-

α_2 Ti₂NbAl, NbO₂ peaks were also observed (Figure 4.3.23). Figure 4.3.24 documents the growth of the (113) peak of α -Al₂O₃ for oxidation of super- α_2 Ti₂NbAl at 1300° F (700° C). The alumina peaks were slightly shifted for the Ti₂NbAl alloy containing Nb compared to the α_2 -Ti₃Al, and were more prominent.

4.3.2.4 *In-situ* Determination of Stress in Oxide Scales and Substrates by X-ray Diffraction

The resistance of metal alloys to high-temperature oxidation is strongly linked to oxide adherence and thus is dependent on the internal stresses of the metal-oxide system. Adherence of a protective scale is highly influenced by the stresses that may exist in the oxide, in the substrate and at the metal-oxide interface. These stresses arise from stresses imposed on a component during its use, from differential thermal expansion and contraction of scale and substrate during thermal cycling, and from growth alone of an oxide layer. Such stresses cause scale fracture, buckling or spallation of the oxide from the underlying substrate, and may (as observed in the ESEM experiment described above) initiate propagation of scale cracks into embrittled coatings or substrates. It was deemed useful to develop an *in-situ* technique for measurement of stresses arising in scales and in the near-surface region of alloy substrates in the absence of imposed external stresses (but including differential thermal stresses) to complement the dynamic *in-situ* observations using ESEM. With the ESEM straining stage, only the externally-imposed stress and not the internal stresses generated by oxidation processes are quantifiable.

Although the existence of oxidation stresses is easily demonstrated, an evaluation of their origin and magnitude is a more difficult task. Typical average values of measured stresses in attached oxides of up to several mm thick are on order of several ten thousand psi (a few hundred MPa) in compression, although some values reported in Cr₂O₃ [19] and Al₂O₃ [20] are as high as several hundred thousand psi (several thousand MPa). Determination of the origin of residual stresses is problematic because the measured strain is only that part of the strain history that is preserved at room temperature. The residual strain measured at room temperature is a complex sum of the growth strain, that develops at elevated temperature as the oxide nucleates and grows, and the differential thermal strain that develops upon cooling.

Thermal stresses can readily be calculated given the appropriate thermal expansivities and elastic constants, assuming no stress relaxation occurs through microstructural changes such as creep or fracture. Growth stresses are superimposed on thermal stresses and can either add to or subtract from the thermal stresses. Thus, room temperature residual stress measurements reveal little about the magnitude of the individual growth and thermal stress components.

The individual contributions of the growth and thermal stress components to the residual stress is best resolved by direct *in situ* measurements at temperature. A high temperature X-ray diffraction method was therefore used to investigate stresses during oxidation and during cooling to room temperature in both the oxide and substrate. The simple systems NiO/Ni and Cr₂O₃/Cr were chosen for initial study, because only a single oxide grows on the substrate in either case, because the oxidation behavior is well known, and because residual stress determinations have already been performed at room temperature. A commercial chromia-forming alloy, Inco's mechanically-alloyed MA754 (Ni-20wt%Cr-0.5wt%Ti-0.3wt%Al-0.05wt%C-0.6vol%Y₂O₃) was also investigated. Finally, the aluminide alumina-formers, Ni-30wt%Al (β -NiAl), in both single-crystal and polycrystalline form, and the three titanium aluminide alloys.

High-Temperature X-Ray Stress Measurement

A Rigaku RU-200 X-ray generator with a rotating Cu anode was run at 60kV and 200mA (12 kW), yielding a primary beam of Cu K radiation ($\lambda = 0.154$ nm) with diameter 0.020 in (0.5 mm) at the specimen. Cu-K_b peaks were eliminated by using a curved graphite-crystal monochromator. Samples were mounted at the center of a heated ceramic stage in a Rigaku CN23 11B1 high-temperature camera . The furnace has a maximum temperature of 2550°F (1400°C), regulated by a programmable temperature controller and Pt/Pt-Rh thermocouple, and can be run in either ambient air, vacuum, or selected gaseous environments. All samples were cold-rolled (Ni, Ni-Cr, MA754) or ground (NiAl, Ti aluminides) to thicknesses of 0.050-0.060" (1.2-1.5mm), cut to shape (0.6x1", 15x24 mm), polished with 600-grit SiC and recrystallized in argon-filled capsules for appropriate times and temperatures prior to oxidation. X-ray diffraction spectra were collected during oxidation in ambient air at 1830°F (1000°C) for Ni/NiO system, at 1660 F (940°C) for Cr/chromia, Ni-20wt.%Cr/chromia, MA754/chromia, at 2060°F (1125°C) for NiAl/alumina, and at 1475° F (800° C) and 1300° F (700° C) for γ -TiAl, α_2 -Ti₃Al and super- α_2 Ti₂NbAl/(TiO₂ + Al₂O₃) systems, as well as during step-by-step cooling to room temperature.

Once a sample and the furnace were positioned, a baseline room-temperature spectrum of the metal was collected; no oxide was detectable by X-ray diffraction at this point. The samples were heated stepwise in flowing nitrogen, to minimize oxidation during heat-up, and air introduced once the oxidation temperature was reached. Data were collected throughout the heat-up and oxidation periods and also as the sample temperature was stepped down to room temperature. A final spectrum was obtained after 12-24 hr at room-temperature to assess any relaxation of residual stresses over time.

We use the "sin²y" method which provides complete information on the residual stresses in the scale [21]. The basis of the method is that lattice spacings change in response to residual stresses and temperature. Planar d-spacings were measured from diffraction peaks for planes approximately parallel to the substrate surface in reflection geometry, as shown in Figure 4.3.25. The oxides produced are sufficiently fine-grained that optimal diffraction conditions were satisfied without rotating the sample during experiment. X-ray diffraction measurements of strain are ideally made at diffraction angles 2θ approaching 180° , because the error in measured d-spacing approaches zero as 2θ approaches 180° . This is a direct consequence of differentiating Bragg's law, which can be written in terms of strain ϵ to estimate the uncertainty in strain measurement

$$\partial\epsilon = \frac{\cos\theta}{\sin\theta} \sin(\partial\theta) \quad (4.3.1)$$

The alternative transmission (Laue) geometry used *e.g.* by Shores *et al.* [22], which requires use of more penetrating Mo K α radiation ($\lambda = 0.07$ nm), operates at 2θ angles of $10\text{-}30^\circ$ and, for $\partial\theta \approx 0.009^\circ$, the estimated strain resolution is $\partial\epsilon \approx 0.04\%$. Our system, configured instead in reflection geometry with the longer wavelength Cu K α radiation, operates in the 2θ range $40\text{-}80^\circ$ with an estimated strain resolution $\partial\epsilon \approx 0.01\%$, four times smaller. Also, much thicker substrates (limited only by the specimen mounting parameters) are able to be used in the reflection mode.

The lattice strain is calculated for each diffraction peak using the equation

$$\epsilon = \frac{d(T) - d_0(T)}{d_0(T)} \quad (4.3.2)$$

where $d_0(T)$ is the unstrained lattice spacing at the measurement temperature. The measured strain for our geometry therefore represents the strain approximately *normal* to scale/metal interface. In-plane strains *parallel* to the interface are of opposite sign (because Poisson's ratio ν is positive) and scaled by a factor involving $1/\nu$.

The strain calculation depends sensitively on the choice of $d_0(T)$, which influences both the magnitude and sign of the calculated strain. A large disparity in thermal expansion values exists within the literature data for NiO, chromia, alumina and titania; the reported values vary with measurement technique and material properties such as purity and porosity. For this reason, $d_0(T)$ was measured as a function of temperature for chromia, alumina and titania directly in our same *in situ* system, using the pure oxides (Figure 4.3.26). NiO thermal expansion values were obtained from the measurements of Taylor [23]. Meaningful changes in metal substrate lattice parameters, other than those due to temperature, could not be measured with the present arrangement because of the large depth of substrate from which diffracted X-rays emerged in conventional θ - 2θ diffraction geometry and the large strain gradient obtaining over this depth. Hence, for the metal, d_0 was taken as the measured value at room temperature, and the strains reported reflect principally thermal expansion. A subsequent refinement of the technique, which we have recently successfully employed, is to use glancing-angle incidence to achieve sampled depths more nearly comparable to the oxide thicknesses, so that average strain in the substrate layers immediately adjacent to the scale may also be measured.

During cooling to room temperature, an additional and larger component of stress is induced by the different thermal expansion coefficients of the metallic substrate and oxide. Therefore the total stress applied to the oxide scale will be the sum of the growth stress and the thermal stress

$$\sigma_{TOT} = \sigma_{GR} + \sigma_{TH} \quad (4.3.3)$$

As noted by Tien and Davidson [24], when the ratio of the scale thickness to the sample thickness is very small, the average compressive thermal stress σ_{TH} can be expressed as

$$\sigma_{TH} = \frac{E_{ox} \Delta T (\alpha_m - \alpha_{ox})}{1 - \nu} \quad (4.3.4)$$

where ΔT is the cooling amount and $\alpha_m - \alpha_{ox}$ is the thermal expansion difference between oxide scale and the substrate, ν is Poisson's ratio and E_{ox} is Young's modulus. These stresses will be compressive in the oxide and tensile in the metal upon cooling because of the generally smaller thermal expansion of oxides. The total stress σ_{TOT} is given by

$$\sigma_{TOT} = \sigma_{GR} + \frac{E_{ox} \Delta T (\alpha_m - \alpha_{ox})}{1 - \nu} \quad (4.3.5)$$

In-situ X-ray diffraction measurements were made of the elastic strains developing during all phases of the oxidation process --heating, isothermal oxidation, and cooling. From these measurements, the corresponding stresses have been deduced, assuming elastic behavior. Of course, once plastic yield occurs, for example by creep in the substrate or oxide, then no further increase in measured strain is observed; and if scale adhesion is additionally lost, the attendant stresses may be relieved.

NiO/Ni System

Stress measurements were made for oxidation of pure Ni (99.9% purity) at 1830°F (1000°C) in room air and during step-by-step cooling to room temperature. The Ni substrates were cold-rolled, then recrystallized at 200°F (1100°C) for 6 hours in argon-filled capsules. The (111), (200) and (220) planes of NiO and (111) and (200) planes of Ni were chosen to perform stress analysis with Cu K α radiation. The strain behavior of Ni/NiO system is shown in Figure 4.3.27.

All values given represent the elastic strain measured in the direction normal to the sample surface. The results are retained in terms of strain rather than stress owing to the lack of reliable modulus data for the oxide over the temperature range of interest. Figure 4.3.26 reveals a small apparent tensile strain in the pure Ni before the beginning of oxidation. After the introduction of air, an additional increase in strain is observed in the metal. This increase coincides with the appearance of the measurable oxide diffraction peaks, shown in Figure 4.3.28. As oxidation proceeds, the strains in the oxide scale increase quickly initially, then remain relatively constant. The strains derived from each of the three oxide reflections (111), (200) and (220) achieve

approximately equal values during oxidation, as shown in Figure 4.3.26, which confirms isotropic elastic behavior. The positive strains in a direction normal to the sample surface imply that the oxide scale is under a net in-plane *compressive* (-) stress parallel to the oxide/metal interface. It thus appears that NiO scale is subjected to an in-plane compressive stress during oxide growth at temperature, with average in-plane strain $\approx -0.8\%$, corresponding to an average in-plane stress $\approx -384,000$ psi (-2560 MPa). The breadth of the oxide Bragg peaks shows a regular decrease, shown in Figure 4.3.29, as oxidation time increases, implying that the defect content (largely dislocation density) *decreases* as oxidation proceeds and the scale becomes thicker; this result has been confirmed by direct cross-section TEM [14].

Upon cooling, the NiO oxide continues to exhibit compressive residual strain. The average values of thermal expansion coefficients for Ni and NiO are equal to 17.6×10^{-6} and $14.5 \times 10^{-6} \text{ K}^{-1}$, respectively, and $E_{\text{ox}} = 220 \text{ GPa}$ at room temperature [23]. Using eqn (1), the theoretical differential thermal in-plane stress was calculated to be -142,000 psi (949 MPa). The residual in-plane stress value at room temperature deduced from our experimental data was -495,000 psi (3300 MPa), 111,000 psi (740 MPa) of which must be attributable to differential thermal strain. Due to the relatively high rate of cooling, the creep relaxation of oxide stresses is relatively small in comparison to conditions obtaining in other studies [25], and most of the differential thermal strain contributes to the measured stress. The thermal stresses calculated using eqn (1) are average stresses in the oxide, whereas a more detailed analysis has shown that the stress gradient will exist in both materials, especially in the thick metal substrate[25]. The compressive residual room-temperature strain measured in the NiO scale is consistent with those obtained by using conventional *ex-situ* measurement techniques (in-plane $\epsilon \approx -0.6\%$ compared to our measured value of -0.8%). (Our results agree with those obtained in three other investigations[22,23,26] and differ only from those obtained by a fourth [27].) The slight discrepancy between *in-situ* and *ex-situ* values is likely explained by different creep rates on cooling in the two types of stress measurement. The strains in both the oxide and metal remain relatively constant during the oxidation period, suggesting that yield has occurred either in the oxide or, as confirmed directly in TEM observations of substrate creep microstructures [14], in the metal. As noted earlier, the X-ray diffraction technique measures only elastic strains; once yield has occurred, no further increase in elastic strain is observed. The growth and thermal stresses for NiO are summarized in Table 4.3.1.

Table 4.3.1. Measured and Calculated In-plane Stresses in Oxide Scales

Alloy	σ_{growth} , MPa	$\sigma_{\text{thermal,}}(\text{theory})$ MPa	$\sigma_{\text{thermal,}}(\text{measured})$ MPa	$\sigma_{\text{residual,}}$ MPa
Ni	-2560	-949	-770	-3330
Cr*	+3120	-1534	+1560	+4680
MA754*	+3900	-4032	-3120	+780
Ni-20%Cr*	+546	-5630	-378	+168
NiAl (single crystal)	+814	-1194	-608	+206
NiAl (polycrystalline)	+108	-1194	-42	+150

* Stresses are calculated using Young's moduli, Poisson's ratio and thermal expansion coefficients from [25].

Chromia/Cr, chromia/MA754 and chromia/Ni-17.6wt%Cr systems

Electrolytic high-purity Cr (99.99%), Ni-17.6wt%Cr alloy and MA754 produced by Huntington Alloys were prepared and annealed similarly to the Ni samples and oxidized at 1725°F (940°C) in room air. (104), (110) and (116) chromia peaks were monitored during oxide growth and step-by-step cooling to room temperature. The three substrates are typical chromia-formers during high-temperature oxidation, but they have somewhat different mechanical properties; the thermal expansion coefficient for Cr is much less than for that for Ni-17.6wt%Cr and MA754, while Young's moduli vary in the order E(Cr₂O₃)>E(Cr)>E(Ni-17.6wt%Cr)>E(MA754). MA754 exhibits a much lower creep rate in the low-stress region than either Cr or Ni-17.6wt%Cr [25]. The measured oxidation strain behavior for chromia scales formed on the three alloys is presented in Figures 4.3.30-4.3.32. Stress values calculated from eqns (1) and(2) are listed in Table 4.3.1.

There are some important differences between the Cr₂O₃/chromia-former results and those previously discussed for Ni/NiO. The thermoelastic behavior of chromia is more complicated than that of NiO because of its rhombohedral symmetry. The thermal expansion of Cr₂O₃ is anisotropic, with the a-axis direction being about 40% more expandable than the c-axis direction. This means that diffraction planes such as (110) in Cr₂O₃ serve as a more sensitive strain gauge than do reflections such as (116) and (104). This behavior has important consequences for the development of thermal stresses upon cooling to room temperature, because the Cr has a thermal expansivity value between the a-direction and c-direction expansivities of the oxide. In calculating the thermal stress in either the oxide or the metal using the Tien-Davidson formulation [24], the sign can be either positive or negative, depending on the crystallographic orientation of the oxide. This means that the corresponding thermal stress can be either compressive or tensile depending on oxide orientation. From a practical standpoint, Cr₂O₃ scales which grow with their c-axes normal to the metal interface should have a minimal in-plane stress and should be more resistant to failure. Also, to make sense of measured data, stress measurements should be augmented by pole-figure analysis of oxide orientation texture, or by direct TEM evaluation of orientation morphologies. Scales formed on Ni-17.6wt%Cr can be duplex and contain chromia, NiO and NiCr₂O₄ phases [15], which complicates the growth stress situation and thermal stress predictions, although our oxidations at 1725°F (940°C) yielded only chromia.

Alumina/NiAl System

A NiAl single crystal grown by General Electric-Evendale using the floating zone method was homogenized as described earlier and cut into coupons with (100) surfaces. Polycrystalline NiAl material was recrystallized at 2100°F (1150°C) for 6 hr in argon prior to oxidation. Sample surfaces were polished to 600-grit SiC and cleaned in acetone before oxidation. *Ex-situ* X-ray diffraction analyses were performed using a Rigaku automated powder diffractometer in standard Bragg configuration using Cu K_α radiation. *In-situ* stress determinations were conducted during isothermal oxidation at 2050°F (1125°C) in room air, as well as during step-by-step cooling to room temperature.

(110), (200) and (220) peaks of NiAl polycrystalline substrates, as well as (102) θ -alumina and (110) α -alumina reflections, were monitored during isothermal oxidation and cooling. The (100) and (200) peaks of NiAl single crystal substrates, as well as the (012) α -alumina reflection, were similarly monitored. The strain behavior of these alumina/NiAl systems for both polycrystalline and single-crystal substrates is presented in Figures 4.3.33 and 4.3.34, respectively. Corresponding calculations of the stresses developed in α -alumina scales, using various relevant data collated elsewhere [28,29], are listed in Table 4.3.1. The measured thermal stress was derived from the measured growth and total stresses using eqns (1) and (2).

The *in-situ* results for the alumina/NiAl system for both polycrystalline and single crystal substrates indicates that strains in the metal and oxide again are established almost immediately upon introduction of air and remain constant over the oxidation period, as can be seen in Figures 4.3.33 and 4.3.34. The constant strain values suggest that the elastic limit is quickly reached in the alloy. During the oxidation period and subsequent cooling, the coexistence of two phases, θ - and α -alumina was observed. In Figure 4.3.35, the evolution of (104) and (110) α -alumina peaks as well as (110) θ -alumina during cooling is shown. Similar comments apply to the anisotropy of α -alumina expansion as were discussed for chromia and may explain the difference in measured thermal stress between single- and polycrystalline substrates. The measured stresses were of the same sign as for chromia scales, but consistently much smaller.

(Alumina+rutile)/Titanium Aluminides

The three titanium aluminide alloys obtained from Wright-Patterson AFB were utilized in the as-received condition. Samples were sectioned to the dimensions described in §4.5.1, polished with 600-grit SiC and washed in acetone prior to oxidation in Ar-20%O₂. As indicated in §4.4, the scales exhibited mixed composition (both rutile and alumina), and stresses in both oxide phases were monitored. From the peaks positions, strains were deduced by comparison to measured thermal expansion data for the scale constituents (in this case TiO₂ rutile and α -Al₂O₃). An isotropic value for the rutile expansion coefficient, $8.9 \times 10^{-6} \text{ K}^{-1}$, valid over the temperature range 68-1475° F (20-800° C), was obtained by averaging over the five reflections in Figure

4.3.25c. For α -Al₂O₃ over the same temperature range, a value of $7.55 \times 10^{-6} \text{ K}^{-1}$ was obtained by averaging over the three reflections in Figure 4.3.25b. Thermal expansion data for the γ -TiAl and α_2 -Ti₃Al alloy substrates were taken from the work of Schütze [30]. The thermal expansion for α_2 -Ti₃Al was assumed for super- α_2 Ti₂NbAl in the absence of experimental for the latter.

Figures 4.3.36 and 4.3.37 show the measured strain values normal to the scale/substrate interface for scales grown on γ -TiAl and super- α_2 Ti₂NbAl alloy substrates at 1300° F (700° C). The corresponding measurements for α_2 -Ti₃Al oxidized at 1300° F (700° C) and 1475° F (800° C) are compared in Figures 4.3.38 and 4.3.39. These were converted to in-plane growth and thermal stresses (upon cooling to room temperature) parallel to the scale/substrate interface, which appear in Table 4.3.2.

Table 4.3.2. In-Plane Growth and Thermal Stresses for Oxidation of Ti-Al Alloys at 700° C (1300° F) and 800° C (1475° F)

Alloy	σ_{growth} , MPa alumina	σ_{thermal} , MPa (σ_{residual} , MPa) alumina	σ_{growth} , MPa rutile	σ_{thermal} , MPa (σ_{residual} , MPa) rutile
γ -TiAl [700°C]	+2149	-1145 (+999)	+758	-631 (+182)
super- α_2 Ti ₂ NbAl [700°C]	+1475	-969 (+421)	+834	-534 (-257)
α_2 -Ti ₃ Al [700°C]	+2775	-969 (+1152)	+1516	-534 (-295)
α_2 -Ti ₃ Al [800°C]	+2289	-1158 (+853)	+947	-617 (-1061)

The in-plane at-temperature growth stresses for all three scales and both oxides appearing were tensile (+) and were reduced on cooling by the compressive (-) contribution for differential thermal contraction with respect to the substrate. The room-temperature residual stresses were compressive in rutile (and have reversed sign) for α_2 -Ti₃Al and super- α_2 Ti₂NbAl and slightly

tensile for γ -TiAl, but remained substantially tensile for alumina in all alloys. No attempt has been made to model the differential contraction effect of distinct multilayered scales. The crazing and cracking noted in the scales in ESEM (Figures. 4.3.8 and 4.3.16) were therefore more likely to have occurred as a consequence of growth, rather than differential thermal contraction.

4.3.2.5 Oxidation Kinetic Measurements for Titanium Aluminides

Measurements of oxidation kinetics are a useful adjunct to observations of scale morphological and microstructural development because, like measurements of oxidation stresses, they average over microstructure; they also provide useful comparisons of oxidation behavior for different alloys, alloy treatments, and oxidation environments and (to the extent they can be extrapolated from laboratory time-scales) an indication of long-term alloy performance in oxidation environments. Measurements of oxidation kinetics in the three titanium aluminide compositions were made at both 1475° F (800° C) and 1300° F (700° C). It is not anticipated that α_2 -based alloys, would be utilized at temperatures of above 800-900° C (1475-1700° F), and the lower temperature of 700° C (1300° F), slightly above the upper bound for super- α_2 Ti₂NbAl projected use, was therefore chosen for the comparative study of kinetics, morphologies and microstructures. There have been no detailed studies of oxidation behavior of Ti-Al alloys at this temperature. For comparison to reported literature values of titanium aluminides, the Ti-Al series was oxidized at 800°C. Results for 20-hr kinetics in Ar-20%O₂ are shown in Figure 4.3.40.

Thermogravimetric measurements were made on alloy coupons suspended in a tube furnace through which selected oxidant gases were passed at low flow velocities. Isothermal data were collected for up to 100 hours. Scales grown on Ti-Al alloys at 1300° F (700° C) remain thin (< 0.5 mm for super- α_2 , < 0.1 mm for γ -TiAl), so weight-gain measurements had to be made in some cases close to the instrumental sensitivities (10-50 mg) of the microbalances. Two microbalances, a Cahn 1000 unit and a DuPont 990 unit with a smaller furnace tube, were used; the latter was more restrictive of sample size, but a cantilever beam shorter than the hang-down chain in the Cahn reduced static charge and noise difficulties for small weight gains. Figure 4.3.41 shows the reproducibility and a comparison of the two instruments for 20-hr scale growth kinetics for the three alloys at 700° C (1300° F) in air.

Figure 4.3.42 compares the 20-hr kinetics in dry air with those for the three alloys in pure oxygen at 1300° F (700° C). The presence or absence of nitrogen in the oxidizing gas has been reported to have a significant impact on the oxidation of these alloys. TEM cross-section studies of air-oxidized γ -TiAl have revealed TiN and aluminum oxynitrides ($\text{Al}_{27}\text{O}_{39}\text{N}$, or "ALON") at or near the scale/alloy interface [16] at higher temperatures. Indeed, Figure 4.3.42 does reveal small consistent differences in the oxidation kinetics of γ -TiAl in dry air and pure oxygen. There is, however, a very marked effect, evidenced reproducibly in our measurements for oxidation of super- α_2 in 100% oxygen, which greatly accelerates the oxidation kinetics. The oxidation kinetics for super- α_2 in dry air are close to parabolic, with a parabolic rate constant of $0.49 \times 10^{-13} \text{ g}^2/\text{cm}^4 \text{ s}$ averaged over 20 hours, but accelerates dramatically and reproducibly to $24 \times 10^{-13} \text{ g}^2/\text{cm}^4$ in pure oxygen. The dramatic effect does not appear to be due to presence or absence of nitrogen, since kinetics in Ar-5%O₂ and N₂-5%O₂ were similar (see Figure 4.3.43), but instead to an effect of oxygen content alone. The same effect is seen in Figure 4.3.44 for Ar-20%O₂ and N₂-20%O₂.

Because oxide weight gains were small at this temperature, much longer times than even 20 hours are required to effect appreciable scale growth and development of representative steady-state scale morphologies and microstructures. With many other alloy systems (such as Ni-Al) exhibiting slow-growing protective scales, the slow rate of oxide growth can be accelerated to experimentally more accessible values by elevating the temperature; but, in the Ti-Al system, the composition and phase distribution of the scale can alter dramatically at higher temperatures, so longer oxidation times are required at temperatures approximating those for projected uses. For oxidation in air over 100 hours, the average parabolic rate constant for super- α_2 increased slightly to $7.3 \times 10^{14} \text{ g}^2/\text{cm}^4 \text{ s}$. Figure 4.3.43 compares oxidation kinetics for the three alloys in N₂-5%O₂ and Ar-5%O₂ or 100 hours oxidation at 1300° F (700° C). Our study is one of a very few that have reported such results at a lower temperature where a more protective scale is likely to have formed. Here, at low oxygen content, there are only small differences for super- α_2 with or without the nitrogen. The largest differences are seen for $\alpha_2\text{-Ti}_3\text{Al}$ and $\gamma\text{-TiAl}$, and in all three cases oxidation was *slower* with nitrogen in the atmosphere.

Figure 4.3.45 shows in amplified detail the oxidation kinetics for γ -TiAl oxidized in pure oxygen for 20 hours with the DuPont microbalance and 100 hours with the Cahn unit. Evident in both oxidation runs is cyclic breakaway oxidation, occurring for the first time between 10 and 20 hours, then repeated at roughly 20-hr intervals. Owing to the very small weight gains, this cyclic behavior is less evident in thermogravimetric plots comparing γ -TiAl behavior with that of other more rapidly oxidizing alloy compositions. The conventional wisdom for higher oxidation temperatures [17] is that faster-growing TiO_2 forms in the regions of accelerated kinetics as Al is depleted in forming a partly protective alumina layer and the alumina layer dissolves into the outermost TiO_2 layer.

That the oxidation of super- α_2 is *faster* than that of γ -TiAl (and therefore of Nb-doped γ -TiAl which offers even better oxidation resistance, at least at higher temperatures [10,11,17]) suggests that the inhibition of alumina dissolution into the outer TiO_2 layer effected by the Nb additions (possibly by doping of TiO_2) must eventually saturate, and that the incorporation of Nb into slow-growing Nb-rich oxide phases such as NbO_2 may give way to more rapidly-growing Nb_2O_5 -like products. That it is considerably *slower* than oxidation of $\alpha_2\text{-Ti}_3\text{Al}$ suggests that, on the other hand, that the Nb substitution is having a substantial effect on maintaining continuous quasi-protective alumina and/or NbO or NbO_2 layers in the scale. Figures 4.3.47 and 4.3.48 illustrate the effect of oxygen content on the oxidation rates of super- α_2 . Small amounts have very little effect on the rate, but the pure oxygen rate is significantly higher than the oxygen-argon mixtures. The same holds true for oxygen-nitrogen mixtures, but the kinetic rates are lower with the presence of nitrogen. The effect of oxygen content and nitrogen presence has a greater impact on the oxidation of super- α_2 than that of γ -TiAl or $\alpha_2\text{-Ti}_3\text{Al}$.

4.3.3 Publications for This Task Element

B. A. Pint, M. Treska and L. W. Hobbs, "The effect of various oxide dispersions on the phase composition and morphology of Al_2O_3 scales grown on β -NiAl," *Oxid. Metals* **46** (1996) 505-24.

D. Clemens, V. Vosberg, L. W. Hobbs, U. Breuer, W. J. Quadakkers and H. Nickel, "TEM and SNMS studies of protective alumina scales on NiCrAlY-alloys, *Fresenius J. Anal. Chem.* **355** (1996) 703-06.

4.3.4 Theses Published Based on This Task Element

DeWolf, Jeffrey, "The Determination of Stresses in Metal/Oxide Systems During High Temperature Oxidation Using the In-Situ X-Ray Diffraction Technique", B.S. Materials Science and Engineering, June 1994.

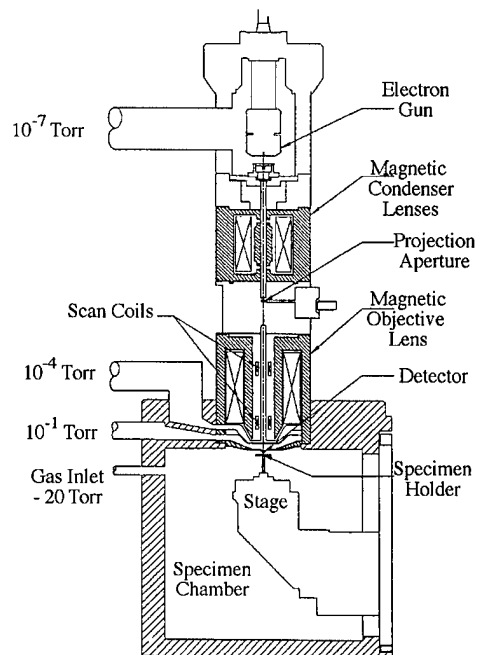
Duncan, Julia C., "High Temperature Environmental Degradation of Titanium Aluminides", Sc.D. Materials Science and Engineering, expected February 1998.

4.3.5 References for This Task Element

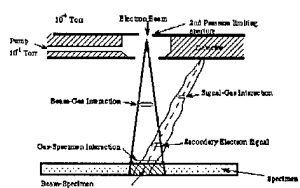
1. B.A. Pint and L.W. Hobbs, "The Formation of α - Al_2O_3 Scales at 1500°C," *Oxidation of Metals* **41** (1994) 203-33.
2. B.A. Pint, A.J. Garratt-Reed and L.W. Hobbs, "The Reactive Element effect in commercial ODS FeCrAl alloys," *Materials at High Temperatures* **13** (1995) 3-16.
3. B.A. Pint, J.R. Martin and L.W. Hobbs, "The oxidation mechanisms of the θ - Al_2O_3 scales," *Solid States Ionics* **78** (1995) 99-107.
4. B.A. Pint, M. Treska and L.W. Hobbs, "The effect of various oxide dispersions on the phase composition and morphology of Al_2O_3 scales grown on β -NiAl," *Oxid. Metals* **46** (1996) 505-24.
5. B.A. Pint, A.J. Garratt-Reed and L.W. Hobbs, "Analytical Electron Microscopy Study of the Duplex Scale Formed on an ODS Ni_3Al Alloy", in: *Microscopy of Oxidation*, ed. S. B. Newcomb and M. J. Bennett (Institute of Metals, London, 1993) 423-434.
6. A. Rahmel, W.J. Quadakkers and M. Schütze, *Materials and Corrosion* **46** (1995) 271.
7. S. Becker, A. Rahmel, M. Schorr and M. Schütze, *Oxid. Metals* **38** (1992) 425.
8. W.E. Dowling and W.T. Donlon, *Scripta Metall.. Mater.* **27** (1992) 1663; R. W. Beyer and R. Gronsky, *Acta Metall. Mater.* **42** (1994) 1373.

9. U. Figge, A. Elschner, N. Zheng, H. Schuster and W. J. Quadakkers, *Fresenius J. Anal. Chem.* **34** (1993) 75.
10. H. Nickel, N. Zheng, A. Elschner and W. J. Quadakkers, *Mikrochim. Acta* **199** (1995) 23.
11. B.G. Kim, G.M. Kim and C.J. Kim, *Script Metall. Mater.* **33** (1995) 1117.
12. G. Qiu, J. Wu, L. Zhang and D. Lin, *Scripta Metall. Mater.* **35** (1995) 213.
13. R.G. Rowe, *Adv. Mater. Proc.* **3** (1992) 33.
14. L.W. Hobbs, M.T. Tinker and H.T. Sawhill, *Jap. Inst. Metals Supplement [JIMIS-3]* (1983) 115.
15. S.B. Newcomb and L.W. Hobbs, in: *Microscopy of Oxidation*, ed. M. J. Bennett and G. J. Lorimer (Institute of Metals, London, 1991) 329-35.
16. C. Lange and M. Schütze, "TEM studies of the mechanisms in the early stages of TiAl oxidation," in: *Proc. Third International Conference on Microscopy of Oxidation*, Cambridge, UK, 16-18 September 1996, Cambridge, UK (in press, 1997).
17. C. Lange and M. Schütze, "The initial stages in the oxidation of TiAl," submitted to *Materials and Corrosion* (1996).
18. J.C. Duncan and L.W. Hobbs, "Electron microscopic investigations of high-temperature corrosion of titanium aluminide intermetallics," platform presentation at *Third International Conference on Microscopy of Oxidation*, Cambridge, UK, 16-18 September 1996, Cambridge, UK.
19. C. Diot, P. Choquet, and R. Mevrel, in "International Conference on Residual Stresses II" (ICRS II) G. Beck, S. Denis and A. Simon (ed.) Elsevier Applied Science, Nov. 23-25, 1988, Nancy, France, (1989) 273.
20. M.J. Bennett in "High Temperature Corrosion of Advanced Materials and Protective Coating" Y. Saito, B. Onay and T. Maruyama (ed.) Elsevier Science Publisher, 1990 Japan, (1991) 51.
21. I.C. Noyan and J.B. Cohen, *Residual Stress Measurement by Diffraction and Interpretation* (Springer-Verlag, New York, 1987).
22. J. Stout, J. Goedjen, Q. Guo, D. Shores in: *Proceedings of the Symposium on X-ray Methods in Corrosion and Interfacial Electrochemistry*, (Electrochemical Society, Pennington, NJ, 1992) Vol. **92-1**, 101-14.
23. D. Taylor, *Trans. Brit. Ceramic Soc.* **83** (1989) 5.
24. J.K. Tien and J.M. Davidson, in: *Stress Effects and the Oxidation of Metals*, ed. J. V. Cathcart (Metallurgical Society AIME, Detroit, MI, 1975) 200.
25. J.J. Barnes, J.G. Goedjen and D.A. Shores, *Oxid. Met.* **32** (1989) 449.

26. A. Aubry, F. Armanet, G. Beranger, J.L. Lebrun, G.M. Mader *Acta Metall.* **36**, (1988) 2779.
27. C. Liu, A.M. Huntz and J.L. Lebrun, in "International Symposium on High Temperature Corrosion and Protection", June 1990, Shenyang, China, (1990).
28. M. Schutze in: *High Temperature Corrosion of Advanced Materials and Protective Coatings*, ed. Y. Saito, B. Onay and T. Maruyama (Elsevier Applied Science Publishers, Amsterdam, 1992) 39-49.
29. J. Jedlinski and G. Borchardt, *Oxid. Metals* **35** (1991) 317.
30. M. Schütze, in: *Corrosion Science* **35** (1993) 955.



a)



b)

Figure 4.3.1 Electro-Scan environmental scanning electron microscope, a) schematic and b) electron-specimen-gas interactions and imaging mechanism.

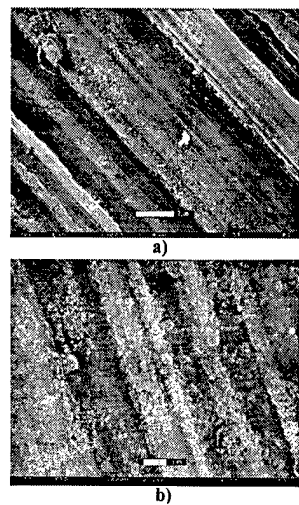


Figure 4.3.2 *In-situ* ESEM micrograph of a) γ -TiAl at 595°C (1100°F) in air and b) α_2 -Ti₃Al after *in-situ* exposure to air at 700°C (1300°F).

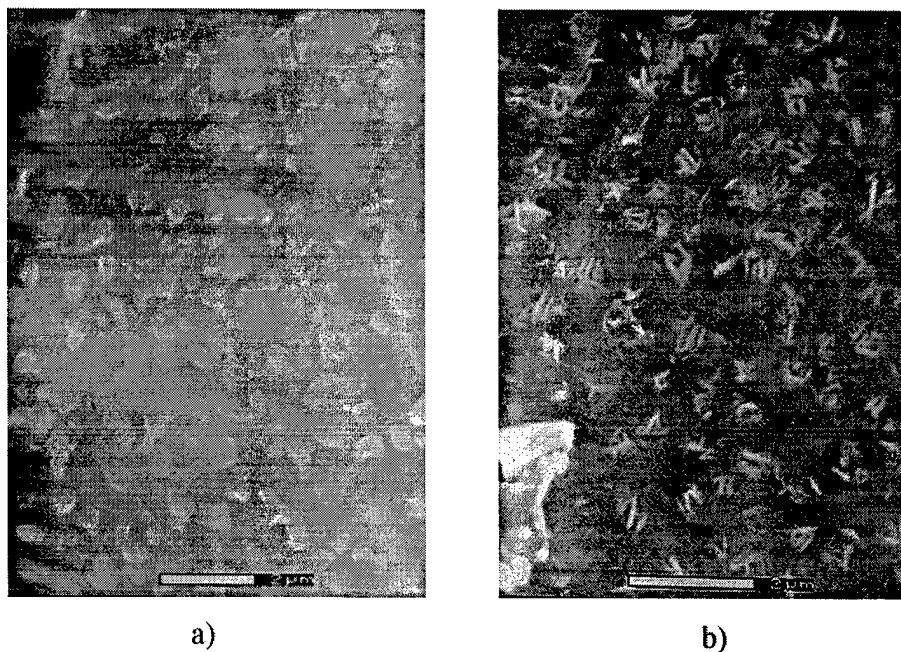
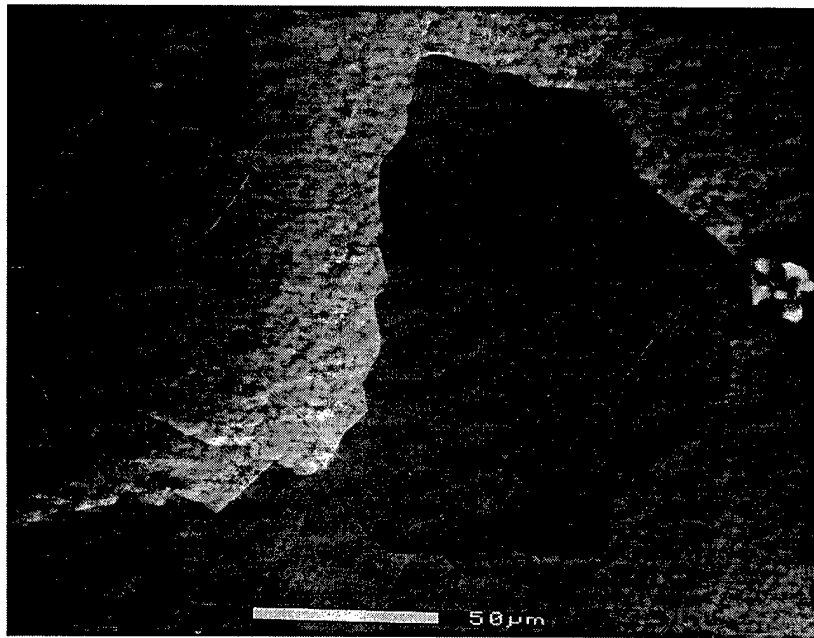
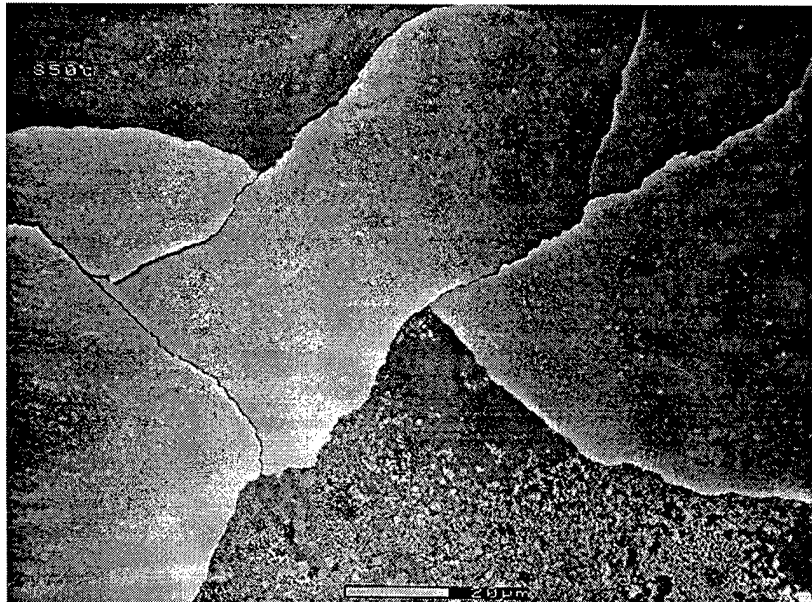


Figure 4.3.3 Development of chromia scale morphologies during *in-situ* ESEM oxidation of pure Cr: a) island formation, b) whisker growth.

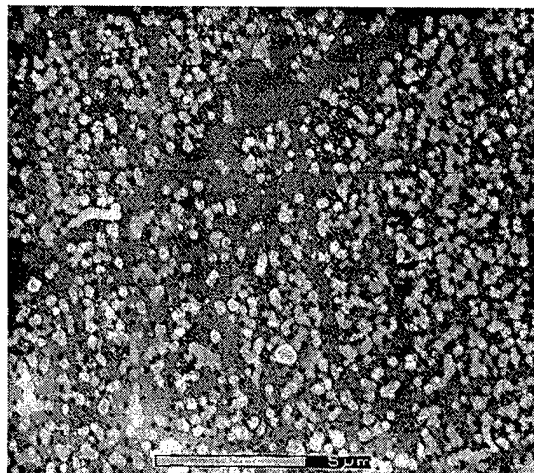


a)

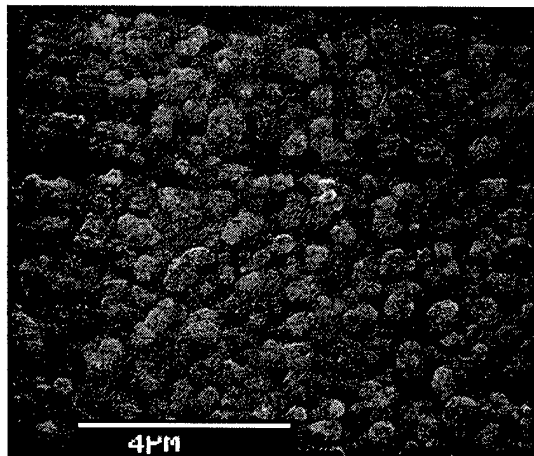


b)

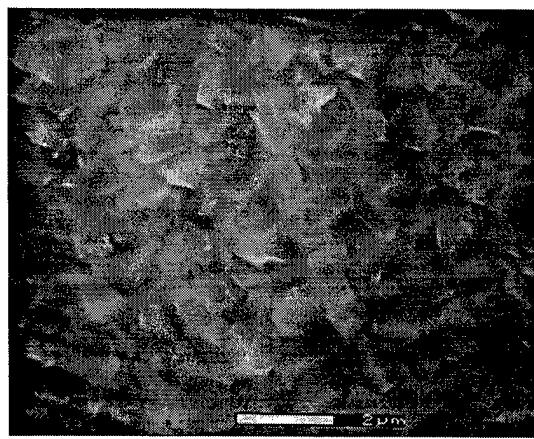
Figure 4.3.4 Cracking and spallation of chromia scales formed *in situ* in the ESEM upon cooling: a) chromia scale formed on pure Cr, b) duplex scale formed on Ni-17.6wt%Cr.



a)

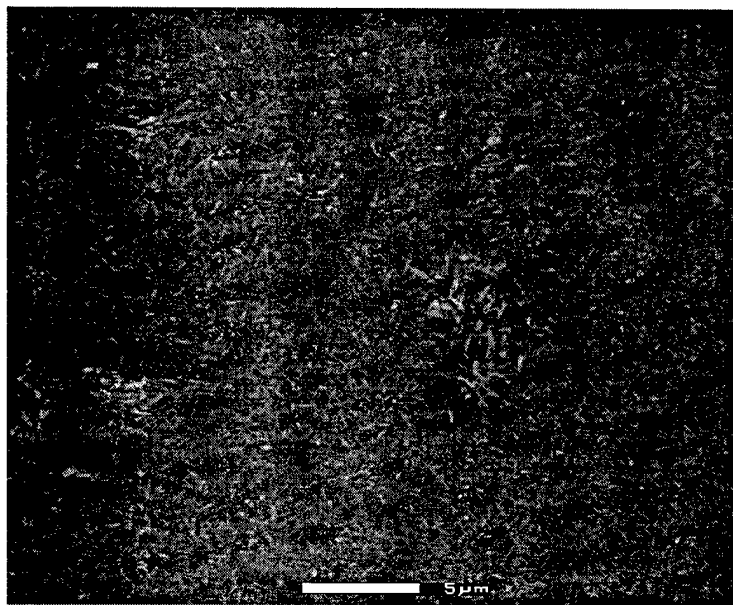


b)

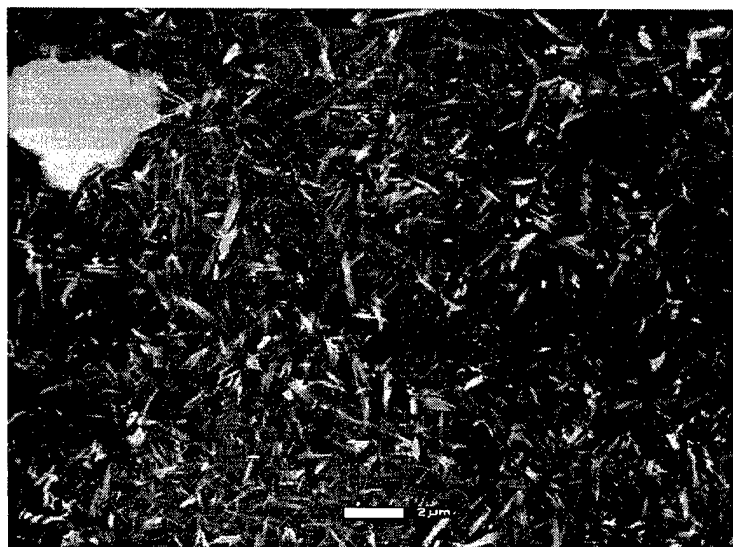


c)

Figure 4.3.5 Three surface morphologies observed for oxide scales growing on Ni-17.6wt%Cr during *in-situ* ESEM oxidation.



a)



b)

Figure 4.3.6 Development of scale surface morphology for polycrystalline α_2 - Ti_3Al oxidized at 800°C (1500°F) in a) moist air in the ESEM after 1 hr, showing whisker growth; b) after 2 hours showing rutile needles at surface.

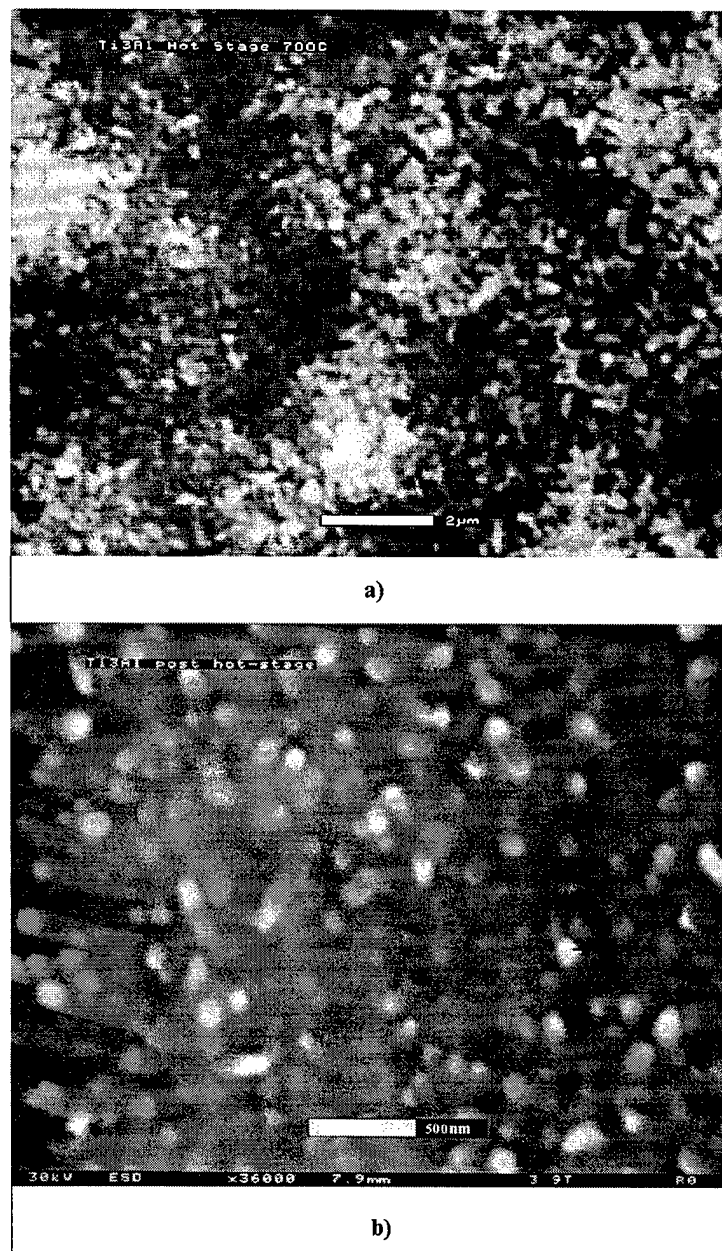


Figure 4.3.7 Development of scale surface morphology for polycrystalline α_2 -Ti₃Al a) oxidized at 700°C (1300°F) in moist air in the ESEM after 2 hours showing rutile needles at surface and b) after *in-situ* exposure to air at 700°C (1300°F) showing early TiO₂ nodule formation.

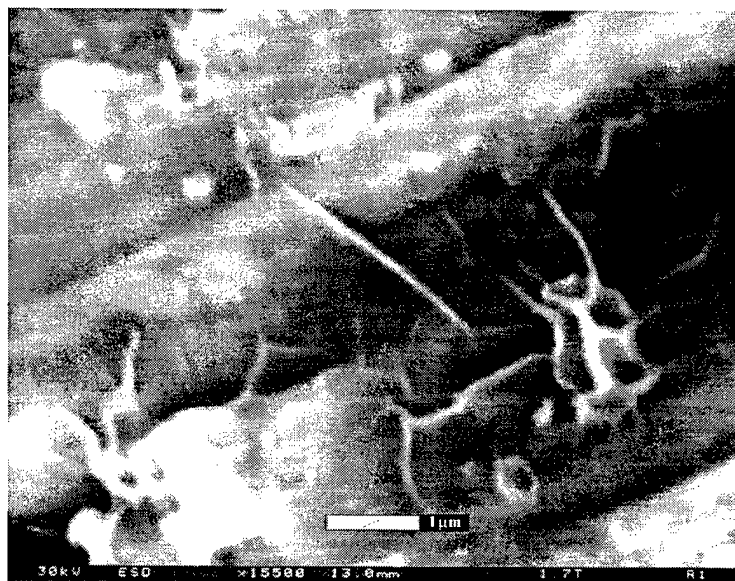


Figure 4.3.8 *In-situ* ESEM micrograph of α_2 -Ti₃Al at 665°C (1230°F) in air .

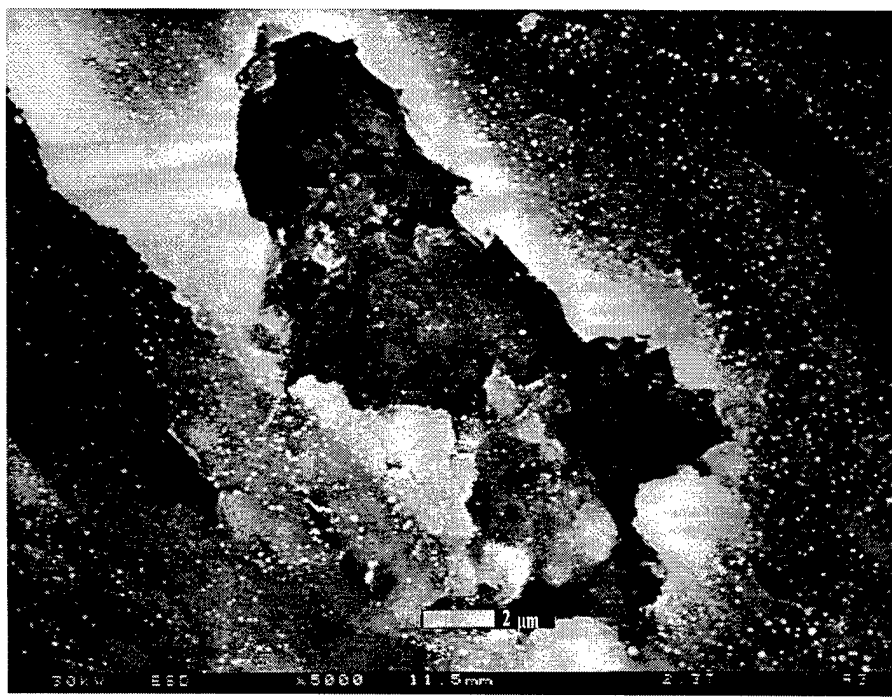


Figure 4.3.9 ESEM micrograph of γ -TiAl after *in-situ* exposure to air at 700°C (1300°F).

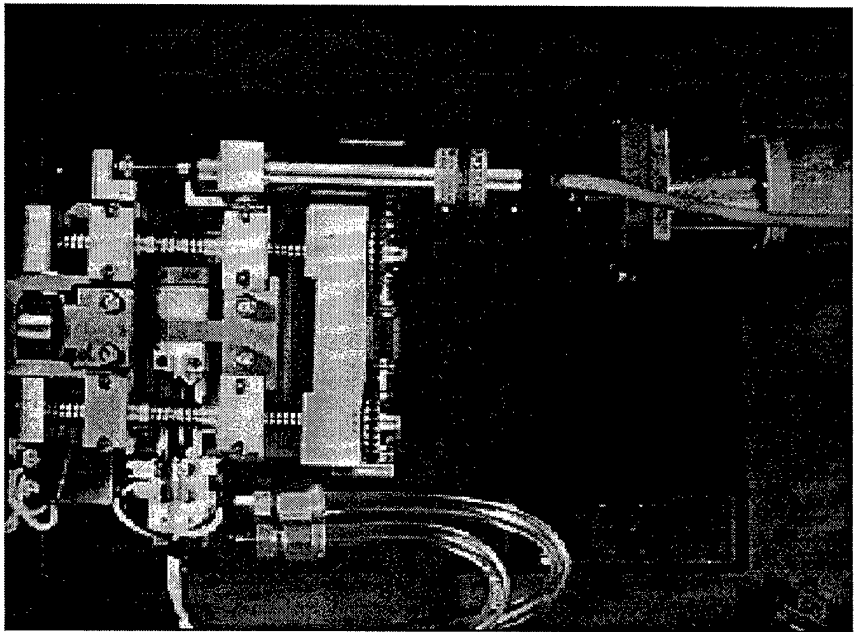


Figure 4.3.10 Heating-straining stage constructed for the ESEM.

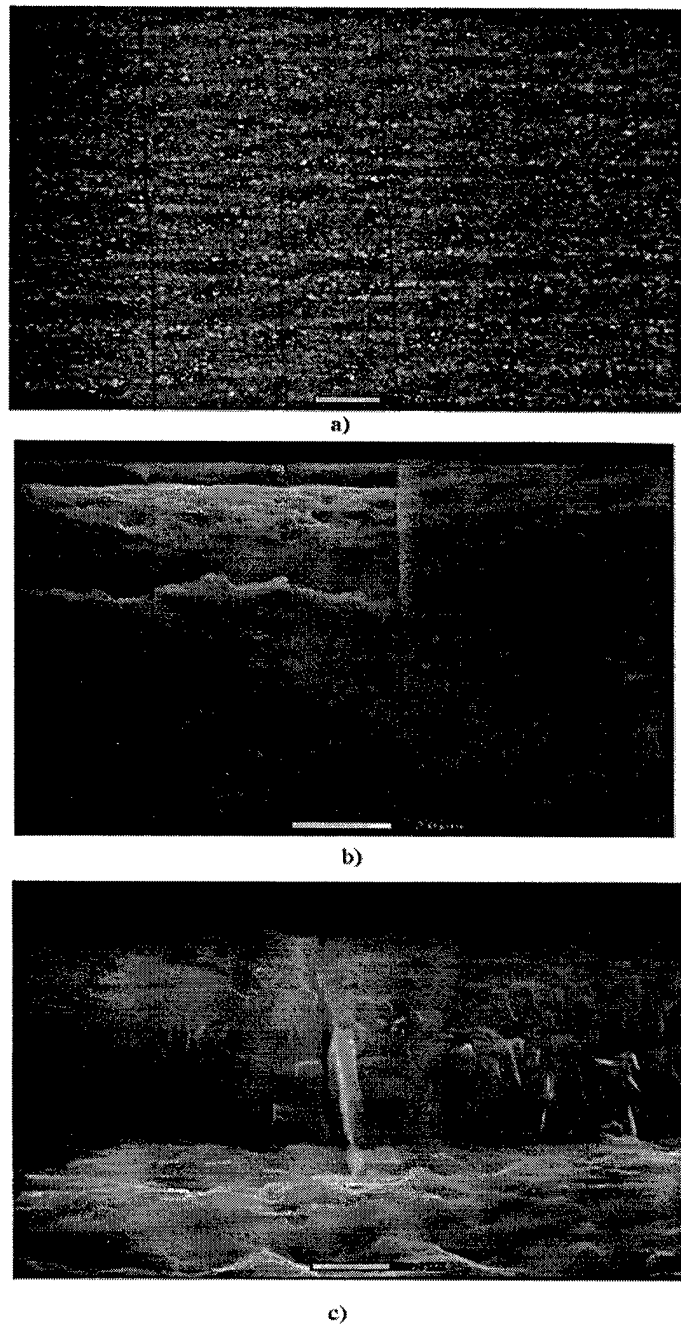
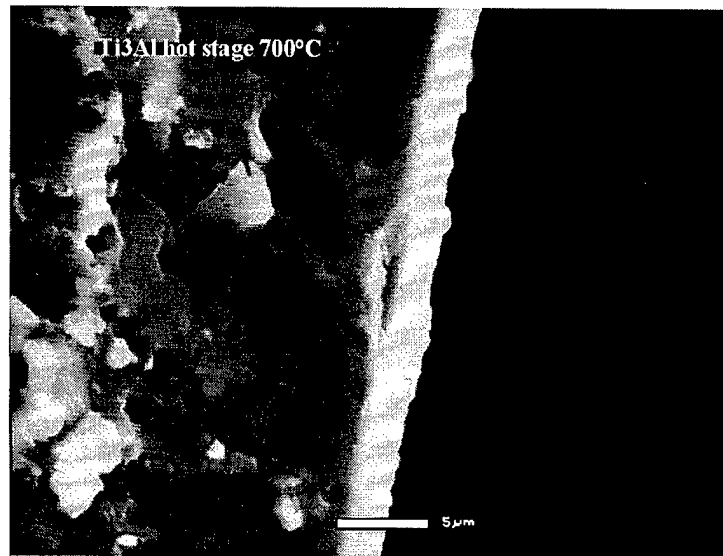
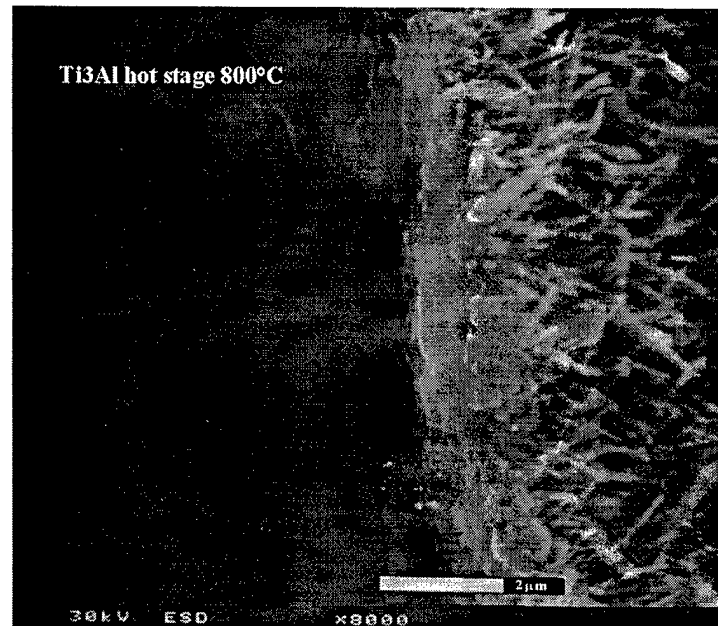


Figure 4.3.11 Cracks developing in oxide scale formed *ex-situ* on MA956 alloy at 2200°F (1200°C) and subjected to tensile strain of the substrate at 1300°F (700°C) in the ESEM:
a) regular cracks appearing on the scale surface normal to the tensile axis, b) region of oxide spallation, showing extension of oxide crack into substrate, c) view into a crack where the oxide had spalled .



a)



b)

Figure 4.3.12 ESEM micrograph of α_2 -Ti₃Al fracture cross sections a) after exposure to air at 700°C (1300°F) for 3 hours and b) after exposure to air at 800°C (1475°F) for 3 hours .

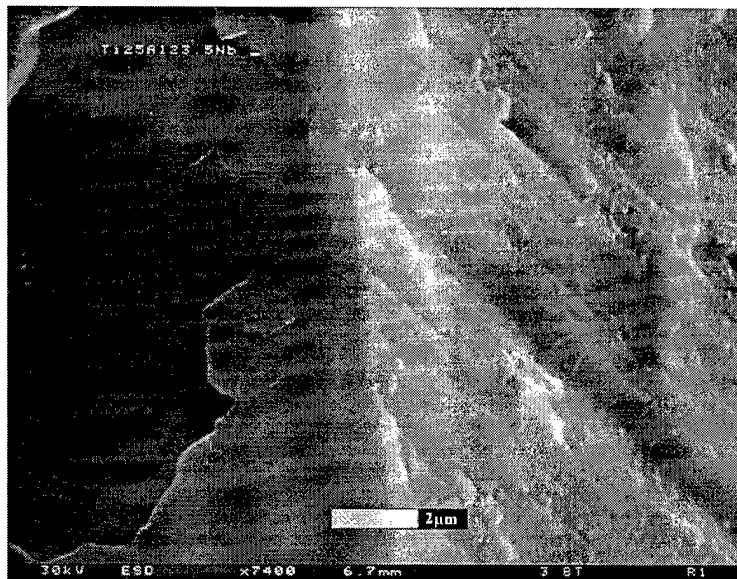


Figure 4.3.13 ESEM micrograph of super- α_2 Ti_2NbAl fracture cross section after exposure to air at 700°C (1300°F) for 3 hours .

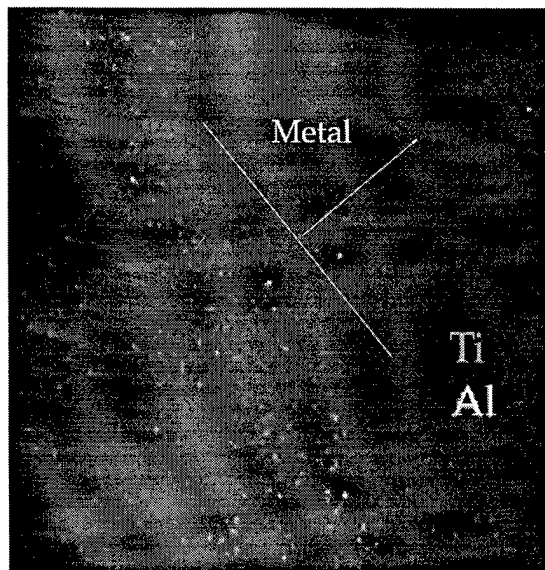
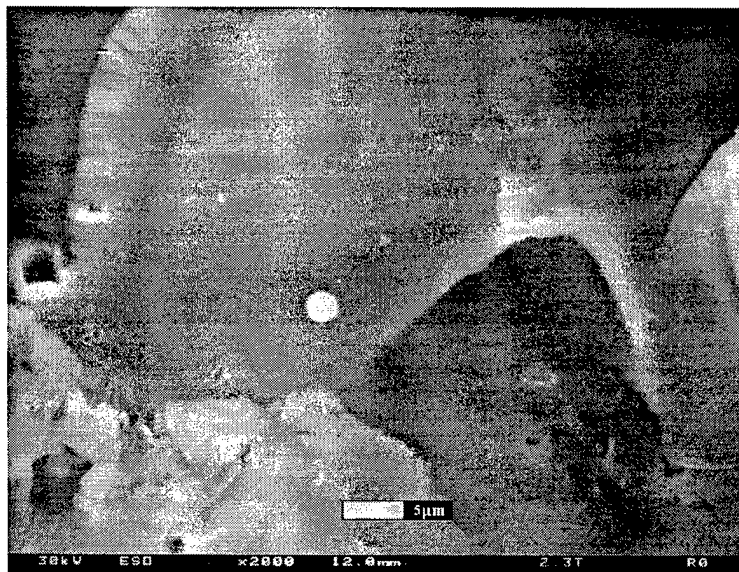


Figure 4.3.14 Digital X-ray map of Al and Ti distribution in α_2 - Ti_3Al after exposure to Ar-20% O_2 at 700°C (1300°F) for 3.5 hours.



a)



b)

Figure 4.3.15 ESEM micrograph of super- a_2 Ti_2NbAl a) after exposure to N_2 -5% O_2 at $700^\circ C$ ($1300^\circ F$) for 100 hours and b) after exposure to Ar -5% O_2 at $700^\circ C$ ($1300^\circ F$) for 100 hours.



(a)



(b)

Figure 4.3.16 ESEM micrograph of super- α_2 Ti₂NbAl after exposure to Ar-20% O₂ at 700°C

(1300°F) for 3.5 hours .

- a) dual-magnification of buckling and cracking with regrowth of oxide under the scale
- b) branching.

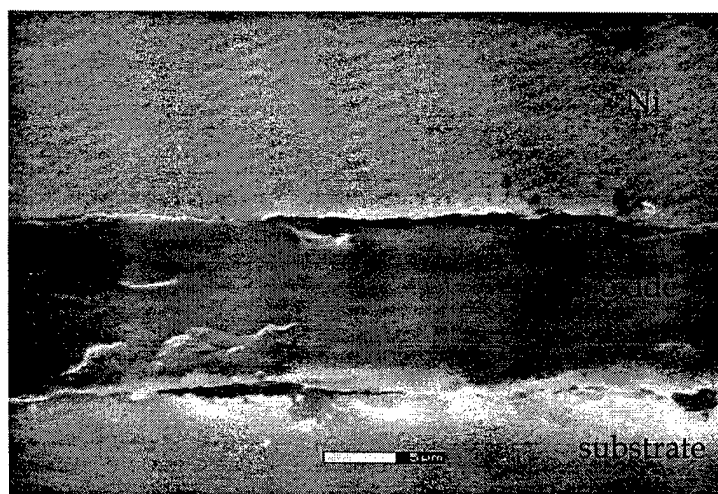


Figure 4.3.17 ESEM micrograph of nickel-plated polished cross-section of γ -TiAl after exposure

to air at 700°C (1300°F) for 3.5 hours .

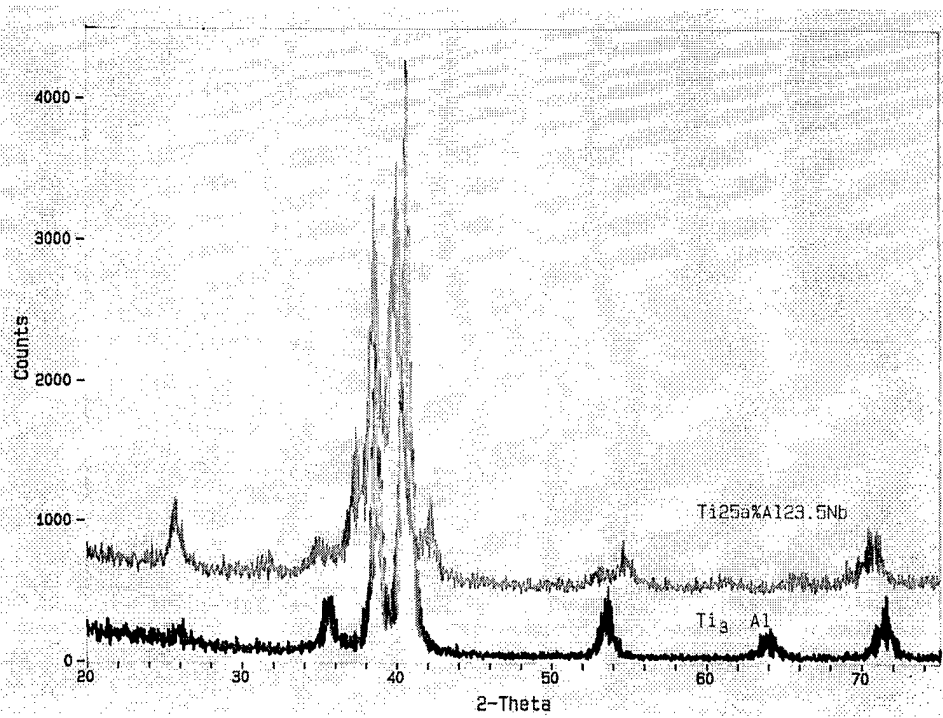


Figure 4.3.18 GAXRD spectra comparing α_2 -Ti₃Al and super- α_2 Ti₂NbAl substrates.

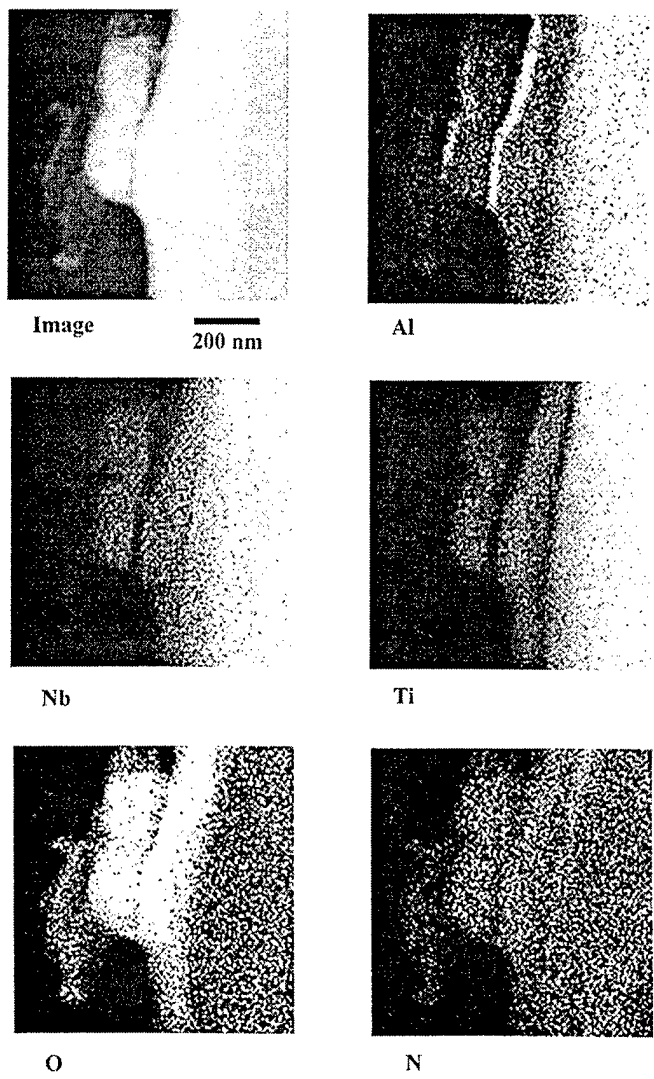


Figure 4.3.19 STEM image and corresponding digital XEDS maps of super- α_2 Ti_2NbAl after exposure to N_2 -5% O_2 at $700^\circ C$ ($1300^\circ F$) for 100 hours.

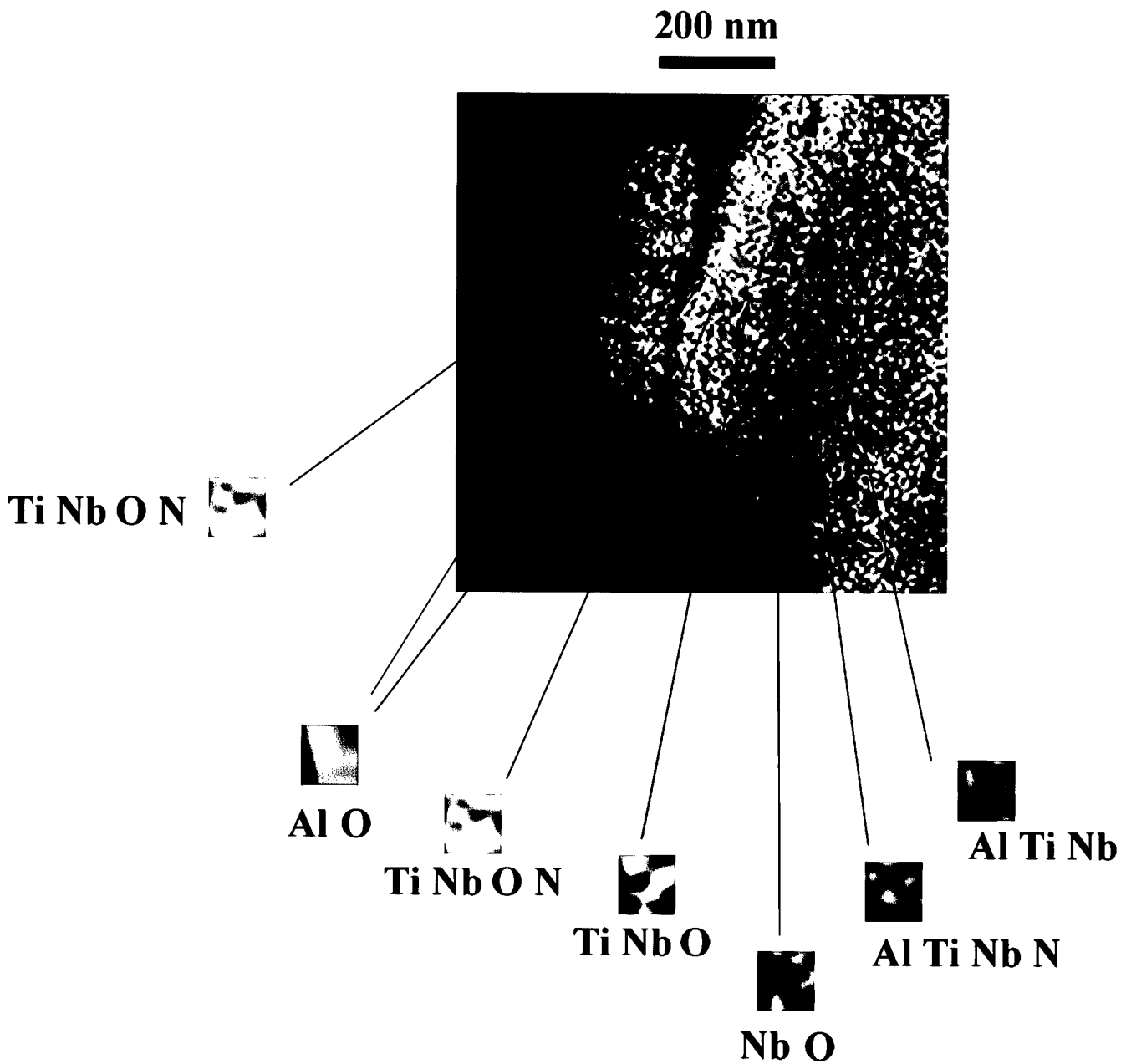


Figure 4.3.20 Synthesized colored XEDS map of super- α_2 Ti_2NbAl after exposure to N_2 -5% O_2 at 700°C (1300°F) for 100 hours.

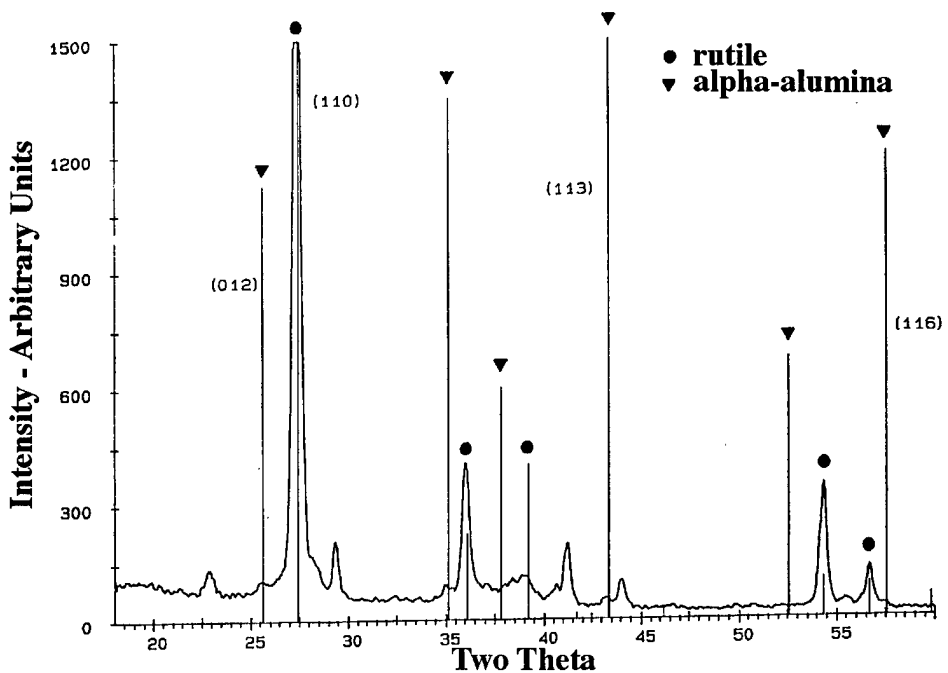


Figure 4.3.21 Glancing-angle (0.9°) X-ray diffraction profile of scale formed on polycrystalline Ti_3Al oxidized 3 hours at $1500^\circ F$ ($800^\circ C$) in Ar-20%oxygen in the X-ray high-temperature camera.

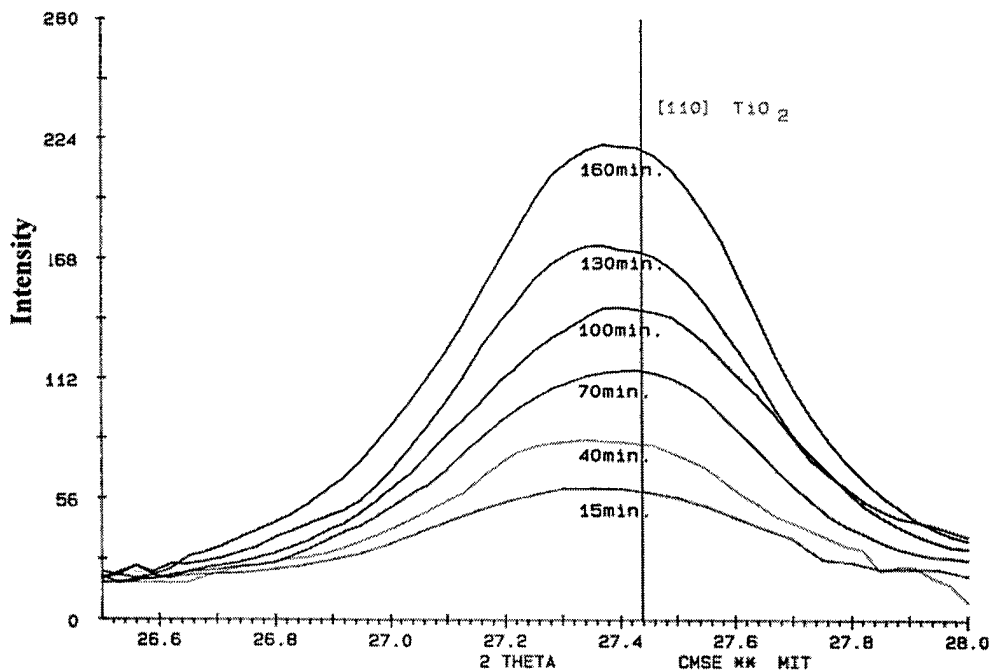
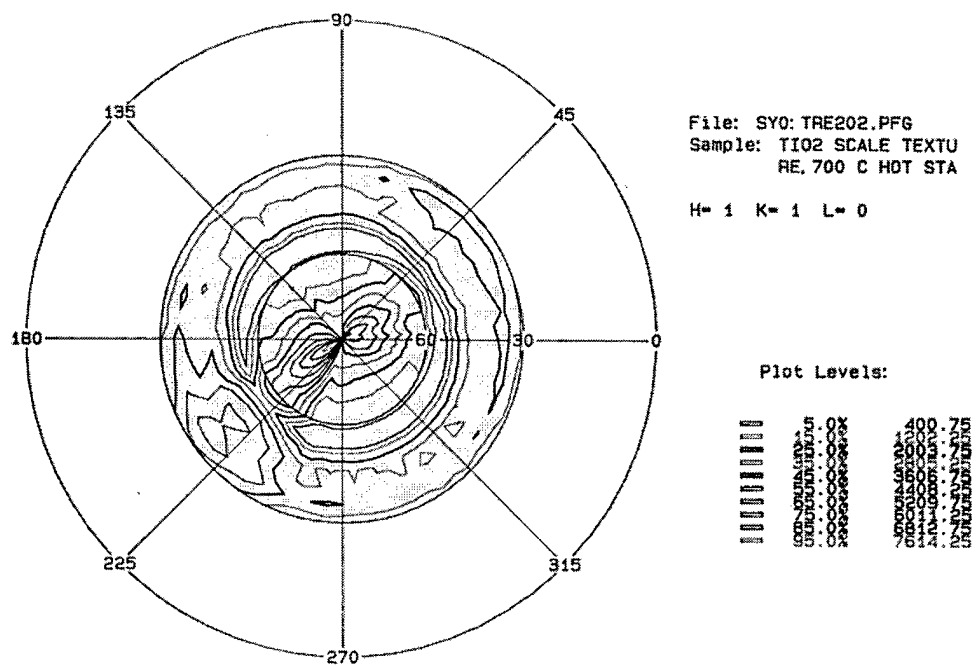


Figure 4.3.22 Evolution of (110) rutile peak with oxidation time for α_2 - Ti_3Al in Ar-20% O_2 at $700^\circ C$ ($1300^\circ F$).



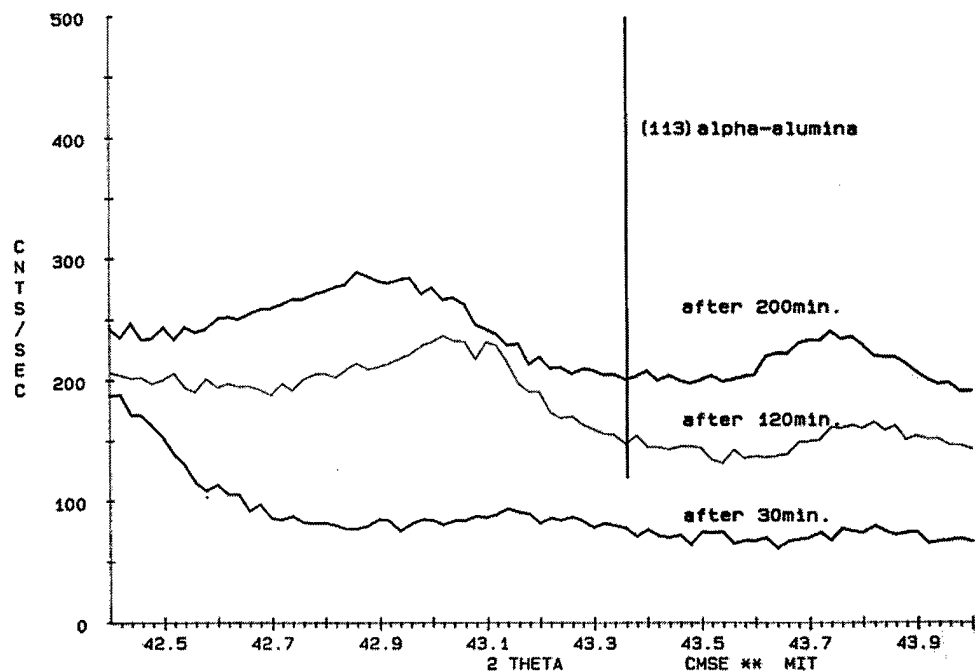


Figure 4.3.25 Evolution of (113) alpha-alumina peak with oxidation time for super- $\alpha_2\text{Ti}_2\text{NbAl}$ in Ar-20% O₂ at 700°C (1300°F).

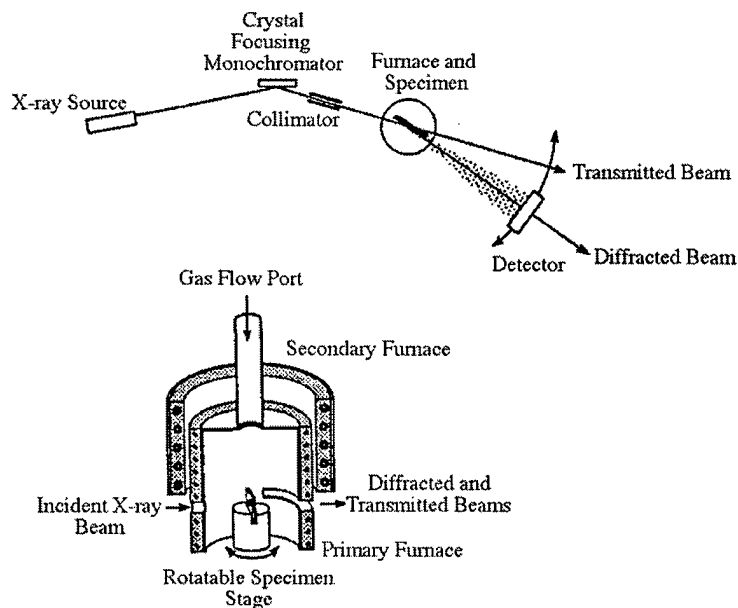
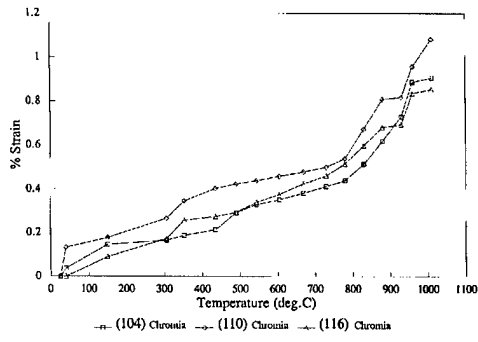
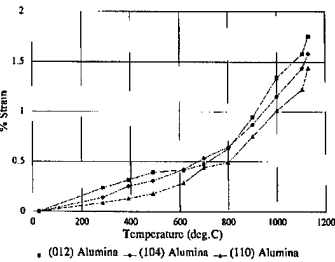


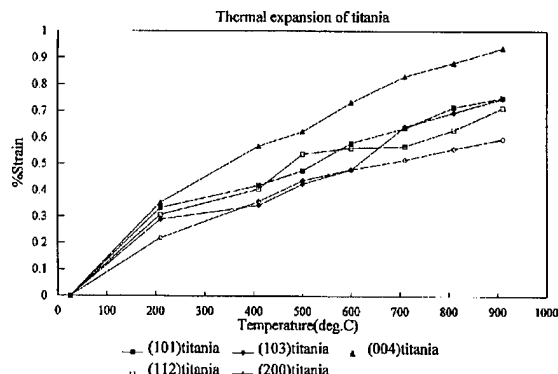
Figure 4.3.26. Reflection geometry and high-temperature camera for *in-situ* determination of oxidation strains by X-ray diffraction.



a)



b)



c)

Figure 4.3.27 Anisotropic thermal expansion measurements for a) chromia, b) α -alumina and c) titania.

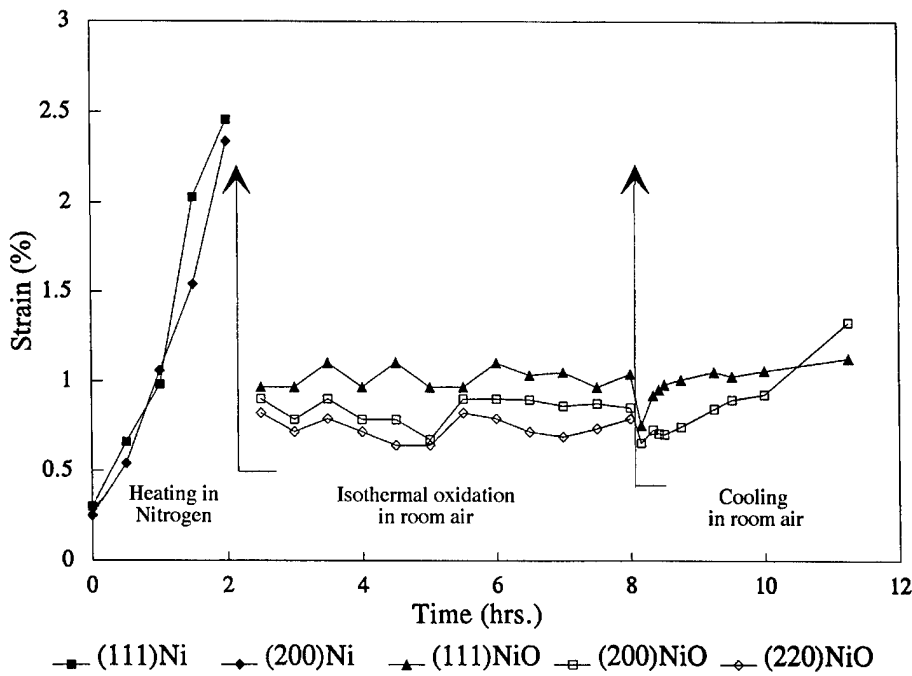


Figure 4.3.28 Evolution of strains in NiO/Ni system during heating, isothermal oxidation at 1830°F (1000°C), and subsequent cooling to room temperature.

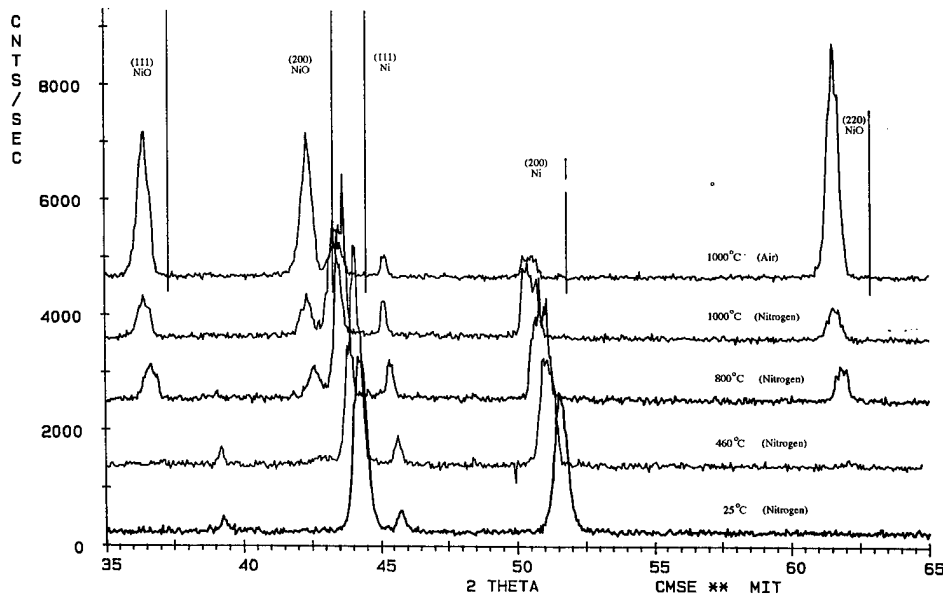


Figure 4.3.29 Evolution of Ni and NiO X-ray peaks as a function of temperature.

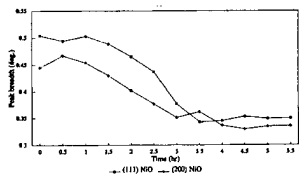


Figure 4.3.30 Evolution of peak breadth for (111) and (200) NiO peaks with oxidation time at 1830°F (1000°C).

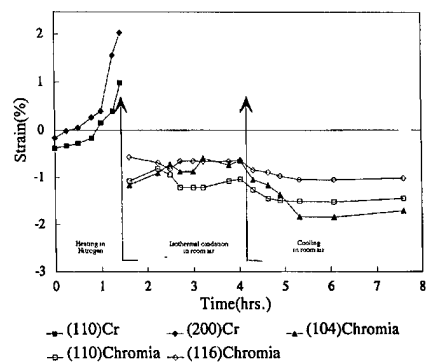


Figure 4.3.31 Evolution of strains in chromia/Cr system during heating, isothermal oxidation at 1725°F (940°C), and cooling to room temperature.

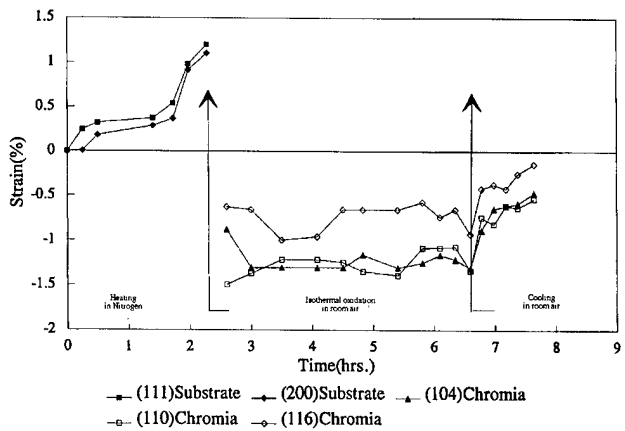


Figure 4.3.32 Evolution of strains on chromia/MA754 during heating, isothermal oxidation at 1725°F (940°C), and cooling to room temperature.

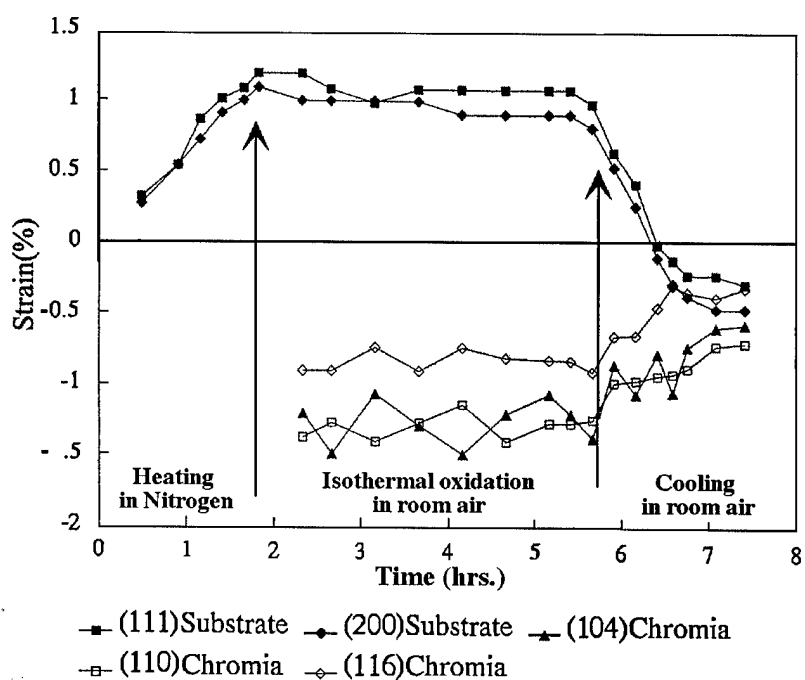


Figure 4.3.33 Evolution of strains in chromia/Ni-17.6wt%Cr system during heating, isothermal oxidation at 1725°F (940°C), and cooling to room temperature.

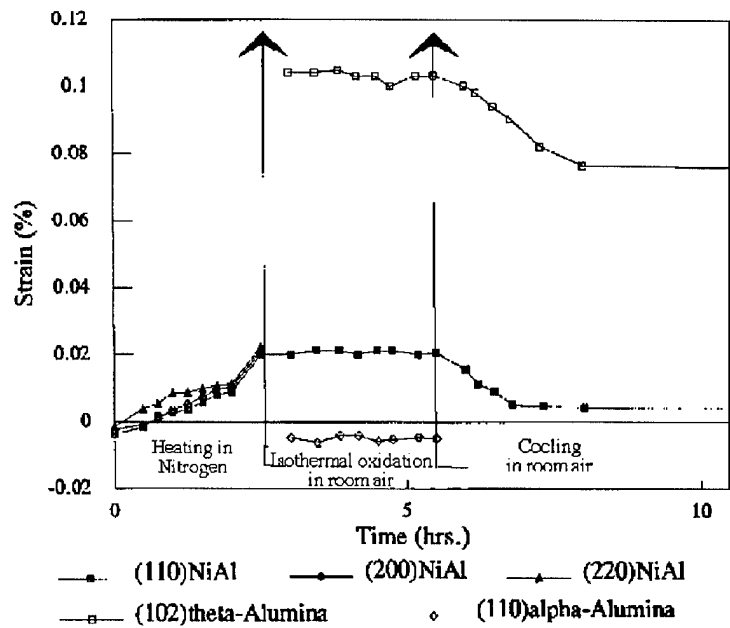


Figure 4.3.34 Evolution of strains on alumina/polycrystalline Ni-30wt%Al system during heating, isothermal oxidation at 2050°F (1125°C), and cooling to room temperature.

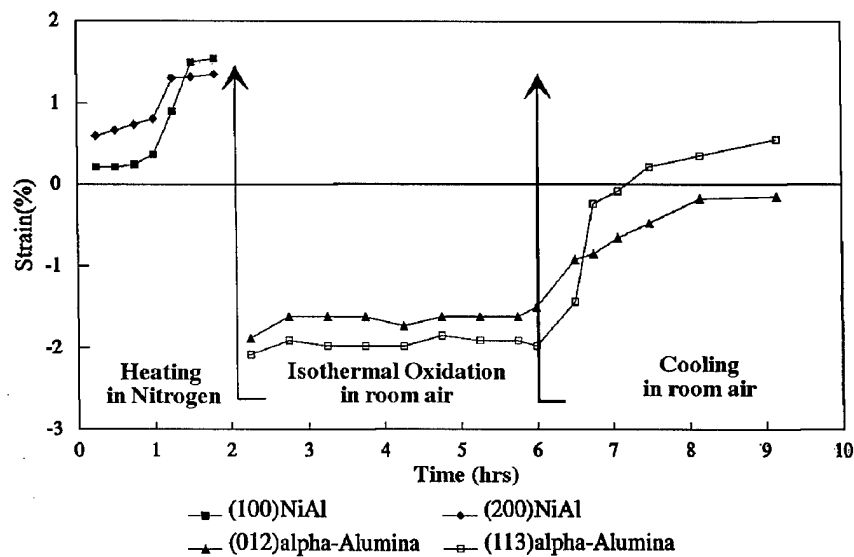


Figure 4.3.35 Evolution of strains on alumina/single-crystal Ni-30wt%Al system during heating and isothermal oxidation at 2050°F (1125°C).

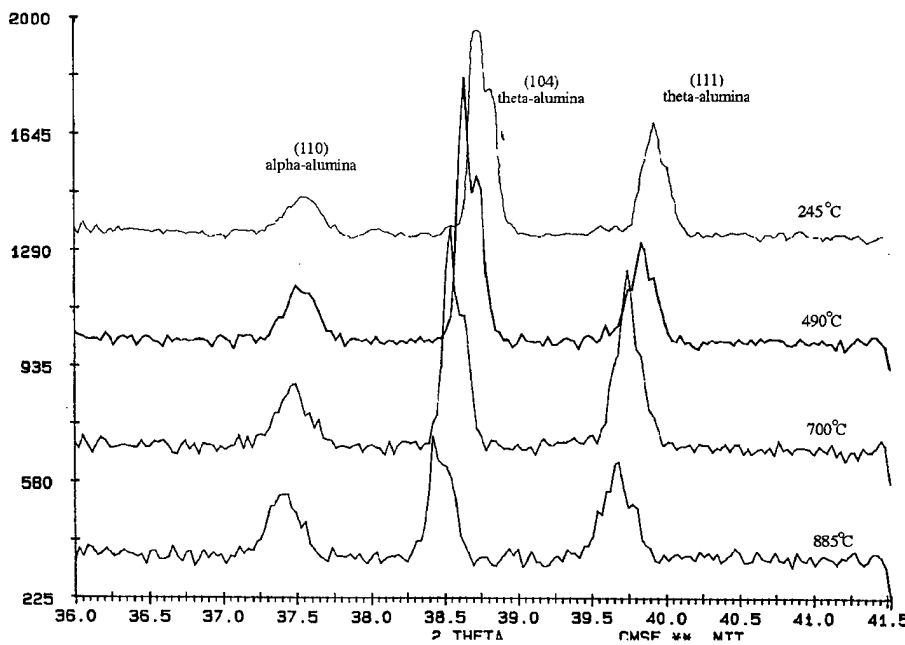


Figure 4.3.36 Evolution of (104) and (110) peaks of α -alumina and the (110) peak of θ -alumina, formed on Ni-30wt%Al at 2050°F (1125°C), during subsequent cooling.

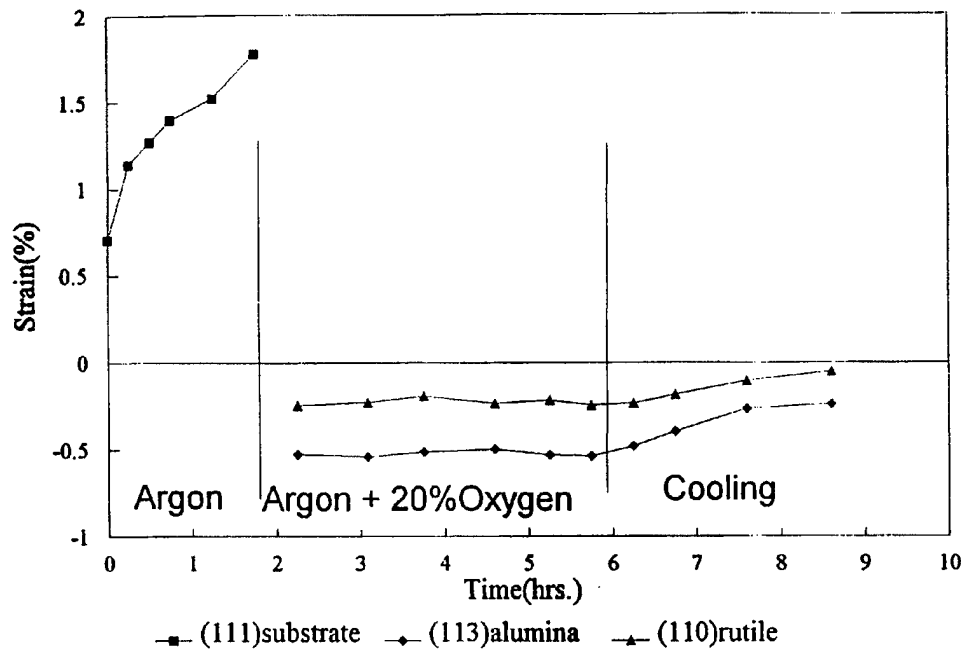


Figure 4.3.37 Strains in polycrystalline γ -TiAl and rutile and alumina scale phases measured by GAXRD normal to the scale/substrate interface during heating to 700°C (1300°F), oxidizing in Ar-20% O₂ and recooling to room temperature. The measured lattice parameters have been corrected for thermal expansion of rutile and alumina.

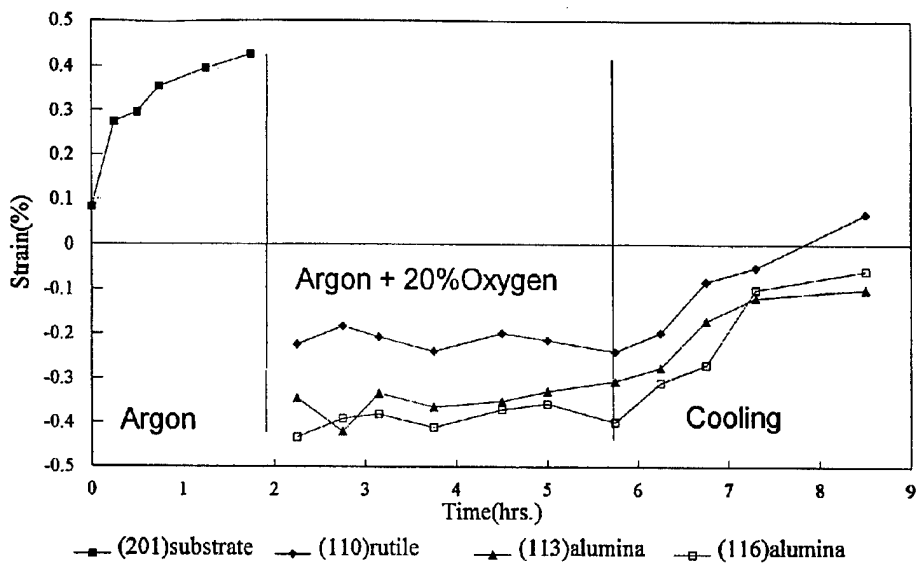


Figure 4.3.38 Strains in polycrystalline super- α_2 Ti_2NbAl and rutile and alumina scale phases measured by GAXRD normal to the scale/substrate interface during heating to 700°C (1300°F), oxidizing in Ar-20% O₂ and recooling to room temperature. The measured lattice parameters have been corrected for thermal expansion of rutile and alumina.

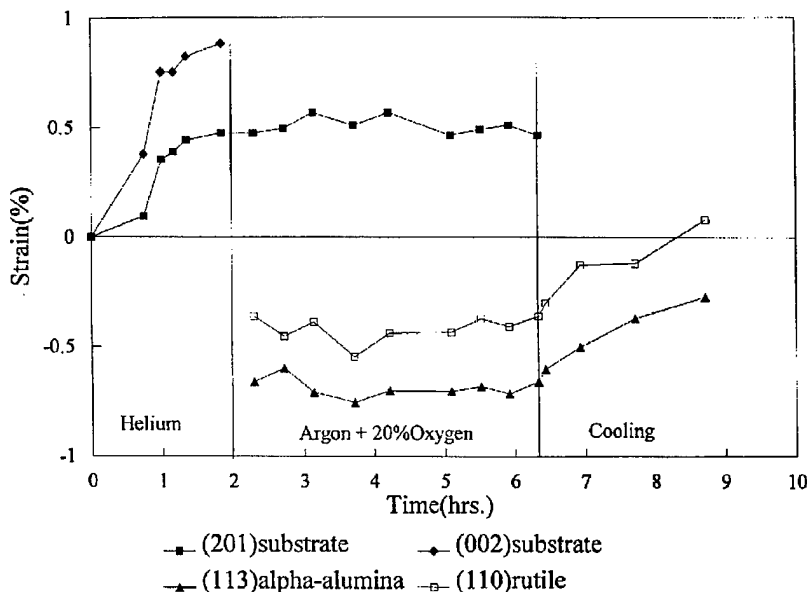


Figure 4.3.39 Strains in polycrystalline α_2 - Ti_3Al and rutile and alumina scale phases measured by GAXRD normal to the scale/substrate interface during heating to 700°C (1300°F), oxidizing in Ar-20% O₂ and recooling to room temperature. The measured lattice parameters have been corrected for thermal expansion of rutile and alumina.

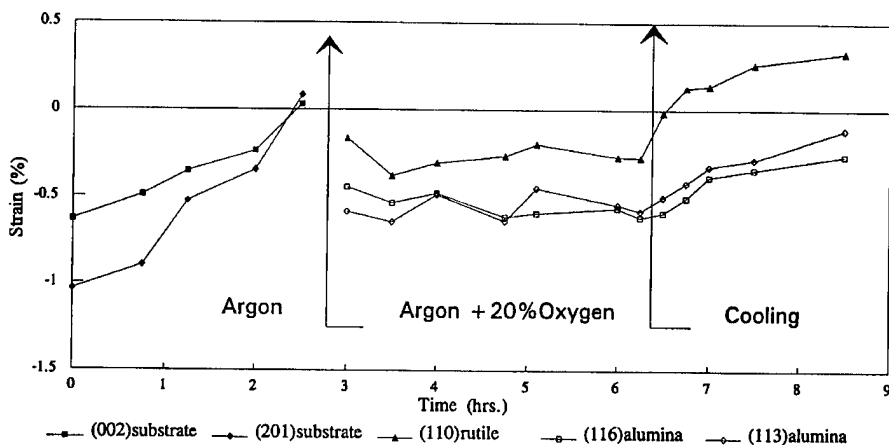


Figure 4.3.40 Strains in polycrystalline Ti_3Al and titania and alumina scale phases measured by GAXRD normal to the scale/substrate interface during heating to 1500°F (800°C), oxidizing in Ar-20% O₂ and recooling to room temperature. The measured lattice parameters have been corrected for thermal expansion of titania and alumina.

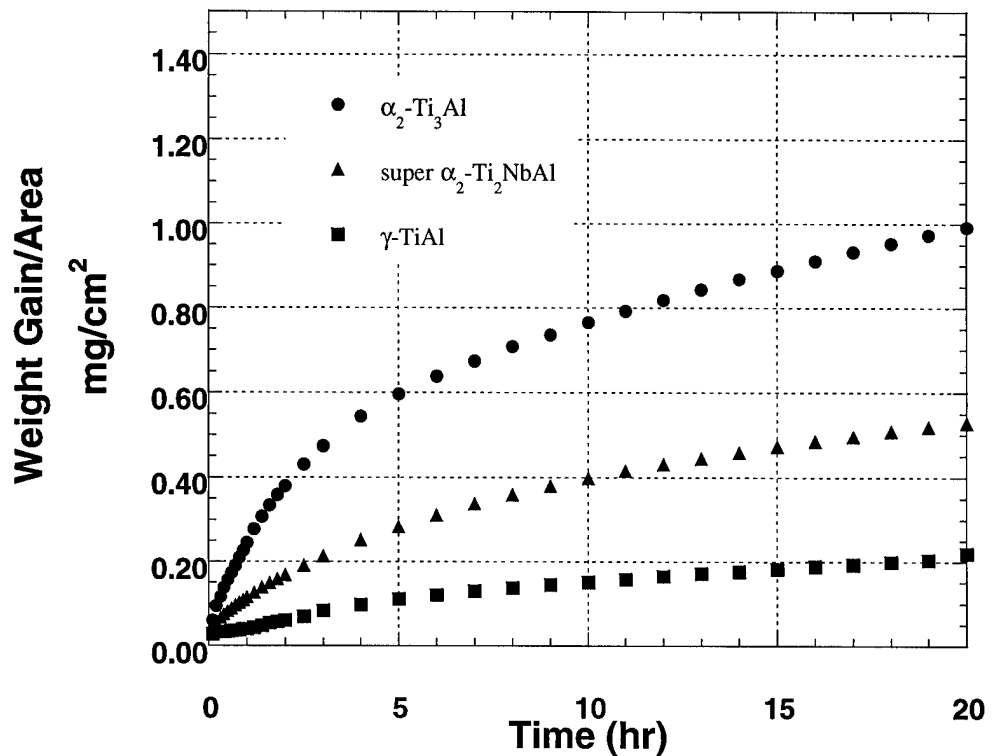


Figure 4.3.41 Thermogravimetric oxidation kinetics for titanium aluminides at 800°C (1300°F) for 20 hours in Ar-20% O₂.

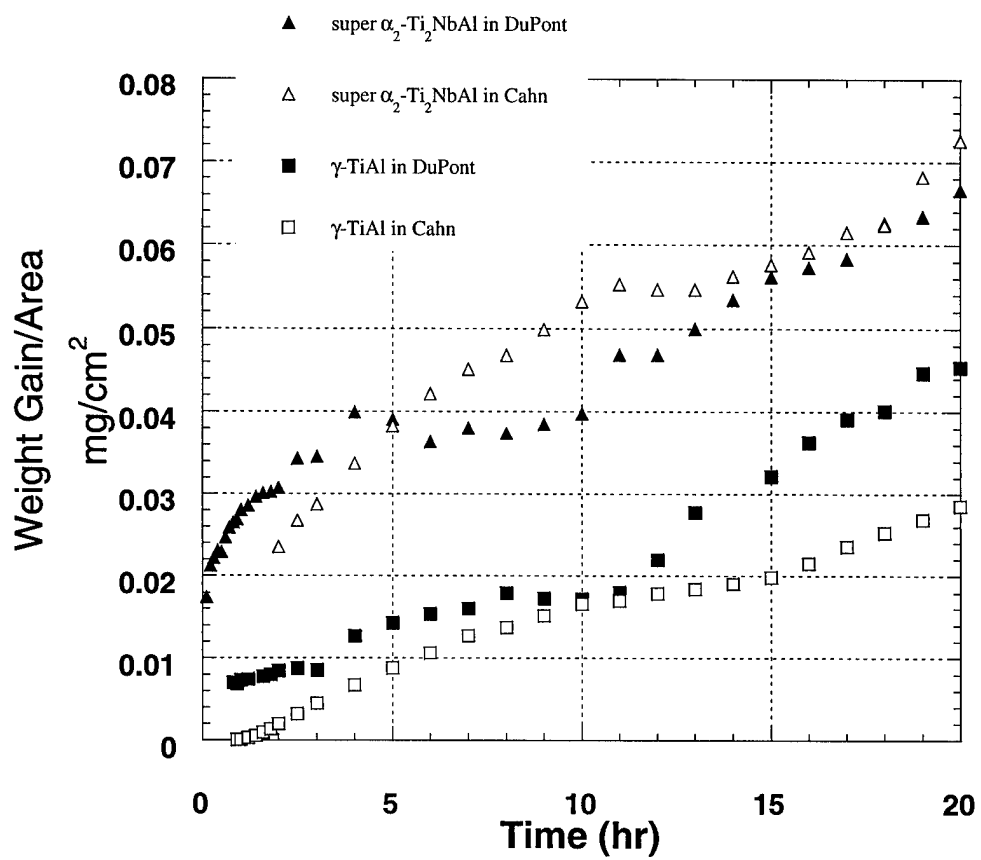


Figure 4.3.42 Thermogravimetric oxidation kinetics for titanium aluminides in dry air at 700°C (1300°F) comparing the measurements on the Cahn and DuPont 990 microbalances.

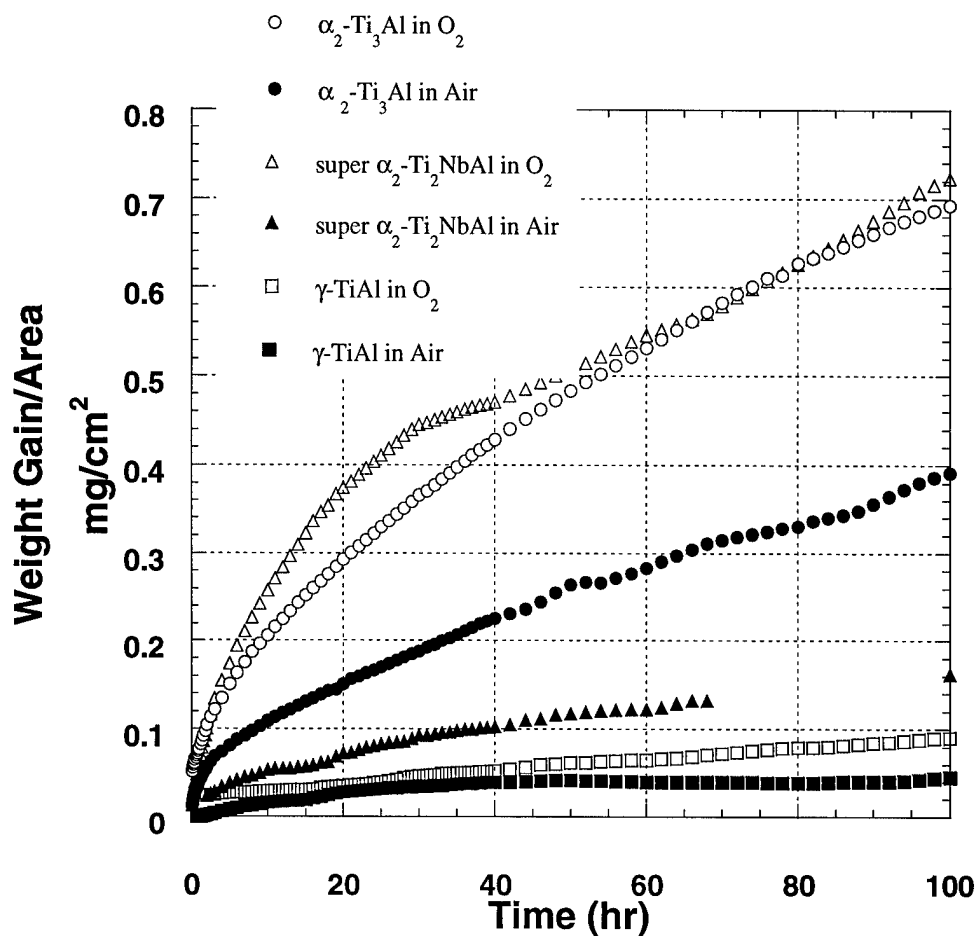


Figure 4.3.43 Thermogravimetic oxidation kinetics for titanium aluminides at 700°C (1300°F) for 20 hours comparing dry air and pure oxygen.

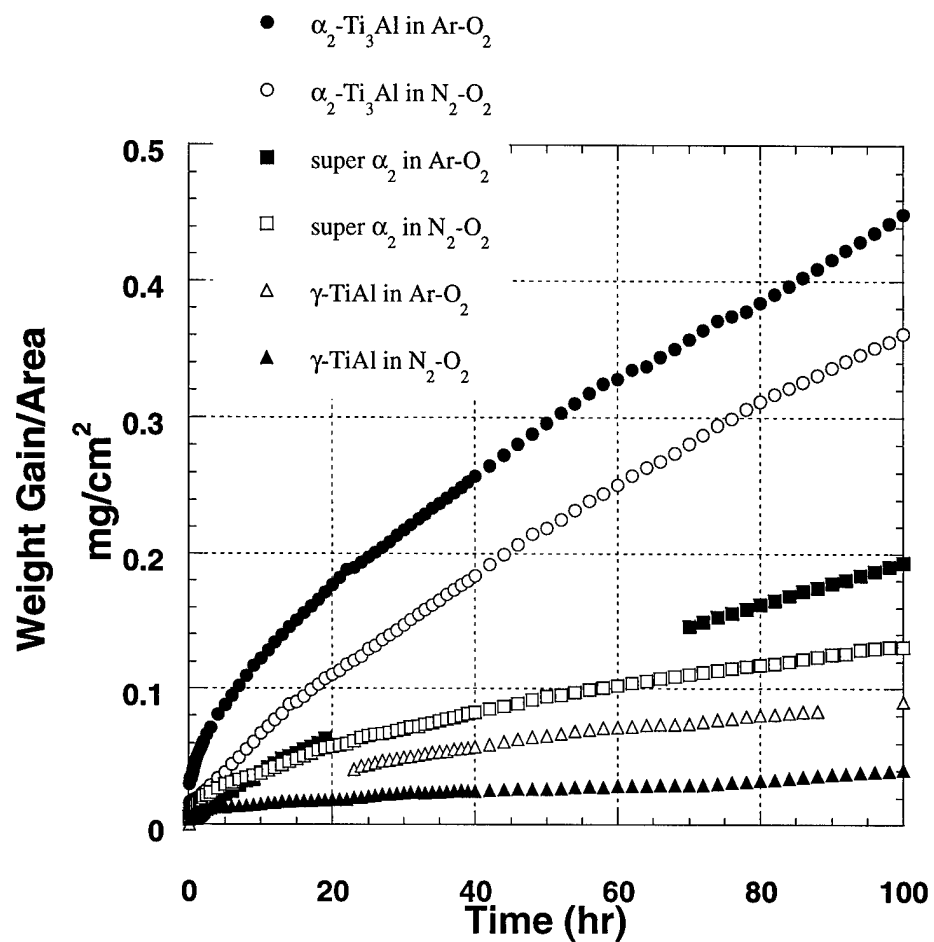


Figure 4.3.44 Thermogravimetic oxidation kinetics for titanium aluminides at 700°C (1300°F) for 100 hours comparing N₂-5% O₂ and Ar-5% O₂.

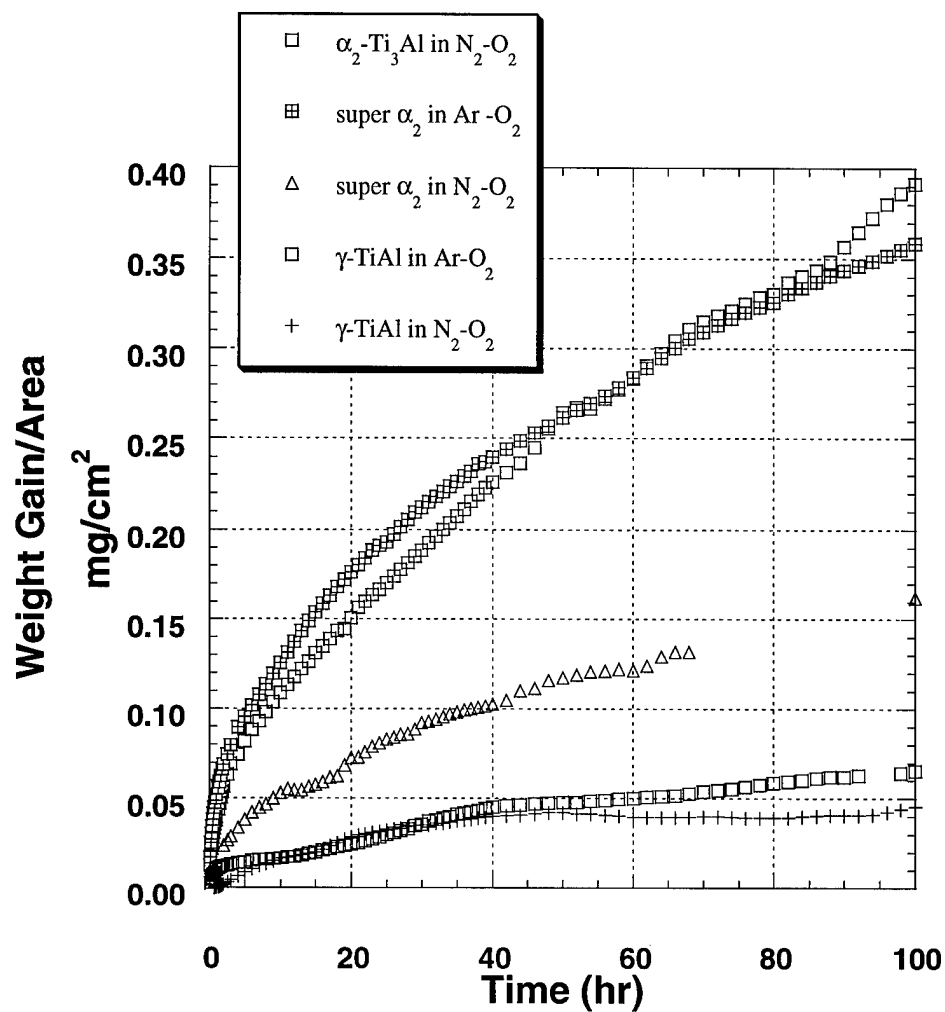


Figure 4.3.45 Thermogravimetic oxidation kinetics for titanium aluminides at 700°C (1300°F) for 100 hours comparing $\text{N}_2\text{-20% O}_2$ (air) and Ar-20% O_2 .

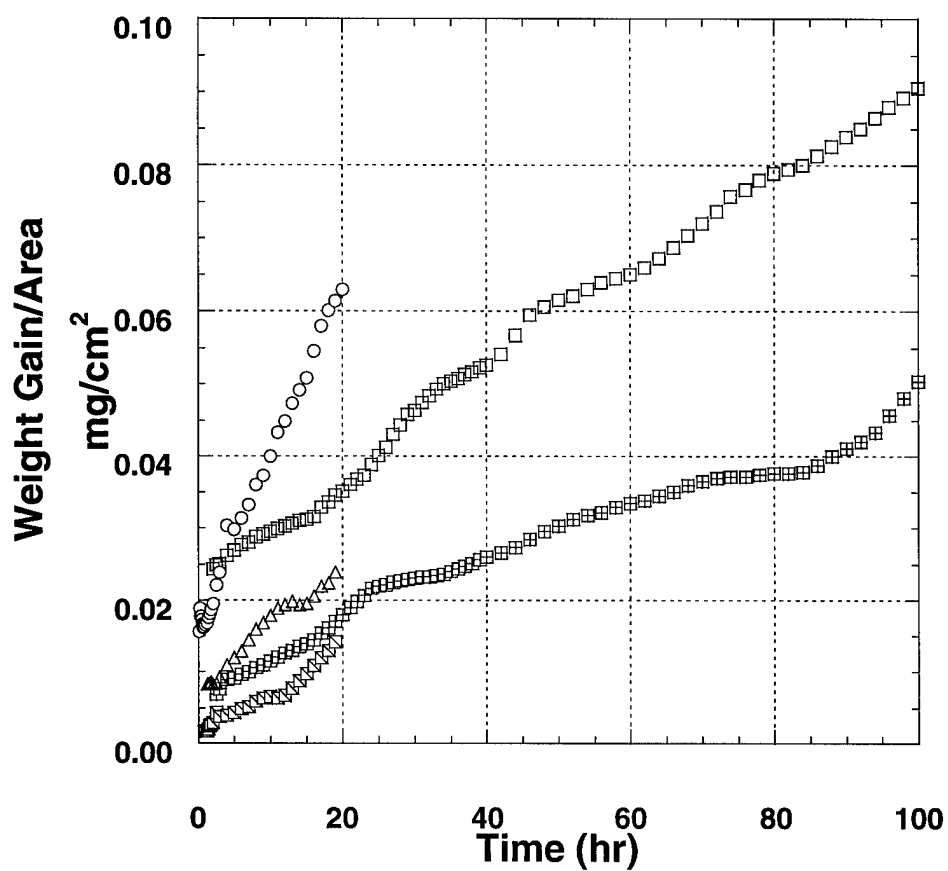


Figure 4.3.46 Thermogravimetic oxidation kinetics for γ -TiAl at 700°C (1300°F) in pure oxygen.

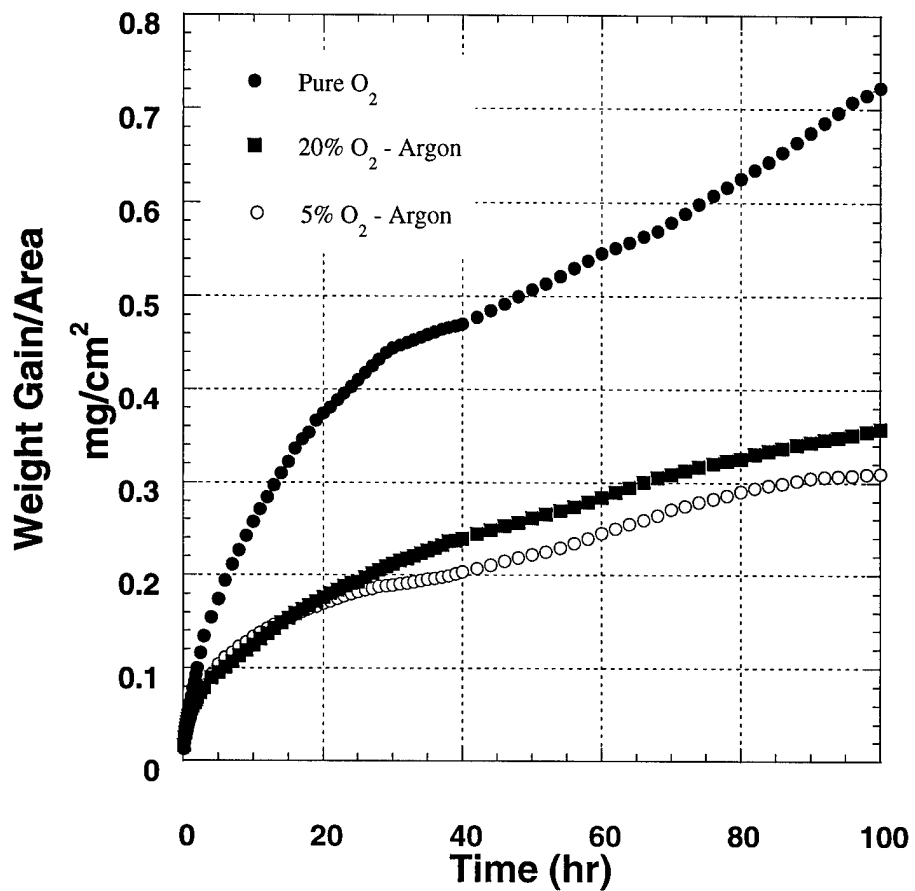


Figure 4.3.47 Thermogravimetic oxidation kinetics for super- α_2 Ti₂NbAl at 700°C (1300°F) for 100 hours showing effect of oxygen content in O₂-Ar mixtures.

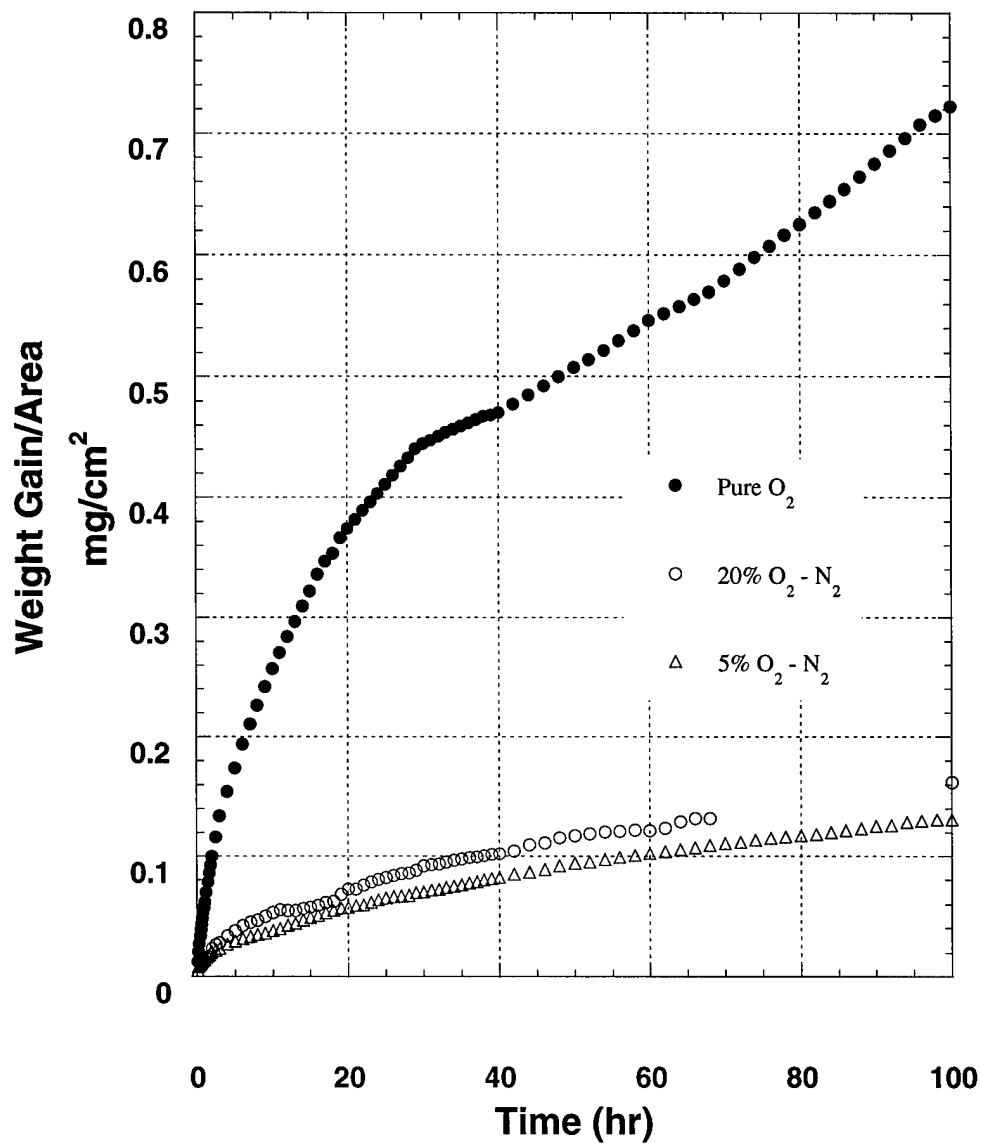


Figure 4.3.48 Thermogravimetic oxidation kinetics for super- $\alpha_2\text{Ti}_2\text{NbAl}$ at 700°C (1300°F) for 100 hours showing effect of oxygen content in $\text{O}_2\text{-N}_2$ mixtures.

4.4 Predictive Model Development

In this project we have identified the importance of the pitting process in the initiation of environmental degradation of aluminum alloys. Both corrosion fatigue and stress corrosion cracks initiate from pits. The role of inclusions as local sites for pit initiation have also been identified and reported on. In this section we develop predictive models for the transition from pit to crack. The modeling work used alloy 2091-T351 as a model material

4.4.1 Task Element Accomplishments

Accelerated corrosion fatigue tests were carried out by polarizing 2091-T351 aluminum-lithium alloy 30 mV above its pitting potential. Because the alloy does not suffer from intergranular corrosion, the simulation reproduced accurately the relative amount of fatigue and corrosion which are experienced by aging aircraft in service conditions.

Three regimes of fatigue crack initiation have been identified depending upon the depth of the pits which initiated a fatigue cracks. Small pits initiated crystallographic fatigue cracks, whereas large pit formation involved general corrosion at the surface. Between these two extremes, fatigue and corrosion had a synergistic effect which lead to the formation of semi-elliptical flaw which propagate by a mixed mode of fatigue and corrosion. In this regime, a transition zone between pitting and fatigue was observed and interpreted as the fractographic signature of competition between pitting and fatigue.

A Fracture Mechanics approach was used to model the semi-elliptical flaw. The use of L.E.F.M. was justified by the presence of the transition zone which acted as a pre-crack. Furthermore, the pit size was in the range of 150 to 600 μm , which minimizes the short crack problem. The short crack issue was treated by considering fatigue propagation below the fatigue threshold for non-propagating long cracks. Pitting rates were derived from independent corrosion experiments carried out in the same environment. A power law of exponent 2/3 was a good approximation for the analytical function representing pit depth as a function of time.

Fatigue cracks initiated from multiple pits, interact and coalesce to form a through thickness crack. The model attempted to connect the scatter in the number of fatigue initiation sites to the

scatter in pit depth that is observed on fracture surfaces. The agreement was quite good for pits whose depths ranged from 150 to 600 μm . Fatigue life were also well derived for the same regime of fatigue initiation. When general corrosion took place, competition between pitting and fatigue is better described by a unidimensionnal model. When pits are small, the transition from pitting to fatigue takes place rapidly when compared to other damage processes such as corrosion. A estimate can be derived by integrating the $\text{da}/\text{dN}-\Delta K$ curve from an initial crack size equal to the pit depth at the onset of surface fatigue to complete failure of the specimen.

4.4.2 Results & Discussion: Model of Corrosion Fatigue Life Prediction Applied to 2091-T351 Aluminum-Lithium Alloy in a Pitting Environment.

4.4.2.1 Introduction

The current model is based on experiments carried out on aluminum-lithium 2091-T351 in a sodium chloride environment. Details of the experimental set-up and results were discussed in the second annual report. This introduction will simply recall the experimental facts on which this model is based.

In 1M NaCl, at a potential of -660 mV(SCE) and at room temperature, 2091-T351 suffers from pitting corrosion. In this environment, corrosion fatigue cracks initiate from pits. Depending upon the values of test frequency and stress range, three regimes of fatigue crack initiation have been identified.

The first regime is characterized by small pits of the order of 10 to 60 μm from which crystallographic cracks, or stage I fatigue, initiate.

The second regime is characterized by pits of the order of 100 to 600 μm . Semi-elliptical flaws initiate from these pits and propagate by a mixed mode of fatigue and corrosion. Fatigue takes place at the surface of the flaw, where the stress intensity factor range is the highest and the corrosion rate the lowest. Dissolution takes place at the tip of the flaw where the stress intensity factor range is the lowest and the corrosion rates the highest. Between these two extremes, a transition zone is observed. This zone is characterized by a flat and slightly corroded surface

which is perpendicular to the stress axis. Its features are different from standard corrosion fatigue, but both are transgranular cracking processes. The transition zone has been explained by competition between pitting and fatigue as suggested by Kondo [1]. In the second regime, pitting takes place at different locations and flaws initiate which interact and coalesce with each other to form a through thickness crack. The fatigue initiation life can be characterized as a microscopic multi site damage process.

The third regime is characterized by pits of the order of 800 to 1200 μm deep. The metal surface at the rivet bore suffers from general corrosion. The crack front propagates parallel to the rivet bore axis. No semi-elliptical flaw is visible.

The mechanistic model, developed in this section, applies to the second regime of fatigue crack initiation. Some extensions will be suggested for the two other regimes and in particular a lower and an upper bound will be derived for fatigue lives and pit depths. Finally, a mapping of the three regimes of fatigue initiation will be explained in terms of the competition approach at the very early stage of corrosion fatigue.

4.4.2.2 Propagation, Interaction and Coalescence of Semi-Elliptical Flaws.

Figure 4.4.1 illustrates the geometry of the semi-elliptical flaw as it is seen on fractographs and as it is defined in the current model. The parameters defined in Figure 4.4.1 are used in the calculation of the stress intensity factor range of the Newman-Raju's formula [2]

$$K = S_t \left(\frac{\pi a}{Q} \right)^{1/2} F_{sh} \left(\frac{a}{c}, \frac{a}{t}, \frac{r}{t}, \frac{r}{b}, \frac{c}{b}, \phi \right) \quad (4.4.1)$$

Where Q is the shape factor which is equal to $Q = 1 + 1.464 * \left(\frac{a}{c} \right)^{1.65}$ for aspect ratios (a/c) less than 1. S_t is the remote applied stress.

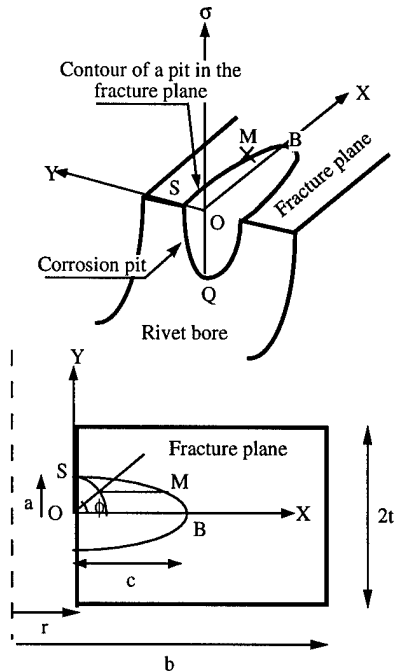
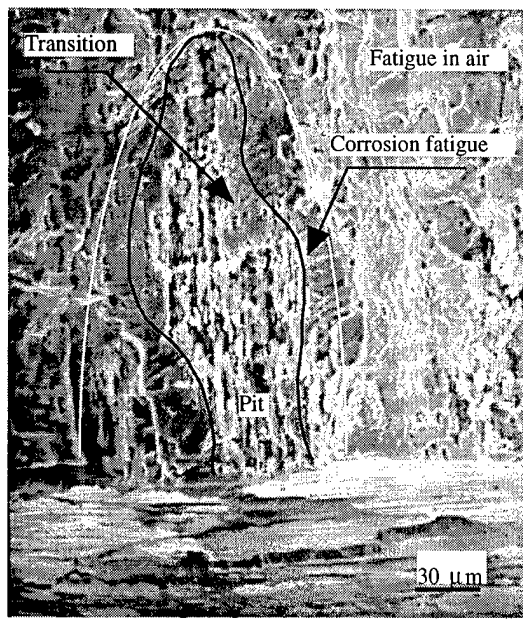


Figure 4.4.1: Corrosion fatigue flaw in regime II of fatigue crack initiation.

The corrosion fatigue flaw is assumed to remain semi-elliptical throughout the component life, which simplifies the model by allowing the application of the algorithm for flaw propagation at the ellipse apexes only. The surface of the flaw is designated as point S in Figure 4.4.1 which is the intercept between the flaw and the inner walls of the rivet hole. The tip of the flaw is identified as point B in Figure 4.4.1 and is the deepest point on the front of the flaw.

Figure 4.4.2 illustrates the algorithm for flaw propagation. At each cycle, flaw increments are calculated by comparing pitting rates and corrosion fatigue rates at both apexes. The resulting increments are added to the current flaw radius (a) and depth (c) to yield the new flaw dimensions, which are used in the new iteration. If the stress intensity factor range is less than a threshold, which will be estimated later, the flaw increment is determined by pitting only.

As is illustrated in Figure 4.4.3a, a fatigue crack has initiated from a corrosion pit. A shallow corrosion pit, 12 μm in depth and 6 μm in diameter, is visible at the surface. A semi-circular fatigue crack is centered on the pit which is clearly the cause of initiation. The tip of the pit is in contact with the apex of the crack, which leads to the conclusion that pitting was still active at the tip of the crack when the test was stopped. By calculating an equivalent stress intensity factor range for the crack of Figure 4.4.3a, the graph of Figure 4.4.3b was derived. Based on this analysis an estimate of the fatigue threshold is between 0.6 and 1.2 $\text{MPa}\sqrt{\text{m}}$. A value of

$1\text{MPa}/\text{m}$ was chosen for convenience but has very little effect on simulated pit depth and fatigue life.

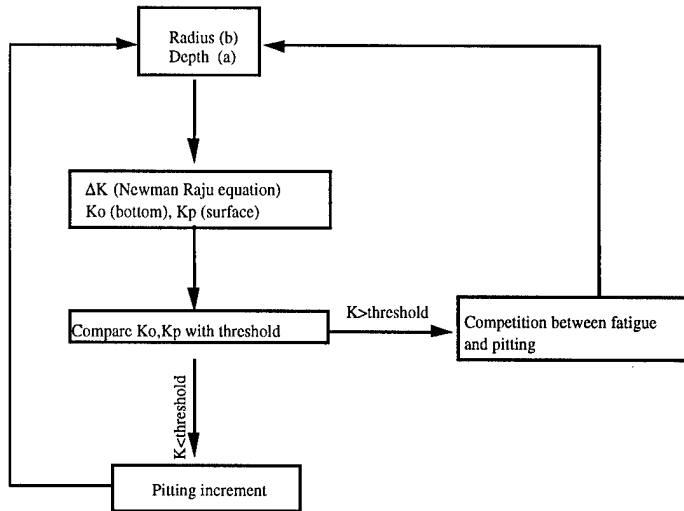
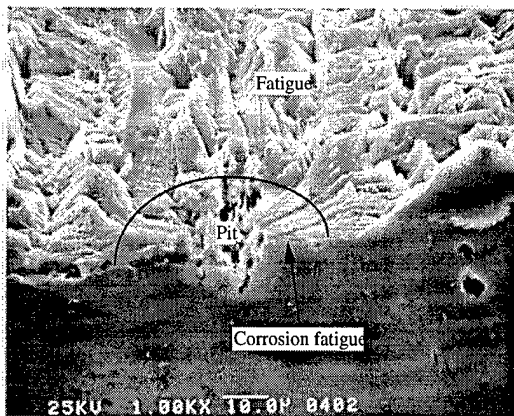


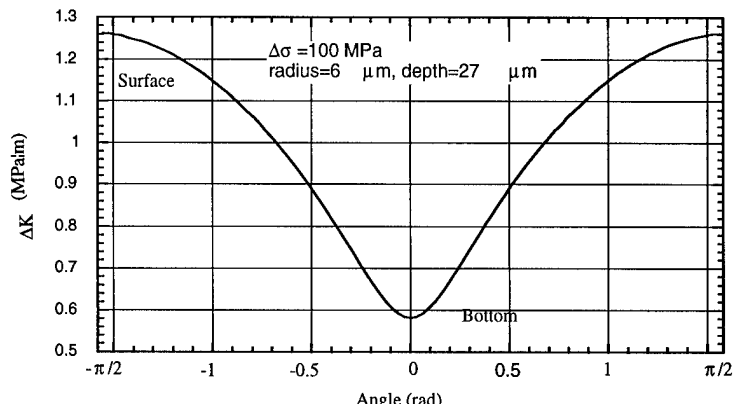
Figure 4.4.2: Model for the propagating of a semi-elliptical flaw. At each cycle, the local flaw increment is determined by the largest of the corrosion and corrosion fatigue increments. Corrosion fatigue becomes active beyond a fatigue threshold.

Corrosion fatigue rates were derived from the calculation of a local stress intensity factor, which is used with the experimental $da/dN-\Delta K$ data to yield the final fatigue increment. The local stress-intensity factor range is computed with Newman-Raju's formula [2]. The surface stress intensity factor range is multiplied by a factor of 0.9, based either on experimental observations [3] or to account for crack closure at the surface [4].

Pitting rates are derived from the experimental maximum pit depth data. Since the algorithm is based upon a series of iterations (one per fatigue cycle), the pitting depth, which is expressed currently as a function of time, must be converted into a function of the number of cycles, N , and test frequency, f . Furthermore, the resulting function must be differentiated in order to get an estimate of the equivalent pitting rate per cycle. The results are:



(a)



(b)

Figure 4.4.3: Test aborted in the early stages of pitting. $\Delta\sigma=100$ MPa, $f=1$ Hz. A crack has initiated from a corrosion pit. (a) Crack emanating from a pit. (b) Stress intensity factor as a function of angle.

For times less than 24,400 seconds, at the tip of the pit:

$$dc = \frac{2}{3} \cdot 0.74 \cdot \left[\frac{N}{f} \right]^{-1/3} \frac{dN}{f} \text{ } \mu\text{m} \quad (4.4.2)$$

For times greater than 24,400 seconds, at the tip of the pit:

$$dc = \frac{1}{3} \cdot 25 \cdot \left[\frac{N}{f} \right]^{-2/3} \frac{dN}{f} \text{ } \mu\text{m} \quad (4.4.3)$$

A pit aspect ratio of 0.2 (derived from static corrosion experiments) is taken into account by applying a correction factor of 0.2 to the pitting increment at the surface. The faster of the two calculated flaw increments, either by pitting or by fatigue, determines the propagation mode at each apex. Depending on the local conditions, the flaw increment can be due to pitting at the tip of the flaw and due to fatigue at the surface of the flaw.

Corrosion fatigue flaws are subject to mutual interaction and coalescence because of their fatigue component. Figure 4.4.4 shows a fractograph where this process has occurred.

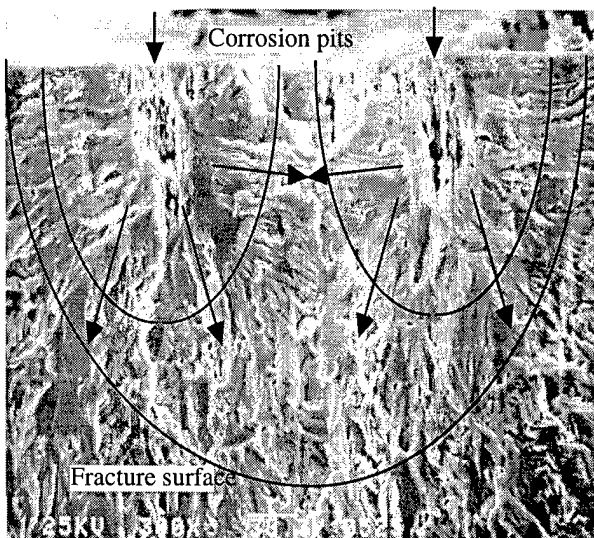


Figure 4.4.4: Interaction and coalescence of semi-elliptical flaw. $\Delta\sigma=100$ MPa, $f=10$ Hz.

The two black arrows at the top of Figure 4.4.4 point to two pits which have both initiated a semi-elliptical crack outlined by a small ellipse. After interaction and coalescence, the two individual semi-elliptical cracks merge into a single semi-elliptical crack outlined by the large semi-ellipse. The process is illustrated by the river lines which indicate the directions followed by the crack front.

The interaction that precedes coalescence translates into an increase in the stress intensity factor range. This variation is dependent upon the location on the front of the flaw. For an aspect ratio (radius/depth or a/c) less than 1, the increase in stress intensity range is almost nil at the tip of the flaw but can be significant at the surface. For example, Figure 4.4.5 illustrates the increase in the

stress intensity factor range at the flaw surface for two interacting identical semi-elliptical cracks under tensile stress.

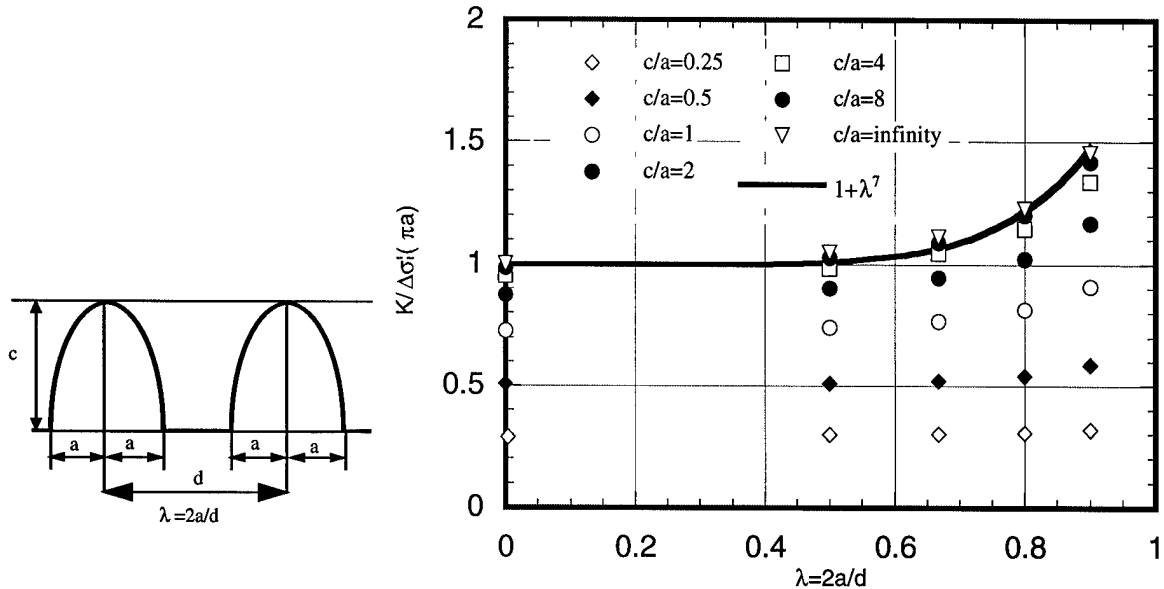


Figure 4.4.5: Effect of the interaction of two identical semi-elliptical cracks on the stress intensity factor range at the surface of the flaw as a function of the interaction parameter $(2a/d)$.

On the ordinate is plotted F_A equal to $F_A = K_A / [\sigma \sqrt{\pi a}]$, the dimensionless stress intensity factor. On abscissa is plotted the interaction parameter, λ , which is equal to the ratio of the crack diameter, $2a$ to the distance separating the crack centers, d . As the distance between crack tips decreases, the stress intensity factor increases. The results were plotted assuming two similar semi-elliptical cracks under tension in a plate. It is assumed that the same behavior is valid for a stress field at a notch, at least for the crack tips at the surface. Only collection of discrete data points derived from finite element analysis are available in the literature. The application of our model requires an analytical expression of the curves presented in Figure 4.4.5. For this case, we model the system using a polynomial function to represent the shape of the curve:

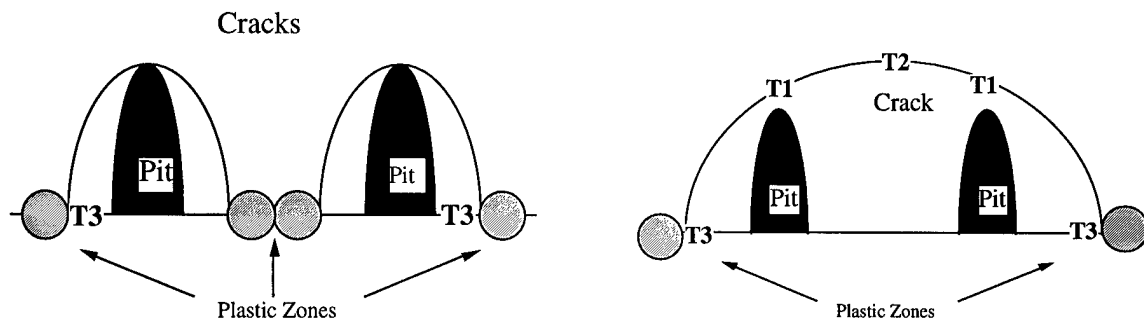
$$K = K * (1 + \lambda^7) \quad (4.4.4)$$

Figure 4.4.6 illustrates the criterion used for crack coalescence at the rivet bore. Flaw coalescence is modeled by using the criterion of overlap between the plastic zones ahead of the

crack tips. This criterion is valid since it applies to the crack tips at the rivet bore surface where the flaws propagate by corrosion fatigue. The cyclic plastic zone size is given by [6]:

$$r_p = \frac{1}{\pi} \left(\frac{\Delta K}{2 * \sigma_y} \right)^2 \quad (4.4.5)$$

As the stress intensity factor range increases, the plastic zone size increases and the time for the overlap of the plastic zones is reduced. Fatigue crack interaction results in hastening fatigue crack coalescence.



4.4.6a: Individual flaw before coalescence

4.4.6b: Overall flaw after coalescence

Figure 4.4.6 : Illustration of the coalescence process between two neighboring flaws.

Flaw coalescence in itself raises sharply the stress intensity factor at the tip of the flaw. For example, Figure 4.4.7 is a graph representing the local stress intensity factor range value along the front of the flaw as a function of angle ϕ defined in Figure 4.4.1. The bottom curve represents the variation of the stress intensity factor range along the front of an individual flaw as represented in Figure 4.4.6a. The top curve represents the variation of the stress intensity factor range along the front of the overall flaw after coalescence as represented in Figure 4.4.6b.

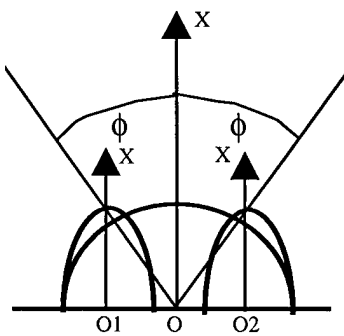
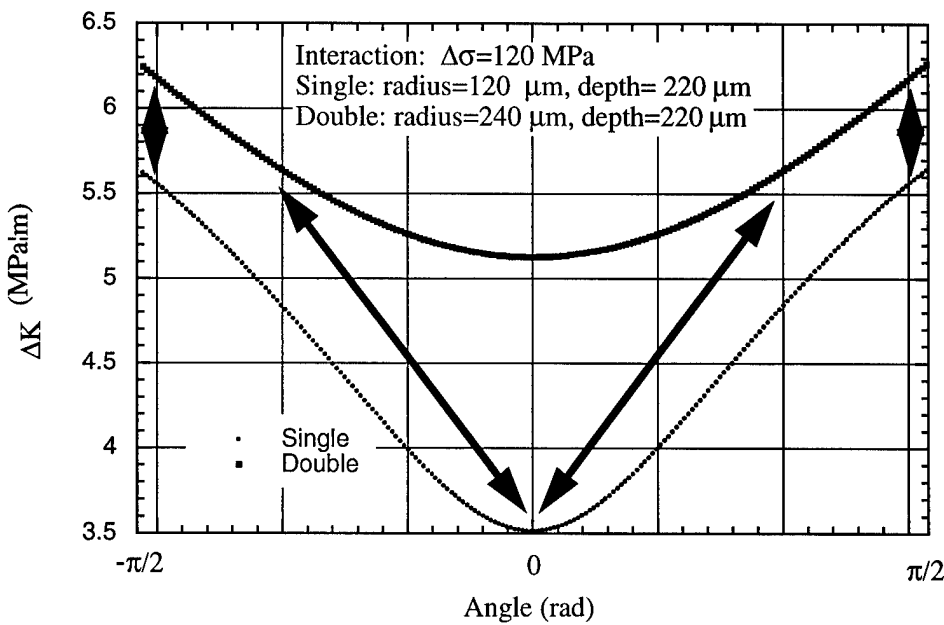


Figure 4.4.7: Variation of stress intensity factors ranges during coalescence.

The stress intensity factor at the tip of the individual cracks of Figure 4.4.6a is represented by the value at the zero angle of the bottom curve ($3.5 \text{ MPa}\sqrt{m}$). After coalescence, the tips of the individual cracks are now located at point T1 in Figure 4.4.6b and the corresponding angle in the new reference system of the overall crack is $\pi/4$ ($5.6 \text{ MPa}\sqrt{m}$). Flaw coalescence increases the stress intensity factor at the tip of the initial flaws according to the arrows at 45° in the graph of Figure 4.4.7. The tip of the final flaw after coalescence is located at point T2 in Figure 4.4.6b. Its stress intensity factor after coalescence is given by the value at the zero angle of the top curve ($5.2 \text{ MPa}\sqrt{m}$). After and before coalescence, the stress intensity factors at the surface for points T3 of Figures 4.4.6a and 4.4.6b are given by the value at angle $\pi/2$. The increase in stress

intensity factors is outlined by the vertical arrows in the graph of Figure 4.4.7 (From $5.5 \text{ MPa}\sqrt{\text{m}}$ to $6.2 \text{ MPa}\sqrt{\text{m}}$).

The increase in stress intensity factors may stop pitting and hasten the end of the transition to corrosion fatigue. The depths of pits from which a fatigue crack initiates may thus be reduced by the interaction and coalescence process. The extent of reduction will depend upon the degree of interaction between flaws, which is measured by the inter pit distance. The closer the pits are, the more likely the flaws are to interact with each other. The inter pit distance is determined by dividing the sheet thickness by the number of fatigue initiation sites.

Figure 4.4.8 illustrates our approach for simulating multiple interacting pits. For simplicity, the fatigue life model assumes that pits are evenly spaced from each other. The outer surfaces of the sheet are modeled as if they were behaving as pits in terms of interaction and coalescence. This approach implies that pit coalescence takes place at the same time as the formation of a through thickness crack. It also simplifies the simulation greatly by limiting the calculation to a single pit. A correction factor accounting for interaction is simply applied to the stress intensity factors of one isolated flaw contained in a simulation cell. As an illustration of the simulation cell, three phases are presented in Figure 4.4.8. Phase I shows a flaw which propagates in a sheet of thickness d ("interpit distance"). Phase II illustrates the time when the plastic zones come into contact with the outer surface. This outer surface can either be the real outer surface or an interface with a neighboring simulation cell containing an identical flaw. At that point, the semi-elliptical flaw is transformed into the through thickness flaw of phase III.

The inter pit distance ("d") is given by the ratio of the sheet thickness to the number of initiation sites (number of pits which initiate a fatigue crack). The effect of this parameter on final pit depth is measured by varying the number of fatigue initiation sites. Thus, the current model establishes a connection between the scatter in inter pit distance and the scatter in final pit depth.

Figure 4.4.9 illustrates the effect of heavy pitting on the fatigue crack initiation behavior and the transition from pitting to fatigue.

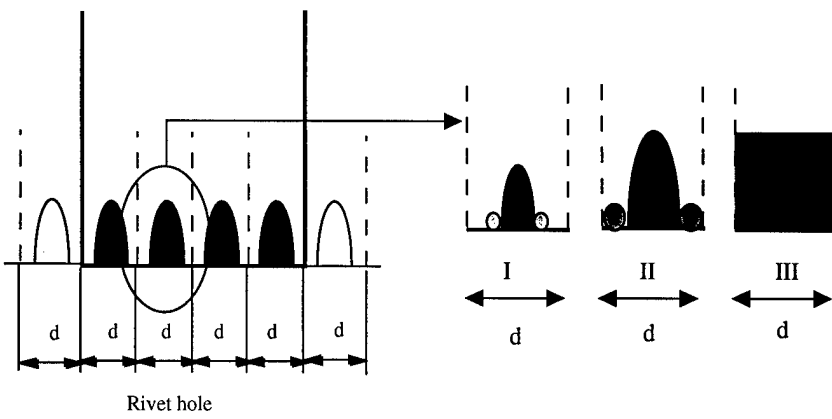


Figure 4.4.8: Cross-section of a fatigue specimen at the level of the fracture surface and detail of a simulation cell.

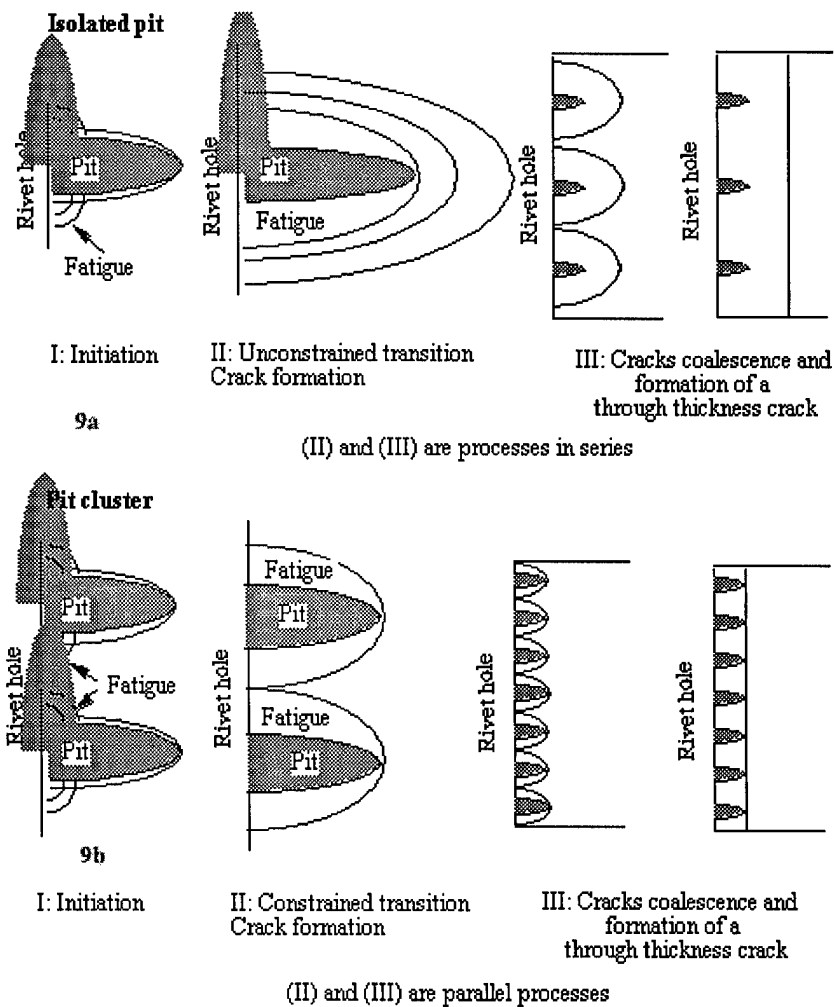


Figure 4.4.9: Fatigue cracking sequence for an isolated pit and pits in a cluster.

When pits are largely spaced as in Figure 4.4.9a, the transition from pitting to fatigue takes place without interaction between semi-elliptical flaws. For an aspect ratio of 0.2, fatigue initiates first at the flaw surface and then slowly outpaces pitting along the whole front of the flaw. When pits are closely spaced as it is the case in the cluster of pits of Figure 4.4.9b, the transition from pitting to fatigue is subject to the phenomena of flaw interaction and coalescence. As was stated earlier, the end of the transition will take place earlier than in the previous case of largely spaced pits. Flaws will interact and coalesce before the final transition takes place at the tip of the flaw. The process results into the simultaneity of the through thickness crack formation and the halt in pitting. Thus, final pit depth will be shortened.

4.4.2.3 Simulation Results and Discussion

Micro Simulation of a Pit: The Shape of the Transition Zone.

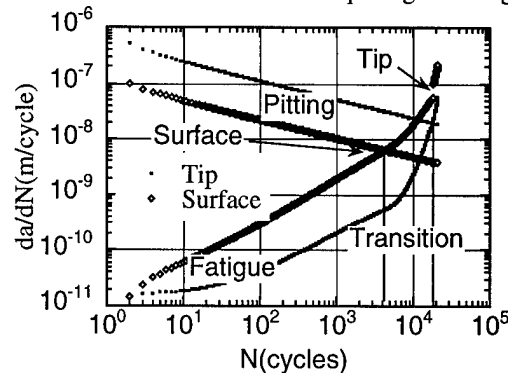
In the flaw the degree to which fatigue or active dissolution (pit growth) dominates will depend on the local relationship between the value of K and the pitting rate.

Two simulations are run at 100 MPa for frequencies of 1 and 10 Hz. Simulation are based on fatigue initiation from a single pit of initial dimensions $1\mu\text{m} \times 1\mu\text{m}$. The results are shown in Figure 4.4.10.

The intercept between the pitting curve and the fatigue curve yield the number of cycles at which transition from pitting to fatigue occurs. Figure 4.4.10 illustrates the transition in terms of ΔK , at the tip (4.4.10b) and at the surface (4.4.10c).

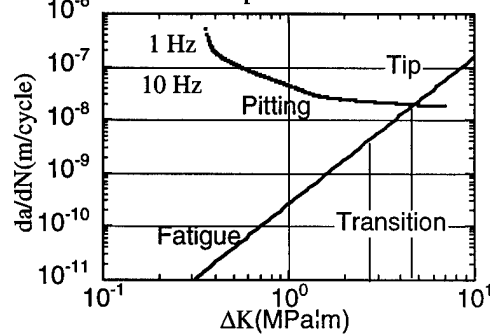
In terms of ΔK , the model estimates a transition at $3 \text{ MPa}\sqrt{\text{m}}$ at the surface and $4.8 \text{ MPa}\sqrt{\text{m}}$ at the tip. Based on the fractographic evidence, the stress intensity are estimated respectively to $3.6 \text{ MPa}\sqrt{\text{m}}$ (Greater than 3, then fatigue) and $2 \text{ MPa}\sqrt{\text{m}}$ (Less than $4.6 \text{ MPa}\sqrt{\text{m}}$, then corrosion), which is consistent with the experimental observations. The fractography indicates a pit slightly larger than predicted ($260 \mu\text{m}$ instead of $200 \mu\text{m}$). If a simulation is run with pitting rates that account for the difference, the final pit dimensions are $260 \mu\text{m} \times 108 \mu\text{m}$ and 4000 cycles is just the onset of surface fatigue. This is still in good agreement with the model.

2091-T351: Transition between pitting and fatigue.



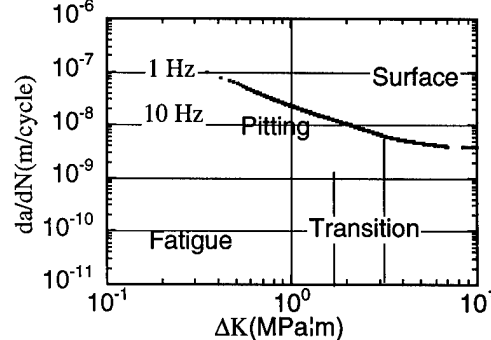
(10a)

2091-T351: Transition between pitting and fatigue at the tip of the flaw



(10b)

2091-T351: Transition between pitting and fatigue at the surface of the flaw

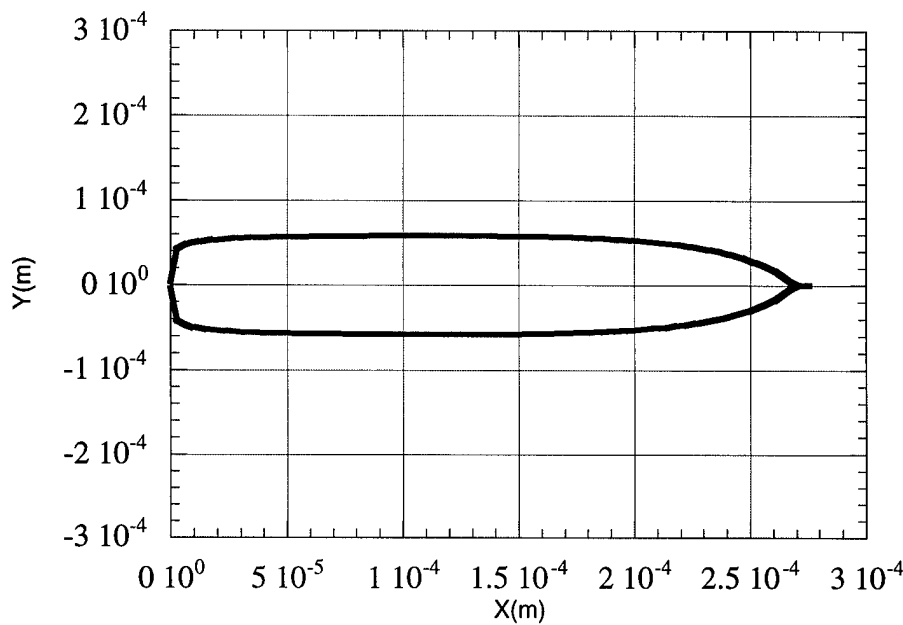


(10c)

Figure 4.4.10. Results of transition model. (4.4.10a): Output of a simulation. Fatigue initiation takes place from a single pit (4.4.10b): Fatigue and pitting rates as a function of ΔK at the tip of the flaw (4.4.10c): Fatigue and pitting rates as a function of ΔK at the surface of the flaw.

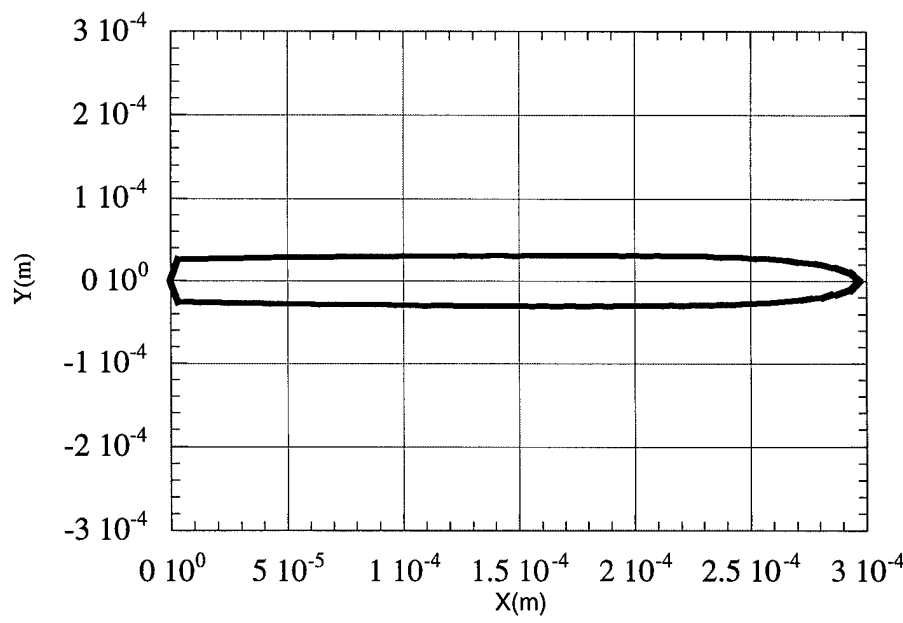
A simulation is run at 120 Mpa-1Hz for pit aspect ratios of 0.2 and 0.4. The initial defect size is $1\mu\text{m} \times 1\mu\text{m}$. The model yields the coordinates of the points which are at the transition between pitting and fatigue. Figure 4.4.11 shows the transition zone contour in the X-Y plane for aspect ratios of 0.2 and 0.4. The general elliptical shape is well reproduced. An aspect ratio of 0.2 corresponds to the pit contour whereas an aspect ratio of 0.4 would better correspond to the transition zone contour. It is likely that the fracture process alters the corrosion behavior of 2091 by opening corrosion paths that would have not been otherwise accessible for the environment. However, an aspect ratio of 0.2 is the only experimental data that is available directly and will consequently be used in further simulations.

$\Delta\sigma=120$ MPa, $R=0.05$, $f=1$ Hz
Aspect ratio=0.4, 1 pit



(11a)

$\Delta\sigma=120$ MPa, $R=0.05$, $f=1$ Hz
Aspect ratio=0.2, 1 pit

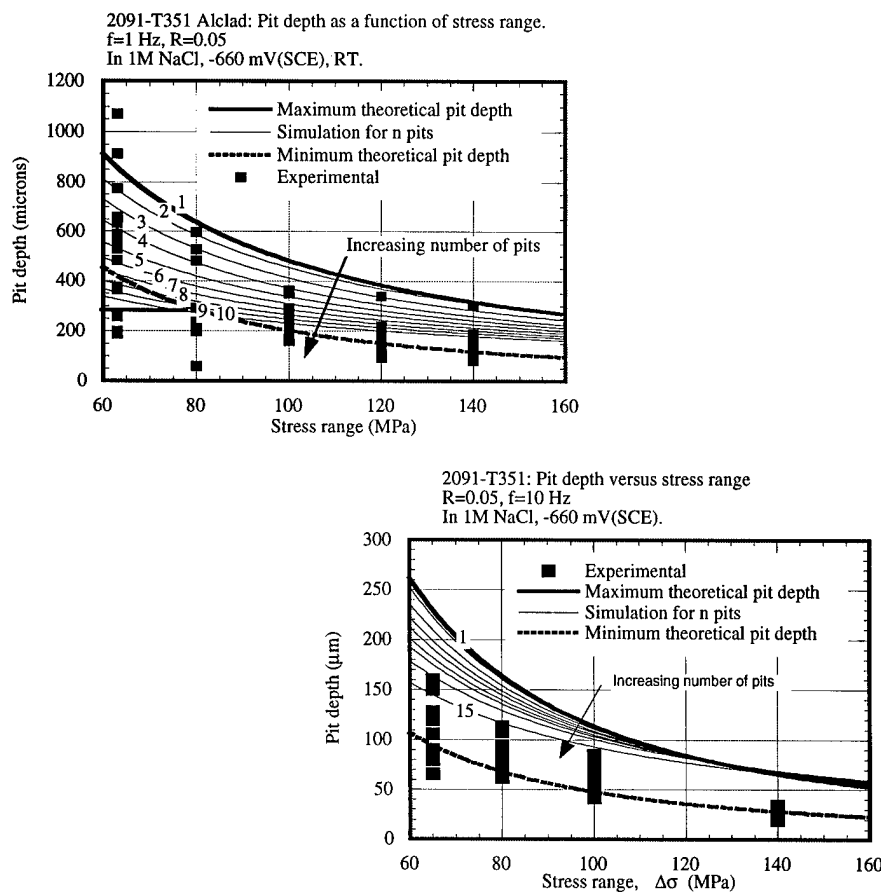


(11b)

Figure 4.4.11: Contour of the transition between pitting and fatigue in the fracture plane.

4.4.3 Fatigue Life and Pit Depth Predictions

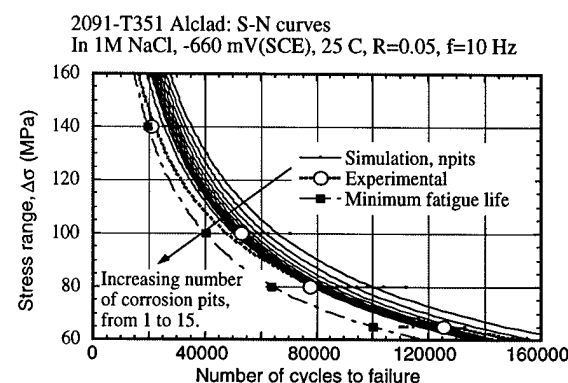
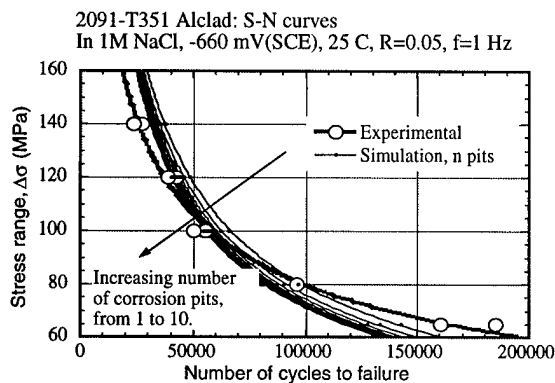
A simulation was run for thirteen different cases of frequency and stress range. The number of fatigue initiation sites was varied from 1 to 10. The initial pit size was arbitrarily chosen at $1\mu\text{m} \times 1\mu\text{m}$ to yield a finite aspect ratio in the first cycle. This choice had little effect on the simulations because of the high pitting rates of the early stages. Fatigue initiates at the flaw surface and the two dimensional flaws propagate by a mixed mode of pitting and fatigue until a through thickness crack is formed. At this point, the program integrates the $\text{da/dN}-\Delta K$ fatigue curve. The initial crack length is equal to the through thickness crack length. The final crack length at fracture is estimated for a fracture toughness of $28 \text{ MPa}\sqrt{\text{m}}$. The results are shown in Figure 4.4.12 for pit depth and Figure 4.4.13 for total fatigue life.



12a: 1Hz, clad.

12b: 10 Hz, unclad.

Figure 4.4.12: 2091-T351. Upper and lower bound for pit depth.



13a: 1Hz, clad.

13b: 10 Hz, unclad.

Figure 4.4.13: 2091-T351, S-N curves.

Since the simulated pit depth and fatigue life are not independent parameters, their agreement with the corresponding experimental values needs to be checked simultaneously.

For instance, Figure 4.4.14 explains the procedure used to check the validity of the test at 100 MPa and 1Hz. The simulation is run for a number of fatigue initiation sites ranging from 1 to 10.

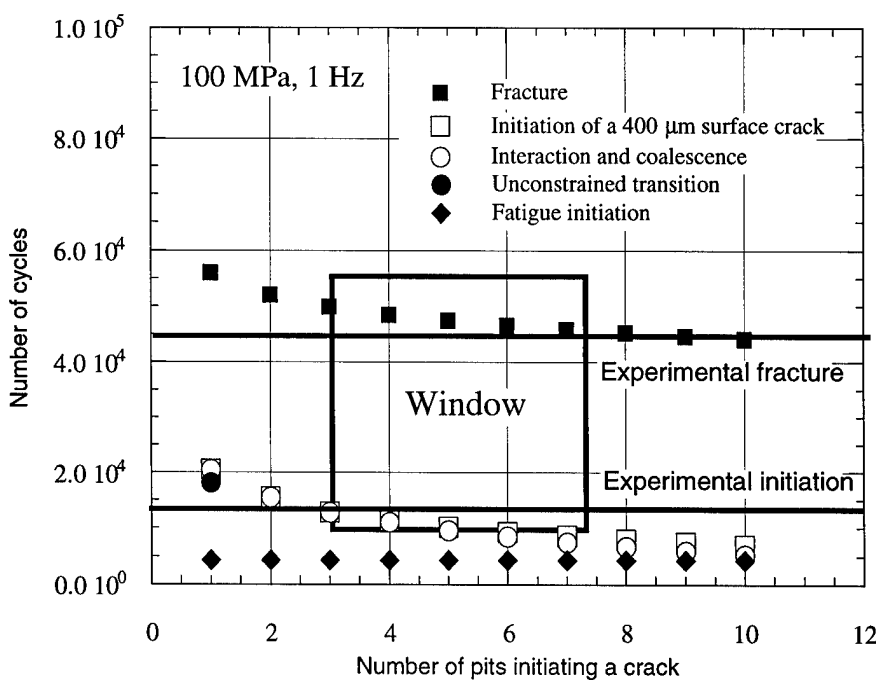


Figure 4.4.14: Example of a validity check for the simulation at 100 MPa and 1 Hz.

The program returns the number of cycles corresponding to different stages in the cracking process. Stage I is fatigue initiation at the surface of the flaw. Considering an edge crack geometry and integrating the $da/dN-\Delta K$ curve from an initial crack size corresponding to the pit depth at stage I of the simulation to failure yields the curve entitled “Minimum fatigue life” in Figure 4.4.13b. Stage II is the unconstrained transition from pitting to fatigue which takes place when the number of fatigue initiation sites is low enough. Stage III is the interaction and coalescence phenomenon which leads to the formation of a through thickness crack. Stage IV is the observation of a 400 μm long surface crack. Depending upon the length of the through thickness crack at the coalescence stage, stage IV may never happen. This is the case when the coalescence process leads directly to a through thickness crack longer than 400 μm . Stage V is the final stage and corresponds to failure of the specimens.

The experimental values of the number of cycles are corresponding to stage IV, when it exists, or stage III, and stage V. In Figure 4.4.14, the experimental values are given by the solid horizontal lines. They have been corrected by subtracting 10,000 cycles which corresponds to the time necessary to dissolve the cladding. During these 10,000 cycles, it has been verified that no fatigue initiation takes place because there is no pitting.

From the comparison of the experimental values with the results of the simulation, a window of possible numbers of fatigue initiation sites is derived. This window corresponds to a range in pit depth since every number of fatigue initiation sites yield a unique final pit depth. This range of pit depth is compared to the experimental range of pit depth as it is measured on fracture surfaces. If the two ranges are similar, the simulation is considered as successful.

At a frequency of 1 Hz, results are in very good or reasonably good agreement with the experimental results. At 10 Hz, results are only in moderate agreement in terms of pit depth and number of cycles. The two dimensional flaw model overestimates both fatigue life and pit depth. Everything happens as if fatigue transition from pitting to fatigue takes place earlier than predicted.

At 0.1 Hz, the simulation seems to agree with the experimental values, but the fractography shows clearly that general pitting took place and a simulation based on initiation from a single pit

should not describe the fatigue initiation process properly. Agreement, in this case, would seem to be fortuitous.

At 65 MPa and 1 Hz, the pit depth range agrees reasonably well with the prediction but the number of cycles to initiation and failure is clearly underestimated. At 80 MPa-1 Hz and 100 MPa-0.5 Hz, the simulation is reasonably good but severe pitting is observed.

Except in the cases of general corrosion, the model based on a semi-elliptical flaw yields an upper bound to fatigue lives and pit depth when it is applied to a single fatigue initiation site. When the transition is assumed to start and finish when fatigue initiates at the surface, a lower bound for pit depth can be derived. A lower bound is derived by integrating the $da/dN-\Delta K$ curve from an initial crack size equal to the minimum pit depth presented earlier to total failure. This assumption is supported by Figure 4.4.15 where multiple fatigue initiation sites are surrounded by crystallographic cracks whose facets are uncorroded. This proves that the passage from a pit to a through thickness crack was fast compared to other phenomena. The number of cycles to create the through thickness crack is negligible. By integration of the $da/dn-\Delta K$ curve from an initial crack size equal to the pit size, 30 μm , the total life is 18869 cycles, which is very close to the experimental value, and much better than the result given in the first simulation.

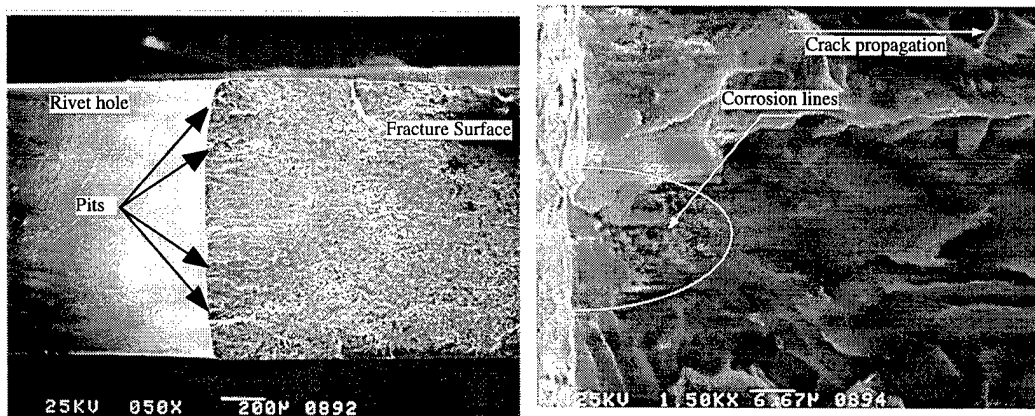
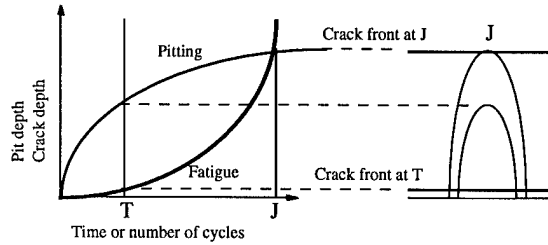
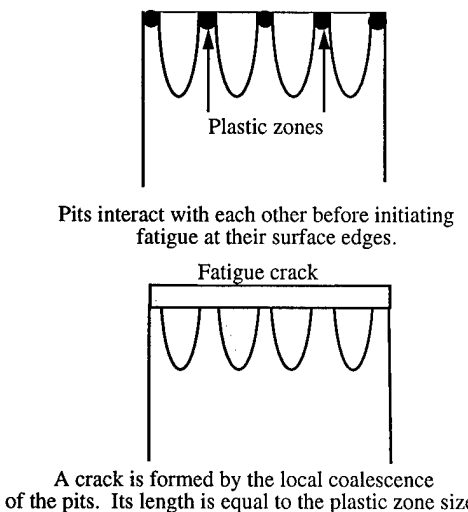


Figure 4.4.15: 2091-T351. $f=10$ Hz, $\Delta\sigma=140$ MPa. Fatigue cracks which initiate from these pits exhibit some stage I crystallographic features.

When general corrosion is involved at the surface, fatigue initiation does not proceed as described in the model. Crack tip blunting may occur and is difficult to quantify. However,

another explanation can be provided by extending the current model to the limiting case of pitting such as that described in Figure 4.4.9b. In this case, pits are considered so closely spaced that the equivalent plastic zone size before fatigue starts is large enough to trigger interaction and coalescence. This theoretical approach yields a critical plastic zone size value which is taken as the initial length of an edge crack. This edge crack propagates independently from the tip of the pits which are already deep in the material at the onset of surface fatigue. In this case, the competition between pitting and fatigue becomes unidimensionnal as shown in Figure 4.4.16.

Prediction of general corrosion



J: Time at which the crack tip gets in contact with the tip of the pit.

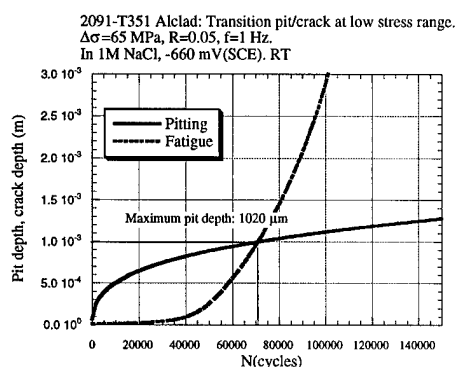
4.4.16a: Prediction of general corrosion

4.4.16b: 1D model of competition

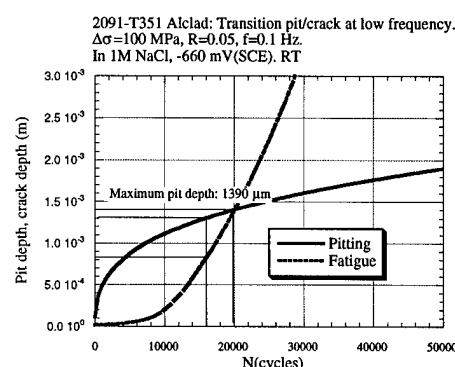
Figure 4.4.16: Prediction of general corrosion and unidimensionnal model of competition.

For instance, at 65 MPa and 1Hz, a through thickness crack is predicted at 4900 cycles, yielding a ΔK of $2.74 \text{ MPa}\sqrt{\text{m}}$ corresponding to a plastic zone size of $8.5 \mu\text{m}$. The da/dN integration yields 154,000 cycles to which 10,000 cycles for the cladding (10,000 seconds/1Hz) and 4900 cycles for the through thickness crack initiation time need to be added. This yields the value of 170,000 cycles for fracture (160,000 and 185,000 cycles experimental) and 71,000 cycles for initiation of a $400 \mu\text{m}$ crack (76,000 and 80,000 cycles experimental). Figure 4.4.17a illustrates the unidimensionnal competition between pitting and fatigue with the above values. The simulated pit depth is found to be $1020 \mu\text{m}$ and the number of cycles at the transition between pitting and fatigue are 80,000 cycles ($70,000+10,000$ cycles).

At 100 MPa-0.1Hz, a through thickness crack is created at 414 cycles, yielding a ΔK of 3.47 MPa \sqrt{m} corresponding to a plastic zone size of 14 μm . The 400 μm surface crack initiation is simulated at 13533 cycles (12533+1000 cycles) for an experimental value of 11,000 cycles. The da/dN integration yields a crack depth of 814 μm at 16,000 cycles. If one adds 1000 cycles corresponding to cladding dissolution time, the total number of cycles is 17,000 cycles. The measured crack depth at 17,000 cycles is between 800 μm and 1 mm. Figure 4.4.17b illustrates the competition process between pitting and fatigue. According to this simulation, the test was stopped too early to yield the maximum pit depth of 1390 μm . At 16,000 cycles, the maximum pit depth is calculated to be 1300 μm . One observes 1200 μm at most. It is still better than the 900-1000 μm given by the raw model of crack initiation. A net section effect may have accelerated fatigue crack growth rates, thus shortening the observed pit depth.



4.4.17a: 65 MPa, 1Hz



4.4.17b: 100 MPa, 0.1 Hz.

Figure 4.4.17: Cases of general corrosion

As a conclusion, when corrosion outpaces fatigue, the model of bidimensionnal fatigue flaw is no longer valid. Fatigue and corrosion are temporary decoupled. The final pit depth is given by an unidimensionnal model of competition between pitting and fatigue.

4.4.4 Mapping the Regimes of Fatigue Crack Initiation in the $\Delta\sigma$ -f Space.

Three regimes of fatigue initiation have been identified. The first regime is characterized by small pits of the order of 10 to 60 μm from which crystallographic cracks, or stage I fatigue, initiate. The second regime is characterized by pits of the order of 100 to 600 μm . Semi-

elliptical flaws initiate from these pits and propagate by a mixed mode of fatigue and corrosion. The third regime is characterized by pits of the order of 800 to 1200 μm deep. The metal surface at the rivet bore suffers from general corrosion. The crack front propagates parallel to the rivet bore axis. No semi-elliptical flaw is visible.

The extent of pitting in the early stages of fatigue cracking determines the dominant regime of fatigue initiation. Pit depth is given by Equation (4.4-6) that is differentiated into Equation (4.4-7):

$$a = C_p t^{2/3} = C_p \left(\frac{N}{f} \right)^{2/3} \quad \text{or} \quad \left(\frac{N}{f} \right) = \left(\frac{a}{C_p} \right)^{3/2} \quad (4.4.6)$$

$$da = \frac{2}{3} \cdot C_p \left(\frac{N}{f} \right)^{-1/3} \frac{dN}{f} \quad (4.4.7)$$

For a given crack depth, a , corresponding to a time t , the ratio of the fatigue increment to the pitting increment is given by:

$$r = \frac{da(\text{fatigue})}{da(\text{pitting})} = \frac{A \cdot \Delta K^n dN}{\frac{2}{3} C_p t^{-1/3} dt} = \frac{A \cdot \Delta K^n dN}{\frac{2}{3} C_p \left(\frac{N}{f} \right)^{-1/3} \frac{dN}{f}} \quad (4.4.8)$$

The number of cycles can be eliminated with Equation (4.4-6):

$$r = \frac{da(\text{fatigue})}{da(\text{pitting})} = \frac{A \cdot \Delta K^n dN}{\frac{2}{3} C_p \left(\frac{a}{C_p} \right)^{-1/2} \frac{dN}{f}} = \frac{3}{2} \cdot \frac{A}{C_p^{3/2}} \cdot \Delta K^n \cdot f \cdot a^{1/2} \quad (4.4.9)$$

The stress intensity factor is a function of crack length and geometry and Equation (4.4-9) can be written as:

$$r = \frac{da(\text{fatigue})}{da(\text{pitting})} = \frac{3}{2} \cdot \frac{A}{C_p^{3/2}} \cdot \Delta \sigma^n \cdot f \cdot a^{(n+1)/2} \cdot F(\phi, \frac{a}{c}, \frac{a}{t}, \frac{r}{t}, \frac{r}{b}, \frac{c}{b}) \quad (4.4.10)$$

Where F is a function of the parameters which are in brackets. When the crack length goes to zero for a constant aspect ratio, F is equivalent to a function of ϕ only. For short crack lengths, r can be approximated by:

$$r = \frac{da(\text{fatigue})}{da(\text{pitting})} = S(\Delta\sigma, f) \cdot a^{(n+1)/2} \cdot F(\phi) \quad (4.4.11)$$

$s(\Delta\sigma, f)$ is a parameter characterizing the relative importance of fatigue and pitting at the early stages of corrosion fatigue. If S is large, small pits surrounded by crystallographic cracks is expected. If S is low, general pitting is expected. In between, a transition zone is expected. Since no information is available about the absolute magnitude of this parameter, a normalized parameter is introduced. The experimental condition taken as a reference is ($\Delta\sigma_0=100$ MPa, $f_o=1\text{Hz}$). It has been observed that corrosion fatigue is characterized by a transition zone in this domain. The normalized parameter is now:

$$s = \left(\frac{\Delta\sigma}{\Delta\sigma_o} \right)^{2.76} \cdot \left(\frac{f}{f_o} \right) \quad (4.4.12)$$

The values of s are shown in Table 4.4.2 for the thirteen previous cases.

The solid lines are the boundaries of the domain where the two-dimensional flaw model works well. It is interesting to notice the correspondence between cases of different stress range and test frequency. (100 MPa, 0.5 Hz) and (80 MPa, 1Hz) were cases considered as border line in the simulation and they are almost on the same contour. It is the same for (65 MPa, 1Hz) and (140 MPa, 1Hz). (65 MPa, 1Hz) and (100 MPa, 0.1 Hz) fall in the same domain.

Once the relative strength of corrosion and fatigue are known for one case, it should be possible to derive the domain boundaries where one mechanism prevails over the others. In this case, life predictions will be easier to make.

These boundaries are not defined accurately. The underlying mechanisms supporting the suggested partition are as follows: when pit size at the transition between pitting and fatigue becomes of the same order as the grain size, a small crack effect takes place as seen by stage I fatigue in the extreme case. Fatigue initiation takes place as if it was triggered by the stress intensity factor at the surface. When pitting becomes very severe, pits link-up at the rivet bore

surface before initiating a semi-elliptical flaw. A through thickness fatigue crack is formed and it front propagate independently from the tip of the pits which were deep in the material at the time of fatigue initiation.

Table 4.4.2: Values of the parameter S for the thirteen experimental conditions.

Stress range (MPa)	Frequency (Hz)	$S = \left(\frac{\Delta\sigma}{\Delta\sigma_o} \right)^{2.76} \cdot \left(\frac{f}{f_o} \right)$
100	0.1	0.1
100	0.3	0.3
100	0.5	0.5
65	1	0.3
80	1	0.54
100	1	1
120	1	1.65
140	1	2.53
65	10	3
80	10	5.4
100	10	10
140	10	25.3
140	0.3	0.76

The plane ($\Delta\sigma, f$) can now be mapped by contour of constant s as in Figure 4.4.18.

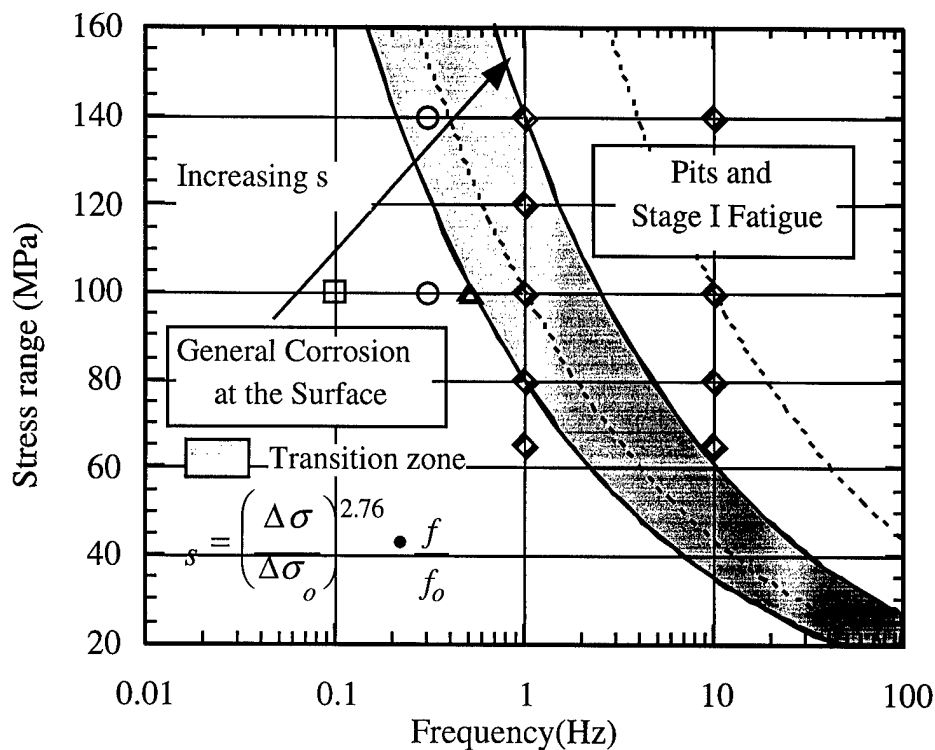


Figure 4.4.18: Domains of dominant mechanisms of fatigue initiation.

4.4.5 Theses Published Based on This Task Element

Au, H. K., "Pitting and Crack Initiation in High Strength Aluminum Alloys for Aircraft Applications", January 1996

Genkin, Jean-Marc P , "Corrosion Fatigue Crack Initiation in 2091 Aluminum-Lithium", June 1996.

4.4.6 References For This Task Element

1. Y.Kondo, Prediction of Fatigue Crack Initiation Life Based on Pit Growth, Corrosion, Vol.45, No.1, pp.7-11, 1989.
2. J.C.Newman and I.S.Raju, Stress Intensity Factor Equations for Cracks in Three-Dimensionnal Finite Bodies Subjected to Tension and Bending Loads, In Computational

Methods in the Mechanics of Fracture, Edited by S.N.Atluri, Elsevier Science Publisher, pp.312-344, 1986.

3. J.C.Newman and I.S.Raju, An Empirical Stress Intensity Factor Equation for the Surface Crack, Engineering Fracture Mechanics, Vol.15, pp.185-193, 1981.
4. C.M.Suh, K.B.Yoon and N.S.Hwang, A Simulation of the Behavior of Multi-Surface Fatigue Cracks in Type 304 Stainless Steel Plate, Fatigue and Fracture of Engineering Materials and Structures, Vol.18, No.4, pp.515-525, 1995.
5. Y.Murakami and S.Nemat-Nasser, Interacting Dissimilar Semi-elliptical Surface Flaws Under Tension and Bending, Engineering Fracture Mechanics, Vol.16, No.3, pp.373-386, 1982.
6. S.Suresh, Fatigue of Materials, Cambridge Solid State Science Series, p.163, 1992.